Understanding and Controlling Reusability, Aging Kinetics, and Sustainability of Polyamide 12 in Selective Laser Sintering

Feifei Yang

A dissertation

submitted in partial fulfillment of the

requirements for the degree of

Doctor of Philosophy

University of Washington

2022

Reading Committee:

Xu Chen, Chair

Ramulu Mamidala

Mark Ganter

Program Authorized to Offer Degree:

Mechanical engineering

University of Washington

Abstract

Understanding and Controlling Reusability, Aging Kinetics, and Sustainability of Polyamide 12 in Selective Laser Sintering

Feifei Yang

Chair of the Supervisory Committee:
Associate Professor Xu Chen
Mechanical engineering

Capable of building high-quality, complex parts directly from digital models, selective laser sintering (SLS) additive manufacturing is a core method of agile manufacturing. The semi-crystalline polymer polyamide 12 has been extensively used in SLS thanks to its superior mechanical property, stable thermal property, broad sintering window for ease of processibility, low melt viscosity to reduce porosity, and high melting enthalpy to minimize secondary sintering. However, low utilization of the costly feedstock hinders the long-term sustainability of SLS in industry, and the feedstocks undergo complex thermal and chemical degradations in SLS. Understanding and controlling on reusability, aging kinetics, and sustainability of degraded polyamide 12 in SLS remain largely unexploited.

This dissertation proposes (1) a new interlayer heating based process control method to maximize reusability of aged and extremely aged polyamide 12 powders and create parts with improved mechanical properties, (2) a novel process control approach with post-heating for SLS with (extremely) aged polyamide 12 powders to improve surface quality and build interrelations between process parameters and surface quality, (3) a combined theoretical and experimental approach to build a first-instance kinetic model for polyamide 12 degradation considering both the oxygen and laser effects in SLS, identifies (4) quantitative influences of successive reuse on thermal decomposition, molecular evolution and elemental composition of polyamide 12 residues in SLS, proposes (5) a process-oriented and mass-transfer based approach to model and predict volatile organic compound emission in SLS, and conducts (6) an in-process monitoring of temperature profiles from infrared images in various locations when sintering different polyamides in SLS.

Results show (1) the proposed method can yield printed samples with 18.04% higher tensile strength and 55.29% larger elongation at break using as much as 30% of extremely aged powders compared to the benchmark sample, (2) parts 3D-printed using the 30%-30%-40% new-aged-extremely-aged powder mixtures exhibit the smoothest and flattest surface with no unmolten particles and nearly zero porosity, (3) the laser effects are 4-time stronger than oxygen effects on polyamide 12 degradation, and the predicted oxidation matches on average 89.53% with the actual SLS degradation rates, in contrast to a 34.48% accuracy from a basic autoxidation model, (4) laser and heat lower the material onset decomposition temperatures, making the material more labile at a decreased temperature after reuse, and the carbon deposit and degradation raise the atomic percentages of C, (5) the proposed method has an average accuracy of 85.32% to the experiment results in predicting VOC emissions, and the mass-transfer coefficient, diffusion coefficient, and

partition coefficient have different influences on emission, and (6) reclaimed powders absorbed more energy during laser on periods at all positions, and the thermal conductivity for extremely aged powders decrease compared to new powders.

TABLE OF CONTENTS

List of Figures iv

List of Tables ix

Chapter 1. Introduction 1

1.1 Selective laser sintering 1

1.2 Aging behavior of polyamide12 in SLS 1

1.3 Aging mechanism of polyamide 12 powders 2

1.4 Property changes of aged polyamide 12 powders 3

1.5 Property of parts using aged polyamide 12 powders 8

1.6 Parameter setting in SLS using aged polyamide 12 powders 13

1.7 Dissertation objectives 16

Chapter 2. A process control and interlayer heating approach to reuse polyamide 12 19

2.1 Introduction 19

2.2 Proposed active interlayer heating for reusing polyamide 12 powders 22

2.3 Results 30

2.4 Discussions 40

2.5 Conclusions 45

Chapter 3. Process control of surface quality and part microstructure with post-heating 46

3.1 Introduction 46

3.2 The proposed process control with post-heating for reclaimed polyamide 12 47

3.3 Experimental results - Surface quality improvements of the 3D-printed parts 52

3.4 Discussions 61

3.5 Conclusions 64

Chapter 4. A combined theoretical and experimental approach to model polyamide 12 degradation 66

4.1 Introduction 66

4.2 The proposed approach to model polyamide 12 degradation 68

4.3 Results and discussions 77

4.4 Characteristics of the updated modelling degradation rates $\boldsymbol{\mu i}$ 89

4.5 Conclusions 96

Chapter 5. Quantitative influences of successive reuse on polyamide 12 residues 97

5.1 Introduction 97

5.2 Materials and method 98

5.3 Results and discussions 101

5.4 Conclusions 119

Chapter 6. Process-oriented and mass-transfer based methodology to model volatile organic compound emission 121

6.1 Introduction 121

6.2 Process-oriented and mass-transfer based methodology to model volatile organic compound emission 122

6.3 Results and discussions 129

6.4 The effects of h_m, D_m, and K on VOC emissions 138

6.5 Conclusions 141

Chapter 7. In-process monitoring when sintering different polyamides 143

7.1 Introduction 143

7.2 In-process monitoring when sintering different polyamides 143

7.3 Results and discussions 145

7.4 Conclusions 151

Chapter 8. Conclusions and future work 153

8.1 Conclusions 153

8.2 Future work 155

Bibliography 156

LIST OF FIGURES

Figure 1-1 (a) Dehydration polycondensation reaction of polyamide 12, and (b) polyamide 12 unit 2
Figure 1-2 Correlations between chapters 18
Figure 2-1 Proposed method for reusing aged and extremely aged polyamide 12 powders23
Figure 2-2 Powders coated on the powder bed 24
Figure 2-3 In-house built and customized SLS testbeds 26
Figure 2-4 Experiment plans about reusability of aged and extremely aged powders and influences of interlayer heating (The mixed powders are in volume percentages) .. 28
Figure 2-5 Tensile bar dimensions and tensile test machine 30
Figure 2-6 Pictures of some tensile bar samples 33
Figure 2-7 Stress-strain curves of samples printed using pure powders 34
Figure 2-8 Stress-strain curves of benchmark samples 35
Figure 2-9 Stress-strain curves of samples printed using new-extremely aged mixed powders without interlayer heating 37
Figure 2-10 Comparisons of stress-strain curves of benchmark samples and samples using new-extremely aged mixed powders with and without interlayer heating 39
Figure 2-11 Comparisons of stress-strain curves of benchmark samples and samples using new-aged-extremely aged mixed powders with and without interlayer heating 40
Figure 2-12 Comparisons of sample tensile strengths 41
Figure 2-13 Comparisons of sample elongations at break 43
Figure 2-14 Comparisons of sample Young's modulus 44
Figure 3-1 Proposed SLS with post-heating method to improve part surface quality when using reclaimed polyamide 12 powders 48
Figure 3-2 Post-heating based SLS process (The mixed powders are in volume percentages) 51
Figure 3-3 The SEM images of benchmark part using 100% new polyamide 12 powders at different magnification ratios (a) 200, (b) 500, (c) 2000, and (d) 10000 53

Figure 3-4 The part using 100% new polyamide 12 powders with (a) 20 seconds, (b) 60 seconds, (c) 120 seconds and (d) 300 seconds post-heating at a magnification ratio of 500 .. 54
Figure 3-5 Parts printed using 100% extremely aged polyamide 12 powders with and without post-heating 56
Figure 3-6 Parts using new-aged mixed or new-extremely-aged mixed polyamide 12 powders with no post-heating and with 300 seconds post-heating 60
Figure 3-7 Parts using new-aged-extremely-aged mixed polyamide 12 powders with no post-heating and with 300 seconds post-heating 61
Figure 3-8 Comparisons of unmolten particles, coalescence and roughness of parts using polyamide 12 powders of different combinations without post-heating 62
Figure 3-9 Comparisons of unmolten particles, coalescence and roughness of parts using polyamide 12 powders of different combinations with 300 seconds post-heating ... 63
Figure 3-10 Microstructure examinations of (a) polyamide 12 parts without post-heating, and (b) polyamide 12 parts with 300 seconds post-heating at a magnification of 10000 64
Figure 4-1 The proposed approach to build the kinetic scheme of polyamide 12 aging in SLS considering the coupled oxygen and laser effects 68
Figure 4-2 SLS testbed and samples 73
Figure 4-3 Proposed procedures to build the kinetic model of polyamide 12 involving the coupled oxygen and laser-induced aging in SLS 75
Figure 4-4 Experimental relationship between μi and σiolO2 for sample i 76
Figure 4-5 Experimental relationship between μi and ti for sample i 77
Figure 4-6 FTIR test results of different polyamide 12 powders and different 3D-printed part samples with different oxidation time 78
Figure 4-7 Comparisons between the modelling aging rates μi and the actual SLS aging rates ηi for different printed samples using polyamide 12 powders 80
Figure 4-8 Sensitivity analysis and the fitting equations between μi and σiolO2 to an R-squared second-order polynomial 83
Figure 4-9 Sensitivity analysis on concentration changes of the oxidative components as oxidation time ti increases using the updated oxidation model 84

Figure 4-10 Fitting equations between the updated modelling degradation rates μi and oxidation time ti 86
Figure 4-11 The comparisons between the predicted degradation rates μi and the actual SLS degradation rates ηi of the SLS sample group 2 (Parts using polyamide 12 powders of different combinations) 88
Figure 4-12 Curves between the updated modelling degradation rates μi and oxidation time ti with decreasing $\sigma i - SLSolO2$ for different part samples 91
Figure 4-13 Curves between the updated modelling degradation rates μi and oxidation time ti with increasing $\sigma i - SLSolO2$ for different part samples 93
Figure 4-14 Comparisons of μi at 1200 s for different samples to compare material degradation rates at a more stable state 93
Figure 4-15 Curves between the updated modelling degradation rates μi and oxidation time ti with different preheating temperatures for different part samples 95
Figure 4-16 Comparisons of μi at 1200 s (μi@1200 s) between (a) Samples with different preheating temperatures, and (b) Preheating temperatures for different samples 96
Figure 5-1 (a) The flowchart to successively reuse polyamide 12 in the studied SLS process, and (b) Dimensions of ASTM standard Type 5 specimen used in this study 100
Figure 5-2 Samples of parts 3D-printed from the surveyed list of polyamide 12 materials in this research 102
Figure 5-3 Identified differences of the basic flowability energies between powder samples 103
Figure 5-4 Observed differences of particle size distributions between different reclaimed powder samples in this research 105
Figure 5-5 Observed differences of TGA curves between polyamide 12 samples in the air (a) and nitrogen (b) 106
Figure 5-6 Obtained differences of melting curves between polyamide 12 samples - The first heating cycle 109
Figure 5-7 Observed differences of crystallization curves between polyamide 12 samples - The cooling cycle 110

Figure 5-8 Observed differences in melting curves between polyamide 12 samples - The second heating cycle 111
Figure 5-9 Identified differences of ^{1}H NMR (a) general peaks of polyamide 12, and (b) spectra of polyamide 12 powders and printed parts in this research..... 113
Figure 5-10 Analyzed differences of ^{1}H NMR spectra comparisons of polyamide 12 (a) new powders, and (b) part 3D printed using 8-time reused powders in this study 114
Figure 5-11 Obtained differences of elemental atomic percentage between polyamide 12 with different reuse times in this study 115
Figure 5-12 SEM images of polyamide 12 powder samples at a magnification ratio of 500 for new and three classes of reused powders..... 117
Figure 5-13 Obtained SEM images of polyamide 12 part samples at a magnification ratio of 500 for parts using new and three classes of reused powders..... 117
Figure 5-14 Densities of tensile bars 3D printed using differently reused polyamide 12 powders 118
Figure 5-15 Stress-strain curves of polyamide 12 parts..... 118
Figure 6-1 Experiment setup..... 123
Figure 6-2 Average emission-time curve and multi-stage accumulated emission-time curve 125
Figure 6-3 Schematic shown of single-layer model 126
Figure 6-4 Schematic shown of multiple-layer model..... 127
Figure 6-5 Experimentally tested VOC emissions in cases 1-6 (Stages a, b, c, d, and e are respectively background, recoating, preheating, printing, and post-printing stages.)131
Figure 6-6 Modelling of VOC emissions in Case 1 during different stages using different models 132
Figure 6-7 The predictions of VOC emissions in the background stage 133
Figure 6-8 The predictions of VOC emissions in the recoating stage 134
Figure 6-9 The predictions of VOCs emission in the preheating stage 135
Figure 6-10 The predictions of VOC emissions in the printing stage 136
Figure 6-11 The predictions of VOC emissions in the post-printing stage 137

Figure 6-12 Method verification (a) comparison between experiment 05 and modelling, (b) accuracy of the modelling results 138
Figure 6-13 The accumulated VOC emissions with h_m decreasing in cases 1-6 139
Figure 6-14 The accumulated VOC emissions with h_m increasing in cases 1-6 139
Figure 6-15 The accumulated VOC emissions with D_m decreasing in cases 1-6 140
Figure 6-16 The accumulated VOC emissions with D_m increasing in cases 1-6 140
Figure 6-17 The accumulated VOC emissions with K decreasing in cases 1-6 141
Figure 6-18 The accumulated VOC emissions with K increasing in cases 1-6 141
Figure 7-1 Sample position and number 144
Figure 7-2 Different positions on the SLS powder bed heated to different target temperatures 147
Figure 7-3 Energy absorption during laser sintering 147
Figure 7-4 $\sum\Delta T$ during laser on when sintering new, aged and extremely aged powders 149
Figure 7-5 Comparing the energy absorption curves during laser on for new and extremely aged powders 150
Figure 7-6 Thermal conductivity for aged and extremely aged powders 151

LIST OF TABLES

Table 1-1 Aging mechanism of polyamide 12 powders in SLS 3
Table 1-2 The impacts of the low energy density and the high energy density on powder and part properties..... 15
Table 1-3 Recommended process parameter sets for polyamide 12 powder [70, 74, 75] 16
Table 2-1 Printing results about reusability of extremely aged powders and influences of interlayer heating 30
Table 4-1 SLS printed samples using polyamide 12 powders, the calculated density, and oxidation time 72
Table 4-2 The elementary reaction constants for thermal oxidation of polyamide 12 at 160 °C [107, 108, 110]..... 74
Table 4-3 The elementary reaction constants for thermal oxidation of polyamide 12 between 90 and 150 °C [107, 108, 110]..... 77
Table 4-4 SLS sample group 1..... 80
Table 4-5 The calculated coefficients of the coupled oxygen and laser effects, $\sigma i - SLSol$, in the SLS process..... 83
Table 4-6 The coefficients of the actual coupled laser and oxygen effects in SLS, $\sigma i - SLSol$, and the fitting equations between the updated modelling degradation rates μi and oxidation time ti..... 87
Table 4-7 SLS sample group 2..... 87
Table 4-8 Comparisons between the actual SLS degradation rates ηi, the modelling degradation rates μi from the basic autoxidation model, and the updated modelling degradation μi from the proposed kinetic model 89
Table 4-9 The decreasing $\sigma i - SLSol$O2..... 90
Table 4-10 The increasing $\sigma i - SLSol$O2 92
Table 4-11 Comparisons of μi@1200 s between the original $\sigma i - SLSol$O2 and the decreased/increased $\sigma i - SLSol$O2 for different samples 94
Table 5-1 Processing parameters in successive reuse of polyamide 12..... 99

Table 5-2 Identified differences of thermal decompositions between polyamide 12 samples in this study 106
Table 5-3 Identified differences in melting behaviors of polyamide 12 samples in the first heating cycle in this study..... 109
Table 5-4 Analyzed differences of crystallization behaviors between polyamide 12 samples in the cooling cycle in this study..... 110
Table 5-5 Identified differences of melting behaviors between polyamide 12 samples in the second heating cycle in this study..... 111
Table 5-6 Identified differences of elemental compositions between polyamide 12 samples 116
Table 5-7 The comparisons on the mechanical properties of polyamide 12 tensile bars 119
Table 6-1 Processing parameter sets in our study..... 123
Table 6-2 Parameters used in multi-stage emission modeling [161]..... 128
Table 6-3 Parameters h_m, D_m, and K decreasing and increasing 129
Table 6-4 The chosen models for cases 1-6..... 132
Table 7-1 Coordinates of centers and actual data points 144
Table 7-2 The first laser on positions on each part sample..... 147
Table 7-3 Comparisons when sintering new powder and extremely aged powder 150
Table 7-4 Prediction of thermal conductivity for aged and extremely aged powders 151

ACKNOWLEDGEMENTS

I would like to express my thanks to all the people who helped me during the wonderful journey. First and foremost, my sincere thanks are to my advisor Professor Xu Chen for his great support and guidance. I feel grateful and consider myself extremely lucky to work under his supervision in the past years. He has been incredibly patient and nice to provide guidance and encouragement when I feel frustrated and doubted during the journey. He is always generous with words of praise on students' work and gives students good opportunities to present the research.

I also want to sincerely thank my committee members, Professor Ramulu Mamidala, Professor Mark Ganter, and Professor Navid Zobeiry, for the great help and support along the way. Thanks for the recognition and positive comments on my work, which make me more confident. Thanks to the industrial collaborators I have worked with for supporting our projects, Greg Lalier (Unilever), John Bartolone (Unilever), Angela Schnuerch (Xerox), and Chunliang Lu (Xerox).

Working in the Mechatronics, Automation, and Control Systems (MACS) lab has truly been a pleasure. I enjoyed the time spent with the lab mates, studying and discussing together. Thanks to Thomas Chu, Xiaohai Hu, Aaron Khouvong, Anthony Cheng, Win Sheng Khoo, Colin Acton, and all the other graduate students who work and previously worked in the MACS lab.

Finally, I would like to thank my family with all my love. Thanks to my husband Yanbo for the continuous accompany, encouragement and love along the journey. Thanks to my parents for being supportive and considerate when I study to pursue the dream. Thanks to my younger brother for accompanying and looking after the parents for these years.

DEDICATION

to my family

Chapter 1. INTRODUCTION

1.1 Selective laser sintering

Extensively studied and applied to making complex products ranging from micro- to macro-scales directly from a digital model, additive manufacturing is poised to become an underpinning of the next industrial revolution [1-4]. A powder-based additive manufacturing process capable of fabricating complex metallic and high-performance polymeric parts [5, 6], selective laser sintering (SLS) represents one popular and high-end 3D printing technique [7-9]. A typical object in SLS is built from thin layers of powder materials. During the solidification of each layer, a high-power laser moves at several meters per second to form a microscopic melt pool, and selectively sinter/melt the particle powders. After consolidation, the powder bed lowers by the thickness of a new thin layer. New powders are then spread over the current deposit to start the next repetition.

Among the suitable materials for SLS, polymers are the first and one of the most applied [10, 11]. Three types of commonly used polymers are thermoplastics, thermosets, and elastomers, wherein thermoplastics are the most popular due to their high mechanical performance, chemical resistance, and excellent recyclability [12, 13]. Thermoplastics mainly include amorphous polymers such as polycarbonates (PCs), and semi-crystalline polymers, such as nylons (polyamide) [11]. In particular, semi-crystalline polymers have proved to be more suitable for high-strength functional prototypes in SLS than amorphous polymers [14, 15]. Among the semi-crystalline polymers, polyamide 12 has attracted converging interests due to its suitability, ease of processability (i.e., broad sintering window), stability, dimensional accuracy, superior chemical/physical properties [16, 17], widely used in medical, automotive, aerospace, and biomedical industries [1, 18, 19].

1.2 Aging behavior of polyamide12 in SLS

1.2.1 Microstructure of polyamide 12 powders

The microstructures of polyamide 12 (semi-crystalline polymers) consist of amorphous regions and crystalline regions, and the molecule structure of polyamide 12 is a combination of carbon atoms with the amide group (-NHCO-) [20]. The typical crystal structure of polyamide 12 exhibits both α and γ phases. The polymer chains in the α-form are oriented in an unparallel way. In the more stable γ-form with a hexagonal crystal structure, chains are oriented in parallel [21,

22]. The α-form contributes to the brittleness of the crystal, while the γ-form enhances the toughness due to the twisted helical conformations around amide segments. The chain flexibility of the semi-crystalline polymer increases as more amide groups are present. The crystalline and amorphous regions determine the toughness of the polymer because of the irregular arrangement of the molecule chains.

At the molecular level, new polyamide 12 powders contain long molecular chains. The chains form by linking the polyamide 12 monomers together through the polycondensation reaction with the by-product H_2O (Figure 1-1a). In the long molecular carbon chains, a polyamide 12 unit (Figure 1-1b) consists of 11 methylene groups (in a linear chain) linked by an amide group, forming the basic chemical microstructure of the original polyamide 12 powders.

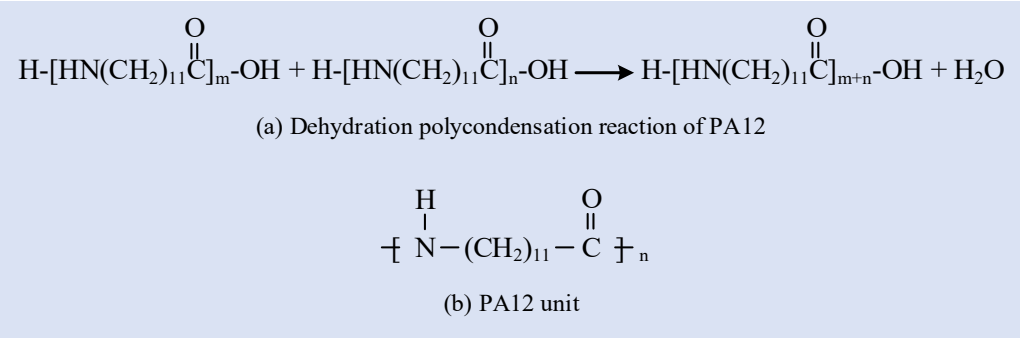

Figure 1-1 (a) Dehydration polycondensation reaction of polyamide 12, and (b) polyamide 12 unit

1.2.2 Aging behavior

Various grades of polyamide 12 powders from different suppliers are used in SLS. New powders go through complex thermal histories during powder coating, energy absorption, material consolidation, and cooling [23]. Only a small part of the new powders is sintered (e.g., 10% ~ 20%) during SLS [24, 25]. A majority of powders remain unmolten and can be reused theoretically. Due to the heating and cooling cycles, both the physical and chemical properties of the unmolten polyamide 12 powders change. Such changes are referred as powder aging. In general, aging negatively impacts powder shape, microstructures, chemical components, molecular chains, flowability, and viscosity. Vacuum and nitrogen atmosphere both reduce oxidative reactions that exacerbate powder aging [26]. Also, during sintering, the unused polyamide 12 powders remain at elevated temperatures below the melting point for an extended period. This creates a denser crystal morphology to increase the melting point, and increases the chain length due to solid-state polycondensation [21].

1.3 Aging mechanism of polyamide 12 powders

The aging mechanism of polyamide 12 powders is complex and covers a series of physical and chemical degradations. We summarize and evaluate the physical and chemical degradations in Table 1-1. Physical degradation is a reversible process, occurring under thermal load/high temperature, and leading mainly to relaxation of orientations, concentration changes, agglomeration, and post-crystallization [23, 27, 28]. Post-crystallization results in increased crystallization degree, increased lamellae thickness, crystal structure change, and spherulite growth. With crystal structure changing, material has shrinkage and warpage. Through spherulite growth, irregular chains begin to form regular chain-folded structures [20]. Aside from the physical degradation, irreversible chemical degradation dominates in the aging process. Generally, chemical degradation changes the chain structures of polymers through chain scission, cross-linking, lengthening, or branching resulting from oxidation, hydrolysis, and post-condensation [19, 28-30]. These behaviors lead to more significant differences between new and aged powders [31]. Previous works have identified that thermal oxidation, solid-state post-condensation, and Brill Transition of peak merging are three main chemical degradation mechanisms of polyamide 12 in SLS [21, 24, 32, 33].

Table 1-1 Aging mechanism of polyamide 12 powders in SLS

Item	Aging mechanism	
	Physical degradation [20, 23, 27, 28]	Chemical degradation [19, 21, 28-30, 34]
Reversibility	Reversible [23]	Irreversible [28]
Role	Secondary	Dominant [24, 34]
Cause	Thermal load/High temperature [28]	High temperature/Oxygen/Laser
Mechanism	• Relaxation of orientations • Agglomeration • Post-crystallization	• Thermal oxidation • Solid-state post-condensation • Brill Transition of peak merging • Hydrolysis
Effects on material	• Concentration change • Particle aggregation • Spherulites growth/structure • Increased crystallization degree • Increased lamellae thickness	• Molecular chain scission • Molecular cross-linking • Chain branching • Chain lengthening • Thermal property change

1.4 Property changes of aged polyamide 12 powders

1.4.1 Particle surface morphology

In SLS, polyamide 12 powders are exposed to a long period of heating cycles during the pre-heating and sintering processes. These processes accelerate the evaporation of moisture or alcohol inside the powders. Moreover, combined with recycling and repeated expansions/shrinkages in the

heating and cooling cycles, surface morphology of aged polyamide 12 powders shows increased cracking or fragmentation [21, 24, 35, 36].

1.4.2 Particle microstructures

In the crystalline region, microstructures of aged polyamide 12 particles exhibit significant differences compared to new particles. For aged polyamide 12, post-crystallization process starts to form spherulite structures when cooling down from the pre-heating temperature. Firstly, nucleation occurs to form spherulite sites for spherulite growth. With temperature reducing, spherulites start to grow, then radiate from the central regions of the spherulite core, and form spherical structures eventually [19, 37]. This behavior leads to spherulite aggregation and crystallite formation.

When temperature is between the pre-heating temperature and the glass transition temperature, the mobility of the molecular chains increases. Free radicals form, attracting nearby molecular chains and other free radicals to form longer and more complex spherulite structures. The longer the powders stay under the heating and cooling cycles, the more complex the spherulite structures become. Thus, in- and post-process aging lead to rapid spherulite growth, dense spherulite structures, and high crystallinity of the particle materials. This explains why the microstructure of the aged powders appears to be more complex than new ones [20, 24]. It is also noteworthy that recycled polyamide 12 powders have more spherulite structures to spread. Therefore, recycled polyamide 12 has a regular chain-folded state to save space while the new powders exhibit an irregular state [20].

1.4.3 Thermo-chemical property changes

Thermo-chemical properties of polyamide 12 powders directly influence particle bonding and fusion in SLS, hence are crucial to degradation and reusability. This subsection evaluates key changes in melting and cooling behaviors after polyamide 12 aging, along with insights into the underlying mechanisms and different causes of the changes.

The powder melting/crystallization are usually evaluated by the Differential Scanning Calorimetry (DSC) technology [16, 21, 24, 38]. Typical DSC graphs with specific heat flow consists of both heating and cooling cycles for semi-crystalline thermoplastics. Melting is endothermic since we have to provide energy to the system, the opposite for crystallization [16]. Crystallization during processing inversely impacts SLS feasibility. To inhibit crystallization, the material temperature is kept between melting and crystallization temperatures [16]. This is critical

to ensure proper adhesion between sintered layers, overall part dimensional stability, and to prevent unused powder from melting around the sintered part.

Compared to the new powders, aged polyamide 12 powders demonstrate noticeable changes in powder melting and crystallization. For EOS GmbH polyamide 12 processed on a DTM Sinterstation 2000 with CO_2 laser (optimal parameters: pre-heating temperature 170 °C, laser power 5 W, scanning speed 600 mm/s, scan spacing 0.3 mm, and layer thickness 0.15 mm), a broadened melting trajectory appears in the heating process of aged powders [24]. It indicates an increased melting shoulder interval, defined as the temperature ranges between the start and final melting points. The melting shoulder interval of aged EOS polyamide 12 is 10.8 °C, while that of new EOS polyamide 12 is 7.9 °C [24].

For VESTOSINT X1556, Evonik polyamide 12 processed on the HK P320 SLS system (optimal parameters: pre-heating temperature 167 °C, laser power 18 W, scanning speed 4000 mm/s, scan spacing 0.3 mm, and layer thickness 0.1 mm), the aged polyamide 12 shows the wider sintering window, defined as the temperature interval between onset melting and onset crystallization [35]. The sintering window of aged polyamide 12 is 31 °C, while that of new polyamide 12 is 29.96 °C [35]. Meanwhile, using the same SLS system and processing parameters, the melting enthalpy and crystallization enthalpy of VESTOSINT X1556, Evonik aged polyamide 12 decrease [21]. The melting enthalpy of VESTOSINT X1556, Evonik aged polyamide 12 is 80.71 J/g, and that of new is 96.62 J/g [21]. The crystallization enthalpy of Evonik aged polyamide 12 is 42.13 J/g in comparison to 45.03 J/g of new polyamide 12.

Due to increased chain length in the aged powder promoted by melt-state polycondensation, the chain mobility decreases in the molten state. As a result, lower crystallinity (VESTOSINT X1556, Evonik polyamide 12; aged: 44.22%; new: 46.94% [35]) and lower crystallization temperature (EOS GmbH polyamide 12; aged: 150.40 °C; new: 152.14 °C) is typically observed during cool-down. This phenomenon is clear from the reduction in the crystallization enthalpy in the aged powder (EOS GmbH polyamide 12; aged: 48.42 J/g; new: 50.15 J/g).

It is worth mentioning that, though references [21, 35] claimed the crystallinity reduction after reuse, references [20, 24] reported increased crystalline ratios with reuse. The main reason for this divergence is that the researchers performed the experiments using polyamide 12 from different vendors. The VESTOSINT X1556, Evonik polyamide 12 was used in references [21, 35], and the EOS GmbH polyamide 12 was applied in references [20, 24]. The results suggest that polyamide

12 material crystalline ratios after reuse may increase or decrease, depending on the source of materials, the fabricating technologies, the producing environment, and the types of additives.

1.4.4 Coalescence behavior

Coalescence behavior represents the phase change of polyamide 12 powders from a solid-state to the molten phase. Hot stage microscopy shows three stages (slow softening, fast coalescence, and molten phase) of the material coalescences [24]. For polyamide 12 EOS GmbH, new powders always coalesce fast during the test: slow softening (from 160 °C to 180 °C), fast coalescence (at 190 °C), and molten phase (at 200 °C). However, aged powders show similar behavior with new ones initially, but need more time to form the molten phase at a higher temperature eventually: slow softening (from 160 °C to 180 °C), fast coalescence (from 190 °C to 210 °C), and molten phase (> 210 °C). It is due to its stable chemical structure and numerous high melting points. Good coalescence is the prerequisite of uniform solidification. Uniform solidification is crucial to form smooth, dense surfaces and good mechanical properties [39].

1.4.5 Molecular weight

The molecular weight of aged polyamide 12 powders increases compared to new ones, and the gel permeation chromatography (GPC) analysis is usually applied to identify the molecular weight distribution [40, 41]. The increased molecular weight of aged polyamide 12 powder is caused by the chain cross-linking from thermal oxidation [24, 26] and the accelerated post-polycondensation [42]. These effects make the material molecular chains longer, denser and more complex. The weight-average molecular weight (M_w) and number-average molecular weight (M_n) rise with the increased aging temperature and aging time [20]. For EOS polyamide 12, when aged at 120 °C for 110 hours, the weight-average molecular weight increased by 0.4×10^5 g/mol compared to new material; when aged at 170 °C for 110 hours, the weight-average molecular weight increased by 2.5×10^5 g/mol; when aged at 120 °C for 180 hours, the weight-average molecular weight increased by 0.6×10^5 g/mol [19]. The weight-average molecular weight and number-average molecular weight of EOS polyamide 12 are respectively 76950 g/mol (M_w, new), 38800 (M_n, new) and 926500 g/mol (M_w, 3-time recycled), 111000 (M_n, 3-time recycled) [20].

Cumulative build time is an important parameter affecting particle molecular weight distribution [38]. With different build time of 10.6 and 26.6 hours (applying the same preheating temperature), the average molecular weights are 49400 g/mol and 61100 g/mol [38]. A longer build time leads to a higher molecular weight.

Pre-heating temperature is another parameter affecting material molecular weight [20]. With different pre-heating temperature of 164 °C, 168 °C, and 172 °C (applying the same build time), the average molecular weights are 42200, 45500, and 49700 g/mol [38]. A higher pre-heating temperature results in a larger molecular weight. However, the cumulative build time has larger influences on material molecular weight than the pre-heating temperatures. The reason is that the pre-heating temperatures are controlled in a limited operation window around 170 °C to ensure process feasibility, while the ranges of the cumulative build time are normally much wider.

1.4.6 Flowability

Good flowability is necessary to enable processibility of raw materials and deposition of the fabricated layers in SLS [43, 44]. Previous works have reported to study the static/dynamic flow behaviors, and to improve the flowability of polyamide 12 powders through adding TiO_2 and silica [44-46]. Particle shape largely affects powder flowability [46]. Usually, particles with high sphericity show high flowability, while the irregular, potato-shaped, or rough-edged particles present low flowability.

Aging causes different effects on flowability of different polyamide 12 powders. For EOS polyamide 12, new powders exhibit good flowability and processability, while flowability of aged powders (reclaimed from an EOS P 390 SLS machine, processing parameters: pre-heating temperature 171 °C, laser power 40 W, scanning speed 2800 mm/s, scan spacing 0.3 mm, and layer thickness 0.15 mm) shows a significant decrease after degradations [36]. The decreased flowability adversely impact powder reuse/recoating. For Sinterit polyamide 12 new powders, the basic flowability energy is 924 mJ, while that of 5-, and 8-time reused powders (reclaimed from a Sharebot SnowWhite SLS 3D printer, processing parameters: pre-heating temperature 160 ºC, layer thickness 0.1 mm, and around 200 minutes for one printing) are 846, and 822 mJ [47]. Reuse improves flowability of Sinterit polyamide 12.

1.4.7 Rheology

1.4.7.1 Viscosity

Due to degradations, aged polyamide 12 powders have longer molecular chains, more complex chemical structures, and increased molecular weight, largely influencing viscosity [21, 24]. EOS polyamide 12 was reported to have increased zero-shear viscosity after aging [19, 24, 48]. Moreover, a higher aging temperature or longer aging time lead to a larger viscosity [24]. The zero-shear viscosity of new EOS polyamide 12 powder is 5.20×10^2 Pa·s, while that of powders

aged 20 hours at 120, 150 and 170 °C are respectively 1.51×10^3, 7.50×10^3 and 1.80×10^5 Pa·s [19]. At 190 °C, the zero-shear viscosity of EOS polyamide 12 powder is around 10^3 Pa·s after 15 minutes aging, while that is around 10^4 Pa·s after 30 minutes [24, 48]. Duraform polyamide 12 has similar phenomena: complex viscosity of new powder is around 10^3 Pa·s, that of reused powder (aged at 170 °C) is 5.0×10^4 Pa·s [49]. The zero-shear viscosity of Orgasol polyamide 12 has little change after aging for 30 minutes at 190, 210, and 230 °C [48]. For the VESTOSINT X1556 polyamide 12, the zero-shear viscosity increases first with reuse and then decreases [21]. These significant time-dependent zero-shear viscosity changes confirm that polyamide 12 demonstrates melt-state polycondensation [21, 50].

1.4.7.2 MVR and MFI

The other indexes to measure material rheological property are the melt volume rate (MVR) and the melt flow index (MFI). MVR is defined as the volume of a thermoplastic polymer, flowing in ten minutes through a capillary for alternative prescribed pressures and temperatures, cm3/10min. MFI is expressed as mass of the polymer, in grams, flowing through a capillary under alternative prescribed pressures and temperatures in ten minutes, g/10min. Measured in capillary rheometers, MVR and MFI can present degradation status of polyamide 12 material in SLS. Generally, new powders have higher MVR and MFI values compared to aged powders. For DuraForm polyamide 12, MFI of new powder is 52.01 g/[10 min], and that of waste powder is 20.38 g/[10 min] [51]. For EOS polyamide 12, MFI of new powder is 50.1 g/[10 min]; MVR of 1-time, 2-time and 3-time reused powders are 28.90, 17.41, and 13.50 g/[10 min] [20]. Both aged at 174 °C, longer aging time results in smaller MVR values (e.g.: in oven, MVR decreases from 65 cm^3/[10 min] to 20 cm^3/[10 min] with 120 hours aging). This attributes to the longer molecular chain in aged powder caused by melt-state polycondensation. The increased chain length reduces chain mobility and increases flow resistance with reduced MVR/MFI. MVR and MFI are inversely proportional to viscosity.

1.5 Property of parts using aged polyamide 12 powders

When properties of the reclaimed powders allow for a successful SLS, the quality of the resulting manufactured parts defines the ultimate applications. The properties of part using aged polyamide 12 powders, such as part microstructure, surface morphology, thermo-chemical property, crystalline structure evolution, and mechanical property, change compared to new part.

Notice that these changes typically follow a standard printing process in the comparison, i.e., the processing parameters are equal or close to the case with new powders.

1.5.1 Surface morphology

Part dimensional accuracy and surface roughness are two common kinds of part surface morphologies and usually degrade when using reclaimed polyamide 12 powders [21, 52].

1.5.1.1 Dimensional accuracy

Since laser sintering is generally free-standing with no applied supports, dimensional accuracy of the 3D-printed part is a primary concern in SLS [53]. Uniform solidification is crucial to forming a part with accurate dimensions [46]. The important consideration to ensure uniform solidification is controlling sintering behavior. Laser energy density and pre-heating temperature are key factors affecting sintering behavior [54]. Laser energy density greatly influences the combination of adjacent particles: insufficient energy density leads to poor coalescence, while excessive energy density results in severe degradations. Certainly, the laser only supplies part of the total energy deposited into the materials. The powder bed should be pre-heated to a suitable temperature to ensure good absorption characteristics of powder feedstock and appropriate sintering behavior. During sintering, the pre-heating temperature is kept just below the melting temperature. This practice ensures part-free strains (i.e., crystallization-induced shrinkage and thermal-induced shrinkage) [54, 55] are minimized while subsequent layers are melted, leading to a low level of residual stress between layers. A final slow cooling comes to get a uniform free strain evolution and part dimensional stability.

High melting enthalpy of material is also essential to ensure appropriate sintering behavior through preventing the unused powder from melting on the part surface. Further, appropriate sintering demands that enough molten material with sufficient viscosity spreads to form necks between adjacent particles, forming an increased dense structure with low porosity and better dimensional accuracy.

Though influenced by various process parameters [56-58], the dimensional accuracy of parts printed using aged polyamide 12 powders decreases compared to the original part using the same parameters [21]. Due to aging, particle shape and surface morphology of aged polyamide 12 powders show obvious differences caused by powder aggregation, expansion, and shrinkage. As a result, the absorption characteristics and uniformity of solidification for aged powders both reduce.

Consequently, the sintered part using aged powders, in general, has decreased dimensional accuracy.

1.5.1.2 Surface roughness

Due to degradation caused particle aggregation and particle sphericity change, sintering with reclaimed polyamide 12 powders generates part surfaces with severe roughness. Previous studies have shown the "orange peel" phenomenon – an undesirable surface effect that occurs commonly when using aged powders [20, 40, 59]. Methods to reduce the surface roughness and eliminate "orange peel" include controlling the SLS process parameters, for instance, energy density and laser scanning strategy [52].

1.5.2 Crystalline structure

1.5.2.1 Microstructure

From Scanning electron microscope (SEM) [24] or optical microscopy [60], the cross-sectional micrograph of a sintered part is divided into four regions. From top to bottom, they are respectively unmolten particle fused to the edge, spherulites from fully melted & crystallized particles, unmolten particle cores, and spherulites from the melted & crystallized region [60]. The microstructure of parts can be simply described as the unmolten particle cores surrounded with spherulites [61]. The cores are the unmolten central regions of the sintered powders coming out when these powders do not get enough energy and heat to fully melt. Besides, the cores are believed to be crucial to part post-crystallization and spherulite growth [60].

1.5.2.2 Post-crystallization and spherulite growth

When going through the sintering process, new and aged powders transfer from their solid states to the molten phase. Dissimilar to new powders, aged powders have numerous high-melting-point pieces in their molten phase. These pieces work as nucleation sites to form the nucleation seeds. As a result, the new powders only have a few nucleation seeds due to their fewer high-melting-pieces. However, a large number of nucleation seeds form in the aged ones. The generated nucleation seeds then serve as the basement for spherulite growth during the cooling process when the temperature is below the material melting temperature. After layers of material solidification, lots of spherulites grow on the amorphous solid region of the aged part and cannot spread smoothly in the limited space, leading to the formation of coarse spherulites. On the other hand, the spherulites are fibrillar smooth when using new powders. Consequently, due to the aging-induced post-crystallization/spherulite growth, the microstructure of the printed part using aged polyamide

12 powders changes from fibrillar spherulites to coarse spherulites [24]. Other work reported the same phenomenon and verified the spherulite growth/coarse spherulites in part using aged polyamide 12 [28, 39].

1.5.2.3 Crystalline structure evolution

X-Ray Diffraction (XRD) or Wide-angle X-ray Scattering (WAXS) spectra are commonly used to detect crystalline structure evolution of polyamide 12. Results provide information on the crystallizing procedures and/or crystal transformations between new and aged parts [21, 24]. Generally, polyamide 12 presents two crystal structures: the γ-phase is stable with parallel chain orientation and twisted helical conformations, while the α-phase is unstable with antiparallel chain orientation [21, 48, 62, 63]. The major difference in XRD results between powder and part is that part exhibits only γ peaks while the powders show mainly α peaks [21]. Under atmospheric pressure, slow crystallization of the 3D-printed part allows the crystalline chains to transform and form a more stable γ form. However, crystal structure stability for new and aged parts exhibit differences. XRD results show that the intensity of preferable γ reflection reduces with aging, attributed to the decreased chain mobility caused by increased molecular weight and viscosity after aging. Therefore, it is more difficult to form a perfect γ crystal structure for the aged part than new part.

Aged powders have a higher crystallinity than new powders (aged: 51%; new: 46%). Due to reduction in chain mobility caused by polycondensation [21], crystalline ratio of aged parts decreases [24, 64]. The crystalline ratio affects surface finish (e.g., roughness) and mechanical properties of the 3D printed specimens. Higher crystalline ratios generally result in increases in tensile strengths and Young's modulus, and decreased elongations at break [65].

1.5.3 Density

Density of SLS polyamide 12 components is a critical factor largely influencing fatigue, ductility and strength, etc [26]. Semicrystalline polymers with high molecular weight and long chemical chains have increased entanglements and bonding, decreased chain ends, and free volume, making it easy to achieve a high density [66]. The long chemical chains, increased entanglements and bonding, and increased crystallinity further tend to lower MVR and increase the viscosity of the polymer, resulting in a significant impact on increasing part density. The degree of branching is another factor that can influence polymer density through changing molecular weight [28]. Besides, the environmental temperature and testing conditions also affect part density.

Given that voids act as stress risers to reduce strength, density can be directly correlated to mechanical performance. When applying the same parameters, the density of parts using aged powders decreases compared to new part. Longer aging time leads to lower part density [26]. Storage at 140 °C, the density of part using EOS polyamide 12 decreases from 1.00 to 0.98 g/cm^3 after 336 hours [28].

1.5.4 Mechanical properties

Tensile strength, Young's modulus, and elongation at break are important for functional applications printed in SLS [26, 27, 59, 60, 67]. The knowledge and theory on mechanical properties of parts using new powders have been studied intensively and show good consistency. However, lots of debates remain on the effects of powder reuse to part mechanical properties. Several reports claimed no significant changes exist in tensile strengths, Young's modulus and elongations at break increase for parts using aged powders [59, 60]. On the other hand, other results report a decreased tensile strength (from 31.65 Mpa to 20.45 Mpa), a decreased Young's modulus (from 2000 Mpa to 300 Mpa), with a decreased elongation at break (from 5.3% to 0.2%) [27, 47, 67], or with an increased elongation at break (from 9% to 46%) [26, 68]. The differences in these studies result from various polyamide 12 powder grades, SLS machines, processing and printing conditions, such as process parameters, test instruments, or humidity conditions. Also, the appropriate selection of process parameters improves the part mechanical properties while multiple-time reuse [69].

When fabricating tensile bars using different PA12 powders and different SLS machines, different sets of processing parameters are applied. However, when processing the same kind of PA12 using different SLS equipment, the different sets of processing parameters are also necessary. When sintering EOS GmbH PA12 to produce parts using the Sinterstation 200 SLS 3D printer, the parameters are preheating temperature 175 °C, laser power 5 W, layer thickness 0.1 mm, and scanning speed 1257 mm/s [27]. When sintering EOS GmbH PA12 using the in-house built and customized SLS testbed, the parameters are preheating temperature 160 °C, laser power 18 W, layer thickness 0.15 mm, and scan speed 3000 mm/s [36].

For semicrystalline polymers, the molecular weight, cross-linking, and crystallinity are the main microstructural factors affecting tensile strength of thermoplastics [70-72]. For PA12, a low molecular weight leads to low tensile strength, where the microstructural carbon layers and chains are weakly connected and can move easily. When the molecular weight increases to a large extent,

the carbon layers and chains become complex, crosslinked, and bonded by strong van der Waals forces, resulting in the high tensile strength [73]. Similarly, the occurrence of chain cross-linking strengthens the microstructural bonding and connection between layers and chains, restricting the chain motions and improving PA12 tensile strength, while chain scission adversely lowers the tensile strength. Furthermore, high crystallinity or large crystalline area raises PA12 tensile strength through the significantly strengthened intermolecular bonding [71]. In addition, product fabricating orientation, testing velocity and temperature also influence polymer tensile strength.

Different from tensile strength, Young's modulus of semicrystalline polymer is not directly affected by molecular weight [74]. Increasing crystallinity during material degradation raises material Young's modulus. As crystallinity increases, the adjacent aligned chain segments strengthen the interchain bonding, which inhibits relative interchain motion as well [75]. Besides, drawing deformation and annealing also help to increase Young's modulus, by producing the oriented molecular structures and enhanced interchain bonding.

A high elongation at break indicates that the semicrystalline polymer has good ductility, which depends largely on the material's chemical composition. Polymer crystallization largely affects elongation at break. The big crystal size means low ductility that the material is brittle and easy to fracture before deforming much under a tensile load, decreasing polymer elongation at break [36]. Materials with a small crystal size are more likely to deform without breaking, leading to a high elongation at break. Though a high crystalline ratio generally increases tensile strengths and Young's modulus, it decreases elongation at break due to the large crystal sizes and reduced flexibility [65]. Mechanical testing velocity, orientation level, and temperature also affect elongation at break. Slow testing velocities, small orientations, and increased temperatures allow for higher elongation at break.

1.6 Parameter setting in SLS using aged polyamide 12 powders

After investigating the powder and part property changes, we provide the parameter setting principles in SLS when using aged polyamide 12 powders. Specifically, we focus on parameters most relevant to process feasibility and material reuse, including pre-heating temperature, energy density, laser power, laser speed, hatch space, and layer thickness [65, 76].

1.6.1 Pre-heating temperature

Before sintering polymeric materials with laser beams, thermal radiation pre-heats the powders and raises the temperature of the powder bed chamber to reduce power density

requirement during SLS [77]. The principles of setting the pre-heating temperatures for new and aged polyamide 12 powders are similar: both should be near or below the onset melting temperature [21, 26, 78]. Polyamide 12 powders from different suppliers differ slightly in the onset melting temperature. In a DTM 2500plus HiQ SLS printer, Duraform polyamide 12 (onset melting temperature is 180.8 °C) was preheated at 175 °C; Orgasol-IS polyamide 12 (onset melting temperature is 173.6 °C) was preheated at 164 °C [78]. Even using the same grade of polyamide 12 powders, different SLS vendors tune the pre-heating temperature differently, primarily due to the different mechatronics of the machines. For EOS polyamide 12 with melting temperature of 184 °C, the pre-heating temperature was 181ºC for the Sinterstation SLS printer and 174 ºC for the Formiga SLS printer [26].

1.6.2 Energy density

Energy density is usually defined as the area energy density (Eq. 1-1) [52, 76, 79] and the volume energy density (Eq. 1-2) [76, 80].

$$E_A\ (J/mm^2) = \frac{LP}{LS \cdot SS} \tag{1-1}$$

$$E_V\ (J/mm^3) = \frac{LP}{LS \cdot SS \cdot LT} \tag{1-2}$$

Here, E_A is the area energy density, and E_V is the volume energy density. LP is laser power, W. LS is laser speed, mm/s. SS is scan spacing, mm. LT is layer thickness, mm.

An appropriate energy density is crucial in the SLS process to guarantee the process feasibility and part quality [81]. Too low or too high energy densities will negatively affect part properties through powder interactions, such as powder bonding, fusion, and degradation. Table 1-2 lists such corresponding impacts. Specifically, an energy density that is too low leads to weak particle bonding, fusion, and decreased powder thermal degradation due to insufficient thermal motivation and heat effects. On the contrary, a high energy density results in strong bonding and fusion of particles, but more severe thermal degradations in the meantime. Moreover, energy density also greatly affects part properties, for instance, part porosity, density, surface roughness, and mechanical properties (Table 1-2).

In general, higher energy density leads to better part density and mechanical properties [76]. Identifying the relationships between part properties and energy density is helpful to improve part quality. Even using different energy densities, the properties of parts using new powders are always better than those using mixed or aged powders. Similarly, the properties of parts using one-

time recycled powders are better than those using two times recycled powders [76]. The quality of parts using mixed powders and recycled powders can be improved with a higher energy density.

Table 1-2 The impacts of the low energy density and the high energy density on powder and part properties

Items		Low energy density	High energy density
Powders	bonding	weak	strong
	fusion	poor	good
	degradation	low	high
Parts	porosity	more	less
	density	low	high
	roughness	rough	smooth
	shrinkage	low	high
	mechanical property	poor	good

It is also worth mentioning that Young's modulus and elongations at break of parts printed with aged powders can also be improved by using higher energy density, as well as a reduced appearance of "orange peel" on part surface. The improvement is mainly caused by better coalescence resulting from high temperatures and high energy [26]. However, it has limitations for the ranges of energy density used in SLS while processing polyamide 12. Previous studies show that the minimum volume energy density of 0.091 J/mm^3 is required to fuse the powder [82, 83], indicating very poor connections between the powders and layers. And the maximum energy density recommended in SLS is 0.48 J/mm^3 when polymer degradation accelerates [83].

1.6.3 Laser power, laser speed, and hatch space

Laser power has significant effects on mechanical properties and dimensional precision of the 3D-printed part in SLS [84]. As the laser power increases, the increased heat-affected zone leads to the growth of width error. Increasing laser power can improve mechanical properties to a certain extent, but higher powers degrade the powders chemically. This negatively affects the durability and long-term performance of the part, and the recommended range is 10 W - 49.5 W. Laser speed (4000 mm/s-11500 mm/s) is related closely to part porosity and part flexural modulus [26, 78, 80, 81]. However, sensitivity analysis suggests that laser speed has fewer influences than laser power on the density and mechanical property of the final manufactured specimens [79]. The hatch space (0.1 mm-0.3 mm) affects energy density (larger hatch space decreases energy density), and is together with the layer thickness both impacting significantly the part density and mechanical property when the remaining parameters are constants [80].

1.6.4 Layer thickness

For polymer SLS, parts are usually fabricated with layer thicknesses from 0.06 mm to 0.18 mm in a layer-by-layer manufacturing style for either new powder or aged powder [26, 80]. Parts with a smaller layer thickness normally have better mechanical properties, due to the better compaction and uniformity between layers when the layer thickness is small. Table 1-3 exhibits the recommended process parameter sets for polyamide 12 powder in SLS processing.

Table 1-3 Recommended process parameter sets for polyamide 12 powder [76, 80, 81]

Item	Recommended Value
Pre-heating temperature	Near the melting point
Energy density	0.091 J/mm³ ~ 0.48 J/mm³
Laser power	10 W ~ 49.5 W
Laser speed	4000 mm/s ~ 11500 mm/s
Hatch space	0.1 mm ~ 0.3 mm
Layer thickness	0.06 mm ~ 0.18 mm

1.7 Dissertation objectives

In SLS, low utilization of the costly polyamide 12 hinders the process long-term sustainability, and the feedstocks undergo complex thermal and chemical degradations. Understanding and controlling about the reusability, aging kinetics, and sustainability of polyamide 12 in SLS have thus appeared as an important and time-sensitive problem. Here, to solve the problem, firstly we will propose new process control approaches to investigate the possibility and feasibility of reusing polyamide 12 powders and creating parts with improved mechanical properties, and to maximize surface quality and part microstructure involving highly degraded polyamide 12 materials. Besides, to understand the material aging kinetics, we will model the polyamide 12 degradations through a combined theoretical and experimental approach considering both the oxygen and laser effects. Then, our further objective is to identify quantitative influences of successive reuse on thermal decomposition, molecular evolution and elemental composition of polyamide 12 residues in SLS. Furthermore, we will propose a first-instance methodology with process-oriented and mass-transfer based approaches to model and predict VOC emission in SLS. Finally, we will perform in-process monitoring of temperature profiles from infrared images in various locations when sintering different polyamides in SLS. The specific aims are listed below:

Objective 1: The possibility and feasibility of reusing the residual polyamide 12 remain not fully exploited. In particular, the reuse of the extremely aged polyamide 12 powders close to the heat-affected zones has not been reported. This work seeks to bridge the missing link and proposes a new method, hereby referred to as active interlayer heating, to build parts with the reclaimed and

extremely aged polyamide 12 powders. We discuss a new process control approach to reuse the polyamide 12 powders of different degradation levels, different mixing percentages, and different combinations with multiple layer printing and superior mechanical properties.

Objective 2: It remains not clear how to maximize surface quality when using reclaimed powders of different combinations. Moreover, there is a lack of understanding in surface characteristics of parts sintered using extremely aged polyamide 12 powders. We show, however, that such expensive materials can be reused to produce parts with fine surface textures, reduced porosities, and free from unmolten particles. The result is obtained by developing a new strategy to control and optimize surface quality using SLS with controlled post-heating. By material preparation, powder and part characterizations and SLS with controlled post-heating, we obtain a series of parts using differently degraded powders and different combinations.

Objective 3: The kinetics and the full modelling of polyamide 12 degradation in the complex SLS remain not well addressed. We propose a first-instance kinetic scheme considering both the oxygen and laser effects to model material degradation in SLS through multi-physics modeling and data-driven parametric identification. We conduct SLS printing experiments and calculate the actual polyamide 12 degradation rates through Fourier-transform infrared spectroscopy (FTIR) results and Beer-Lambert's law. By data-driven parameter identification of the actual SLS degradation rates into the oxidation model, we obtain the coefficients of actual coupled oxygen and laser effects in SLS, as well as the relationship between the material degradation rates and oxidation time. The proposed model can predict material degradation rates using materials density and oxidation time, applicable to both pure and mixed powders.

Objective 4: Quantitative degradation and thermal decompositions of polyamide 12 residues with successive reuse in SLS remain not well understood. The absence of such knowledge hinders sustainable SLS manufacturing in both academia and industry. This work experiments successive reuse of polyamide 12 residues and quantitatively monitors the material thermal decomposition, molecular evolution, and composition changes in SLS. Importantly, we tested basic flowability energy, Thermogravimetric Analysis (TGA), X-ray Photoelectron Spectroscopy (XPS), and 1H Nuclear Magnetic Resonance (NMR) for powders/parts, and found significant changes between differently reused samples. These findings provide first-instance knowledge for polyamide 12 under successive reuse to the best of our knowledge.

Objective 5: The elevated temperature and high-energy laser beam in SLS may cause more detrimental volatile organic compound (VOC) emissions than the other 3D printing. Yet, the modelling and prediction of VOC emission in SLS remain unexploited. This work proposes a first-instance methodology with process-oriented and mass-transfer based approaches to model and predict VOC emission in SLS. We monitor the VOC emissions from polyamide 12 in 6 cases with five printing stages in each case. With emission curve segmentation, we use the mass-transfer based single- and multiple-layer models to simulate the VOC emission. Experimentally measured data verify the accuracy of the obtained model. We also analyze the effects of critical parameters (mass-transfer coefficient, diffusion coefficient, and partition coefficient) on VOC emissions.

Objective 6: Thermography process monitoring or infrared imaging of the powder bed is important, used to monitor surface temperature variations that contribute to part inadequacies. The powder bed temperature profiles of reclaimed polyamide 12 remain largely unexploited, which largely affect SLS sustainability, material reusability and specimen quality. We propose in-process monitoring of temperature profiles from infrared images in various locations when sintering differently degraded polyamides. The heating temperature will be 160 °C with repetitive tests. In one monitoring, the temperature profiles in each printing layer and the identified location are recorded. We also apply interlayer heating and post-heating to printing and investigate the influences of extra heat treatment on powder and part surface temperature profiles.

The proposed objectives will be respectively introduced in detail in Chapter 2, Chapter 3, Chapter 4, Chapter 5, Chapter 6, and Chapter 7. Figure 1-2 present correlations between chapters.

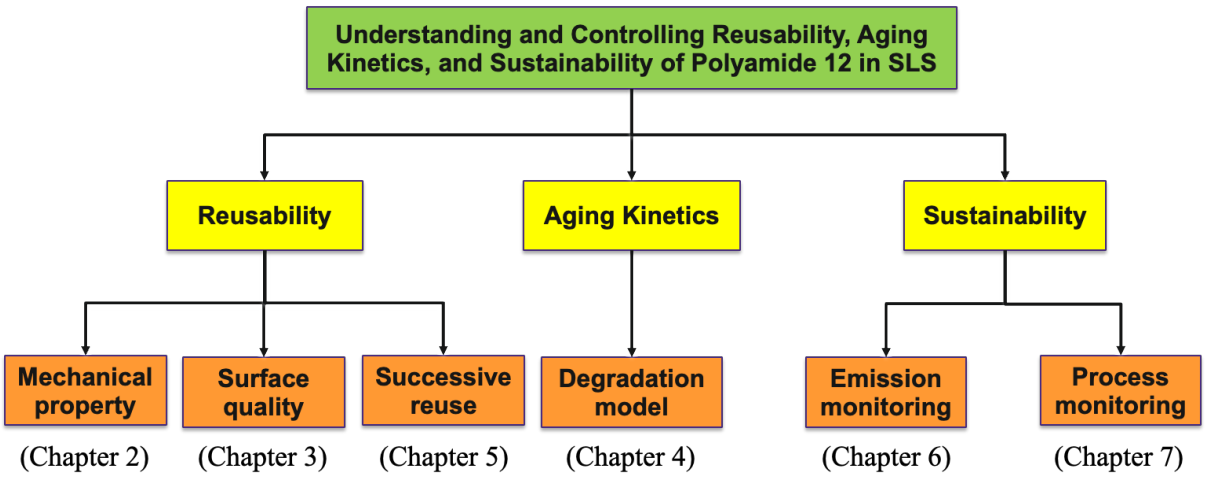

Figure 1-2 Correlations between chapters

Chapter 2. A PROCESS CONTROL AND INTERLAYER HEATING APPROACH TO REUSE POLYAMIDE 12

2.1 Introduction

Capable of processing almost any laser-absorbent materials including polymers, metals, ceramics, and composites, SLS is one of the most well-established and commonly used additive manufacturing techniques to rapidly manufacture three-dimensional components [14, 21, 24, 85]. Polymeric powders, semicrystalline or amorphous, are the first and still the most widely applied materials in SLS [14, 86, 87]. Parts printed using amorphous polymer powders are partially consolidated, and consequently can be useful for applications when the strength and durability of parts are not dominant [88]. On the contrary, parts printed using semicrystalline polymer powders are fully consolidated with high mechanical strength and effectively weakened warpage. Among the semicrystalline polymers, polyamide families are most popular for SLS, and polyamide 12 dominates the market because of the capability to generate strong parts for common applications [21, 24, 89]. To be more specific, parts printed using polyamide 12 powders have superior mechanical properties than that of parts from amorphous polymers. The superior mechanical properties originate from the thermal behaviors of the semicrystalline materials [60, 90, 91], including, e.g., a wide processing window for sintering, high melting enthalpy, and high flowability [19, 21]. The existence of a wide sintering window between melting onset and crystallization onset temperatures is beneficial for maximizing part consolidation to get a fully dense part [16]. High melting enthalpy and high flowability are necessary during laser sintering to get a homogeneous powder layer and to melt the powder locally with high accuracy and reproducibility [19, 85].

Despite the popular applications of the polyamide 12 powders in SLS, the volume ratio of powders that translate to parts is small: e.g., commonly 5% - 15% of the total powders in the build chamber. The 85% to 95% residual powders went through deteriorate physical and chemical degradations in the intricate fabricating processes including preheating, sintering, cooling, and/or post treatment [18, 21], but have the potential to be recycled and reused for further applications [20, 21, 24, 25]. However, the deteriorated powders have reduced surface morphologies, larger

and more complex molecular chains, decreased flowability, and deteriorated mechanical and thermal properties, which make it challenging to reuse them directly [16, 20, 21, 24, 25]. Also, polyamide 12 powder is relatively expensive, priced around $150/kg in 2019 [18]. Abandonment of the residual polyamide 12 powders can cause not only economic losses but also environmental pollution. Thus, reclaim and reuse are difficult yet necessary for a sustainable SLS.

Prior to reuse, characterizations, such as powder flowability, MVR and viscosity, are studied to exhibit the differences between polyamide 12 new powders and reclaimed powders. Sufficient flowability is a necessity in SLS to enable processing of powders and deposition of powder layers [44]. Many efforts have been done to understand the static and dynamic flow behaviors of polyamide 12 powders, and to optimize the flowability [44, 45]. Particle shape significantly impact powder flowability. High sphericity leads to high flowability, potato-shaped particles the next, and rough-edged irregular particles exhibit the lowest flowability [46]. MVR index reveals changing flowability of the powders due to degradation [21, 25, 26]. New polyamide 12 powders have higher MVR values, while reclaimed powders have lower MVR values [26]. Besides, longer aging or multiple times of reusing lead to smaller MVR values. Reclaimed polyamide 12 powders have increased zero-shear viscosity compared to new powders [21, 24]. Moreover, a higher temperature accelerates aging and increases zero-shear viscosity [24]. The increase of zero-shear viscosity for reclaimed powders results from the post-condensation phenomena. It also increases molecular weight of reclaimed polyamide 12 powders, as confirmed by Gel permeation chromatography (GPC) [24].

From there, relevant works on the reuse of the reclaimed polyamide 12 powders have been reported in recent years. L. Feng et al. [18] reclaimed polyamide 12 from SLS and made the powders into filaments for fused deposition modeling (FDM). L. Wang et al. [92] demonstrated a closed-loop recycling of polyamide 12 powder from SLS into milled carbon fiber/recycled polyamide 12 composite filaments for extrusion-based additive manufacturing. The effect of prolonged storage at elevated temperatures on the isothermal crystallization kinetics of polyamide 12 has been studied using Flash Differential Scanning Calorimetry (DSC) experiments by F. Paolucci et al. [19]. Clarifying the aging mechanisms on thermal behavior, coalescence behavior and the resulting crystallinity, microstructure and mechanical properties, and investigating systematic aging mechanisms and microstructural evolution, P. Chen et al. [21] and S. Dadbakhsh et al. [24] characterized the aging process of polyamide 12 powders in SLS. Dotchev et al. [25],

Wegner et al. [26] and Josupeit et al. [91] verified the decreased flowability of the reclaimed polyamide 12 powders compared to new ones through a melt volume rate (MVR) index, which was recommended as a measure of the powder degradation rates. K. Wudy et al. [23, 38] investigated the influences of processing time and temperature on aging effects of polyamide 12 in SLS. In particular, the references (i) studied molecular changes and thermal property changes of polyamide 12 partcake material, and (ii) examined the aging behavior of polyamide 12 in SLS including bulk characteristics and part properties such as porosity and surface roughness. The effect of powder reuse on mechanical properties has been studied by R.D. Goodridge et al. [68] and K. Wudy et al. [27], who pointed out the changes of tensile strength as well as elongation at break in parts built from aged polyamide 12 powders. In addition, the relationships between preheating temperature [26], energy density [26, 80], combined dwelling time between layers, energy density [42], and part quality were studied.

The complex aging mechanism of polyamide 12 powders in laser-sintering involves a set of physical and chemical processes. The reversible physical degradation here mainly leads to changing molecule order or concentration, particle post-crystallization and agglomeration [26]. The chemical degradation, on the other hand, is irreversible and predominant in the aging process. The chemical degradation changes such polymer structures as chain scission, branching and cross-linking caused by oxidation, post-condensation and hydrolyzes. Previous studies have revealed that thermal oxidation and post-condensation are two main aging mechanisms in chemical degradation during SLS [24, 27]. The oxidation process is initiated by free molecule radicals (hydrogen radical) emerging from the decomposition of the polyamide 12. After oxygen addition and transfer, termination reaction occurs to form stable final products (e.g., hydroperoxide and imide groups) and to complete the oxidation reaction. Apart from the thermal oxidation reaction, post-condensation is another irreversible chemical degradation behavior of polyamide 12 that leads to property changes in reclaimed powders [19, 27]. Here, the lengths of polymer molecular chain increase through combinations of free radicals at high temperatures. As a result, the molecular weight, flowability and viscosity of the reclaimed polyamide 12 change.

Although existing efforts have sought to understand the aging mechanisms and reuse of the degraded polyamide 12 powders, the possibility and feasibility of reusing the residual polyamide 12 powders remain not fully exploited. In particular, the reuse of the extremely aged polyamide

12 powders closes to the heat-affected zones (HAZs)[1] has not been reported. This work seeks to bridge the missing link and proposes a new method, hereby referred to as active interlayer heating, to build parts with the reclaimed and extremely aged polyamide 12 powders. We discuss a new process control approach to reuse the polyamide 12 powders of different degradation levels, different mixing percentages, and different combinations with multiple layer printing and superior mechanical properties. The result is that reclaimed polyamide 12 powders can be consistently reprinted into functional samples, with mechanical properties comparable or even superior to current industrial norms. In particular, the proposed method can yield printed samples with 18.04% higher tensile strength and 55.29% larger elongation at break using as much as 30% of extremely aged powders.

2.2 Proposed active interlayer heating for reusing polyamide 12 powders

Figure 2-1 outlines the flowchart of the proposed approach. The main procedures include powder collection, preprocessing, powder mixing, parameter control, interlayer heating, and part characterizations. Below, we discuss each procedure in detail [36, 93].

2.2.1 Materials sample preparation

2.2.1.1 Powder samples

In this study, we collected polyamide 12 powders purchased from EOS Corp. and reclaimed from standard SLS processes on an EOS P 390 machine. The powders cover three levels of degradation: (i) new powders without heat treatment, (ii) aged powders located far away from the HAZs during SLS and currently reused in the industry, and (iii) extremely aged powders located close to the HAZs and not being actively reused in SLS. Strong laser-material interaction occurs during the sintering process at or close to HAZs, leading to complex aging and degradation of the powder materials. The intricate laser-induced thermophysics change properties of polyamide powders such as particle sizes/shapes, microstructures, thermal properties and mechanical properties. Consequently, extremely aged powders are more severely degraded than the aged powders due to its closer location to the HAZs.

[1] Areas close to the laser-material interaction during sintering.

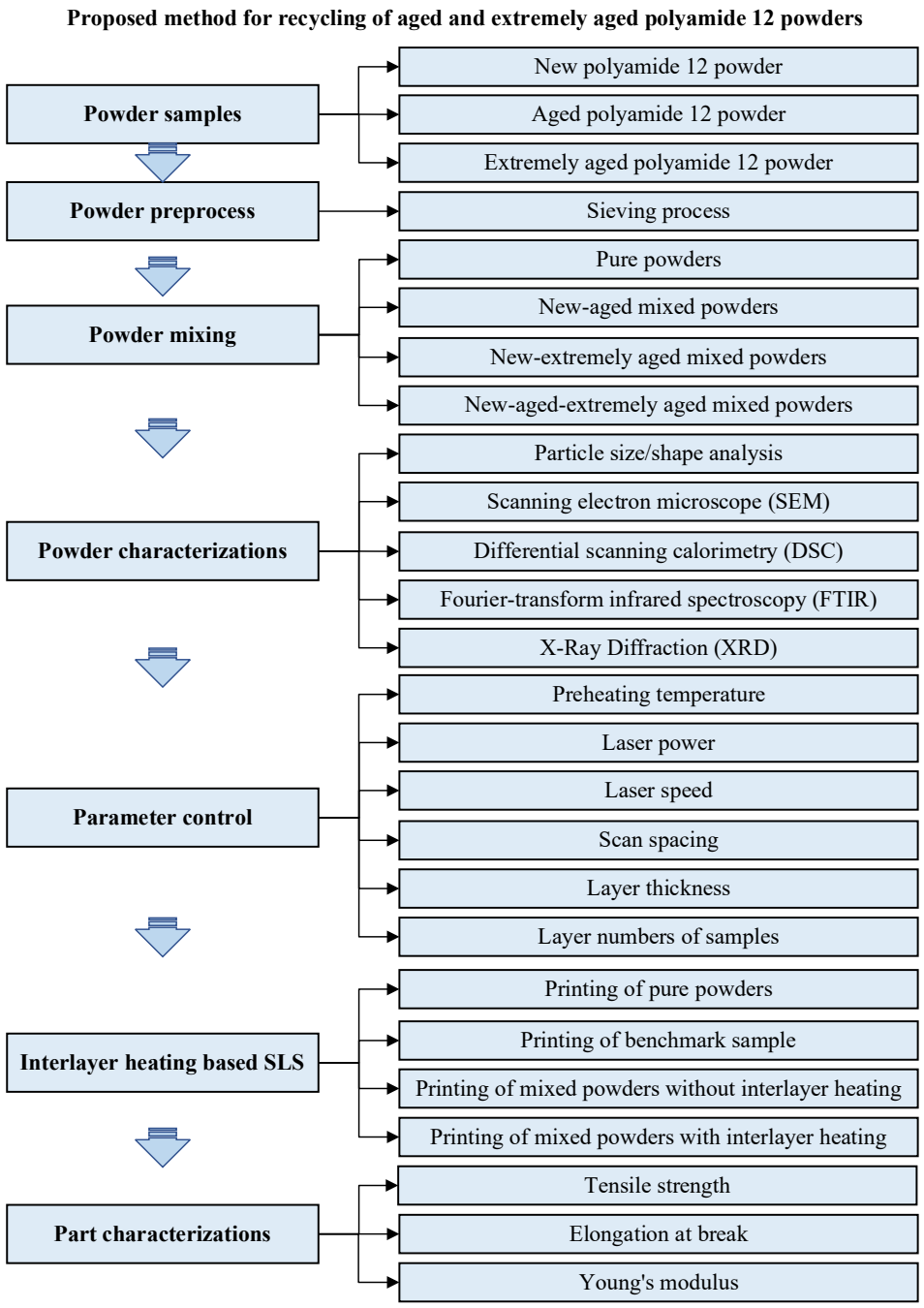

Figure 2-1 Proposed method for reusing aged and extremely aged polyamide 12 powders

2.2.1.2 Powder preprocess

Different from new powders and aged powders, extremely aged powders went through severe degradations induced by high temperature and intense laser-material interactions. Consequently, the collected extremely aged powders clump together and suffer from severe aggregation, which adversely impact the powder coating process. As shown in Figure 2-2 (a), new powders and/or

aged powders could be coated well with a smooth surface on the powder bed, which is conducive to part densification and consolidation. Nevertheless, the extremely aged powders could not be coated smoothly because of the existence of the aggregated large particles, as shown in Figure 2-2 (b), as a result of striking drop in flowability. This was attributed to an increase in the molecular weight, originating from a cross-linking of the polymer material, and an increase of particles of non-spherical, irregular shapes with featured rough edges in extremely aged powders [24]. Preprocessing of extremely aged powders is therefore necessary for a smoother coated surface and improved sintering behaviors.

In this work, a sieving process was applied to the extremely aged powder prior to printing. This process was done in a fume hood using a sieve with the mesh size of 200 μm to grind the powders. The time for sieving a batch of 500 ml powders is around 2 hours with preparation and post cleaning procedures. After the sieving process, about 50 ml~80 ml heavy materials were captured. In all, 84%~90% of the processed materials can be collected and reused.

(a) New/aged powders (b) Extremely aged powders

Figure 2-2 Powders coated on the powder bed

2.2.1.3 Powder mixing

Four different groups of powders were used in experiment (as shown in Figure 2-1): pure powders, mix of new and aged powders, mix of new and extremely aged powders, and mix of new, aged and extremely aged powders, to be specific. For the pure powders, 100% new, 100% aged, and 100% extremely aged powders were prepared. For the mixed powder groups, powders were prepared with various mixing percentages (Figure 2-4). Volume percentages are used in this work to mix powders.

2.2.2 Parameter control

The parameters for new polyamide 12 powders failed to create parts with extremely aged powders. We tested different printing parameters to obtain optimal results for different powders. Figure 2-1 shows six parameters that impact significantly part qualities and were used in this study: preheating temperature, laser power, laser speed, scan spacing, layer thickness, and layer numbers. These parameters were accurately controlled by our in-house developed SLS testbed in experiments. In our study, the same six core parameters are needed for consistent comparison. A variety of parameter settings are suitable for new powders, while few parameter settings are applicable to the cases when using extremely aged powders due to the degraded material properties. In particular, excessive laser power and energy density, along with a high preheating temperature, lead to over melting and deteriorated part properties when sintering extremely aged powders. The general principles to select the optimal parameter settings in this work are that (i) the parameters are set as close to OEM recommendations for regular printing as possible, and (ii) the new, aged and extremely aged polyamide 12 powders can all be successfully printed into parts using the same set of parameters. The selected optimal parameter settings suitable for powders of different degradation levels are: 160 °C preheating temperature; 3000 mm/s scan speed; 18 W laser power; 0.3 mm scan spacing; and 150 μm layer thickness. In our testing, we printed 10-layer tensile bar samples for each powder combination.

2.2.3 SLS with interlayer heating

2.2.3.1 SLS machine

The SLS machine used in the work is an in-house built open-configuration SLS machine/research testbed, as shown in Figure 2-3. Compared to the black box commercial systems, it enables researchers to access as well as manipulate key manufacturing process parameters, build online implementable process models, and discover problems in the complex multi-physical laser sintering process. We designed the machine using a Coherent GEM100A CO_2 laser (the maximum laser power 100 W) and a Scanlab intelliSCAN 14 scanner. The powder bed dimension designed is 250 mm (L) x 250 mm (W) x 150 mm (H) with the layer thickness resolution of 20 μm and theoretical XY positioning resolution of 0.24 μm. The designed typical scan speed is 3.75 m/s and the maximum scan speed is 30 m/s. The powder handling is carried out by one feed cylinder, one build cylinder, and a recoating arm, which are driven by servo motor and leadscrew transmission. It is featured with combined heating method: radiation heating with infrared heaters above the powder bed (200 mm) and conduction heating with a mica heater underneath the powder bed. The

software used to control the machine is an in-house developed LabVIEW program integrated with Scanlab RTC5 API, which can read G-code and send motion command to galvo scanner.

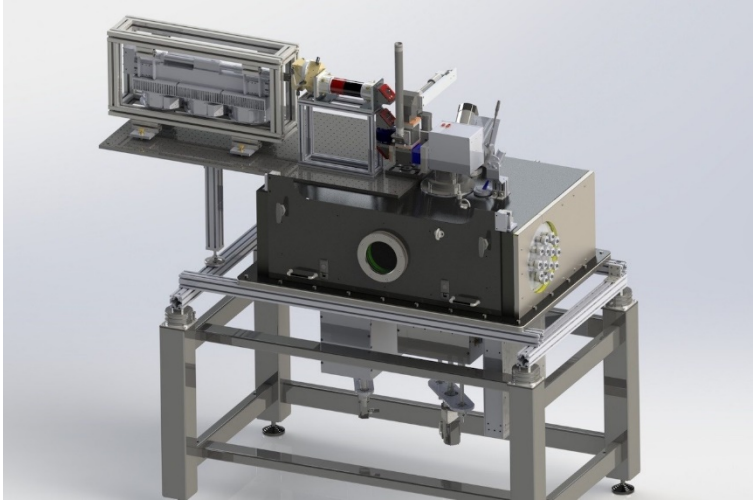

Figure 2-3 In-house built and customized SLS testbeds

2.2.3.2 Proposed SLS with interlayer heating

The SLS with interlayer heating proposed in this work is a process that interlayer heating is applied to the specimens being printed during the SLS process. Between the printing of every two layers, the proposed process maintains the surface temperature of the powder bed the same as the preheating temperature (160 °C) for a controlled period of time. We tested 0 second (no additional interlayer heating) and 60 seconds interlayer heating to powders and powder mixtures with different degradation levels to explore the influences of interlayer heating on part mechanical properties. Through the experiment results, it was verified that 60 seconds interlayer heating can provide samples with enough heat and energy.

We explored the reusability of aged and extremely aged powders and the influences of interlayer heating on part properties, as shown in Figure 2-4. The experiments were separated into six stages, with a distinguish objective for each stage. In the experiment in stage 1, pure powders were used to verify the feasibility of multi-layer printing with reclaimed powders. In stage 2, the currently available industrial reuse combination, 50%-50% new-aged mixed powders were used to print the benchmark samples – samples whose mechanical properties were regarded as the baselines in this research. The aim of stage 3 was to check the part mechanical properties when using new-extremely aged mixed powders with the percentages of extremely aged powders increasing. In stage 4, to examine the influences of interlayer heating on part mechanical properties, all the mixed powder combinations in stages 2 and 3 were reapplied and were printed

with 60-second interlayer heating. By comparing the mechanical properties of samples in stages 2, 3, and 4, information on influences of interlayer heating on part properties were obtained. In stage 5, different from the previous stages using the combinations of *two* kinds of powders, parts were printed with mixed powders composed of all *three* types of powders to verify the feasibility and potential benefits of this practice. To ensure part quality, we selected the combinations of 30% new - 30% aged - 40% extremely aged powders and 30% new - 40% aged - 30% extremely aged powders. To examine the influences of interlayer heating, the experiments in stage 5 were repeated with 60-second interlayer heating in stage 6.

2.2.3.3 Mechanisms of SLS with interlayer heating

Due to the existence of particles with high melting points, the reclaimed polyamide 12 powders are more difficult to melt than new polyamide 12 powders. This has been verified through the hot stage microscopy and the DSC test, where the aggregated spherulite structures and high melting point pieces cannot melt during the regular sintering process [24]. Lack of coalescing polymer chains, insufficient consolidation, partial densification and numerous unmolten particles can thus appear, severely degrading the end mechanical properties. The proposed SLS with interlayer heating aims to provide the needed heating energy to promote coalescence of polymer powders and improve part densification. In the mean time, increased diversity of grain sizes in the mixed new-reclaimed powders can improve part tensile strengths when using reclaimed polyamide 12 powders.

Post-crystallization and recrystallization are different phenomena related to powder aging. Due to post-crystallization, crystallization ratio increases and spherulites grow in reclaimed powders. Recrystallization refers to the transfer of crystalline structures. Both post-crystallization and recrystallization can occur during the SLS process, although it remains unknown which one is dominant. The combined post-crystallization and recrystallization could affect part microstructures such as crystalline ratios and crystal sizes. Parts with small crystal sizes have increased flexibility and decreased brittleness, while parts with larger crystal sizes are easier to break before the separation of crystals. This study will explore the influences of interlayer heating and powder qualities on part microstructures when using reclaimed powder materials (e.g. crystalline ratios and crystal sizes, and part elongation at break).

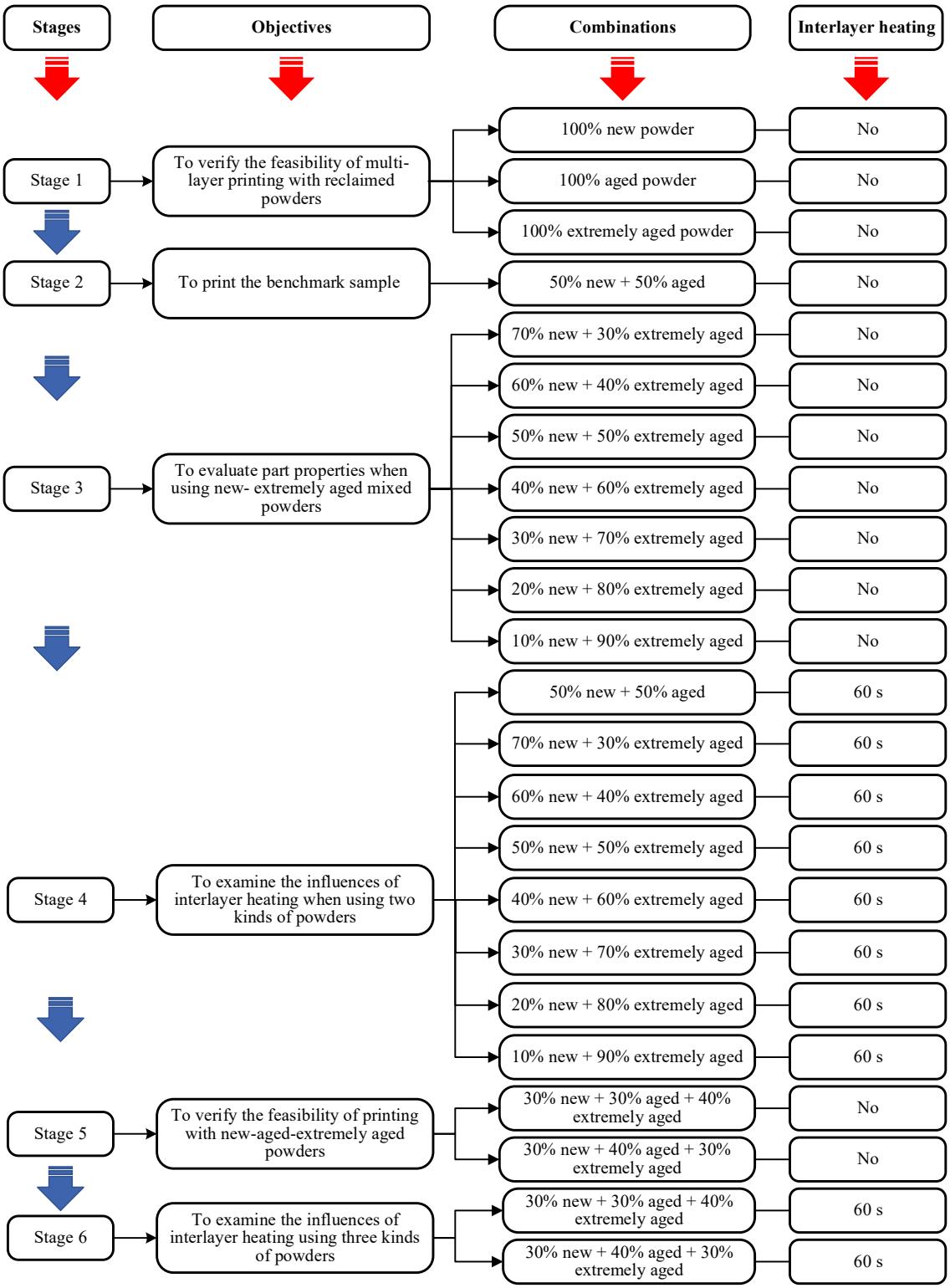

Figure 2-4 Experiment plans about reusability of aged and extremely aged powders and influences of interlayer heating (The mixed powders are in volume percentages)

2.2.4 Part characterizations

Tensile tests were carried out on all the SLS fabricated samples in Figure 2-4. The samples were designed based on ASTM standards and were stretched for each tensile measurement using an Instron 5869 Electromechanical testing system with a maximum load frame capacity of 50 kN equipped with Blue Hill control software, as shown in Figure 2-5. A polishing treatment was done on both the top and bottom surfaces of part to remove any skirmish un-sintered particles prior to the tensile testing for accurate measurement. We used a disc-shaped polishing machine with the diameter of 35 cm and a rubber polishing pad in the polishing treatment. The machine can rotate with running water above to clean the un-sintered particles on the surface of the tensile bars by friction. After polishing to clean the samples for proper surface measurements, tensile tests were conducted using an Instron 5869 Electromechanical testing system at a testing speed of 5 mm/min. After the tensile test, the stress-strain curves, tensile strength, elongation at break, and Young's modulus of various parts were reported.

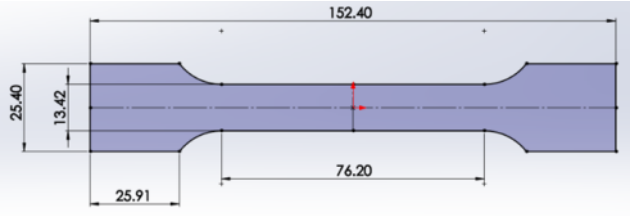

(a) Tensile bar dimensions (unit: mm)

(b) Tensile test machine - Instron 5869

Figure 2-5 Tensile bar dimensions and tensile test machine

2.3 Results

2.3.1 Printing results

Based on the proposed method, the tensile bars with 10 layers were printed. Using differently degraded materials, the same series of optimized parameters were applied to all the designed experiments in Figure 2-4 to ensure the equivalent processing conditions. The printing results are presented in Table 2-1.

Table 2-1 Printing results about reusability of extremely aged powders and influences of interlayer heating

Stages	Powder percentages	Interlayer heating	Sample number	Thickness / mm
Stage 1	100% new powder	No	3	0.88; 0.82; 0.81
	100% aged powder	No	2	0.91; 0.91
	100% extremely aged	No	2	0.65; 0.68
Stage 2	50% new + 50% aged	No	3	1.41; 1.41; 1.40
Stage 3	70% new + 30% extremely aged	No	2	1.46; 1.45
	60% new + 40% extremely aged	No	2	1.25; 1.25
	50% new + 50% extremely aged	No	3	0.98; 0.97; 0.96
	40% new + 60% extremely aged	No	3	1.43; 1.42; 1.41
	30% new + 70% extremely aged	No	2	1.38; 1.36
	20% new + 80% extremely aged	No	2	1.36; 1.34
	10% new + 90% extremely aged	No	3	0.80; 0.78; 0.78
Stage 4	50% new + 50% aged	60 s	3	1.41; 1.41; 1.42
	70% new + 30% extremely aged	60 s	2	1.48; 1.47
	60% new + 40% extremely aged	60 s	3	0.82; 0.83; 1.12
	50% new + 50% extremely aged	60 s	3	1.42; 1.40; 1.40
	40% new + 60% extremely aged	60 s	2	1.36; 1.36
	30% new + 70% extremely aged	60 s	3	1.32; 1.35; 1.30
	20% new + 80% extremely aged	60 s	2	1.00; 1.00
	10% new + 90% extremely aged	60 s	3	1.22; 1.26; 1.14
Stage 5	30% new + 30% aged + 40% extremely aged	No	3	1.40; 1.38; 1.40
	30% new + 40% aged + 30% extremely aged	No	2	1.34; 1.35
Stage 6	30% new + 30% aged + 40% extremely aged	60 s	3	1.40; 1.39; 1.36
	30% new + 40% aged + 30% extremely aged	60 s	2	1.26; 1.33

* Preheating temperature, 160 °C; scan speed, 3000 mm/s; laser power, 18 W; scan spacing, 0.3 mm; layer thickness, 150 μm.

Though we used the same set of parameter settings to print the tensile bar samples, we recoated different combinations of powders to print different samples. Thus, there are sample variations in, e.g., coalescence behaviors, solidification and consolidation effects, yielding variable thicknesses in the generated tensile bars. Such variations, however, do not affect the measured normalized mechanical properties. The width of tensile bars is in good consistence with the dimensions designed in Figure 2-5a. Note that a few samples (e.g. Figure 2-6f) contain deformation in pictures. The reason is that we air cooled all samples outside the chamber after printing, instead of waiting for them to cooldown inside the chamber.

Pictures of tensile bar samples are shown in Figure 2-6. The samples printed using 50%-50% new-aged mixed powders are taken as the benchmark parts. Samples printed using powders of different mixing ratios are listed, with and without interlayer heating. As seen, all samples were successfully 3D printed with no visible differences on the sample surfaces. More part characterizations will be explained in the following sections.

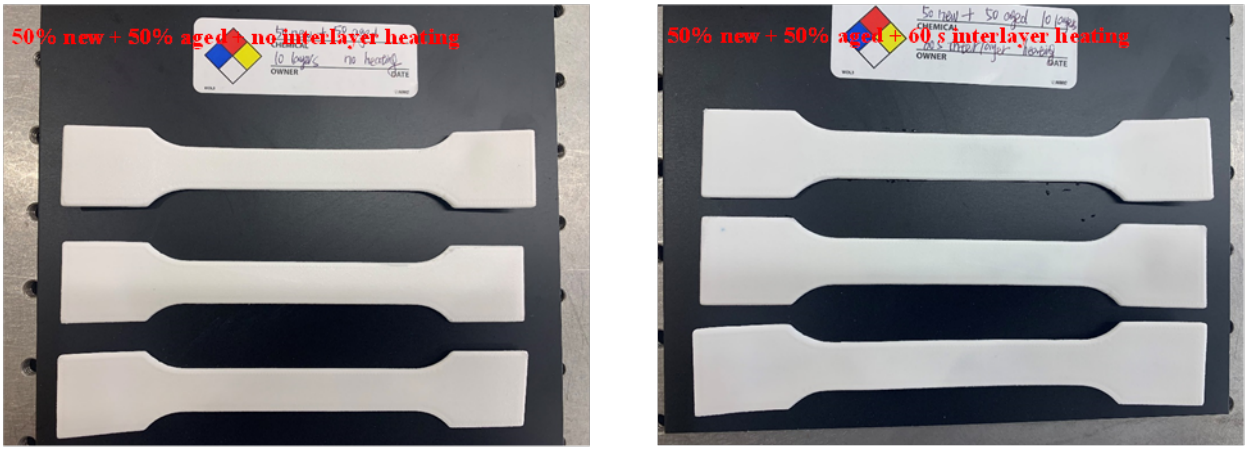

(a) Benchmark tensile bars with and without interlayer heating

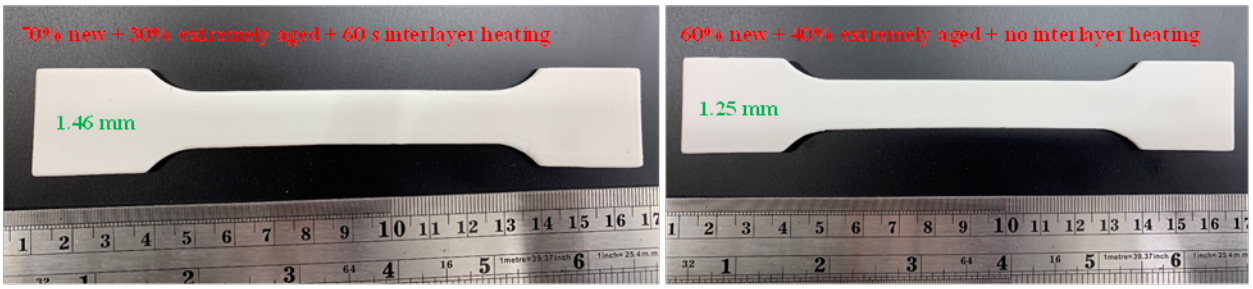

(b) Tensile bars with 30% and 40% extremely aged powders

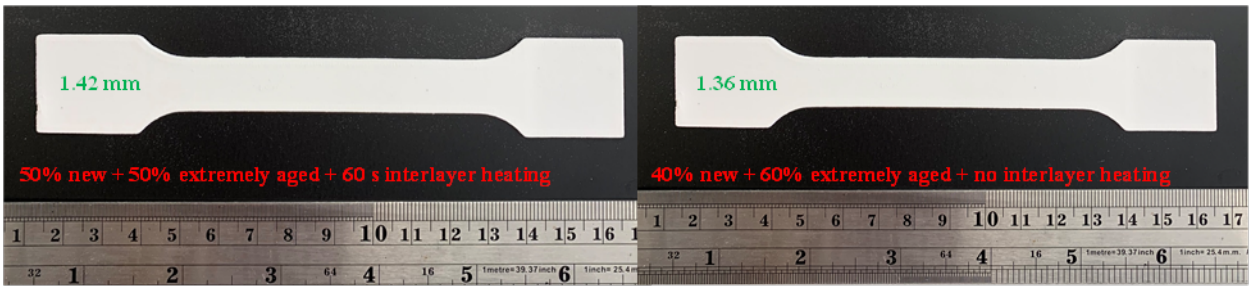

(c) Tensile bars with 50% and 60% extremely aged powders

(d) Tensile bars with 70% extremely aged powders

(e) Tensile bars with 80% extremely aged powders

(f) Tensile bars with 90% extremely aged powders

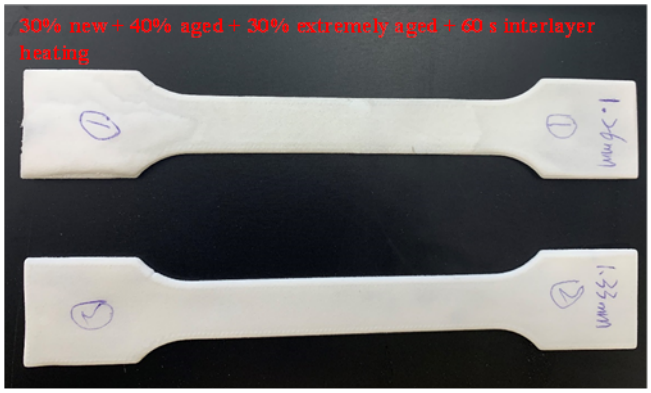

(g) Tensile bars with 30% new + 40% aged + 30% extremely aged powders

Figure 2-6 Pictures of some tensile bar samples

2.3.2 Part test results

2.3.2.1 Stage 1

The stress-strain curves of samples printed using pure powders exhibit in Figure 2-7. As shown, there are several differences between these samples. The average tensile strength of samples printed using new powders, aged powders and extremely aged powders are respectively 22.96 Mpa, 18.12 Mpa, and 11.08 Mpa, and that of samples using aged and extremely aged decreased by 21.09% and 51.75% compared to new ones. Parts using more new powders have larger tensile strength under standard settings. The average Young's modulus of samples printed using new powders, aged powders, and extremely aged powders are respectively 503.67 Mpa, 358.50 Mpa, and 177.00 Mpa, and that of samples using aged and extremely aged decreased by 28.82% and 64.86% compared to new ones. However, the average elongations at break of samples using new, aged, and extremely aged powders are respectively 5.31%, 12.12%, and 9.56%, and that of samples using aged/extremely aged powders increase by 56.20% and 44.46% compared to

new SLS parts. The reason for this is attributed to that the reclaimed materials have smaller crystal size, increased flexibility and decreased brittleness. Inversely, parts using new powders with larger crystal size are easier to break down before the separation of crystals, with decreased flexibility. Using the Scherrer's equation and XRD test results, we calculated the crystal sizes of the printed parts in Figure 2-7. The crystal sizes of new parts, parts using aged powders and parts using extremely aged powders are respectively 5.21 nm, 3.39 nm and 4.53 nm, which are consistent with our previous conclusions.

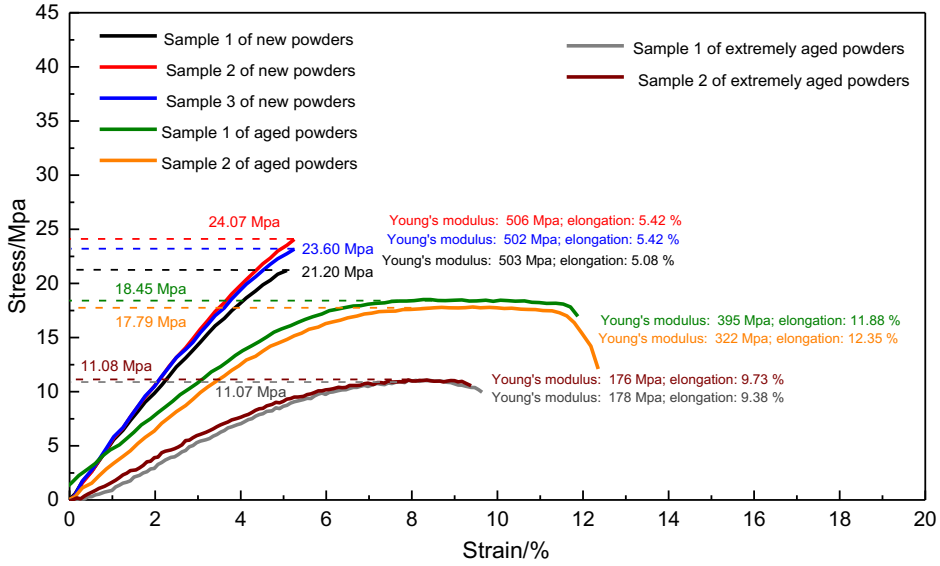

Figure 2-7 Stress-strain curves of samples printed using pure powders

2.3.2.2 Stage 2

As the most popular used mixing percentages for recycling aged powders [24], the samples printed using the 50%-50% new-aged mixed powders are taken as the benchmark samples in this work, of which the mechanical properties are baselines in the proposed method. The stress-strain curves of the benchmark samples are shown in Figure 2-8. There are two breakpoints in the stress-strain curves for these samples due to the layered fabrication process. For sample 1, there is a breakpoint at the strain of 7.82%, and another at 11.57%, indicating that layered fracture occurred during the tensile tests. This is a phenomenon that multiple layers in one tensile bar break down at different times. We recoated different combinations of mixed powders to print different samples. The mixed powders affect sample solidification and consolidation between layers and results in the layered fracture in the parts using mixed powders. Calculating the average mechanical properties of the benchmark samples, the baselines of tensile strength, Young's modulus and

elongation at break are respectively 25.80 Mpa, 568 Mpa, and 11.36%. The average mechanical properties of these samples will be used to evaluate the mechanical properties of the tensile bars in the following stages.

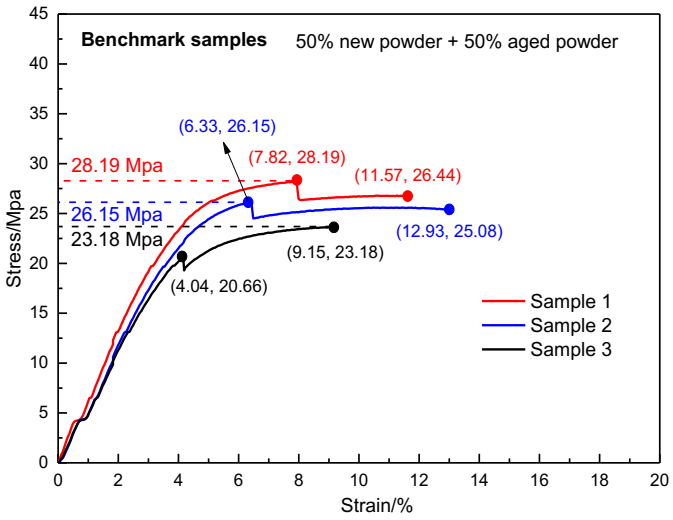

Figure 2-8 Stress-strain curves of benchmark samples

2.3.2.3 Stage 3

In stage 3, samples using new-extremely aged mixed powders without interlayer heating were printed, and the stress-strain curves of these samples are shown in Figure 2-9 (a) - (g). With the percentages of extremely aged powders increasing from 30% to 90%, the average tensile strengths are 24.69 Mpa, 29.18 Mpa, 25.32 Mpa, 25.02 Mpa, 20.93 Mpa, 22.65 Mpa and 29.97 Mpa, and the average elongations at break are 7.10%, 7.76%, 8.60%, 8.43%, 12.33%, 13.38% and 15.36%. The average tensile strength of parts from the combination of 60%-40% new-extremely aged mixed powders to the combination of 30%-70% new-extremely aged mixed powders show a decrease. But this did not apply to the remaining mixing percentages, which can be ascribed to that the mechanical properties of samples are not only related to the properties of powders but also relevant to the thermal or laser conditions in the sintering chamber. It is worth noting that the tensile strengths of 10%-90% new-extremely aged samples appear to be better than the benchmark samples. Due to the severely decreased flowability of the extremely aged powders, the recoating of the extremely aged powders is difficult. The large percentage of the extremely aged powders in the 10%-90% new-extremely aged mixed powders accompanied with sustained high temperature in the SLS chamber failed the recoating process during the printing of the last few layers. And the obtained top layers were sintered multiple times with no powders recoated, which has the similar

effects with printing using improved energy densities. High energy densities lead to high mechanical properties. This is the reason for the large tensile strengths of 10%-90% new-extremely aged samples. Overall, when the percentages of new powders decrease (from 60% to 20%) and the percentages of extremely aged powders increase (from 40% to 80%), the average tensile strengths of samples decrease. However, the elongations at break increase with the increasing of extremely aged powders because the microstructure changes.

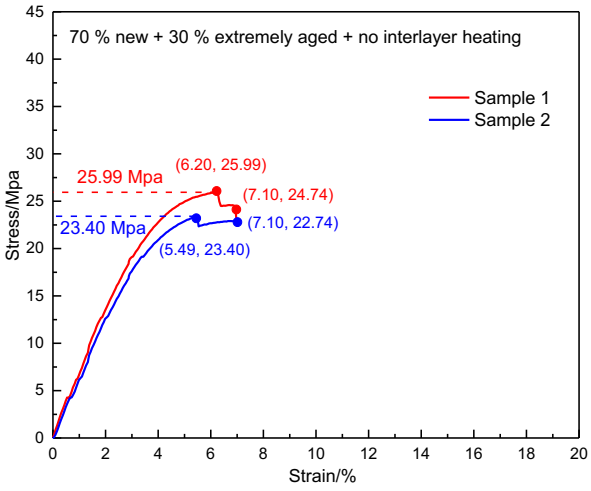

(a) 70% new + 30% extremely aged

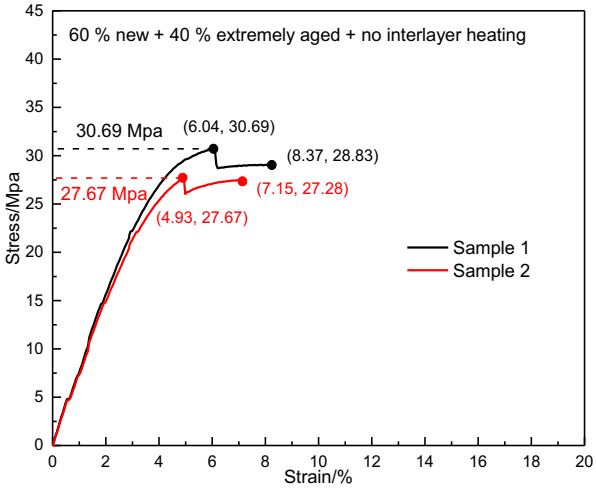

(b) 60% new + 40% extremely aged

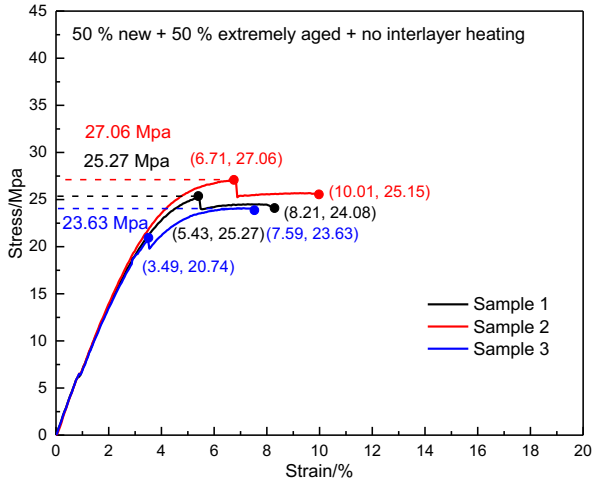

(c) 50% new + 50% extremely aged

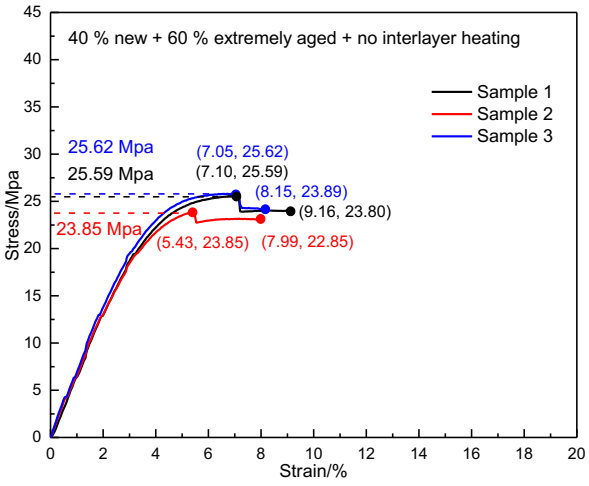

(d) 40% new + 60% extremely aged

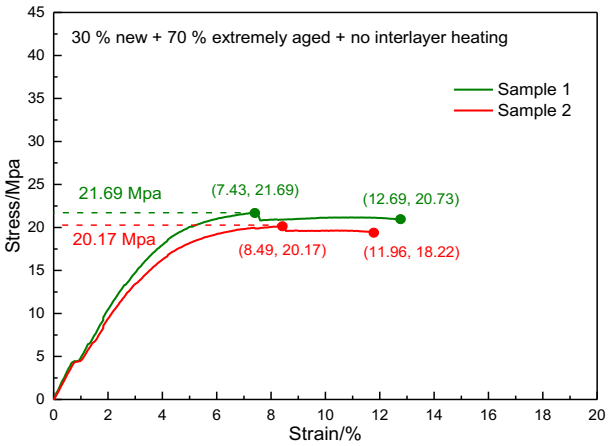

(e) 30% new + 70% extremely aged

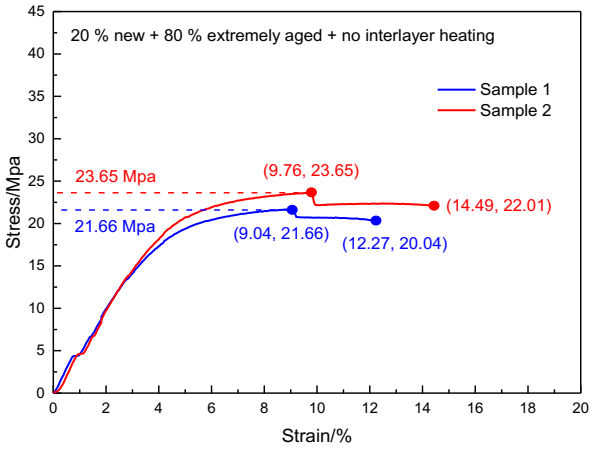

(f) 20% new + 80% extremely aged

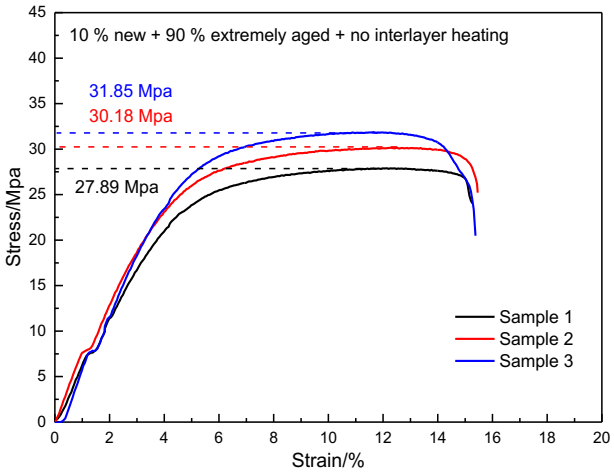

(g) 10% new + 90% extremely aged

Figure 2-9 Stress-strain curves of samples printed using new-extremely aged mixed powders without interlayer heating

2.3.2.4 Stage 4

Figure 2-10 compares stress-strain curves of benchmark samples and samples using new-extremely aged mixed powders with and without interlayer heating. As shown, the tensile strengths of some samples remain no significant changes after interlayer heating, while that of the other samples increase. In Figure 2-10 (a), (b), (c), (e), (f), the tensile strengths of samples with 60-second interlayer heating increased by 25.19%, 36.10%, 30.13%, 5.46% and 22.51%. With 60-second interlayer heating, the average tensile strengths of tensile bars printed using 50%-50% new-aged powder mix, 70%-30% new-extremely aged powder mix, 60%-40% new-extremely aged powder mix, 40%-60% new-extremely aged powder mix and 30%-70% new-extremely aged powder mix are respectively 32.30 Mpa, 33.61 Mpa, 37.97 Mpa, 26.39 Mpa and 25.64 Mpa. With

interlayer heating, tensile bars 3D printed using more new powders tend to have larger tensile strengths. In total, the tensile strengths of samples using mixed powders can be improved to some extent after interlayer heating because of the better melting and coalescence behaviors of particles on each layer. In particular, in addition to the successful reusing of extremely aged powders, the proposed process control yields parts with tensile strength 25.19% higher than default machine configuration using the standard material combination (Figure 2-10a).

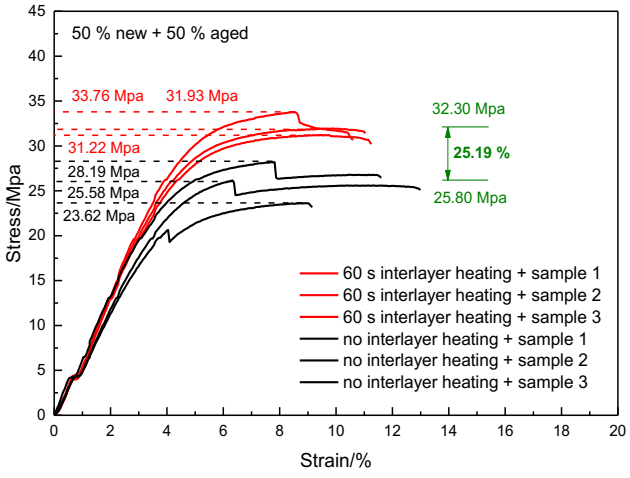

(a) 50% new + 50% aged

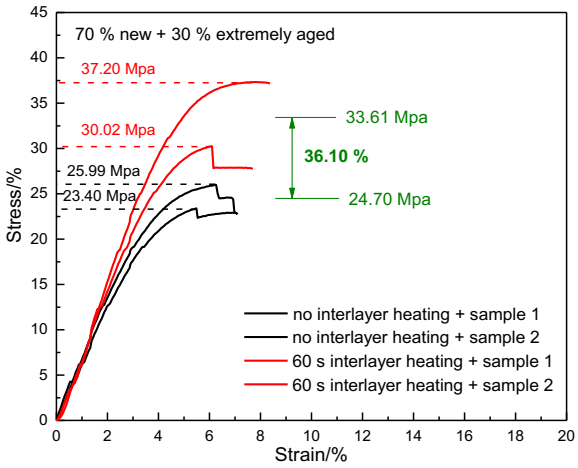

(b) 70% new + 30% extremely aged

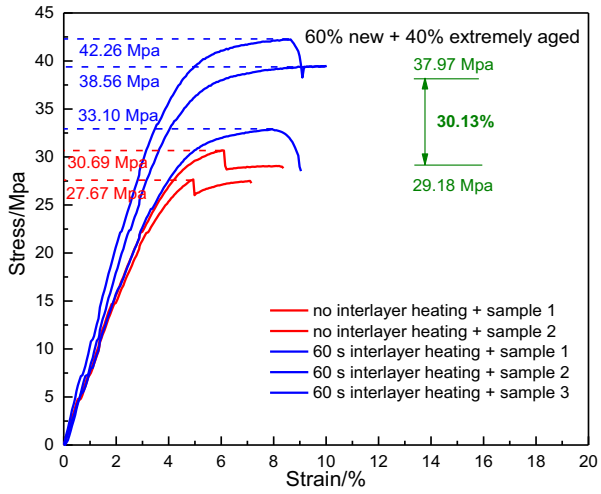

(c) 60% new + 40% extremely aged

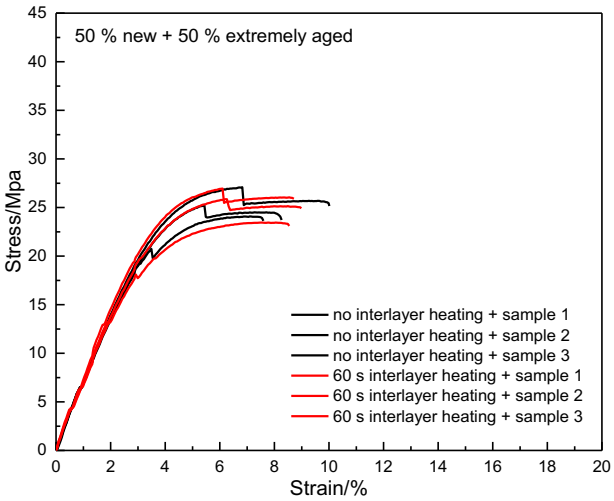

(d) 50% new + 50% extremely aged

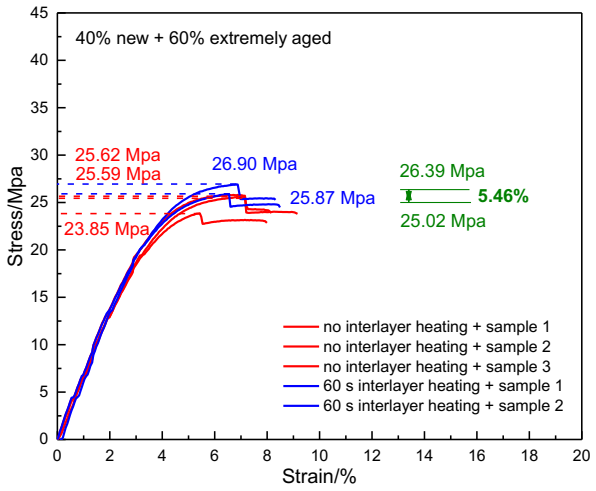

(e) 40% new + 60% extremely aged

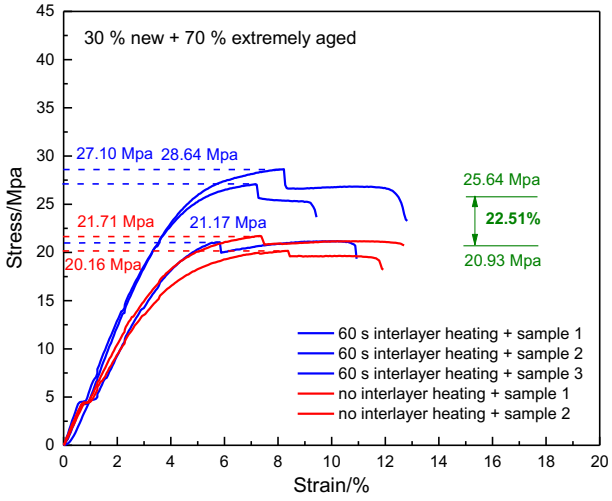

(f) 30% new + 70% extremely aged

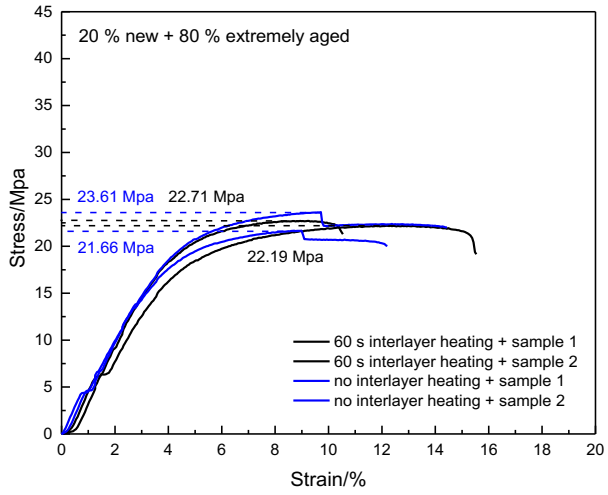

(g) 20% new + 80% extremely aged

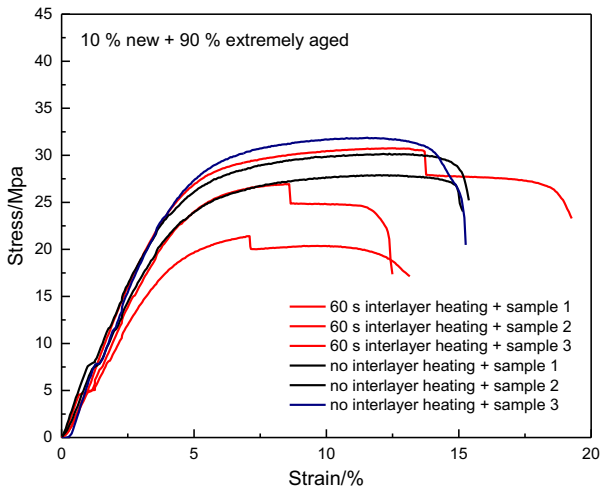

(h) 10% new + 90% extremely aged

Figure 2-10 Comparisons of stress-strain curves of benchmark samples and samples using new-extremely aged mixed powders with and without interlayer heating

2.3.2.5 Stage 5 and Stage 6

Figure 2-11 compares stress-strain curves of samples using new-aged-extremely aged mixed powders with and without interlayer heating. After 60 seconds interlayer heating, the tensile strengths of samples using 30%-30%-40% new-aged-extremely aged mixed powders increase by 1.19%, and that of samples using 30%-40%-30% new-aged-extremely aged mixed powders increase by 18.04%. It is concluded that the tensile strengths of samples using new-aged-extremely aged mixed powders can be improved after interlayer heating.

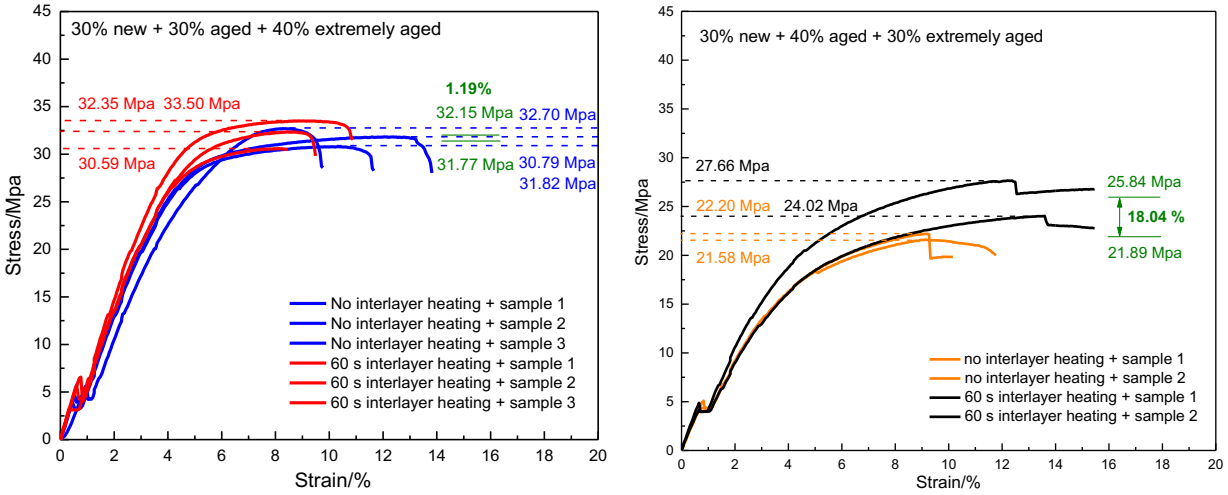

(a) 30% new + 30% aged + 40% extremely aged (b) 30% new + 40% aged + 30% extremely aged

Figure 2-11 Comparisons of stress-strain curves of benchmark samples and samples using new-aged-extremely aged mixed powders with and without interlayer heating

2.4 Discussions

2.4.1 Tensile strength

Figure 2-12 compares tensile strengths of the samples: (a) without interlayer heating, (b) with 60 seconds interlayer heating. The baseline here is the samples printed from the 50%-50% new-aged blend without interlayer heating, i.e., 25.80 Mpa. From Figure 2-12 (a), the powder blends yielding larger tensile strengths than the baseline are: 40%-60% new-extremely aged, 30%-30%-40% new-aged-extremely aged, and 10%-90% new-extremely aged. However, when the percentages of extremely aged powders increased from 50% to 80%, the average tensile strengths decrease. The reasons are that it is more difficult to move dislocations through and between the grains when there are more extremely aged powders. Therefore, *for the samples without interlayer heating, the recommended mixing percentages closest to industry current practice is 60%-40% new-extremely aged and 30%-30%-40% new-aged-extremely aged (13.18% and 23.14% better than baseline)*.

From Figure 2-12 (b), there are three blends with 60 seconds interlayer heating of which the tensile strengths are larger than the baseline (25.80 Mpa): 50%-50% new-aged, 60%-40% new-extremely aged and 30%-30%-40% new-aged-extremely aged (25.19%, 47.17% and 24.69% better than baseline). Thus, *the recommended mixing percentages closest to industry current practice for the samples with interlayer heating are 50%-50% new-aged, 60%-40% new-extremely aged and 30%-30%-40% new-aged-extremely aged.*

Tensile bars using reclaimed powders cannot coalesce well due to the high melting point particles. As a result of the insufficient consolidation, partial densification and numerous unmolten particles, tensile strengths of the 3D printed parts degrade. Thus, tensile bars using more new powders normally have larger tensile strengths. In Figure 2-12b, the tensile bars using 60%-40% new-extremely aged mixed powders with interlayer heating have more new powders and better coalescence behaviors than most of the other parts, resulting in superior tensile strength. For the tensile bars using 70%-30% new-extremely aged mixed powders with interlayer heating, the tensile strength is slightly lower than that of the parts using 60%-40% powder blend. The reason is that the tensile bars using 60%-40% new-extremely aged mixed powders have better densification than that using 70%-30% new-extremely aged mixed powders, which has been verified from our SEM test results.

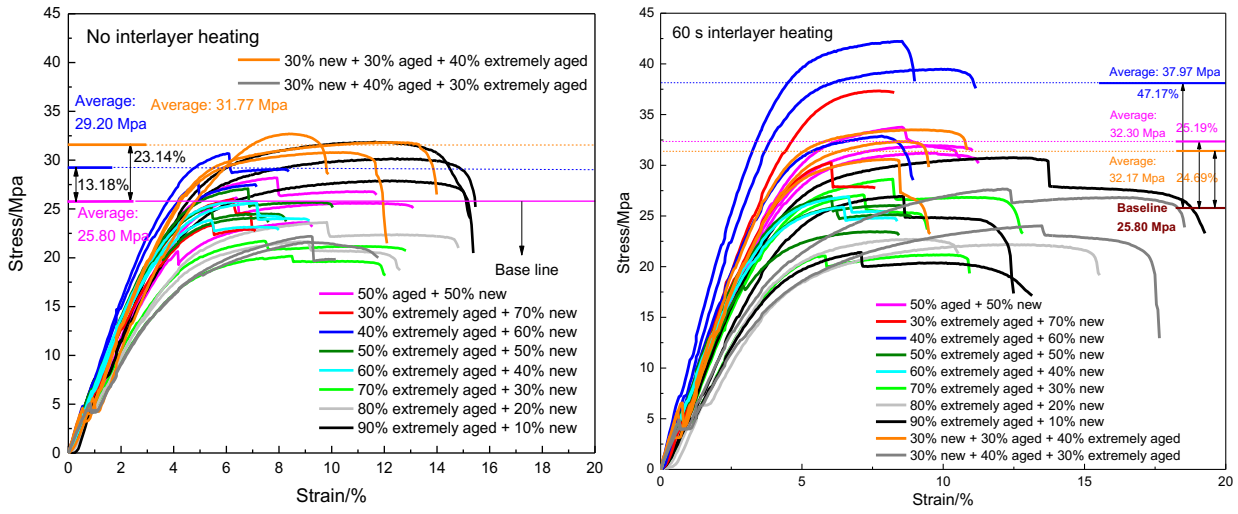

(a) Samples without interlayer heating (b) Samples with 60 s interlayer heating

Figure 2-12 Comparisons of sample tensile strengths

2.4.2 Elongation at break

Figure 2-13 compares sample elongations at break: (a) sample elongations at break, (b) mean values and standard deviations of sample elongations at break. Similar to the tensile strength test, the baseline performance is from the samples printed using 50%-50% new-aged blend without interlayer heating, i.e., 11.36%. From Figure 2-13b, there are several blends that have similar or larger values of elongations at break compared to the baseline. For the samples without interlayer heating (Figure 2-13 b (i)), the samples using more extremely aged powders have larger average elongations. The largest elongation is from the 10%-90% new-extremely aged blend (the average value is 35.30% better than baseline), because increased extremely aged powders yields smaller

crystal size (verified by XRD) and increased flexibility. *The recommended mixing percentages of samples without interlayer heating are 30%-30%-40% new-aged-extremely aged and 30%-40%-30% new-aged-extremely aged mixed blends.* These combinations are close to industry current practice, and the elongations are better than baselines. For the samples with interlayer heating (Figure 2-13 b (ii)), the largest elongation is from the 30%-40%-30% new-aged-extremely aged mixed blend (the average value is 58.97% better than baseline), because interlayer heating enhances particle bonding and microstructures. *The recommended mixing percentage of samples with interlayer heating is 30%-40%-30% new-aged-extremely aged mixed blend*. The part elongation at break of this combination increases by 55.29% after interlayer heating (from 11.63% to 18.06%).

From Figure 2-13b, the samples without interlayer heating have relatively uniform standard deviations on elongations at break. However, the standard deviations on elongations of samples with interlayer heating are irregular. These samples with 70%, 80% and 90% extremely aged powders have larger standard deviations than the remaining ones.

In general, parts using more reclaimed powders have increased elongations at break, while parts using more new powders with larger crystal sizes are easier to break before the separation of crystals. Notice that 10%-90% new-extremely aged powder blends generated competing results regarding elongation at break. The result is attributed to the fact that the reclaimed powders have smaller crystal size, increased flexibility and decreased brittleness. However, considering combined mechanical strength and the large deviation from industrial practice, this powder composition is not recommended for immediate industrial application. Though parts using more reclaimed powders have smaller crystal size, increased flexibility and elongations at break, powder mixing increase diversity of grain sizes in the mixed new-reclaimed powders, contributing to decreased elongations at break.

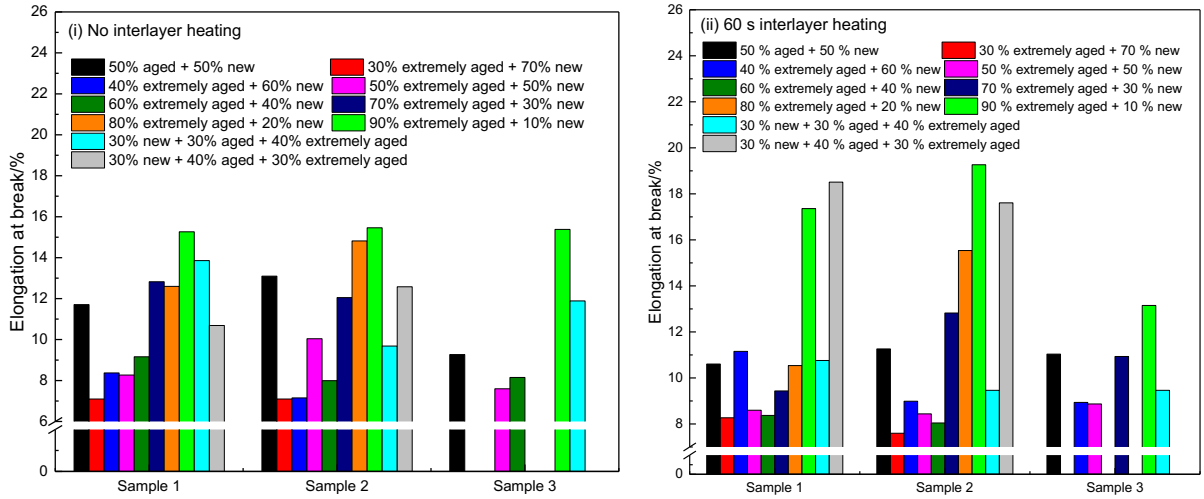

(a) Sample elongations at break

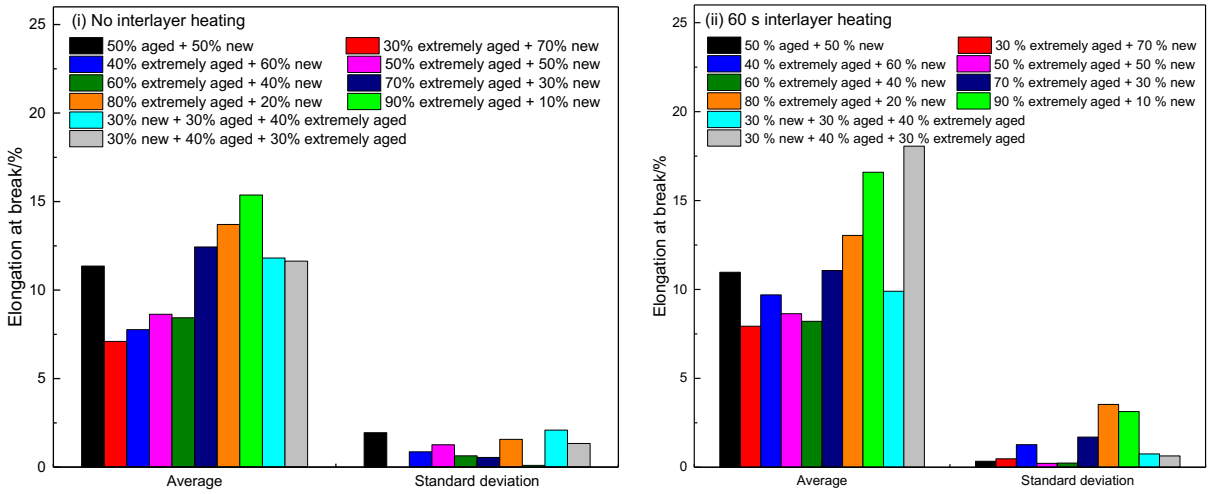

(b) Mean values and standard deviations of sample elongations at break

Figure 2-13 Comparisons of sample elongations at break

2.4.3 Young's modulus and build time

Figure 2-14 compares the Young's modulus of samples printed using powders of different combinations, (a) sample Young's modulus, (b) mean values and standard deviations of sample Young's modulus. The dotted line in Figure 2-14a shows the Young's modulus of the 50%-50% new-aged mixed blend. From Figure 2-14b, parts with high percentages of extremely aged powders, for instance, 70%, 80% and 90%, have lower average Young's modulus. However, there is no distinct rule that the standard deviations of sample Young's modulus are affected by powder combinations or interlayer heating. Also, in presence of recycled materials, the proposed

configuration can consistently control the sample Young's modulus to the same level as the benchmark samples (50%-50% new-aged mixed blend).

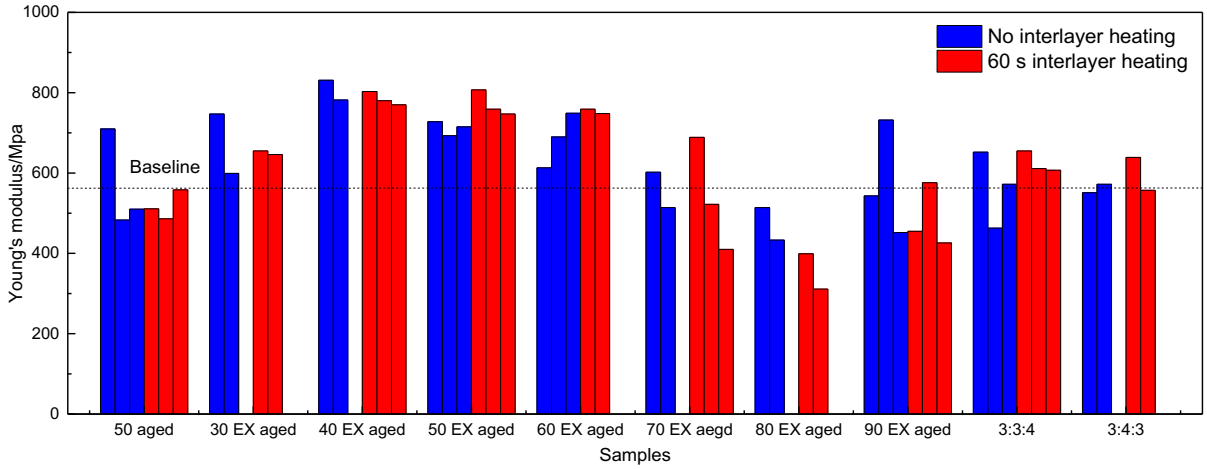

(a) Sample Young's modulus

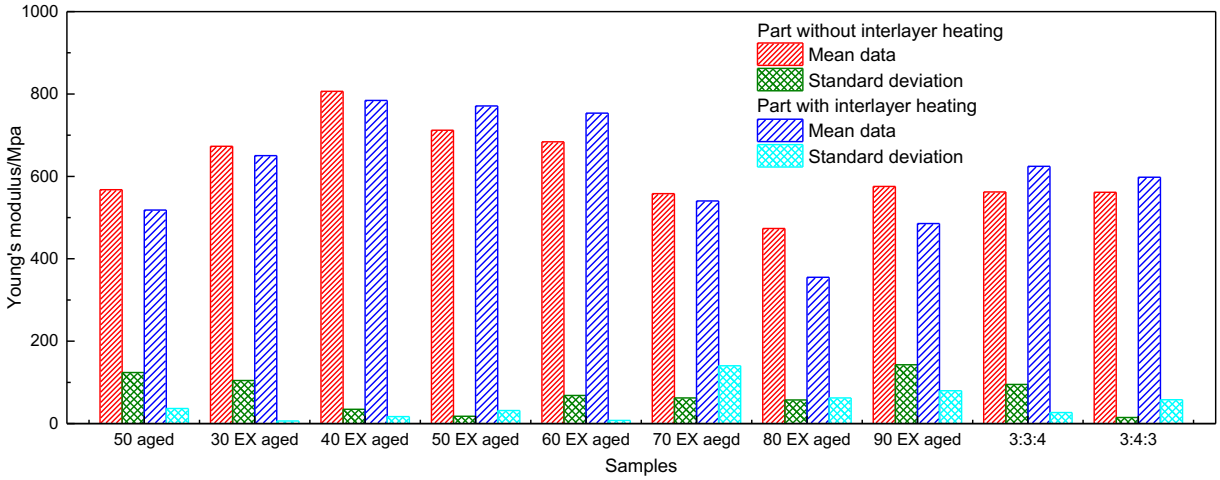

(b) Mean values and standard deviations of sample Young's modulus

Figure 2-14 Comparisons of sample Young's modulus

The total build time for tensile bars without interlayer heating is 35 minutes (25 minutes of preheating and 10 minutes of printing). As a trade-off of successfully reusing extremely aged powders and improved mechanical properties, for the tensile bars with interlayer heating, the interlayer heating time is 10 minutes (60 seconds×10 layers) for a batch. The total build time for tensile bars with interlayer heating is 45 minutes (25 minutes of preheating, 10 minutes of printing and 10 minutes of interlayer heating). The proposed SLS with interlayer heating aims to provide the needed heating energy to improve part mechanical properties through promoting powder coalescence and part densification. In practice, engineering judgements are recommended to

balance material cost, part design, and urgency of the manufacturing task when recycling and reusing the materials.

2.5 Conclusions

A new process control method was proposed in this work to explore the possibility and feasibility of reusing the differently degraded polyamide 12 powders in different combinations. In particular, the proposed method successfully reuses extremely aged polyamide 12 powders close to the heat-affected zones. The proposed method is composed of seven steps, including powders sample collection, powder preprocess, powder mixing, powder characterizations, parameter control, SLS with interlayer heating and part characterizations. This method enabled reusing reclaimed polyamide 12 powders in different situations: only pure powders, new-aged mixed powders, new-extremely aged mixed powders with different mixing percentages and new-aged-extremely aged mixed powders with different mixing percentages.

The proposed method of SLS created parts with improved mechanical properties: the largest tensile strength we obtained is 37.97 Mpa from tensile bars 3D printed using 60%-40% new-extremely aged powders with 60-second interlayer heating, a result 47.17% better than the baseline (25.80 Mpa). The tensile bars which have stably large elongations at break are from the 10%-90% new-extremely aged blends without or with interlayer heating (15.37% and 16.59% respectively). Compared to the baseline sample, the tensile bars 3D printed using 30%-40%-30% new-aged-extremely aged mixed powders with 60-second interlayer heating yield 18.04% higher tensile strength and 55.29% larger elongation at break.

Chapter 3. PROCESS CONTROL OF SURFACE QUALITY AND PART MICROSTRUCTURE WITH POST-HEATING

3.1 Introduction

Capable of fabricating functional parts with diverse materials and complex geometries directly from a digital model, SLS is one of the most widely developed techniques in additive manufacturing to manufacture high-quality polymeric and metallic components [24, 90, 94, 95]. Compared with other SLS materials such as metals and ceramics, polymeric powder materials offer benefits in low processing temperatures, controllable flowability and high corrosion resistance [96-98] in trade of strength. Particularly, as one of the most important semi-crystalline thermoplastic polymer materials, polyamide 12 and its reinforced/filled forms generate SLS parts with superior mechanical properties over general amorphous materials [90].

The microstructures of polyamide 12 materials consist of a series of carbon atoms and the amide groups (-NHCO-), forming carbon-based molecular chains and showing both amorphous regions and crystalline regions [20, 24]. Due to the open chain ends, the molecular structures of polyamide 12 materials are prone to molecular changes at high temperatures and during laser-material interactions. In particular, post-condensation, chain scission and chain crosslinking reactions form the essential degradation mechanisms of polyamide 12 powders [21], and induce different material properties between reclaimed and pristine polyamide 12 powders.

Reduced flowability is a predominant property change for reclaimed polyamide 12 powders [24]. This property change is attributed to (i) the increase of the molecular weight originated from molecular chain crosslinking and spherulite growth [19], and (ii) the formation of large particles aggregated from small pieces. These large particles cause deteriorated surface finish with unmolten high-melting-point pieces in the specimens [99]. With multiple times of reuse and repeated expansion/shrinkage in the fabrication cycles, the surface of the reclaimed polyamide 12 powders exhibits increasing cracks and fragments, lowering the part surface quality [35]. Also, compared to 3D printed parts using new powders with fibrillar spherulites dominating the morphologies, parts using reclaimed powders contain coarse spherulites with rough and uneven surface finish due to post-crystallization and spherulite growth [24, 52].

More at the level of part quality, S. Dadbakhsh et al. [24] utilized the scanning electron microscopy (SEM) to exam the surfaces of single layer parts made from new, mixed, and aged powders, aiming to clarify the effects and the corresponding mechanisms of in-process aging on the microstructures of polyamide 12 specimens in SLS. M. Pavan et al. [42] investigated how thermo-temporal effects on the SLS polyamide 12 impact part quality at both micro- (e.g., porosity and crystallinity) and macro-levels (e.g., dimensional accuracy) by testing the samples using a mixing ratio 50/50 new/recycled powder and an alternate x-y scanning pattern. D.T. Pham et al. [100] and W. Yusoff et al. [52] developed different amendment strategies through optimizing the important SLS process parameters to reduce or eliminate the "orange peel" surface texture when using reclaimed polyamide 12. J. Guo et al. [101] presented an experimental and analytical study to improve the surface quality of parts using reclaimed polyamide 12 materials and to clarify the interrelations between surface quality and process parameters.

Despite the aforementioned literature, it remains not clear how to maximize surface quality when using reclaimed powders of different combinations. Moreover, there is a lack of understanding in surface characteristics of parts sintered using extremely aged polyamide 12 powders. Held close to or wrapped by the heat-affected zones (HAZs), these powders go through severe degradations during the sintering process. We show, however, that such expensive materials can be reused to produce parts with fine surface textures, reduced porosities, and free from unmolten particles. The result is obtained by developing a new strategy to control and optimize surface quality using SLS with controlled post-heating. By material preparation, powder and part characterizations and SLS with controlled post-heating, we obtain a series of parts using differently degraded powders and different combinations. Then after surface cleaning, we examine the surface morphologies of these parts and evaluate the characteristics of the surface morphologies. The result is that the undesirable surface finish of parts printed using reclaimed polyamide 12 powders can be optimally improved after using the proposed strategy. In particular, parts 3D-printed using the 30%-30%-40% new-aged-extremely-aged powder mixtures exhibit the smoothest and flattest surface with no unmolten particles and nearly zero porosity.

3.2 The proposed process control with post-heating for reclaimed polyamide 12

The proposed method involves (Figure 3-1) material preparation (Step 1) and SLS with post-heating (Step 2). More specifically, Step 1 includes powder collection and powder preprocess, and Step 2 covers powder/part characterizations, powder mixing, parameter control, SLS with post-

heating and evaluation [39, 102]. Details of these procedures are explained in the following sections.

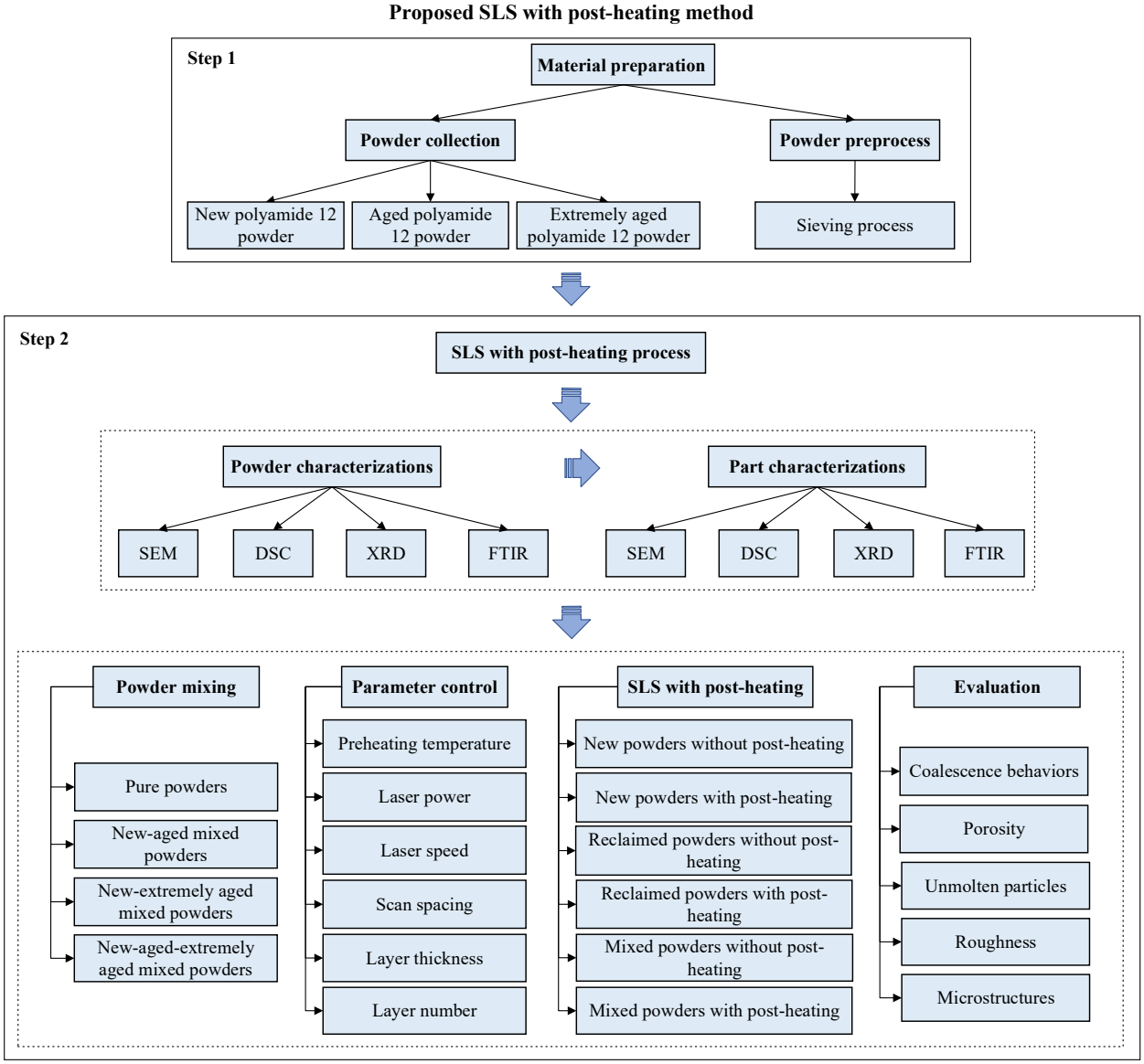

Figure 3-1 Proposed SLS with post-heating method to improve part surface quality when using reclaimed polyamide 12 powders

3.2.1 Material preparation

Powder collection: Pristine or new polyamide 12 powders were purchased from EOS Corp, and the reclaimed powders were collected from standard SLS processes on an EOS P 390 machine. Polyamide 12 powders with 3 different degradation levels were used in this work: (1) new polyamide 12 powders with no additional heat treatment; (2) aged polyamide 12 powders located far away from the HAZs in the SLS chamber and are reused in industries; (3) extremely aged

polyamide 12 powders adjacent to or wrapped by the HAZs that are not reused in industries currently.

Powder preprocess: Due to the large particles or part debris caused by the high temperature and laser induced degradation/aging, when recoating with the extremely aged powders, the powder bed is uneven and rough on surface. A sieving process was applied to preprocess the extremely aged powders for an even recoating surface. This process was conducted in a fume hood using a sieve with a mesh size of 200 um. The time for sieving a batch of 500 ml powders is around 2 hours including preparation and post cleaning. After sieving, 84%~90% of the reclaimed materials can be collected and well recoated.

3.2.2 Proposed SLS and post-heating

3.2.2.1 Powder mixing

Four different kinds of powder combinations were used in this work: (i) pure powders, (ii) new and aged powder mixture, (iii) new and extremely aged powder mixture, and (iv) new, aged, and extremely aged powder mixture. We conducted various volume mixing percentages for these powder combinations.

3.2.2.2 Parameter control

Before presenting the main surface improvement control proposed in this work, we discuss the overall parameter control that significantly influences the properties of the sintered parts. Six key parameters were tested in the experiments: preheating temperature, laser power, laser speed, scan spacing, layer thickness and layer numbers of samples (Figure 3-1). A variety of parameter settings are suitable for new powders. However, existing parameter settings seldom apply to the case using extremely aged powders in presence of the degraded material properties. The general principles to select the proposed parameter settings are that (i) these parameters are equal or close to industrial norms and (ii) the pure new, aged and extremely aged polyamide 12 powders can all be successfully printed into parts. The nominal parameter settings selected in this work were: preheating temperature, 160 °C; scan speed, 3000 mm/s; laser power, 18 W; scan spacing: 0.3 mm; layer thickness, 150 μm. In this work, samples are all printed with 3 layers and using the optimized parameter settings selected to explore the part surface quality improvement.

3.2.2.3 SLS with post-heating

Hardware: The SLS machine used in the work is an in-house built open-configuration research testbed, with features comparable to commercial machines (the same machine used in Chapter 2, Figure 2-3).

Process: The proposed SLS and post-heating control apply tailored heating after the core laser-material interaction with optimized processing parameters. The post-heating here keeps parts at the preheating temperature (160 °C) for a controlled time after the sintering process. In this work, we tested 0 second (no post-heating), 20 seconds, 60 seconds, 120 seconds, and 300 seconds of post-heating to different specimens to explore the influences of post-heating on part surface morphologies. Figure 3-2 shows details of the proposed five-stage SLS. In Stage 1, we 3D printed the benchmark part using 100% new powders with no additional post-heating, and the part was used as a reference to evaluate the surface qualities of other parts. In Stage 2, parts were printed using 100% new powders with different post-heating time (20 seconds, 60 seconds, 120 seconds, and 300 seconds) to identify the influences of post-heating on part surface qualities when using 100% new powders. In Stage 3, we printed parts with 100% extremely aged powders at different post-heating time. After comparing the surface qualities of parts using reclaimed powders with and without post heating, 300-second post heating appears most effective for reclaimed powders. In Stage 4, parts were 3D printed using different powder mixtures; parts were also 3D printed with and without 300-second post-heating to study the effects of post-heating on part surface quality when using mixed powders. In Stage 5, we used the mixtures of three differently degraded powders (new, aged, and extremely aged powder mixtures) with and without 300-second post-heating. The results form the basis to identify the effects of post-heating on part surface morphology.

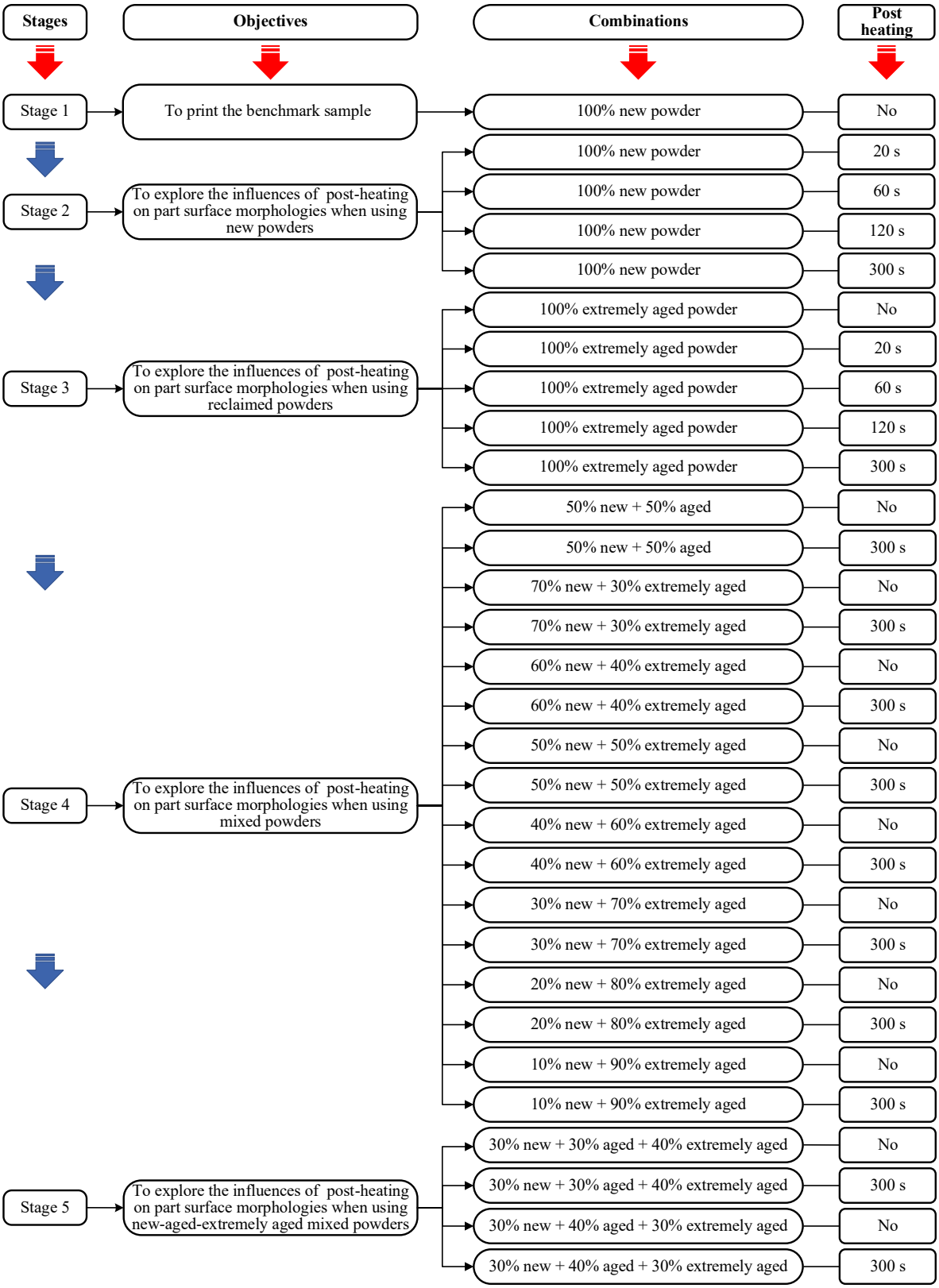

Figure 3-2 Post-heating based SLS process (The mixed powders are in volume percentages)

Mechanism: It has been verified that the pieces with a high melting point in the reclaimed polyamide 12 powders require a higher temperature to form the molten phase [24]. Thus, reclaimed polyamide 12 powders are more difficult to melt and coalesce compared to new powders under the same sintering conditions, leading to worse surface qualities with insufficient coalescence and numerous unmolten particles. In addition, the numerous unmolten pieces in the reclaimed powders act as the nucleation sites for the formation of nucleation seeds. Spherulite structures grow on the nucleation seeds once the temperature is below the melting point. In this way, numerous spherulite structures grow on the amorphous solid phase of parts after the layer solidifies, forming coarse spherulites and a rough surface. On the other hand, when using new powders, the generated parts have fibrillar spherulites and smooth surface subject to little unmolten pieces and nucleation seeds. Our proposed SLS with customized post-heating provides additional and enough energy to promote coalescence of the reclaimed powders and to accelerate the phase change of high-melting-point pieces. The method is also helpful to avoid the formation of numerous spherulite structures and decrease the surface roughness. In addition, the parts using pure new powders can have high porosity immediately after printing. The new and reclaimed powder mixtures used in the proposed method explore the possibility of reducing part porosity.

Evaluation: After surface cleaning to remove debris on the part surface, we used SEM to compare surface morphologies between the benchmark part and the evaluated parts in Figure 3-2. Compared features include particle coalescence performances, part porosity, the number of unmolten particles, surface microstructures and roughness. The parts were found to have significantly different surface properties when using different powders and powder mixtures. The details are explained in the next section.

3.3 Experimental results - Surface quality improvements of the 3D-printed parts

3.3.1 Stage 1: printing the benchmark sample

Figure 3-3 presents the SEM images of the 3-layer benchmark sample printed using 100% new polyamide 12 powders without additional heat treatment. As seen from Figure 3-3 (a) - (c), the part exhibits a smooth and flat surface with no unmolten particles. Meanwhile, high porosity is observed from these images, suggesting an insufficient densification. At a high magnification ratio of 10000 (Figure 3-3 d), some fine lamellae or spherulitic regions in an amorphous matrix are observed. The spherulites radiate from the center and grow in a ringed extinction pattern. These

surface characteristics of the benchmark part are used as references to evaluate the surface quality of the other parts.

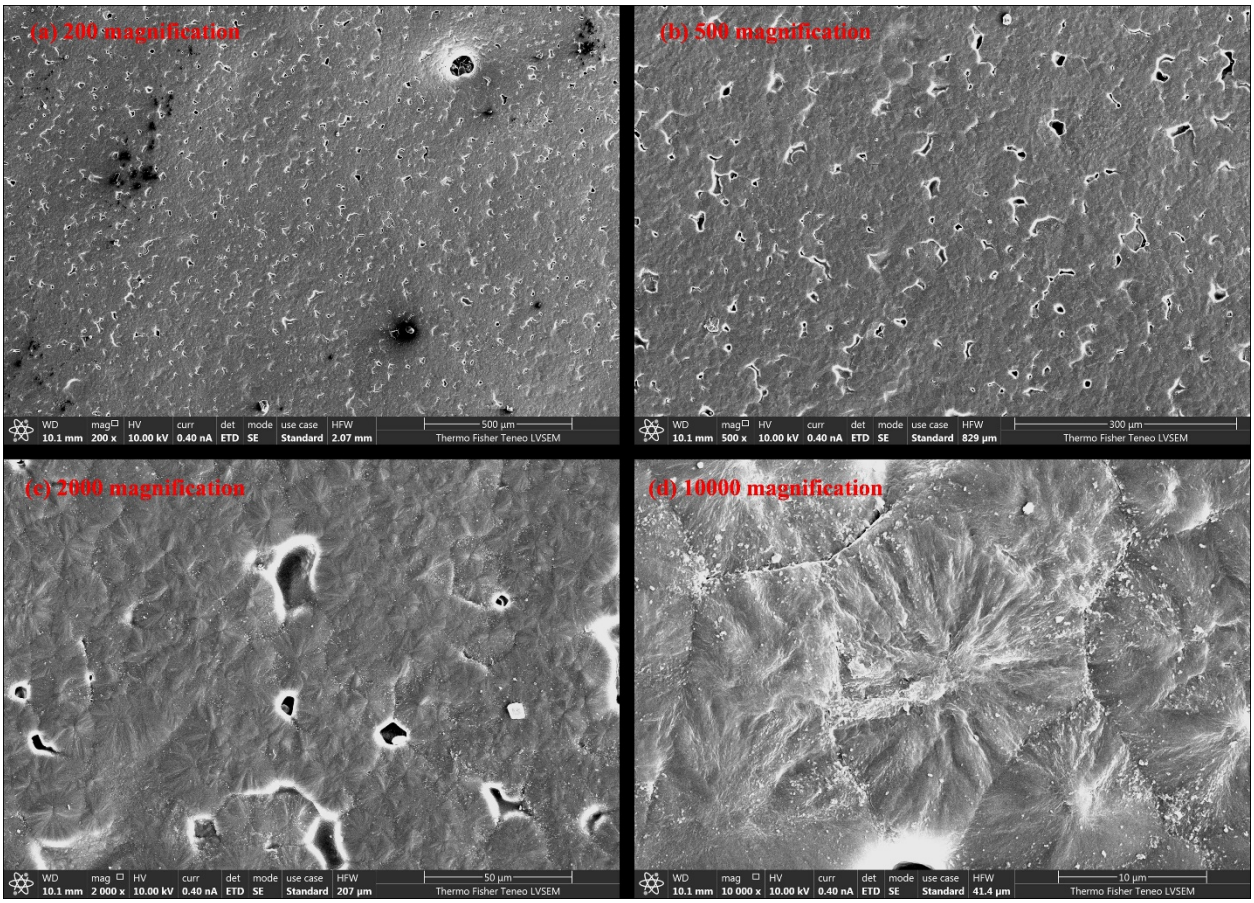

Figure 3-3 The SEM images of benchmark part using 100% new polyamide 12 powders at different magnification ratios (a) 200, (b) 500, (c) 2000, and (d) 10000

3.3.2 Stage 2: the influences of post-heating on part surface morphology when using new powders

Dissimilar to Figure 3-3, Figure 3-4 shows the SEM results of the parts using 100% new polyamide 12 powders with 20 seconds, 60 seconds, 120 seconds and 300 seconds post-heating at a magnification ratio of 500. In Figure 3-4, no obvious differences are observed for the parts using different post-heating time. Compared with Figure 3-3b (100% new samples with no post-heating), the parts obtained in Stage 2 (printed using the same powders and different post-heating time) exhibit a very similar surface morphology of a smooth and flat surface with high porosity and no visible unmolten particles (Figure 3-4). The result suggests that the parts in Stage 2 have similar coalescence, densification and consolidation characteristics with the parts in Stage 1, a further

indicator that the post-heating barely has an effect on the surface qualities of samples 3D printed using new polyamide 12 powders.

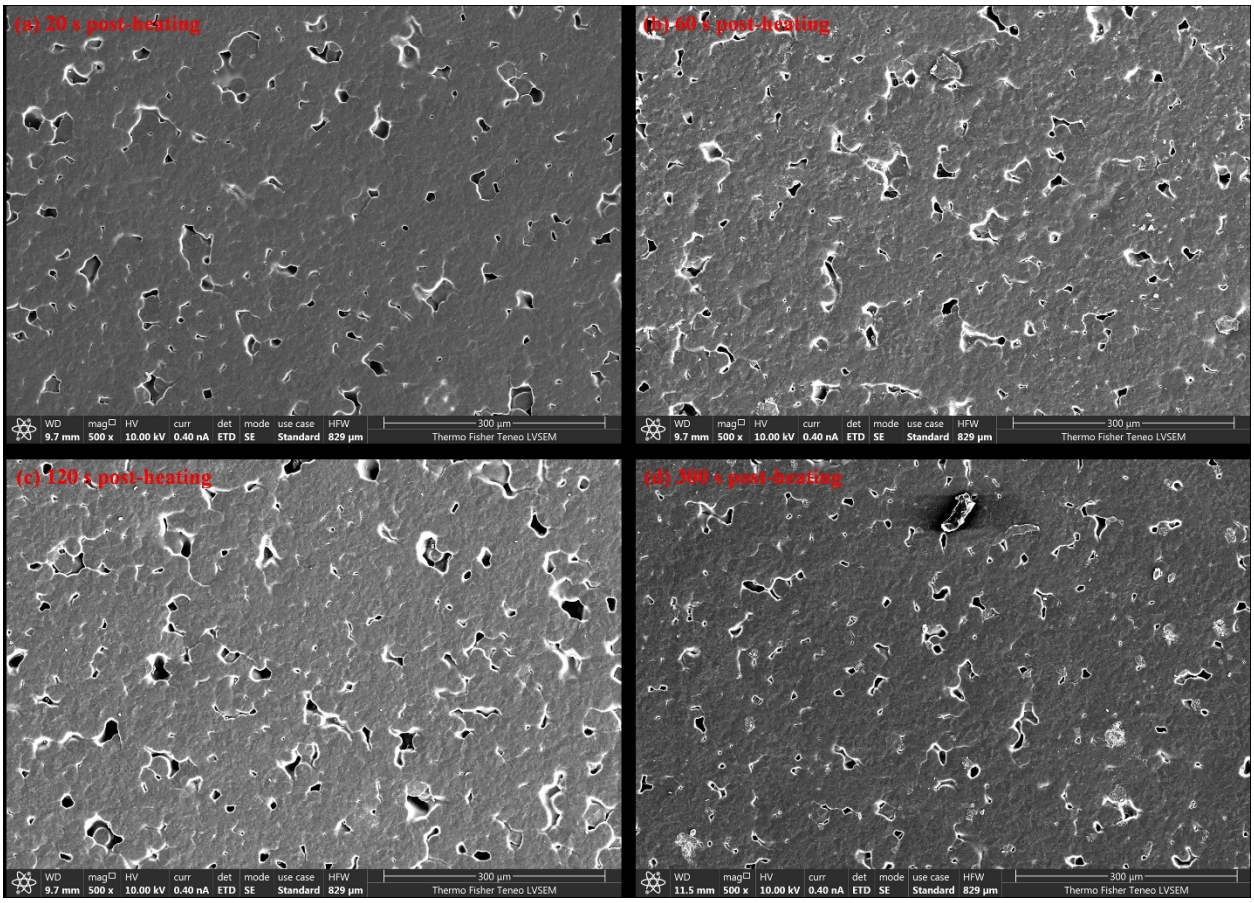

Figure 3-4 The part using 100% new polyamide 12 powders with (a) 20 seconds, (b) 60 seconds, (c) 120 seconds and (d) 300 seconds post-heating at a magnification ratio of 500

3.3.3 Stage 3: the influences of post-heating on part surface morphology when using reclaimed powders

Figure 3-5 exhibits the SEM images of parts using 100% extremely aged powders with 0 second (no post-heating), 20 seconds, 60 seconds, 120 seconds, and 300 seconds post-heating at magnification ratios of 500 and 2000. From Figure 3-5 a to e, we observe a gradual melting and coalescing process with post-heating time increasing. In Figure 3-5a (no post-heating), multiple layers of insufficiently melt particles are observed, and every two or more particles form a neck-like bonding due to the reduction of the free surface energies of the particles triggered by high temperature and intense laser-material interaction. With 20 seconds of post-heating (Figure 3-5b), the particles bonded by the neck-like structures migrate together. The migration becomes stronger

with longer post-heating (Figure 3-5 c and d). Finally, a large unit, a well-consolidated surface forms with little porosity and few unmolten pieces (Figure 3-5e).

Comparing Figure 3-3 (100% new powders with no post-heating) with Figure 3-5a (100% extremely aged powders with no post-heating), we observe an obvious difference in surface morphology. Numerous visible unmolten particles arise and fuse together to form porous structures in the parts 3D printed using extremely aged powders (Figure 3-5a). The results indicate the existence of high-melting-point pieces in the extremely aged powders, matching well with the DSC results that the peak melting temperature and melting enthalpies of deteriorated polyamide 12 powders increase. Given the above, we conclude that the post-heating process helps to improve the surface quality of the printed parts using extremely aged powders by maximizing the coalescence and consolidation, and a well-consolidated surface obtains with 300 seconds post-heating (Figure 3-5e).

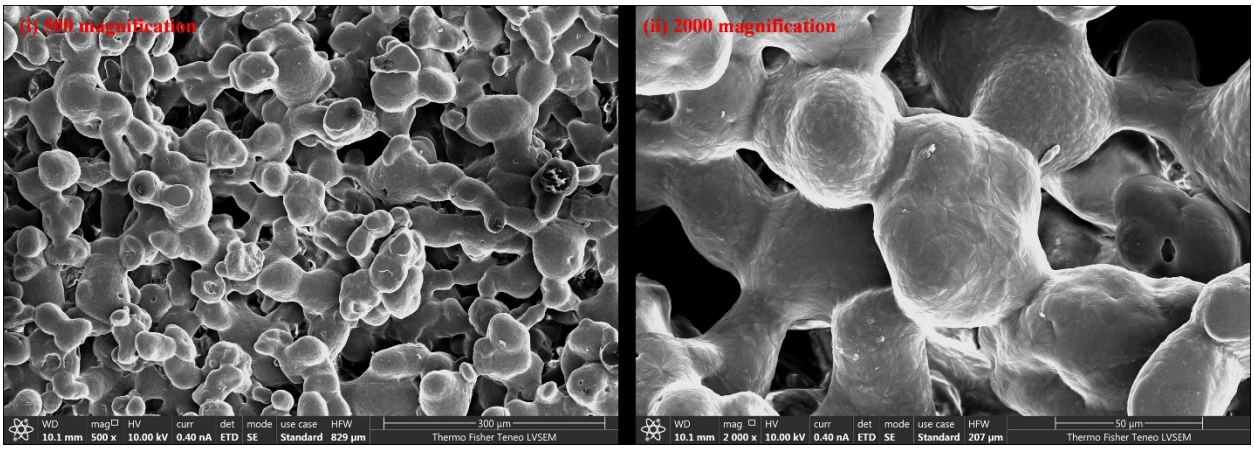

(a) Parts using 100% extremely aged polyamide 12 powders without post-heating

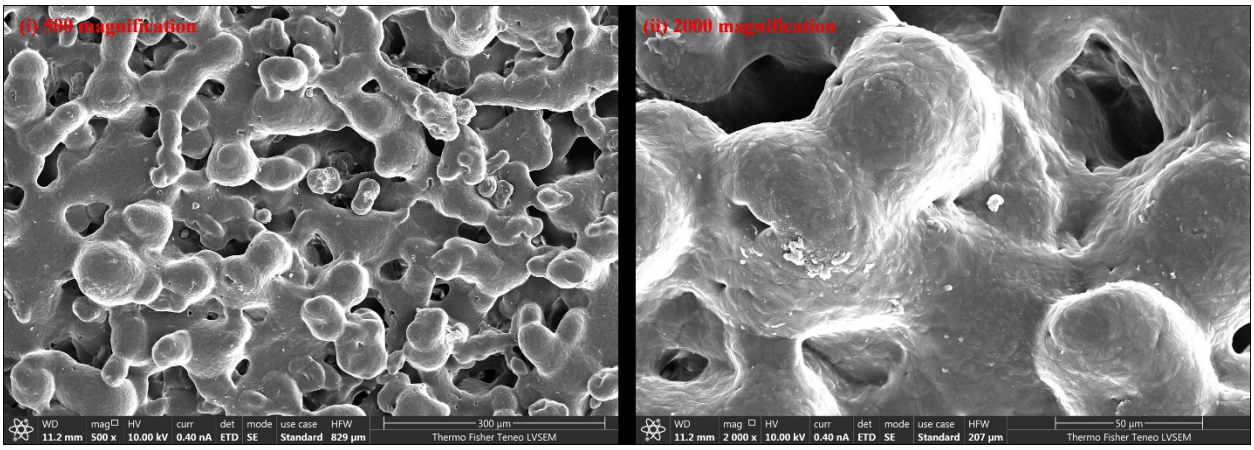

(b) Parts using 100% extremely aged polyamide 12 powders with 20 seconds post-heating

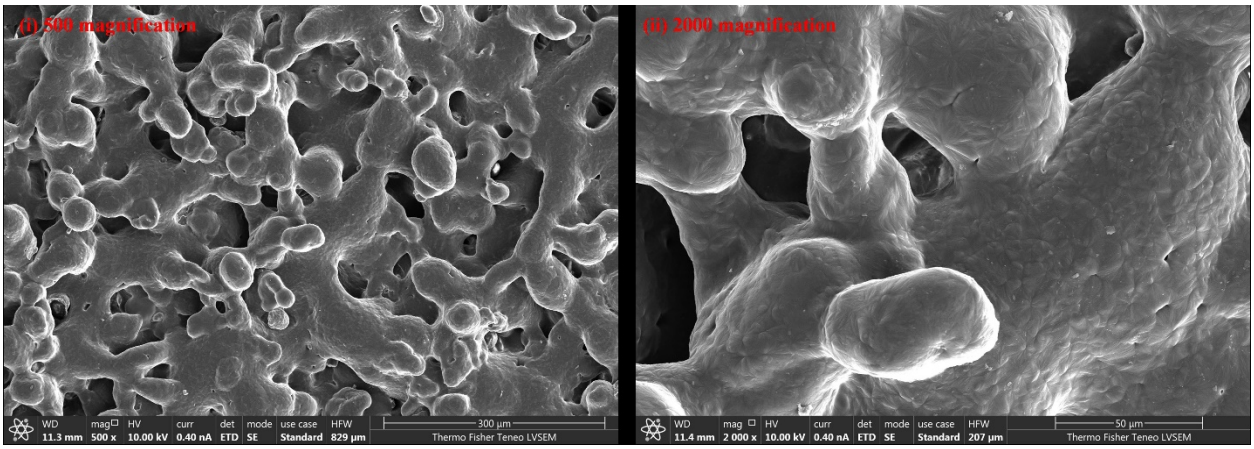

(c) Parts using 100% extremely aged polyamide 12 powders with 60 seconds post-heating

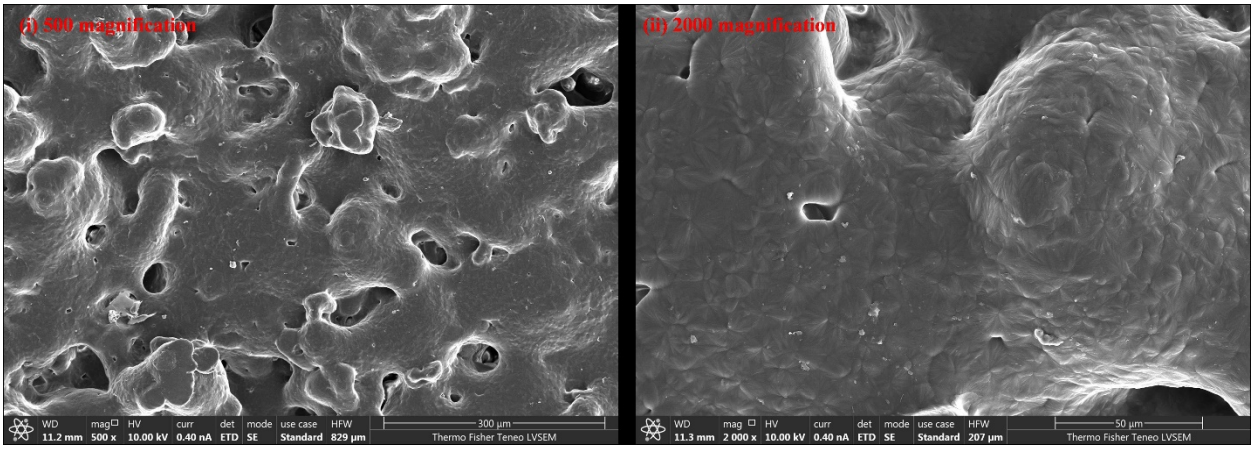

(d) Parts using 100% extremely aged polyamide 12 powders with 120 seconds post-heating

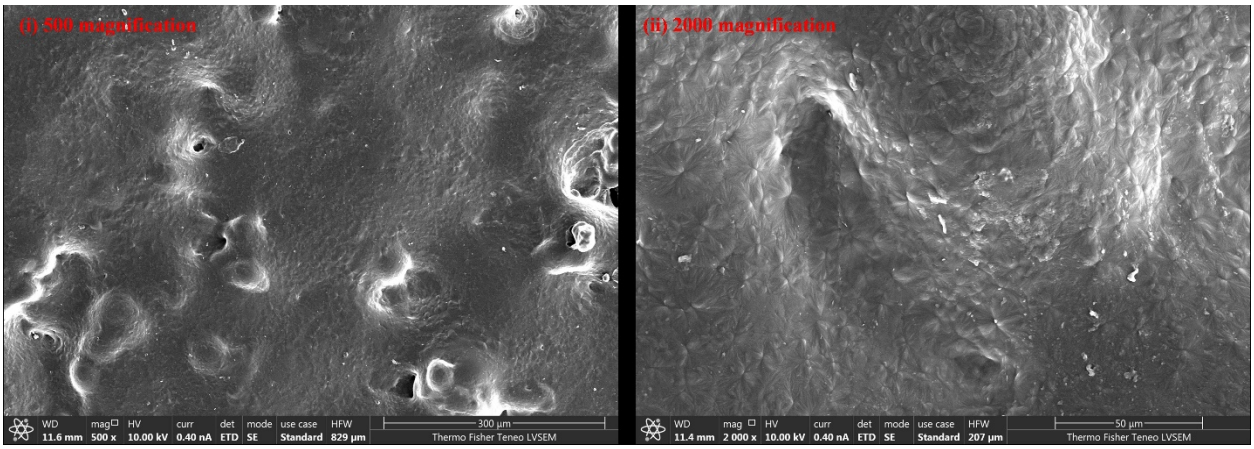

(e) Parts using 100% extremely aged polyamide 12 powders with 300 seconds post-heating

Figure 3-5 Parts printed using 100% extremely aged polyamide 12 powders with and without post-heating

3.3.4 Stage 4: the influences of post-heating on part surface morphology when using mixed powders

Figure 3-6 presents the SEM images of the parts using new-aged polyamide 12 powder mixtures and new-extremely-aged polyamide 12 powder mixtures with (i) no post heating and (ii) 300 seconds post-heating. Figure 3-6 (a) - (d) shows the SEM images of parts 3D printed using 50%-50% new-aged mixed powders, 70%-30% new-extremely-aged mixed powders, 60%-40% new-extremely-aged mixed powders, and 50%-50% new-extremely-aged mixed powders, respectively. The left and right subfigures, indicated by (i) and (ii), show the results of no post heating and 300 seconds post-heating, respectively. Smooth and flat surfaces with several unmolten particles are observed with no post heating (Figure 3-6 a (i), b (i), c (i) and d (i)), suggesting that good particle coalescence behaviors are achieved when using 50% or more new powders. Meanwhile, the unmolten particles dramatically decrease, and smooth and flat surfaces with high porosity are obtained with 300 seconds post-heating (Figure 3-6 a (ii), b (ii), c (ii) and d (ii)). These surfaces are similar to those of parts using 100% new powders, suggesting a significant improvement of surface qualities by our post-heating.

Figure 3-6 (e) - (f) show the SEM images of parts 3D printed using 40%-60% new-extremely-aged mixed powders and 30%-70% new-extremely-aged mixed powders, respectively. The left and right subfigures, indicated by (i) and (ii), show the results of no post-heating and 300-second post-heating, respectively. With no post-heating, samples exhibit severe deteriorated and distorted surface morphologies with irregular holes or porous and plenty of unmolten particles (Figure 3-6 e (i) and f (i)). With 300-second post-heating, the improved surfaces have relatively flat morphologies with several unmolten particles (Figure 3-6 e (ii) and f (ii)). Through comparisons, the parts using 30%-70% new-extremely-aged powder mixtures (Figure 3-6 f (ii)) exhibit a smoother surface with lower porosity. Such improvement can be attributed to the better densification and consolidation due to weak gas adsorption in the reclaimed powders when enough energy was supplied.

Figure 3-6 (g) - (h) exhibit the SEM images of parts 3D printed using 20%-80% and 10%-90% new-extremely-aged powder mixtures, respectively. Subfigures (i) and (ii) are results of no post-heating and 300-second post-heating, respectively. With no post-heating, the SEM images exhibit little completed surfaces with numerous unmolten particles and multi-layer porous structures (Figure 3-6 g (i) and h (i)). These surfaces are similar to the SEM images when using 100% extremely aged powders. With 300-second post-heating, the images exhibit very smooth

and flat surfaces with almost no porous and several unmolten particles (Figure 3-6 g (ii) and h (ii)). The quality of the obtained surfaces are even better than the part printed using 100% new powders.

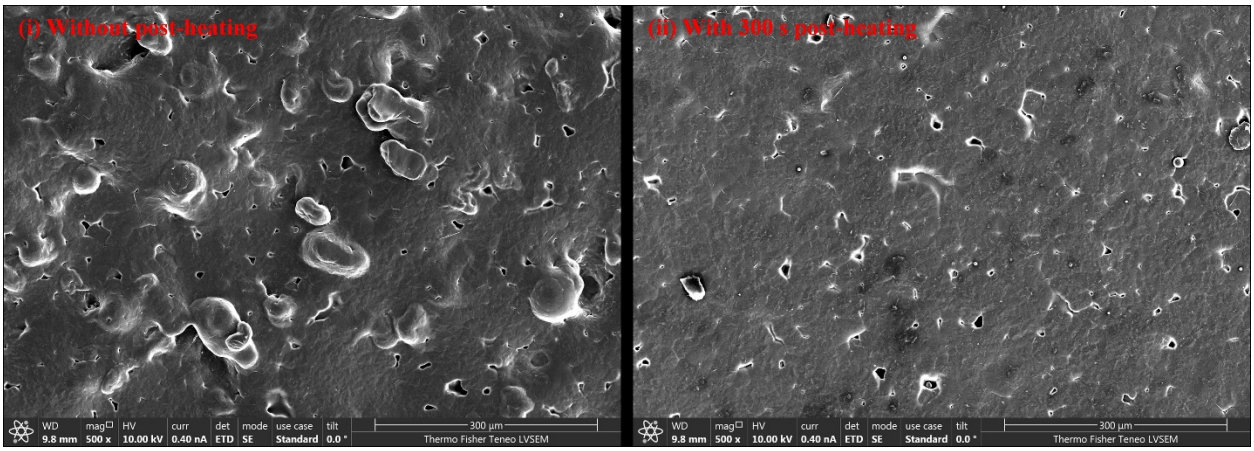

(a) Parts using 50% new + 50% aged mixed polyamide 12 powders

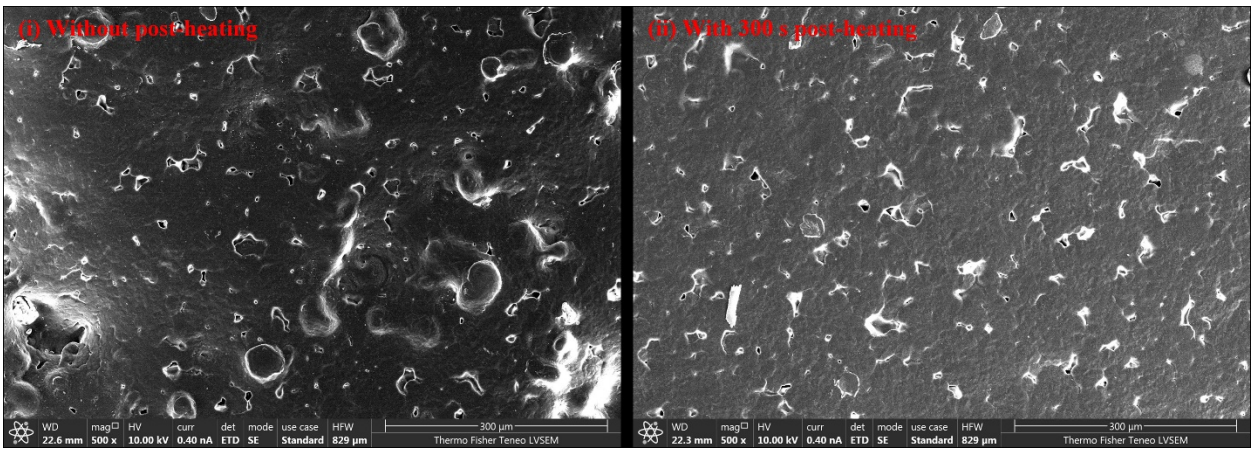

(b) Parts using 70% new + 30% extremely aged mixed polyamide 12 powders

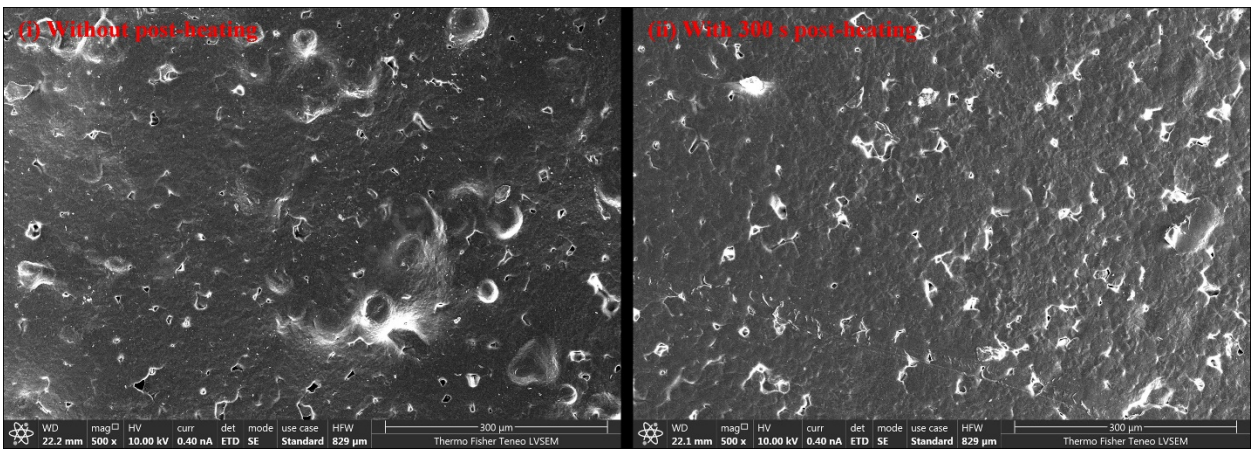

(c) Parts using 60% new + 40% extremely aged mixed polyamide 12 powders

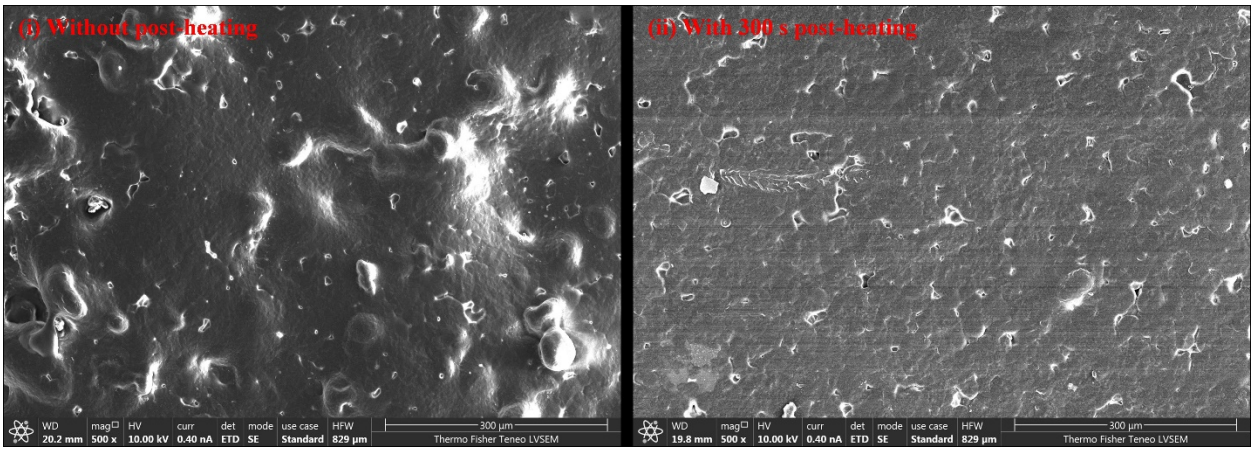

(d) Parts using 50% new + 50% extremely aged mixed polyamide 12 powders

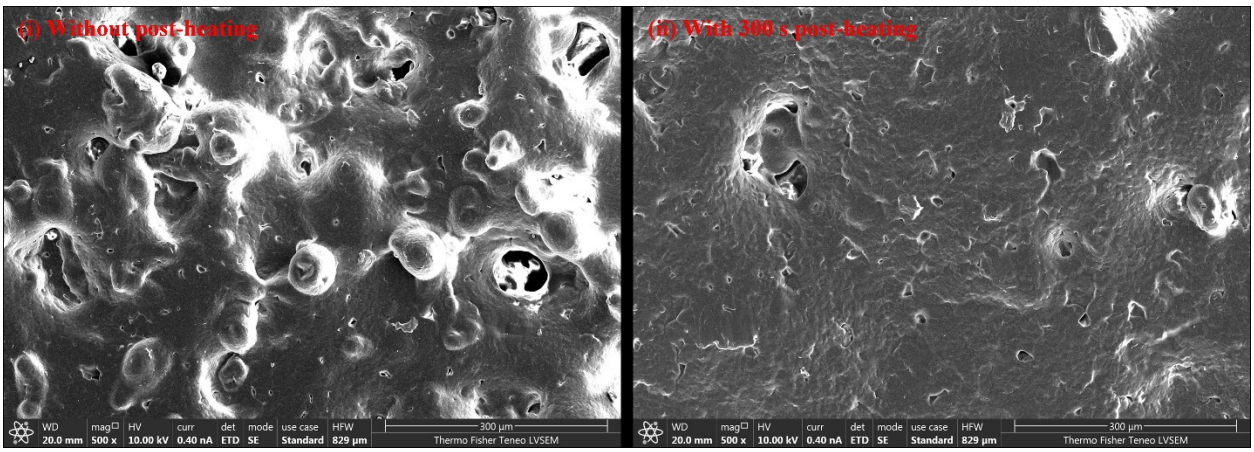

(e) Parts using 40% new + 60% extremely aged mixed polyamide 12 powders

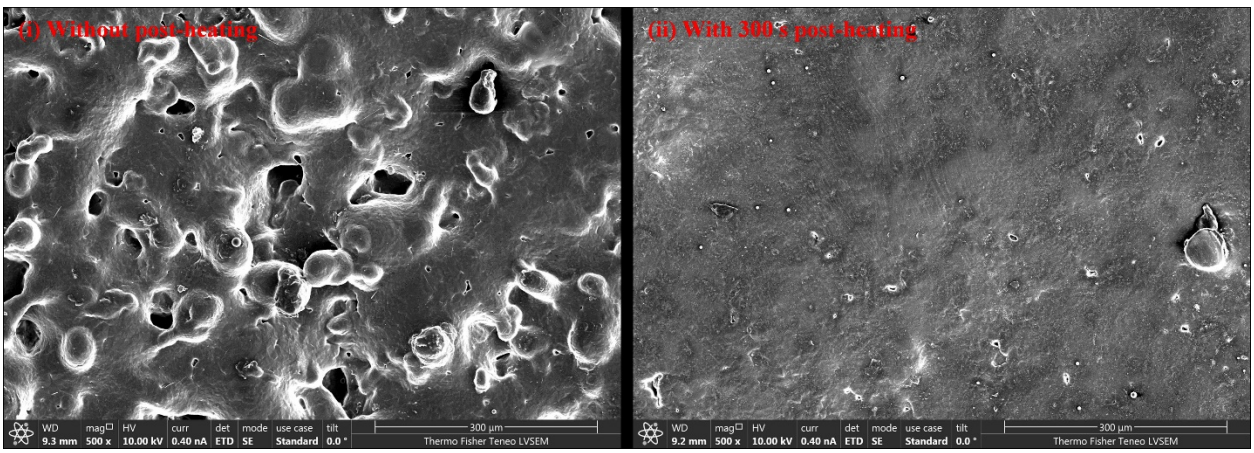

(f) Parts using 30% new + 70% extremely aged mixed polyamide 12 powders

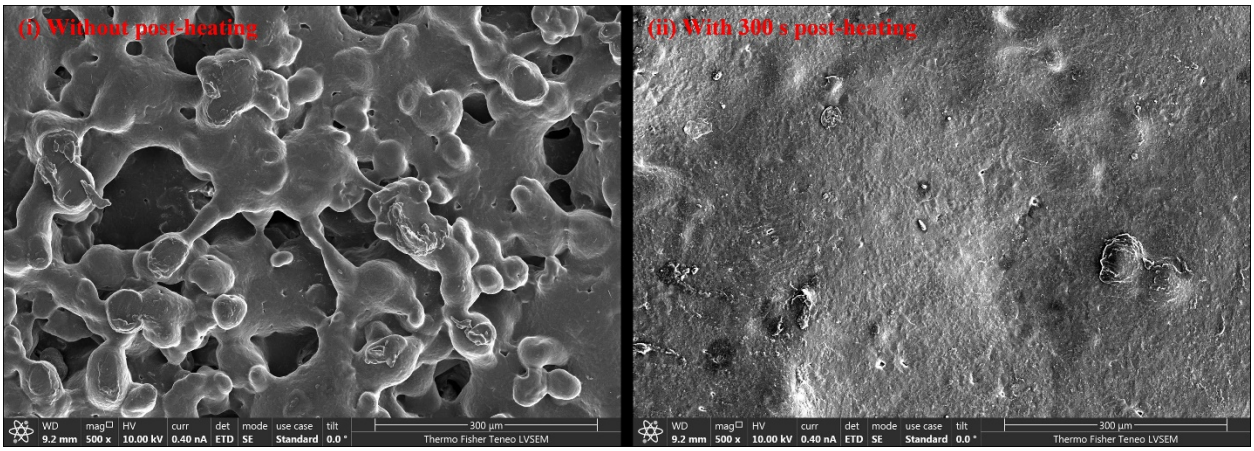

(g) Parts using 20% new + 80% extremely aged mixed polyamide 12 powders

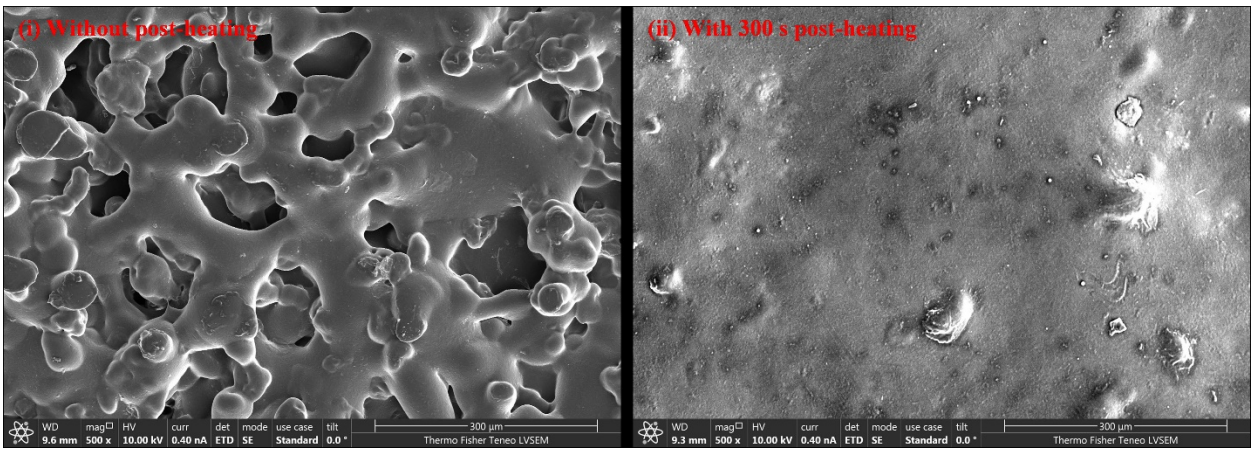

(h) Parts using 10% new + 90% extremely aged mixed polyamide 12 powders

Figure 3-6 Parts using new-aged mixed or new-extremely-aged mixed polyamide 12 powders with no post-heating and with 300 seconds post-heating

3.3.5 Stage 5: the influences of post-heating on part surface morphology when using new, aged, and extremely aged powder mixtures

Figure 3-7 demonstrates the images of parts using new-aged-extremely-aged mixed polyamide 12 powders with (i) no post-heating and (ii) 300 seconds post-heating. The mixtures used are 30%-30%-40% and 30%-40%-30% new-aged-extremely-aged mixed polyamide 12 powders. In these combinations, 30% new powders and 70% reclaimed powders were used. All using 30% new powders with no post-heating, the parts in Figure 3-7 a (i) and b (i) have better-coalesced surfaces compared to the part in Figure 3-6 f (i). Because much more extremely aged powders were used in Stage 4 (Figure 3-6 f, 70%) than in Stage 5 (Figure 3-7, 30% and 40%), making it more difficult to fuse the materials. With 300-second post-heating, the parts exhibit superior surface morphologies with smoother surfaces and less unmolten particles and porosity (Figure 3-7 a (ii)

and b (ii)) than the parts with no post-heating (Figure 3-7 a (i) and b (i)). In particular, the part 3D printed using 30%-30%-40% new-aged-extremely-aged mixed powders has the smoothest and flattest surface with no unmolten particles and almost no porosities (Figure 3-7 a (ii)).

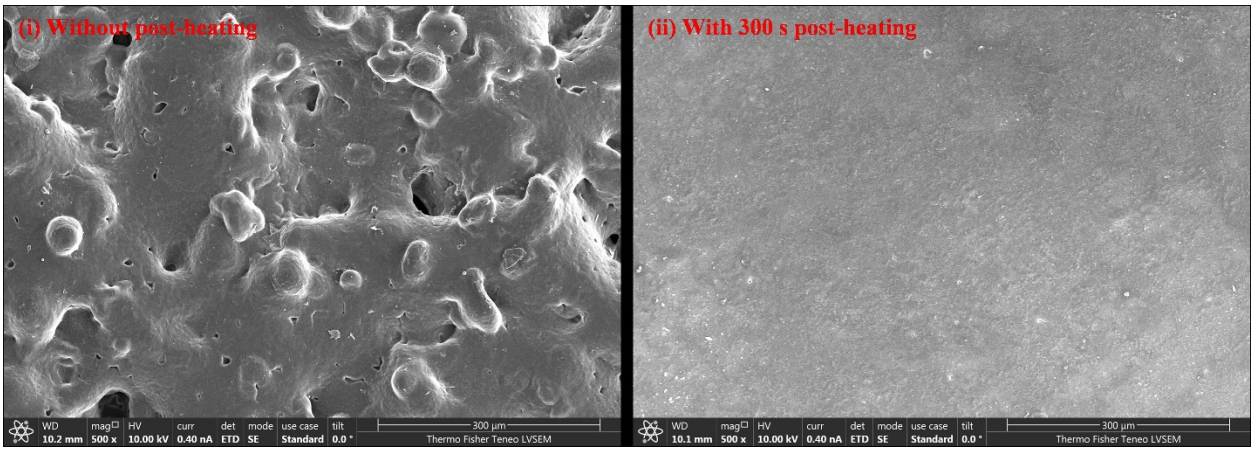

(a) Parts using 30% new + 30% aged + 40% extremely aged mixed polyamide 12 powders

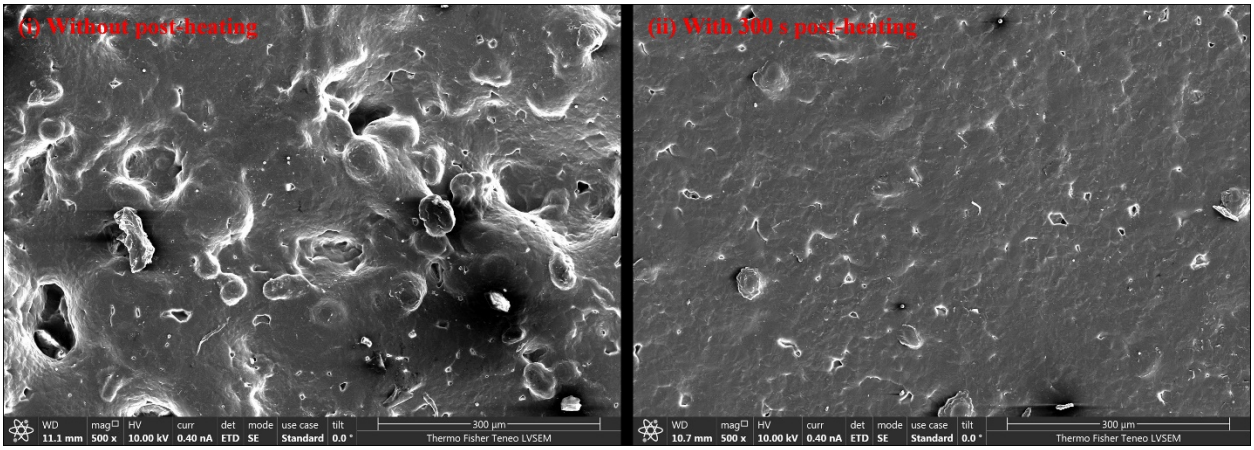

(b) Parts using 30% new + 40% aged + 30% extremely aged mixed polyamide 12 powders

Figure 3-7 Parts using new-aged-extremely-aged mixed polyamide 12 powders with no post-heating and with 300 seconds post-heating

3.4 Discussions

3.4.1 Unmolten particles, coalescence, roughness and porosity

To compare the number of unmolten particles, coalescence performances and roughness of the sintered parts with no post-heating, the 3-layer parts were printed using different polyamide 12 combinations, with the SEM images shown in Figure 3-8. In general, parts using 100% new powders have the best coalescence performance, and almost no unmolten particles (Figure 3-8 a). However, parts using more extremely aged powders exhibit worse coalesced surfaces with drastically increased unmolten particles (Figure 3-8 (b)-(l)). Parts using more new powders have

smoother and flatter surfaces, while parts using mixed powders obtain worse surfaces as the percentages of reclaimed powders increase from 30% to 70%, as shown in Figure 3-8 (b)-(g) and Figure 3-8 (k)-(l). In particular, when using 80%~100% extremely aged powders (Figure 3-8 (h)-(j)), numerous insufficiently melt particles are observed, and no consolidated surfaces form.

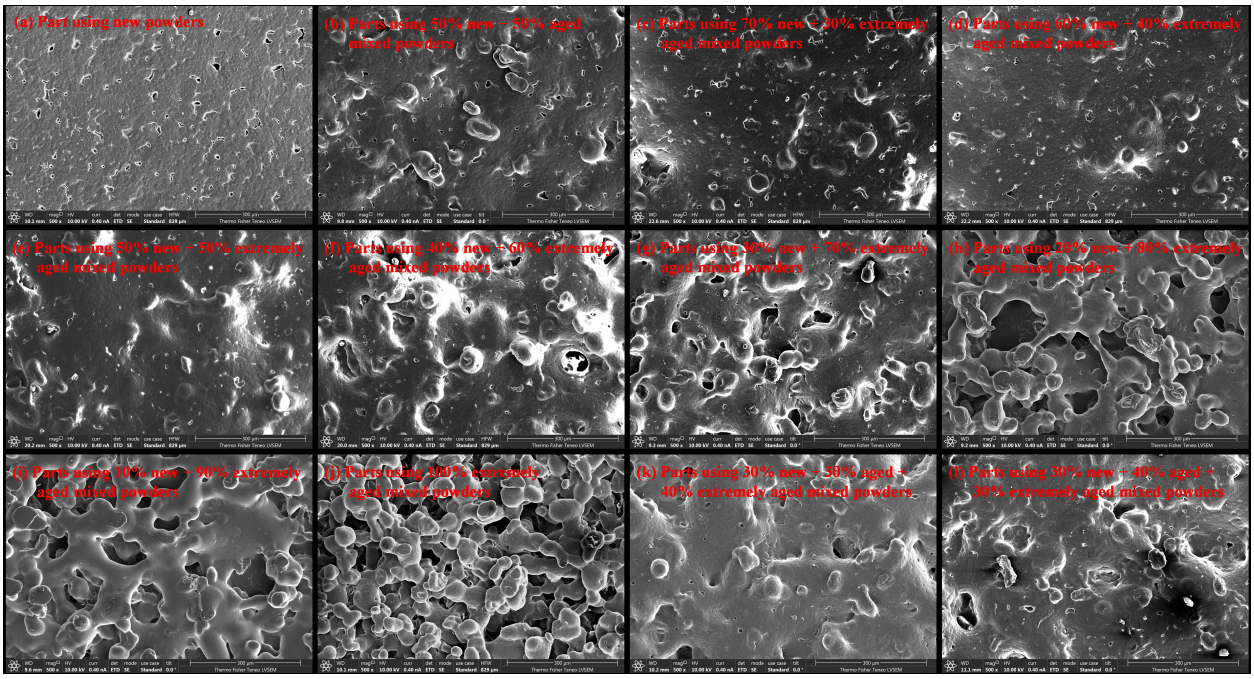

Figure 3-8 Comparisons of unmolten particles, coalescence and roughness of parts using polyamide 12 powders of different combinations without post-heating

The 3-layer parts with 300 seconds post-heating were also printed using different polyamide 12 combinations. To compare the number of unmolten particles, coalescence performances and roughness, Figure 3-9 shows the SEM images of these 3D printed parts. Except for the part using 100% new powders, the images in Figure 3-9 exhibit better surfaces with enhanced coalescence, decreased unmolten particles and improved smoothness with the proposed post-heating. In Figure 3-9 (a)-(e) and (k), the images of parts printed using 100% new powders, 50%-50% new-aged mixed powders, 70%-30% new-extremely-aged mixed powders, 60%-40% new-extremely-aged mixed powders, 50%-50% new-extremely-aged mixed powders and 30%-30%-40% new-aged-extremely-aged mixed powders, respectively, the surfaces are smooth and flat without any unmolten particles. However, in Figure 3-9 (f)-(j) and (l), the images of parts printed using 40%-60% new-extremely-aged mixtures, 30%-70% new-extremely-aged mixtures, 20%-80% new-extremely-aged mixtures, 10%-90% new-extremely-aged mixtures, 100% extremely aged powders and 30%-40%-30% new-aged-extremely-aged mixtures, respectively, the parts exhibit

several unmolten pieces. These results indicate that the parts using a high percentage of new powders obtain improved smooth and flat surfaces with no unmolten particles with post-heating. These surfaces are comparable to those of part using new powders. The parts using a high percentage of extremely aged powders get improved surfaces with post-heating, but there still exist several unmolten particles.

As for the SEM image in Figure 3-9, the parts also display different porosities. In Figure 3-9 (a) to (d), the images of parts printed using 100% new powders, 50%-50% new-aged mixtures, 70%-30% new-extremely-aged mixtures and 60%-40% new-extremely-aged mixtures, respectively, there are more large size pores than the other parts. In Figure 3-9 (e), (f) and (l), the images of parts printed using 50%-50% new-extremely-aged mixtures, 40%-60% new-extremely-aged mixtures and 30%-40%-30% new-aged-extremely-aged mixtures, respectively, the number and size of pores decrease significantly. In the remaining images of Figure 3-9 (g)-(k), almost no pores are observed. These results suggest that the parts using more new powders tend to have more pores. The parts using more extremely aged powders with post-heating display lower porosity due to better consolidation.

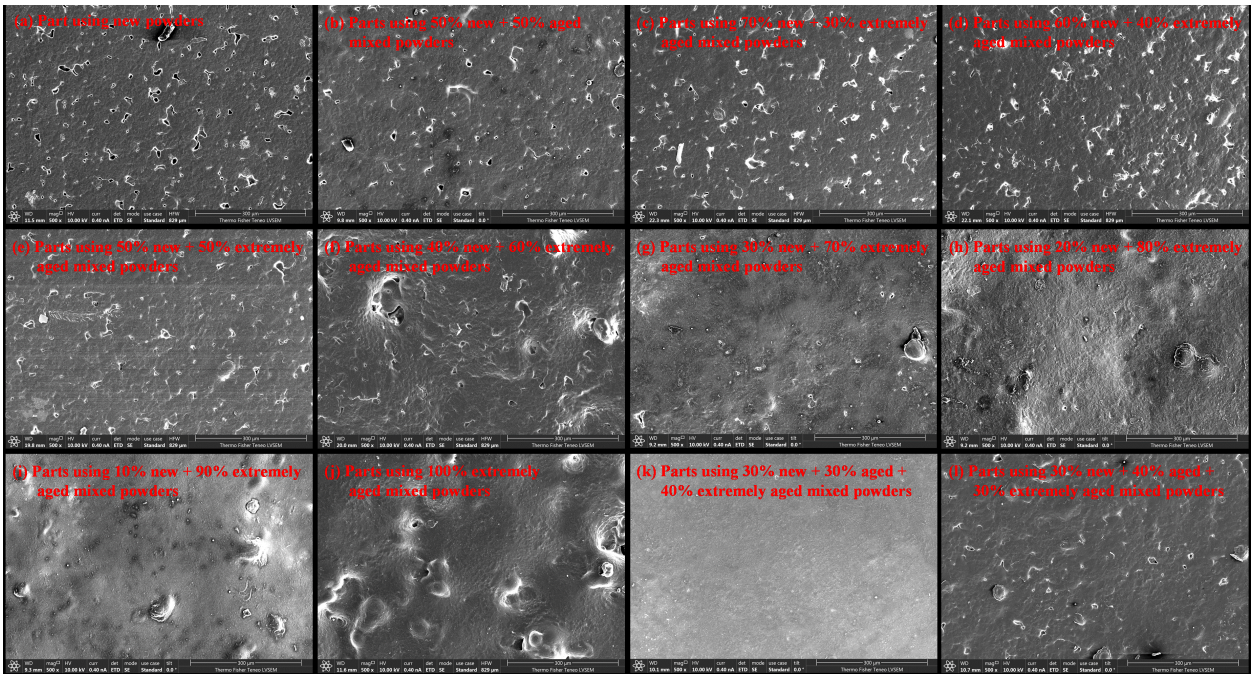

Figure 3-9 Comparisons of unmolten particles, coalescence and roughness of parts using polyamide 12 powders of different combinations with 300 seconds post-heating

3.4.2 Microstructures

Microstructure is another important variable in the printed parts when using reclaimed powders. Figure 3-10 a and b present the microstructures of the parts with no post-heating and with 300 seconds post-heating at a magnification ratio of 10000, respectively. Different powders and powder mixtures yield different microstructures. Parts using new powders exhibits fine fibrillar/lamellae spherulitic regions in amorphous matrixes (Figure 3-10a), due to the aggregations of chain-folded crystallites radiating from the center and growing to be spherical in shape. On the other hand, the parts using extremely aged powders present coarser spherulites spreading all over the matrix (Figure 3-10a). Due to the slightly aging, the spherulite roughness in the part using aged powders behaves in the middle between those observed in the parts using new and extremely aged powders.

The parts using different powders with 300 seconds post-heating show similar characteristics (Figure 3-10b). Parts using new powders show fine lamellae. Extremely aged powders lead to coarse spherulites. And parts using aged powders show intermediate morphologies. It can be concluded that the microstructures of parts are largely impacted by the aging status of powders rather than post-heating.

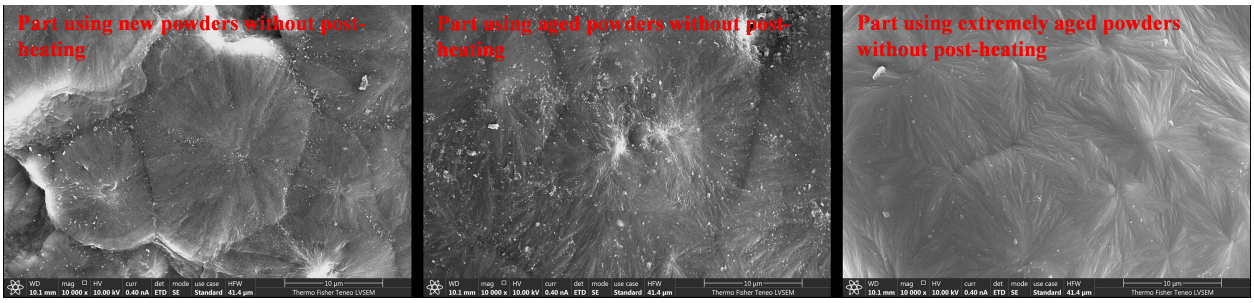

(a) Polyamide 12 parts without post-heating

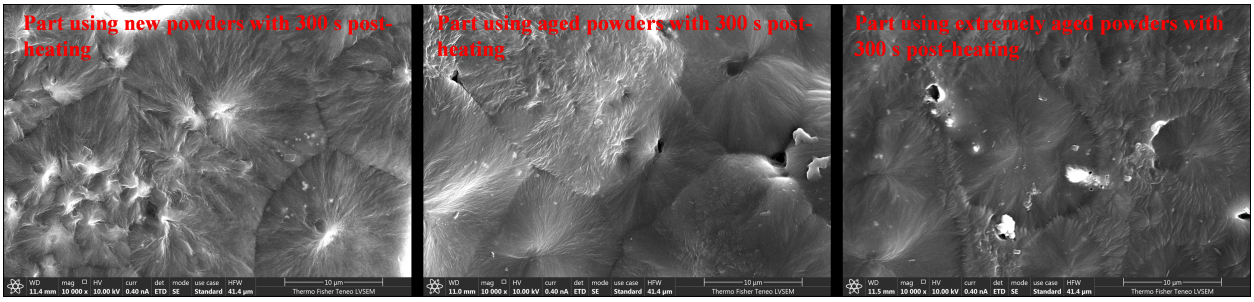

(b) Polyamide 12 parts with 300 seconds post-heating

Figure 3-10 Microstructure examinations of (a) polyamide 12 parts without post-heating, and (b) polyamide 12 parts with 300 seconds post-heating at a magnification of 10000

3.5 Conclusions

This work proposes an SLS with post-heating to improve surface quality of 3D printed parts using reclaimed polyamide 12 powders. The proposed method decreases roughness and porosity of the printed parts, and eliminates unmolten particles. The effects of post-heating on the surface quality using different powder mixtures were studied. In particular, SEM reveals surface features, including the number of unmolten particles, coalescence performances, roughness, porosity and microstructures.

The tested parts using 100% new powders with different post-heating time show similar surface properties, suggesting that post-heating barely affected the surface quality of parts using 100% new powders. The parts using 100% extremely aged powders with no post-heating exhibit multiple layers of insufficiently melt particles. However, a 300-second post-heating yields a well-consolidated surface with little porosity and a drastically reduced un-molten particles.

The unmolten particles disappear on the parts using 50% or more new powders with 300-second post-heating, showing smooth and flat surfaces with high porosity. These surfaces are comparable to those of parts using 100% new powders. When using 60% or 70% reclaimed powders with 40% or 30% new powders, severely deteriorated part surface quality with irregular holes and numerous unmolten particles arise in the case with no post-heating. With the proposed 300-second post-heating, we obtain smooth parts with few unmolten particles and drastically decreased porosity thanks to the improved densification and consolidation. When using 80% or 90% reclaimed powders with 20% or 10% new powders, numerous visible unmolten particles and multi-layer porous structures occur in the case with no post-heating. The surfaces are similar to those of the parts using 100% extremely aged powders. With the proposed 300-second post-heating, we obtain smooth and flat surfaces with almost zero porosity and only few unmolten particles. The resulting surface morphologies are even better than parts 3D printed using 100% new powders.

These results validate the effectiveness of our proposed SLS with post-heating in improving the surface qualities when reusing polyamide 12 powders. The improved surface qualities of different powder mixtures may provide useful information for reusing reclaimed polyamide 12 powders in the SLS industry.

Chapter 4. A COMBINED THEORETICAL AND EXPERIMENTAL APPROACH TO MODEL POLYAMIDE 12 DEGRADATION

4.1 Introduction

Additive manufacturing is a collective term with unrivalled design freedom to fabricate functional applications by joining layers of materials on top of each other [72, 103, 104]. SLS is a popular powder-based additive manufacturing process with superior potentials to produce products with high mechanical properties and good thermal stability compared to other 3D additive techniques [38]. The capability to process almost any material, including polymers, metals, ceramics, and many types of composites, further extends the popularity of SLS [14]. Supporting materials are not needed in SLS as the powders can directly act as support to the printed parts [19]. Resulting from the high flowability, high melting enthalpy, and sharp melting peak, polyamide 12 appears to be the most suitable material among the wide-ranging material scope appliable for SLS [105, 106]. Polyamide 12 (and its compounds) takes up approximately 90% of complete industrial consumption [16].

The extensive usage of polyamide 12 powders in SLS results in a large amount of un-sintered powders after going through complex degradations [21, 24, 25]. Previous research revealed that irreversible oxidation and post-condensation dominate the aging process and change the polymer chemical structures by chain scission, branching, and chain cross-linking [24, 31, 107]. The macro-structural chain cross-linking attributes to an increase in the material molecular weight and a decrease in the melt flow index (MFI) [59, 60]. As the molecular weight increases with the powder aging, melt viscosity also increases and powder flowability decreases [25, 31]. Aging affects little the distribution of powder sizes but leads to the deteriorated thermal property and reduced surface morphology [24].

Despite the property changes, a considerable amount of un-sintered polyamide 12 residues (80% - 90%) has the potential to be reused for further applications [25]. One of the solutions to the successful reuse of SLS residue is to fabricate the powder residue into feedstock for other additive manufacturing processes without significantly reducing its value. Polyamide 12 powder for SLS is priced at around $150/kg (in 2020 currency). The cost of extrusion-based additive

manufacturing (EAM) or fused deposition modelling (FDM) polyamide 12 filament is approximate $100/kg, while the cost of polyamide 12 pellets for conventional plastics processing is below $3/kg [92]. It is more economical to process the polyamide 12 powder residue into filaments for EAM or FDM rather than pellets for conventional plastics processing [18, 92]. The common practice of reusing the polyamide 12 powder residue in SLS is to mix 50% new powders with 50% reclaimed powders from past experiments [24, 92].

Besides, several research works dedicated to better understand the aging mechanisms of polyamide 12 in SLS. Diller TT et al. [108] built computational models at two complexity levels, a one-dimensional model and a two-dimensional finite element model, to explore the influences of heat transfer on the aging of polyamide 12 in SLS. Yuan M et al. [109] measured thermal conductivity of fresh and aged polyamide 12 powders to establish a baseline for thermal aging control in SLS. Dadbakhsh S et al. [24] examined new and aged polyamide 12 powders along with their mixtures to identify the effect and mechanisms of in-process aging on material thermal and coalescence behaviors in SLS. Chen P et al. [21] investigated the aging mechanisms and microstructural evolution of polyamide 12 in SLS. Bernard et al. [110] performed thermogravimetric experiments with mass spectrometric analysis to obtain the kinetic parameters on the thermal degradation of polyamide 12 in SLS.

Heated and exposed to intensive laser radiations, the nature of material degradation in SLS involves coupled thermal and laser-induced oxidation reactions. Despite the previous works, the kinetics and the full modelling of polyamide 12 degradation in the complex SLS remain not well addressed. We propose a first-instance kinetic scheme considering both the oxygen and laser effects to model material degradation in SLS through multi-physics modeling and data-driven parametric identification. In this work, we conduct SLS printing experiments and calculate the actual polyamide 12 degradation rates through Fourier-transform infrared spectroscopy (FTIR) results and Beer-Lambert's law. By data-driven parameter identification of the actual SLS degradation rates into the oxidation model, we obtained the coefficients of actual coupled oxygen and laser effects in SLS. Through a further sensitivity analysis, we derive the relationship between the sample degradation rates and oxidation time. The proposed model can predict the degradation rates of materials using materials density and oxidation time. The new kinetic model applies to not only pure material but also mixed powders. Furthermore, using the proposed kinetic model, we identified the influences of the coupled oxygen, laser irradiation, and preheating on the rates of

material degradation in the SLS of polyamide 12. The findings provide new knowledge of quantitative influences of the process parameters on material degradation and on approaches to reduce oxidation in SLS.

4.2 The proposed approach to model polyamide 12 degradation

Figure 4-1 presents an overview of the proposed research approach [34]. We discuss the details of each step in the following sections.

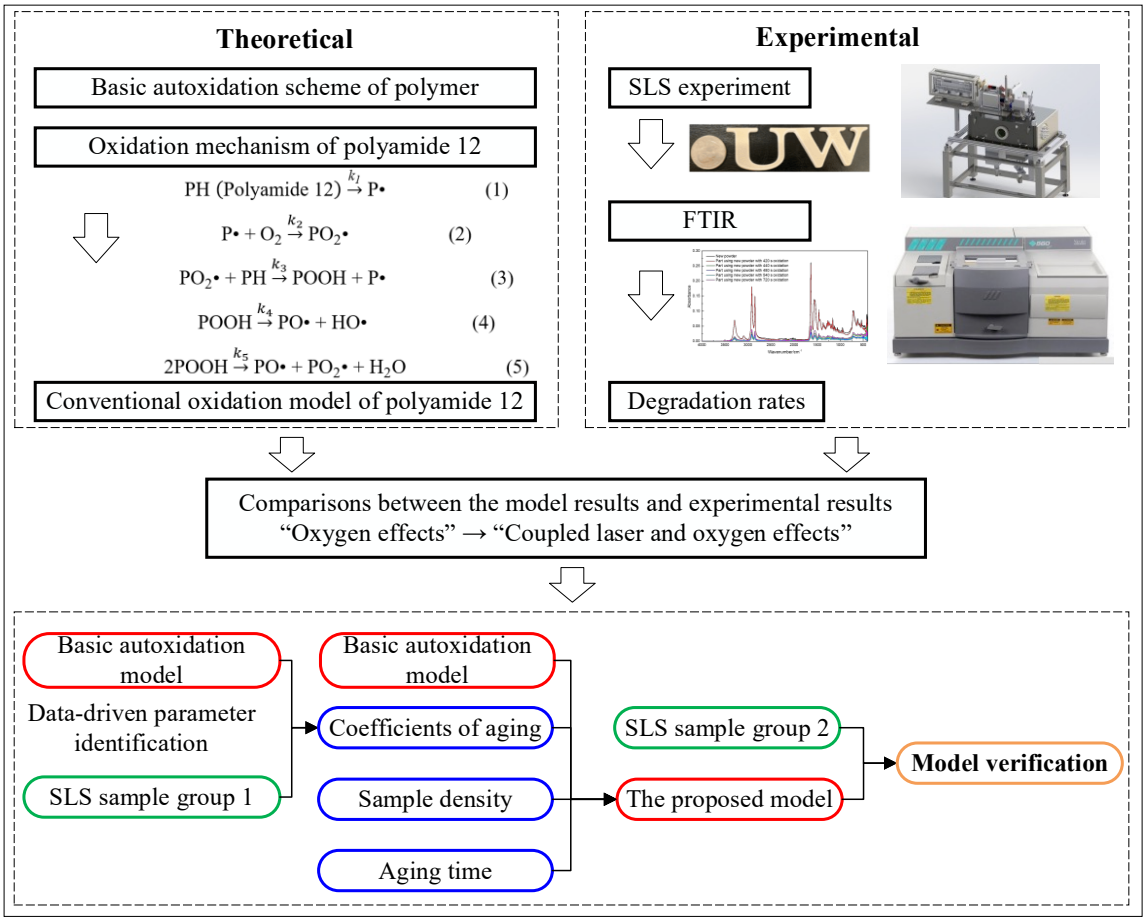

Figure 4-1 The proposed approach to build the kinetic scheme of polyamide 12 aging in SLS considering the coupled oxygen and laser effects

4.2.1 Oxidation model

4.2.1.1 Mechanism of thermal oxidation

Constituted of polymethylenic sequences and the amide group (-NHCO-), polyamide 12 has the following chemical structure:

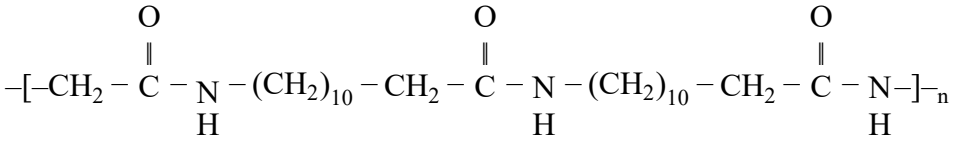

From the basic autoxidation scheme of polymers [111, 112], high temperatures initiate the thermal oxidation of polyamide 12 materials to form alkyl radicals P• (Eq. 4-1). Incorporation of oxygen and abstraction of hydrogen atoms propagate oxidation of polyamide 12 [107]. In the propagation stage (Eqs. 4-2 and 4-3), alkyl radicals P• combine with O_2 to form peroxy radicals PO_2•. PO_2• captures hydrogen atoms from polymer substrates to further produce hydroperoxides. Thermal decomposition of the hydroperoxide groups is the main mechanism of polymer oxidation below 200 °C. Such a process involves a unimolecular mode (Eq. 4-4) and a bimolecular mode (Eq. 4-5) [113, 114]. Hydroxyl radicals PO•, alkoxy radicals HO•, and peroxy radicals PO_2• with polymer substrate rapidly interact and form two balance reactions (Eqs. 4-6 and 4-7) [107]. This process also involves chain scission (S) and hydrogen abstraction.

$$\text{PH (Polyamide 12)} \xrightarrow{k_1} \text{P•} \tag{4-1}$$

$$\text{P•} + O_2 \xrightarrow{k_2} PO_2\text{•} \tag{4-2}$$

$$PO_2\text{•} + \text{PH} \xrightarrow{k_3} \text{POOH} + \text{P•} \tag{4-3}$$

$$\text{POOH} \xrightarrow{k_4} \text{PO•} + \text{HO•} \tag{4-4}$$

$$2\text{POOH} \xrightarrow{k_5} \text{PO•} + PO_2\text{•} + H_2O \tag{4-5}$$

Balance reactions:

$$\text{POOH} \xrightarrow{k_6} 2\text{P•} + PNH_2\text{•} + \text{PH=O} + H_2O + \text{S [-2PH, -CN]} \tag{4-6}$$

$$2\text{POOH} \xrightarrow{k_7} \text{P•} + PO_2\text{•} + PNH_2 + \text{PH=O} + H_2O + \text{S [-PH, -CN]} \tag{4-7}$$

Here, parameters k_i's are a series of elementary reaction constants of the thermal oxidation.

The termination reactions of alkyl radicals P• involve coupling or disproportionation (Eqs. 4-8 and 4-9), where F and X denote double bonds and chain crosslinking (X), respectively. The termination reactions of peroxy radical pairs are ascribed as Eqs. 4-10, 4-11, 4-12, and 4-13. Peroxy radical pairs first react to form the transition cage $[PO\bullet\bullet OP]_{cage}$ with oxygen. The transition cage further generates final products (e.g., POOP, $NH(P=O)_2$, and PNH_2) together with chain crosslinking (X) and scission (S).

$$\text{P•} + \text{P•} \xrightarrow{k_8} \gamma_1\text{PP} + \left(1\text{-}\gamma_1\right)\text{PH} + \left(1\text{-}\gamma_1\right)\text{F} + \gamma_1\text{X}\left[\text{-}\left(1\text{-}\gamma_1\right)\text{PH}\right] \tag{4-8}$$

$$P\bullet + PO_2\bullet \xrightarrow{k_9} \gamma_2 POOP + (1-\gamma_2)POOH + (1-\gamma_2)F + \gamma_2 X\ [-(1-\gamma_2)PH] \quad (4\text{-}9)$$

$$PO_2\bullet + PO_2\bullet \xrightarrow{k_{10}} [PO\bullet\bullet OP]_{cage} + O_2 \quad (4\text{-}10)$$

$$[PO\bullet\bullet OP]_{cage} \xrightarrow{k_{11}} POOP + X \quad (4\text{-}11)$$

$$[PO\bullet\bullet OP]_{cage} \xrightarrow{k_{12}} NH(P{=}O)_2 + PNH_2 + PH{=}O + S\ [-CN] \quad (4\text{-}12)$$

$$[PO\bullet\bullet OP]_{cage} \xrightarrow{k_{13}} 2P\bullet + 2PNH_2 + 2PH{=}O + 2S\ [-2PH, -2CN] \quad (4\text{-}13)$$

4.2.1.2 Basic autoxidation model

The fundamental kinetics led to a basic model on thermal oxidation of polyamide 12 materials, defined as the basic autoxidation model. The solution involves 5 main non-linear differential equations (Eqs. 4-14, 4-15, 4-16, 4-17 and 4-18) [107] indicating the derivatives of the compound concentrations with respect to time. For instance, the rate of concentration changes of [POOH] (Eq. 4-14) equals the formation rates (POOH formed in Eqs. 4-3 and 4-9) minus the consumption rates (POOH consumed in Eqs. 4-6 and 4-7). We define the coefficient of oxygen effect as σ^o (Eqs. 4-15, 4-16, and 4-19), relating close to the oxygen concentrations $[O_2]$. σ^o equals 1 in the basic autoxidation model.

$$\frac{d[POOH]}{dt} = -k_6 f_{PH}[POOH] - 2k_7 f_{PH}[POOH]^2 + k_3[PH][PO_2\bullet] + (1-\gamma_2)k_9 f_{PH}[P\bullet][PO_2\bullet] \quad (4\text{-}14)$$

$$\frac{d[P\bullet]}{dt} = 2k_6 f_{PH}[POOH] + k_7 f_{PH}[POOH]^2 - k_2\sigma^o[O_2][P\bullet] + k_3[PH][PO_2\bullet] - 2k_8[P\bullet]^2 - k_9 f_{PH}[P\bullet][PO_2\bullet] + 2k_{13} f_{PH}[PO\bullet\bullet OP]_{cage} \quad (4\text{-}15)$$

$$\frac{d[PO_2\bullet]}{dt} = k_7 f_{PH}[POOH]^2 + k_2\sigma^o[O_2][P\bullet] - k_3[PH][PO_2\bullet] - k_9 f_{PH}[P\bullet][PO_2\bullet] - 2k_{10}[PO_2\bullet]^2 \quad (4\text{-}16)$$

$$\frac{d[PO\bullet\bullet OP]_{cage}}{dt} = k_{10}[PO_2\bullet]^2 - (k_{11} + k_{12} + k_{13} f_{PH})[PO\bullet\bullet OP]_{cage} \quad (4\text{-}17)$$

$$\frac{d[PH]}{dt} = -2k_6 f_{PH}[POOH] - k_7 f_{PH}[POOH]^2 - k_3[PH][PO_2\bullet] - (1-\gamma_2)k_9 f_{PH}[P\bullet][PO_2\bullet] - 2k_{13} f_{PH}[PO\bullet\bullet OP]_{cage} \quad (4\text{-}18)$$

Here, f_{PH} is defined to avoid negative concentrations of substrate. $f_{PH}=[PH]/([PH]+\varepsilon)$ and $\varepsilon=0.01$ [107]; the parameter itself does not significantly influence the oxidative kinetics.

From the mechanistic scheme in section 4.2.1.1, we also obtain the concentration changes of the following reactants and products [107]:

$$\frac{d[O_2]_{Consumed}}{dt} = k_2\sigma^o[O_2][P\bullet] - k_{10}[PO_2\bullet]^2 \quad (4\text{-}19)$$

$$\frac{d[PNH_2]}{dt} = k_6 f_{PH}[POOH] + k_7 f_{PH}[POOH]^2 + (k_{12}+2k_{13}f_{PH})[PO\bullet\bullet OP]_{cage} \quad (4\text{-}20)$$

$$\frac{d[PH=O]}{dt} = \frac{d[PNH_2]}{dt} \quad (4\text{-}21)$$

$$\frac{d[NH(P=O)_2]}{dt} = k_{12}[PO\bullet\bullet OP]_{cage} \quad (4\text{-}22)$$

$$\frac{d[C\text{-}N]}{dt} = -\frac{d[PNH_2]}{dt} \quad (4\text{-}23)$$

$$\frac{dS}{dt} = \frac{d[PNH_2]}{dt} \quad (4\text{-}24)$$

$$\frac{dX}{dt} = \gamma_1 k_8[P\bullet]^2 + \gamma_2 k_9 f_{PH}[P\bullet][PO_2\bullet] + k_{11}[PO\bullet\bullet OP]_{cage} \quad (4\text{-}25)$$

Chain scission (S) occurs simultaneously with the oxidation-related signal diminishment near the wavelengths of 1369.23, 1159.03, 1062.60, and 948.82 cm^{-1} [21]. In the basic autoxidation model, we define the degree of chain scission (S) (Eq. 4-24) occurring in unit time (s) as *the modelling aging rate* μ_i for polyamide 12 sample i.

$$\mu_i = \frac{\Delta S_i}{t_i} \quad (4\text{-}26)$$

where ΔS_i is the degree of chain scission in oxidation time t_i. We use Matlab ODE23s to solve the model when knowing the initial concentrations of the main component and the elementary reaction coefficients k_i.

At a specific temperature (e.g., a pre-heating temperature of the SLS machine, 160 °C), the elementary reaction coefficients k_i remain unchanged. However, the oxygen effect $\sigma^o[O_2]$ can vary significantly at a specific temperature when at different atmosphere, and largely affects the rates of material degradation. Stronger oxygen effects result in faster degradation rates. In SLS, the nature of material degradation involves the coupled oxygen and laser effects. The laser has even stronger effects than oxygen effects on material degradation. Thus, the coupled laser and oxygen effects are substantially more significant than the single oxygen effects on material degradation. However, it is difficult or impossible to get laser effects using the modelling-only

approach. Through experimentation, we shall get the actual material degradation rates to derive *the coefficients of the coupled laser and oxygen effects*, referred to as σ_i^{ol}, through mapping experimental results to the modelling results. σ_i^{ol} shows the enhancement effects on material degradation from oxygen to the coupled laser and oxygen. $\sigma_i^{ol}[O_2]$ is the coupled laser and oxygen effects in SLS.

4.2.2 Experimentation

4.2.2.1 SLS printing using polyamide 12 powders

We sintered different polyamide 12 combinations. The SLS machine used is an in-house built open-configuration SLS AM research testbed with a 100 W Coherent GEM100A CO_2 laser and a Scanlab intelliSCAN 14 scanner (Figure 4-2). The parameter settings used in the printing experiments are: 160 °C preheating, 3000 mm/s scanning speed, 18 W laser power, 0.3 mm scan spacing, and 150 μm layer thickness. Table 4-1 exhibits the 22 kinds of printed samples with calculated density and oxidation time (time in the chamber), i=1, 2, …22. In detail, the oxidation time is the sum of the preheating, printing and the post-heating time. For part samples in this work, the preheating time is 5 minutes, and the printing time is 2 minutes. We change the post-heating time (20 seconds, 60 seconds, 120 seconds and 300 seconds) to obtain part samples with different oxidation time.

Table 4-1 SLS printed samples using polyamide 12 powders, the calculated density, and oxidation time

Samples	Density/g·cm^{-3}	Oxidation time/seconds
Parts using 100% new powders	0.9	440; 480; 540; 720
Parts using 70% new and 30% aged	0.828	420; 720
Parts using 60% new and 40% aged	0.804	420; 720
Parts using 50% new and 50% aged	0.78	420; 720
Parts using 40% new and 60% aged	0.756	420, 720
Parts using 30% new and 70% aged	0.732	420; 720
Parts using 20% new and 80% aged	0.708	420; 720
Parts using 10% new and 90% aged	0.684	420; 720
Parts using 100% aged powders	0.66	440; 480; 540; 720

* Polyamide 12 new powders are purchased from EOS Corp. Polyamide 12 aged powders are reclaimed from standard SLS processes on an EOS P 390 machine.

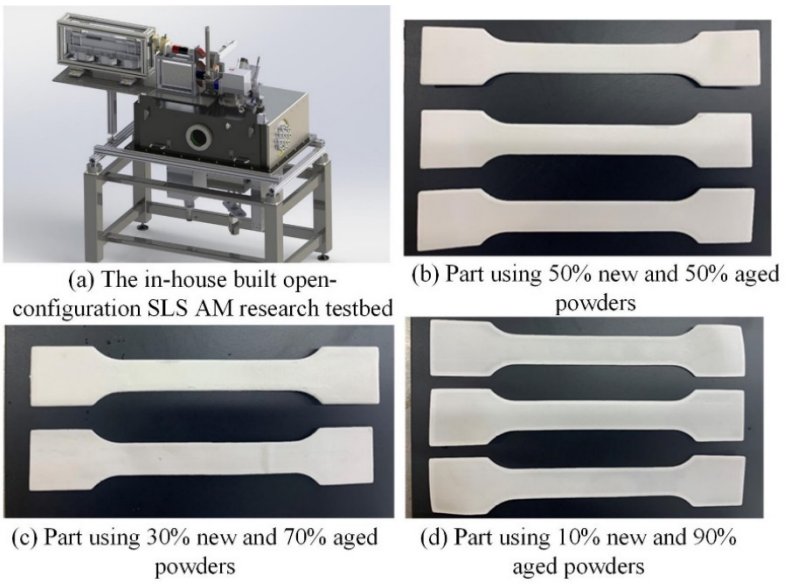

Figure 4-2 SLS testbed and samples

4.2.2.2 Measured material degradation rates

In the polyamide 12 FTIR spectra, the dramatically diminished signals of peaks near wavelengths of 1369.23, 1159.03, 1062.60, and 948.82 cm^{-1} indicate the oxidation of amide groups [21]. We conducted FTIR tests on the specimens in Table 4-1 as well as the pure polyamide 12 powder to examine the aging-related signals using a Nicolet Magna-IR 560 FTIR instrument (wavelength ranges: 6500 cm^{-1}-100 cm^{-1}, spectral resolution: 0.35 cm^{-1}). The FTIR of powder (new powder) serves as the benchmark against the degradation comparison. For specimen i, through the FTIR results and Beer-Lambert's law (Eq. 4-27) [107], we calculated the concentrations of the four oxidation-related components Y_n (n=1, 2, 3,4) (corresponding to peaks near 1369.23, 1159.03, 1062.60, and 948.82 cm^{-1}), respectively.

$$c_{Y_n} = \frac{\mathrm{Abs}(Y_n)}{\varepsilon_{Y_n} L_i} \quad (n=1,2,3,4) \tag{4-27}$$

where $\mathrm{Abs}(Y_n)$, ε_{Y_n} and c_{Y_n} are, respectively, the absorbance, the coefficient of molar absorptivity, and the concentrations of the chemical component Y_n; and L_i is the thickness of the tested sample i. We obtain the absorbances from FTIR results, and get the coefficients of molar absorptivity from the new powder (benchmark sample). For the new powder, we read the tested thickness and absorbances from FTIR, and calculate the molar concentrations using density and molar mass [115]. Then we get the coefficients of molar absorptivity using the Beer-Lambert's law [107], and insert these coefficients in Eq. 4-27 to calculate concentrations of chemical component for part

samples. We write Δc_{Y_n} as the difference of c_{Y_n} between the benchmarked powder materials and the 3D-printed samples. As there are four peaks for each specimen i, we write Δc_i (in mol/L) to denote the average of Δc_{Y_1}, Δc_{Y_2}, Δc_{Y_3}, and Δc_{Y_4} for specimen i. We define *the actual degradation rate* η_i (involving both oxygen and laser effects) as the average concentration changes of the oxidation-related components Δc_i in unit time (Eq. 4-28), in mol/(L·s):

$$\eta_i = \frac{\Delta c_i}{t_i} \tag{4-28}$$

where i is the sample index in Table 4-1, and t_i is the associated oxidation time.

4.2.2.3 Comparisons between the actual SLS degradation η_i and the modelling aging rates μ_i

Specimen density and oxidation time in Table 4-1 are important parameters for the basic autoxidation model. Besides, the initial concentrations of reactants are necessary to run the model. For each specimen i, we get the initial concentrations of reactants, namely, POOH, PH and C-N, in the basic autoxidation model (from Eq. 4-14 to Eq. 4-25) using the molar concentration formula

$$c_i^{reactant\text{-}R} = \frac{q_i}{M} \tag{4-29}$$

where $c_i^{reactant\text{-}R}$ (in molar/L) is the initial molar concentration of reactant R (POOH, PH or C-N) in specimen i; q_i (in g/cm^3) is the density of specimen i; M (in g/mol) is the molar mass of polyamide 12. In the basic autoxidation, the initial concentrations of P•, PO_2•, $[PO\bullet\bullet OP]_{cage}$, $[O_2]_{Consumed}$, PNH_2, PH=O, $NH(P=O)_2$, S, and X are zero because they are intermediate products. The oxygen concentration, $[O_2]$, is 3.6×10^{-4} mol·L^{-1} [107] in the air atmosphere. Table 4-2 lists the elementary reaction coefficients for thermal oxidation of polyamide 12 at 160 °C [113, 114, 116]. Inserting the above parameters in the basic autoxidation model, we get *the modelling aging rate* μ_i for sample i, and compare the result to *the actual degradation rate* η_i.

Table 4-2 The elementary reaction constants for thermal oxidation of polyamide 12 at 160 °C [113, 114, 116]

Parameter	Value	Parameter	Value
k_2 (L·mol^{-1}·s^{-1})	10^8	k_{10} (L·mol^{-1}·s^{-1})	1.6×10^{11}
k_3 (L·mol^{-1}·s^{-1})	45.8	k_{11} (s^{-1})	2.0×10^8
k_6 (s^{-1})	8.0×10^{-4}	k_{12} (s^{-1})	3.4×10^8
k_7 (L·mol^{-1}·s^{-1})	6.0×10^{-3}	k_{13} (s^{-1})	2.2×10^9
k_8 (L·mol^{-1}·s^{-1})	8.0×10^{11}	γ_1 (%)	50
k_9 (L·mol^{-1}·s^{-1})	5.0×10^{11}	γ_2 (%)	50

4.2.3 Kinetic model of polyamide 12 aging in SLS considering the coupled oxygen and laser effects

Figure 4-3 shows the main proposed procedures to build the kinetic model of polyamide 12 aging involving the coupled oxygen and laser effects in SLS.

We separated the printed SLS specimens in Table 4-1 into two sample groups (SLS sample groups 1 and 2). Each group contains SLS samples with different polyamide 12 combinations. The objective is to ensure that the method can derive *the coefficient of the coupled oxygen and laser effects*, σ_i^{ol}, for different polyamide 12 combinations. For samples i in group 1, we performed sensitivity analysis on *the modelling degradation rates* μ_i as the coupled laser and oxygen effects $\sigma_i^{ol}[O_2]$ change, using the basic autoxidation model. Figure 4-4 presents the relationship between μ_i and $\sigma_i^{ol}[O_2]$ for sample i.

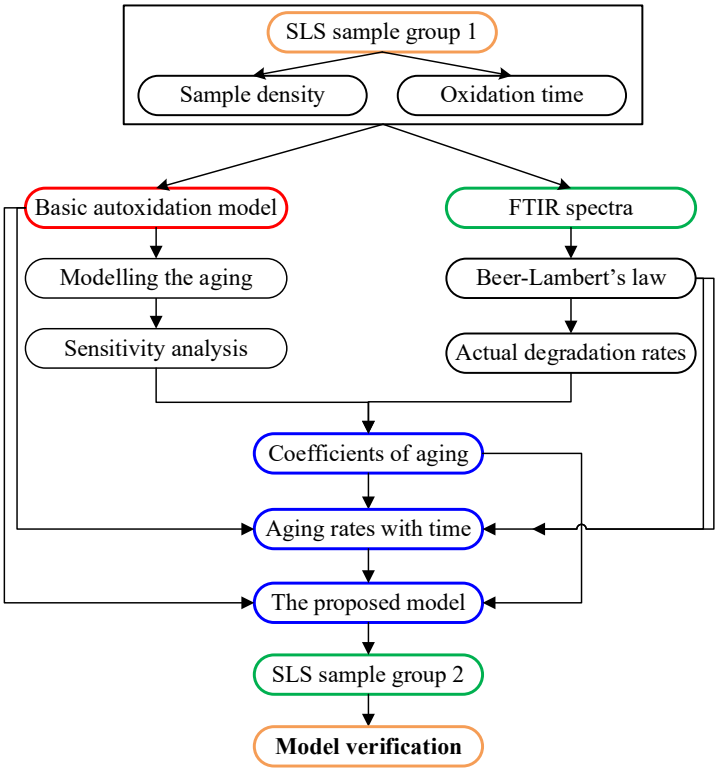

Figure 4-3 Proposed procedures to build the kinetic model of polyamide 12 involving the coupled oxygen and laser-induced aging in SLS

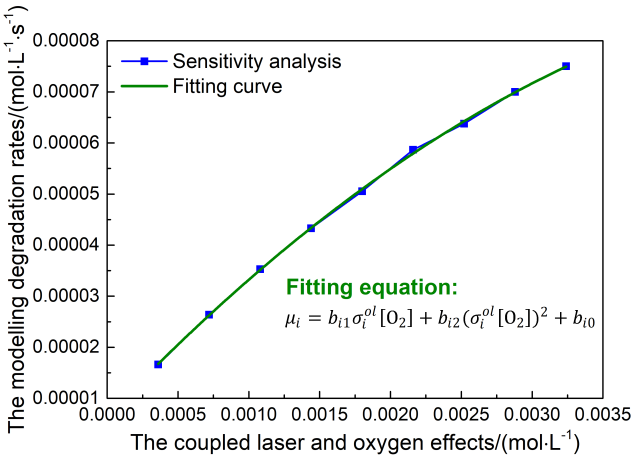

Figure 4-4 Experimental relationship between μ_i and $\sigma_i^{ol}[O_2]$ for sample i

The experimental data suggest a second-order relationship between μ_i and $\sigma_i^{ol}[O_2]$ in the tested operation zone. We thus propose the following second-order correlation mapping

$$\mu_i = b_{i1}\sigma_i^{ol}[O_2] + b_{i2}(\sigma_i^{ol}[O_2])^2 + b_{i0} \tag{4-30}$$

where b_{i0}, b_{i1}, and b_{i2} are constants for sample i. We will perform parameter identification with R-squared regression and a full model verification in the following sections. When *the modelling degradation rate* μ_i equals *the actual degradation rate* η_i (section 4.2.2.2), the corresponding $\sigma_i^{ol}[O_2]$ represents the actual coupled laser and oxygen effects in SLS, defined as $\sigma_{i-SLS}^{ol}[O_2]$.

Replacing σ^o with σ_{i-SLS}^{ol} in the basic autoxidation model, we obtain an updated oxidation model of polyamide 12 in SLS. In this model, we define the material degradation rates as *the updated modelling degradation rates* $\tilde{\mu}_i$. We utilize the updated model to conduct sensitivity analysis on $\tilde{\mu}_i$ and the specimen oxidation time t_i. Figure 4-5 shows the experimentally identified relationship between $\tilde{\mu}_i$ and t_i for sample i.

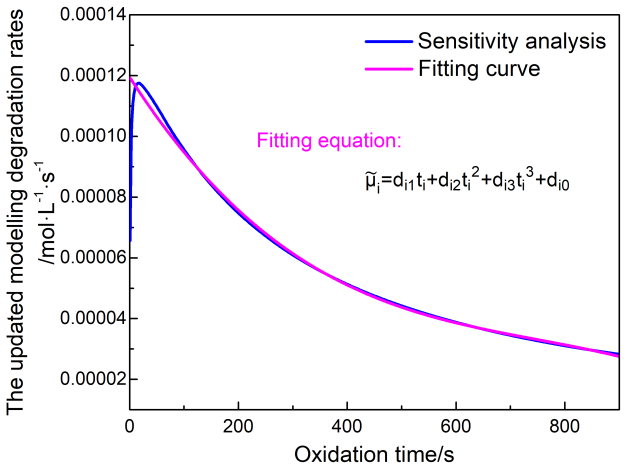

Figure 4-5 Experimental relationship between $\tilde{\mu}_i$ and t_i for sample i

After the initial transient, the relationship between $\tilde{\mu}_i$ and t_i fits an R-squared cubic polynomial, defined as Eq. 4-31.

$$\tilde{\mu}_i = d_{i1}t_i + d_{i2}{t_i}^2 + d_{i3}{t_i}^3 + d_{i0} \tag{4-31}$$

where d_{i0}, d_{i1}, d_{i2} and d_{i3} are constants.

The proposed kinetic model contains the basic autoxidation model, *the coefficient of the actual coupled laser and oxygen effects in SLS*, and the relationships between *the updated modelling degradation rates* $\tilde{\mu}_i$ and specimen oxidation time t_i. To verify the proposed kinetic model, we apply it to the SLS sample group 2 to compare *the updated modelling aging rates* $\tilde{\mu}_i$ and *the actual degradation rates* η_i.

4.2.4 Characteristics of the updated modelling degradation rates $\tilde{\mu}_i$

The actual coupled laser and oxygen effects in SLS, $\sigma_{i-SLS}^{ol}[O_2]$, and the preheating temperature are predominant parameters in SLS affecting the material degradation rates. To understand the process further, we use the proposed kinetic model to identify the influences of $\sigma_{i-SLS}^{ol}[O_2]$ and preheating temperatures (Table 4-2 and Table 4-3) on *the updated modelling degradation rates*, $\tilde{\mu}_i$. These results will be analyzed in the following sections.

Table 4-3 The elementary reaction constants for thermal oxidation of polyamide 12 between 90 and 150 °C [113, 114, 116]

Parameter	Value				
	90 °C	100 °C	120 °C	140 °C	150 °C
k_2 ($L \cdot mol^{-1} \cdot s^{-1}$)	10^8	10^8	10^8	10^8	10^8
k_3 ($L \cdot mol^{-1} \cdot s^{-1}$)	1.6	2.7	7.7	19.6	30.3
k_6 (s^{-1})	8.0×10^{-7}	2.2×10^{-6}	1.8×10^{-5}	1.6×10^{-4}	4.0×10^{-4}
k_7 ($L \cdot mol^{-1} \cdot s^{-1}$)	4.0×10^{-5}	9.0×10^{-5}	5.0×10^{-4}	1.7×10^{-3}	3.5×10^{-3}
k_8 ($L \cdot mol^{-1} \cdot s^{-1}$)	8.0×10^{11}	8.0×10^{11}	8.0×10^{11}	8.0×10^{11}	8.0×10^{11}
k_9 ($L \cdot mol^{-1} \cdot s^{-1}$)	5.0×10^{11}	5.0×10^{11}	5.0×10^{11}	5.0×10^{11}	5.0×10^{11}
k_{10} ($L \cdot mol^{-1} \cdot s^{-1}$)	8.0×10^{9}	2.6×10^{10}	6.0×10^{10}	5.0×10^{10}	9.5×10^{10}
k_{11} (s^{-1})	2.0×10^{8}	2.0×10^{8}	2.0×10^{8}	2.0×10^{8}	2.0×10^{8}
k_{12} (s^{-1})	3.4×10^{8}	3.4×10^{8}	3.4×10^{8}	3.4×10^{8}	3.4×10^{8}
k_{13} (s^{-1})	3.2×10^{8}	4.7×10^{8}	7.9×10^{8}	1.2×10^{9}	1.8×10^{9}
γ_1 (%)	100	95	80	55	55
γ_2 (%)	100	95	80	55	55

4.3 Results and discussions

4.3.1 Comparisons between the modelling aging μ_i and the actual SLS aging rates η_i

We run the basic autoxidation model and get the modelling degradation rates μ_i for each specimen i in Table 4-1, presented in the following section. As for the actual degradation, Figure 4-6 exhibits the FTIR results of the SLS samples in Table 4-1, which we shall now extrapolate into measured degradation rates η_i. The horizontal axis is the wavenumber, and the vertical axis is the absorbance. Our focus here is to get the absorbance differences of oxidation-related wavelengths at 1369.23, 1159.03, 1062.60, and 948.82 cm^{-1}. Then using the Beer-Lambert's law [107], we can calculate the concentrations of the oxidation-related components for each sample. The differences of the concentrations between different samples represent the different oxidation states.

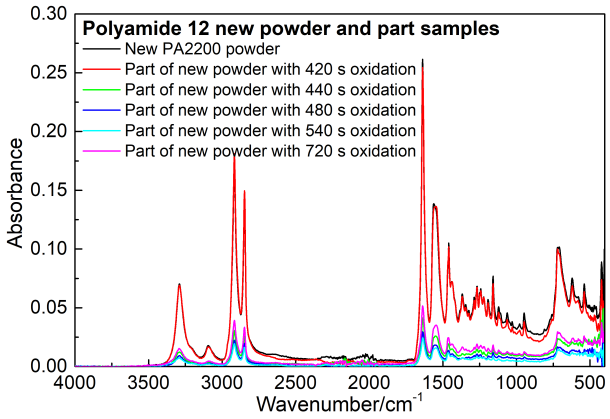

(a) Polyamide 12 new powder and parts

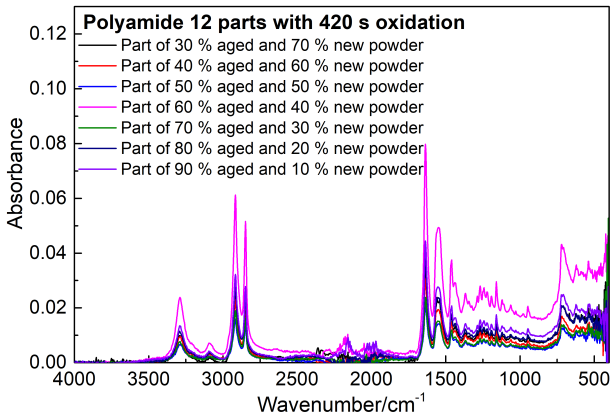

(b) Polyamide 12 parts using mixed powder (420 s)

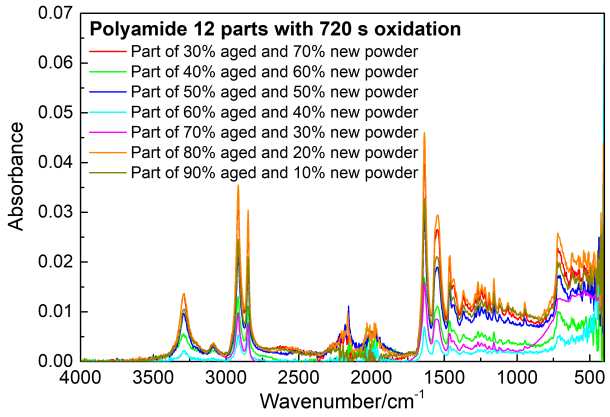

(c) Polyamide 12 parts using mixed powder (720 s)

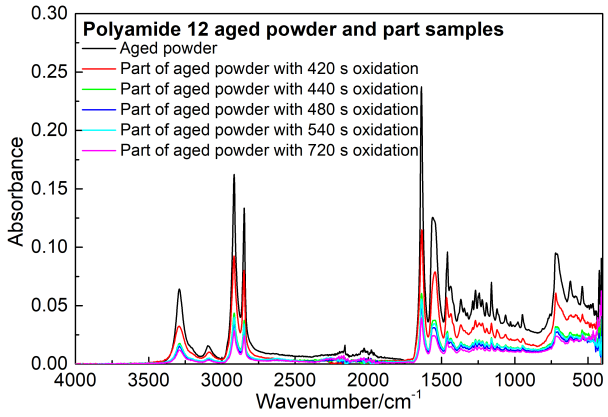

(d) Polyamide 12 aged powder and parts

Figure 4-6 FTIR test results of different polyamide 12 powders and different 3D-printed part samples with different oxidation time

We compared FTIR curves of SLS samples at the oxidation-related wavelengths of 1369.23, 1159.03, 1062.60, and 948.82 cm^{-1}. The diminishment or disappearance of peaks at oxidation-related components indicates the material degradation and oxidization. The peaks decrease more when the aging time increases. As introduced in section 4.2.2.2, we calculated the concentration

changes (mol·L^{-1}) of oxidation-related components for each sample during specific aging durations, and further obtained the actual degradation rates η_i in mol·L^{-1}·s^{-1} using the Eqs. 4-27 and 4-28.

Figure 4-7 compares the modelling degradation rates μ_i and the actual degradation rates η_i. Nontrivial but unsurprising, the actual degradation rates of polyamide 12 are much larger than the modelling degradation rates. This phenomenon exists in all samples, including those using pure new polyamide 12 powders (Figure 4-7a), new-aged mixed powders (Figure 4-7b), and pure aged powders (Figure 4-7c). This core finding indicates that the coupled oxygen and laser age the material much faster than the case with oxygen only. It is thus necessary and important to build the kinetic model of polyamide 12 aging in SLS considering the coupled oxygen and laser effects.

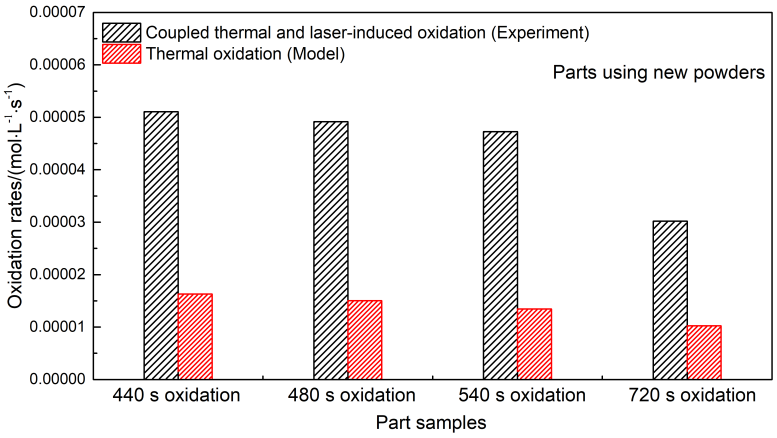

(a) Parts using new polyamide 12 powders

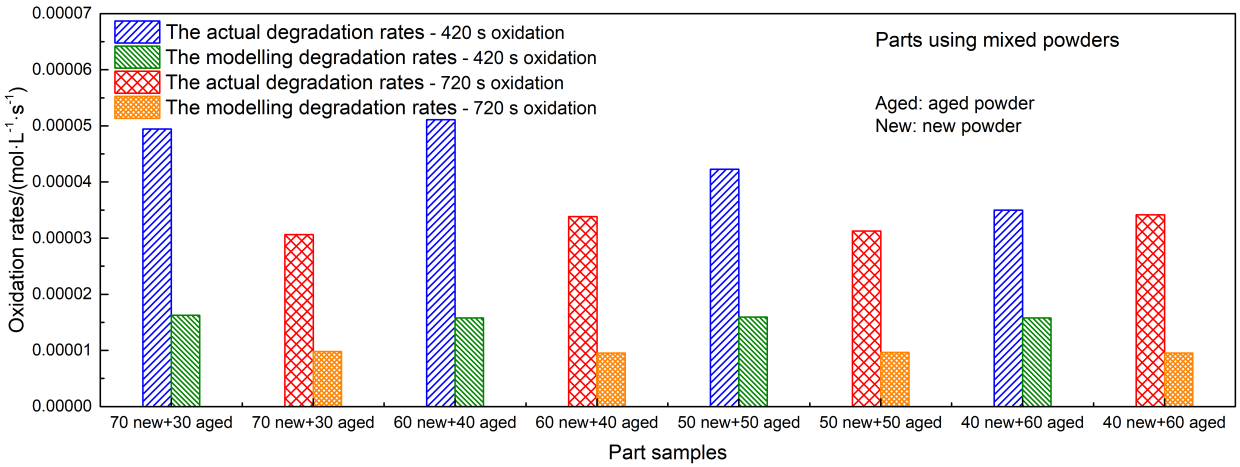

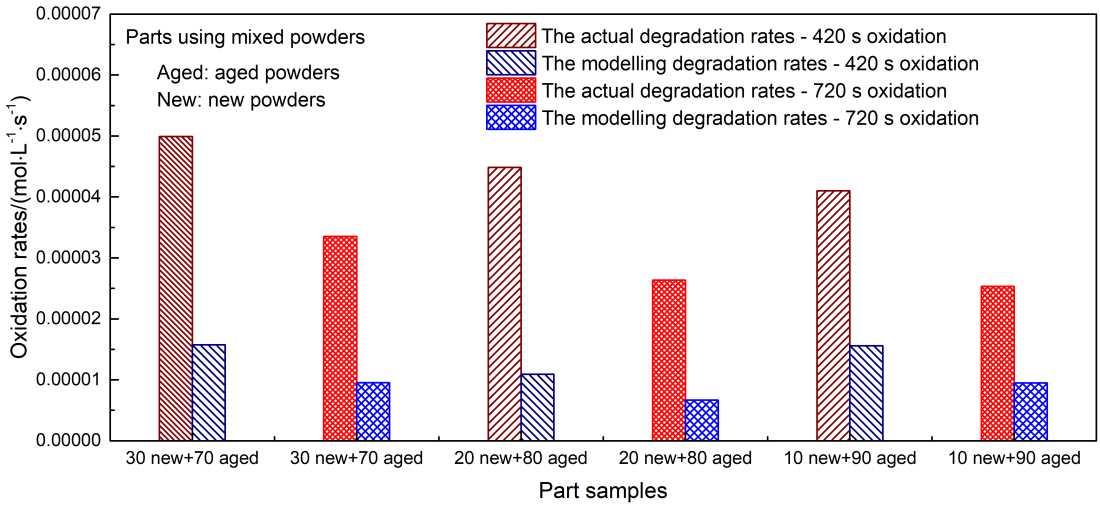

(b) Parts using mixed polyamide 12 powders

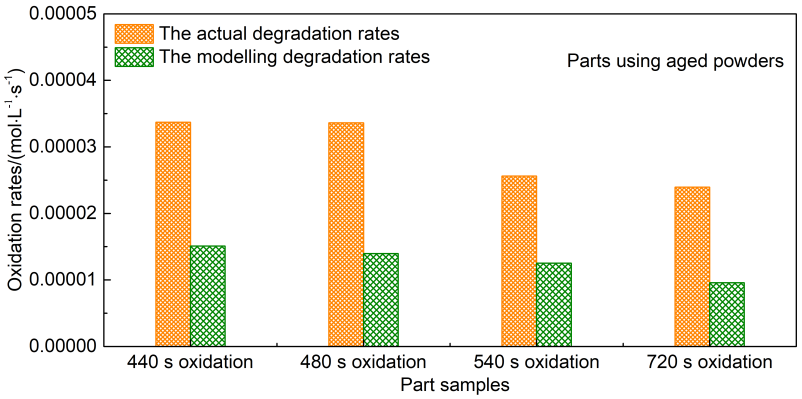

(c) Parts using aged polyamide 12 powders

Figure 4-7 Comparisons between the modelling aging rates μ_i and the actual SLS aging rates η_i for different printed samples using polyamide 12 powders

4.3.2 Building the kinetic model of polyamide 12 aging in SLS considering the coupled oxygen and laser effects

4.3.2.1 Determining the coefficients of the actual coupled laser and oxygen effects in SLS, σ_{i-SLS}^{ol}

Table 4-4 shows the selected SLS sample group 1 and the associated time of oxidation. After performing the sensitivity analysis using the basic autoxidation model, we conducted curve fitting between the modelling degradation rates μ_i and the coupled laser and oxygen effects $\sigma_i^{ol}[O_2]$ to an R-squared second-order polynomial (Eq. 4-30). Figure 4-8 exhibits the results of sensitivity analysis and the fitting equations.

Table 4-4 SLS sample group 1

Sample	Time of oxidation/seconds
Parts using 100% new powders	440, 480
Parts using 70% new and 30% aged powders	420
Parts using 60% new and 40% aged powders	420
Parts using 50% new and 50% aged powders	420
Parts using 40% new and 60% aged powders	720
Parts using 30% new and 70% aged powders	420
Parts using 20% new and 80% aged powders	420
Parts using 10% new and 90% aged powders	720
Parts using 100% aged powders	440, 480

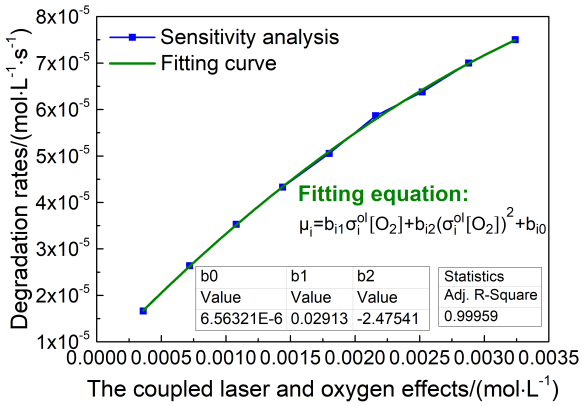

(a) 440 s of oxidation (using new powders)

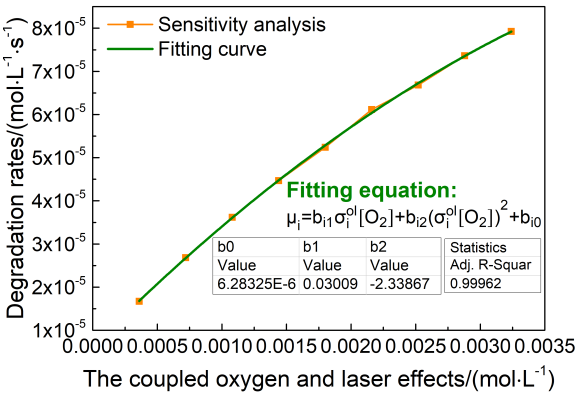

(b) 480 s of oxidation (using new powders)

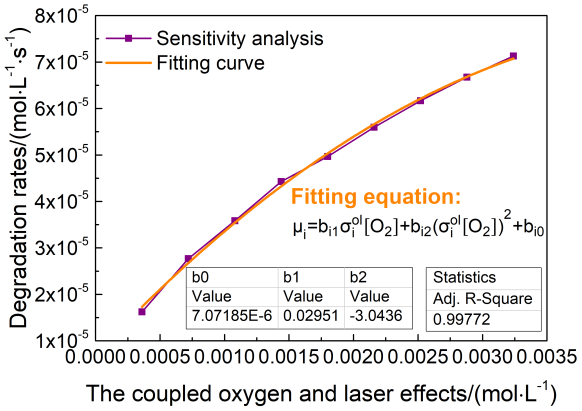

(c) 420 s of oxidation (using 70% new powders)

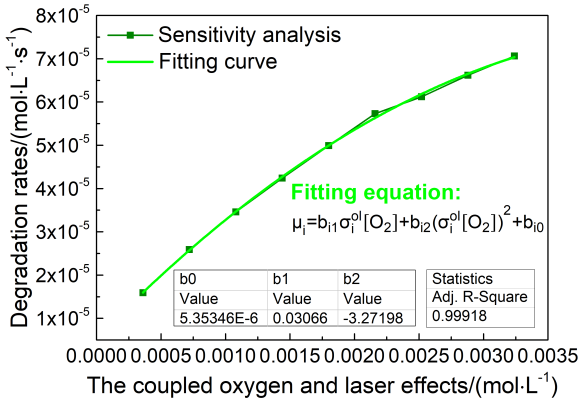

(d) 420 s of oxidation (using 60% new powders)

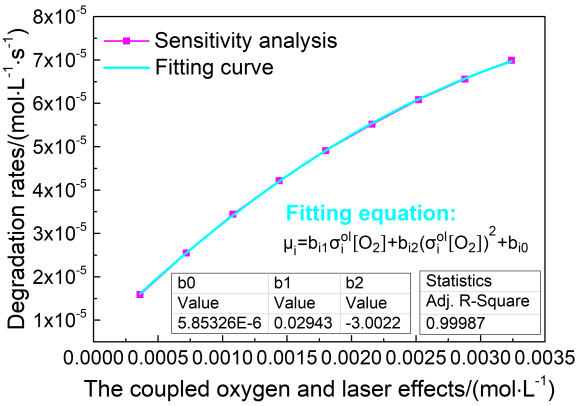

(e) 420 s of oxidation (using 50% new powders)

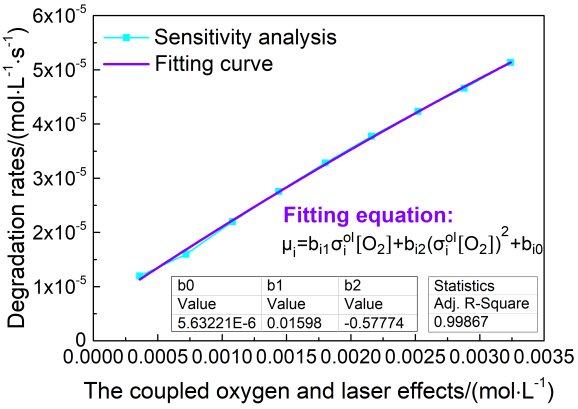

(f) 720 s of oxidation (using 40% new powders)

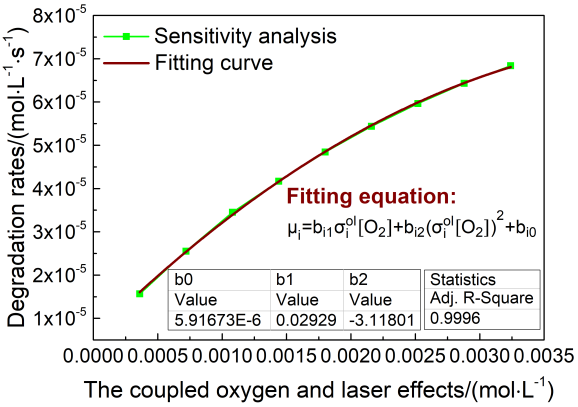

(g) 420 s of oxidation (using 30% new powders)

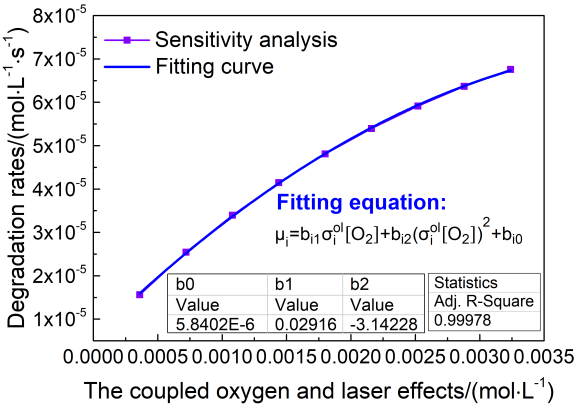

(h) 420 s of oxidation (using 20% new powders)

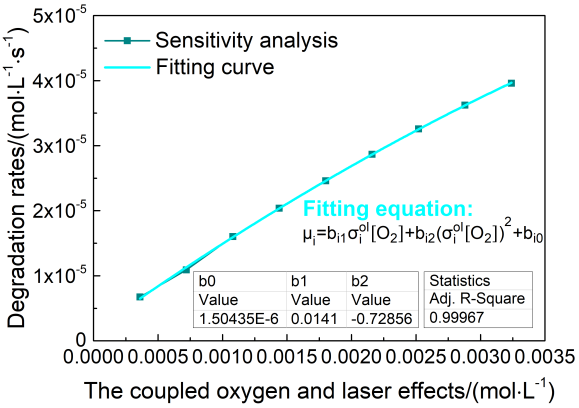

(i) 720 s of oxidation (using 10% new powders)

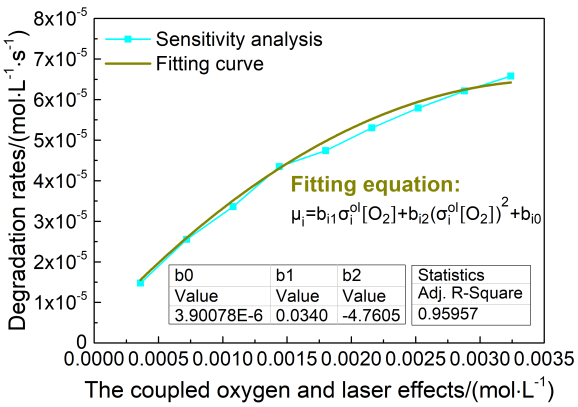

(j) 440 s of oxidation (using aged powders)

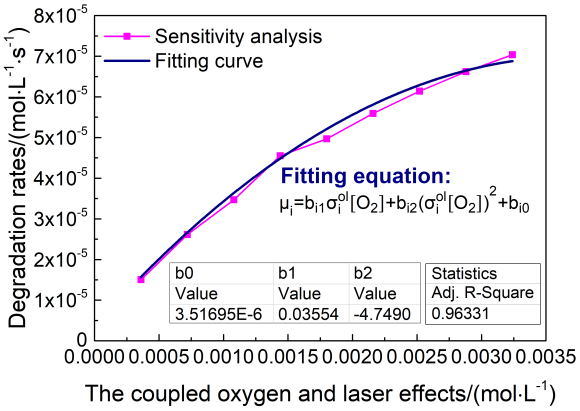

(k) 480 seconds of oxidation (part using aged powders)

Figure 4-8 Sensitivity analysis and the fitting equations between μ_i and $\sigma_i^{ol}[O_2]$ to an R-squared second-order polynomial

In each fitting equation, letting the modelling degradation rates, μ_i, equal to the actual degradation rates η_i, we obtain the actual coupled laser and oxygen effects in SLS, $\sigma_{i-SLS}^{ol}[O_2]$, and the coefficients of σ_{i-SLS}^{ol} (Table 4-5). Here, we obtain the updated oxidation model, including the basic autoxidation model and σ_{i-SLS}^{ol}. The values of σ_{i-SLS}^{ol} indicate that the coupled laser and oxygen effects are about 4 times more than the case with only oxygen (σ^o=1), and *the laser effects are on average 4.4 times stronger than oxygen effects on polyamide 12 degradation*.

Table 4-5 The calculated coefficients of the coupled oxygen and laser effects, σ_{i-SLS}^{ol}, in the SLS process

Sample	Fitting curves between modelling degradation rates (μ_i) and the coupled oxygen and laser effects ($\sigma_i^{ol}[O_2]$)	The actual degradation rates in SLS η_i /mol·L^{-1}·s^{-1}	The actual coupled laser and oxygen effects in SLS, $\sigma_{i-SLS}^{ol}[O_2]$ /mol·L^{-1}	Coefficients of the actual coupled laser and oxygen effects in SLS, σ_{i-SLS}^{ol}/mol·L^{-1}
Figure 4-8a	$\mu=6.563\times10^{-6}+0.029\sigma^{ol}[O_2]-2.475(\sigma^{ol}[O_2])^2$	5.105×10^{-5}	1.804×10^{-3}	5.010
Figure 4-8b	$\mu=6.283\times10^{-6}+0.030\sigma^{ol}[O_2]-2.338(\sigma^{ol}[O_2])^2$	4.916×10^{-5}	1.632×10^{-3}	4.533
Figure 4-8c	$\mu=7.071\times10^{-6}+0.029\sigma^{ol}[O_2]-3.043(\sigma^{ol}[O_2])^2$	4.944×10^{-5}	1.753×10^{-3}	4.868
Figure 4-8d	$\mu=5.353\times10^{-6}+0.031\sigma^{ol}[O_2]-3.272(\sigma^{ol}[O_2])^2$	5.109×10^{-5}	1.861×10^{-3}	5.170
Figure 4-8e	$\mu=5.853\times10^{-6}+0.029\sigma^{ol}[O_2]-3.002(\sigma^{ol}[O_2])^2$	4.228×10^{-5}	1.453×10^{-3}	4.037

Figure 4-8f	$\mu=5.632\times10^{-6}+0.016\sigma^{ol}[O_2]-0.578(\sigma^{ol}[O_2])^2$	3.418×10^{-5}	1.919×10^{-3}	5.332
Figure 4-8g	$\mu=5.916\times10^{-6}+0.029\sigma^{ol}[O_2]-3.118(\sigma^{ol}[O_2])^2$	4.992×10^{-5}	1.878×10^{-3}	5.216
Figure 4-8h	$\mu=5.840\times10^{-6}+0.029\sigma^{ol}[O_2]-3.142(\sigma^{ol}[O_2])^2$	4.486×10^{-5}	1.622×10^{-3}	4.504
Figure 4-8i	$\mu=1.504\times10^{-6}+0.014\sigma^{ol}[O_2]-0.729(\sigma^{ol}[O_2])^2$	2.532×10^{-5}	1.622×10^{-3}	4.505
Figure 4-8j	$\mu=3.900\times10^{-6}+0.034\sigma^{ol}[O_2]-4.761(\sigma^{ol}[O_2])^2$	3.371×10^{-5}	1.022×10^{-3}	2.838
Figure 4-8k	$\mu=3.517\times10^{-6}+0.036\sigma^{ol}[O_2]-4.749(\sigma^{ol}[O_2])^2$	3.363×10^{-5}	9.740×10^{-4}	2.705

4.3.2.2 Determining the relationship between the updated modelling degradation rates $\tilde{\mu}_i$ and oxidation time t_i

This subsection identifies the relationships between the updated modelling degradation rates $\tilde{\mu}_i$ and oxidation time t_i using the updated oxidation model. First, we conducted a sensitivity analysis on concentration changes of oxidative components as oxidation time t_i increases (Figure 4-9). The observation is that the sample using 100% aged powders has the slowest rates of concentration changes when $t_i > 100$ seconds. This is largely due to that the aged powders develop a lot of oxidized components from the thermal history.

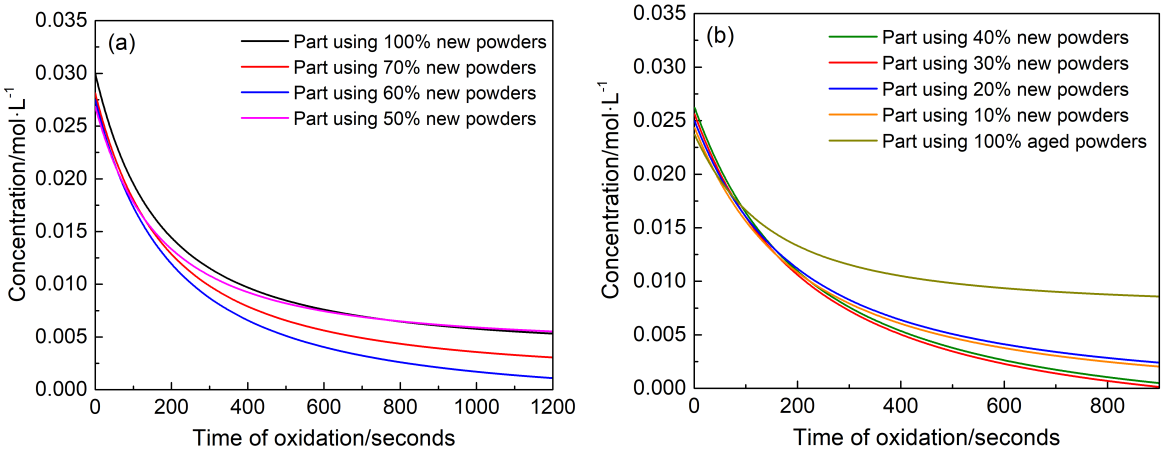

Figure 4-9 Sensitivity analysis on concentration changes of the oxidative components as oxidation time t_i increases using the updated oxidation model

We divided the concentration changes by oxidation time t_i to get degradation curves, and fit the curves to a series of cubic-polynomial (Eq. 4-31). Figure 4-10 shows the fitting equations

between the updated modelling degradation rates $\tilde{\mu}_i$ and oxidation time t_i. In the sensitivity analysis curve, the model output $\tilde{\mu}_i$ goes up quickly from zero to the maximum and then goes down within seconds. The reason is that a strong thermal impetus initiates and simultaneously accelerates the degradation reaction at a time close to zero. At this stage, the impetus dominantly controls the reaction and continuously increases the degradation rates until arriving at the maximum point. However, when the reaction runs normally, the basic parameters, e.g., initial concentrations of components, elementary reaction coefficients, laser and oxygen effects, take control of the reaction. At this stage, the influences of the initiation impetus on degradation rates diminish rapidly and disappear gradually.

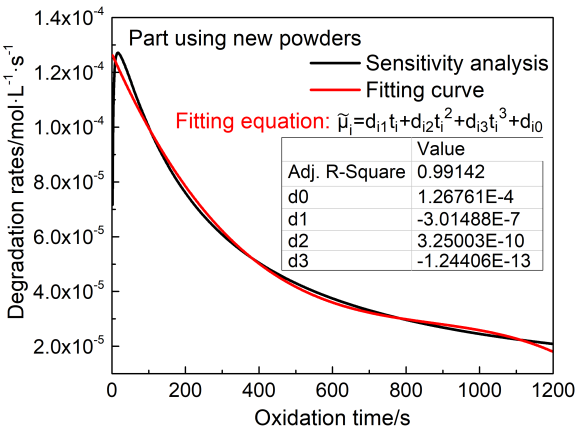

(a) Part using 100% new powders

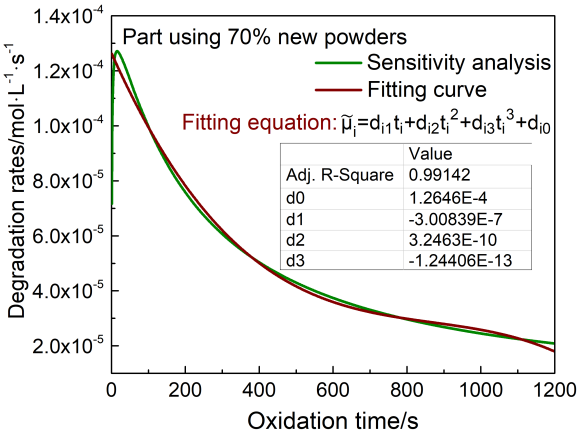

(b) Part using 70% new powders

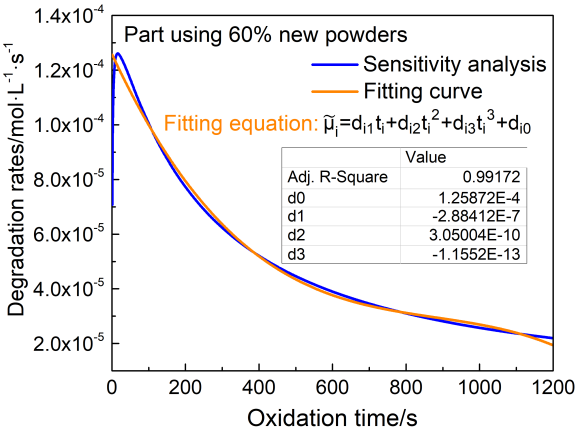

(c) Part using 60% new powders

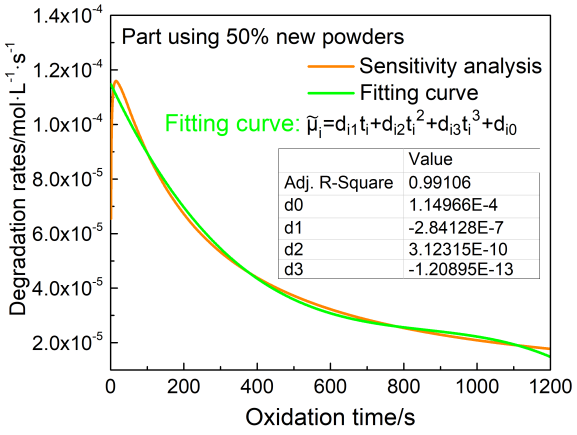

(d) Part using 50% new powders

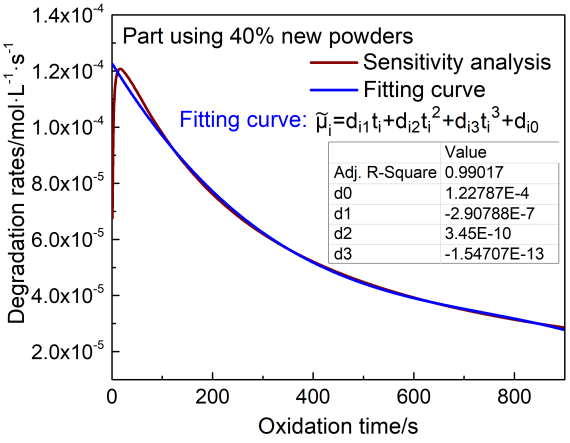

(e) Part using 40% new powders

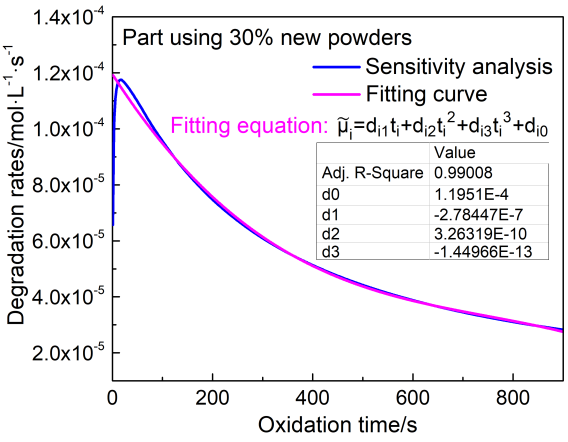

(f) Part using 30% new powders

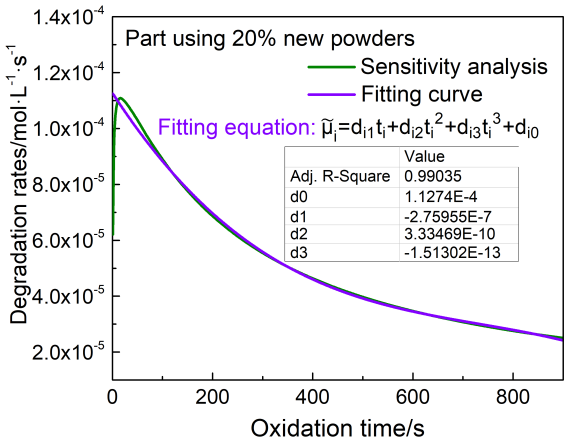

(g) Part using 20% new powders

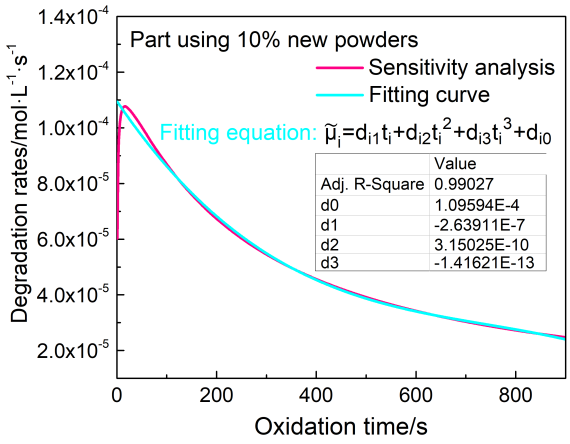

(h) Part using 10% new powders

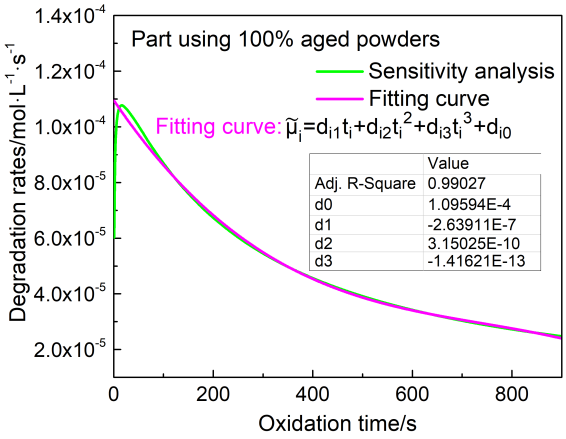

(i) Part using 100% aged powders

Figure 4-10 Fitting equations between the updated modelling degradation rates $\tilde{\mu}_i$ and oxidation time t_i

4.3.2.3 The proposed kinetic model

For different polyamide 12 powder combinations, Table 4-6 lists the coefficients of the actual coupled laser and oxygen effects in SLS, σ_{i-SLS}^{ol}, and the fitting equations between the updated

modelling degradation rates $\tilde{\mu}_i$ and oxidation time t_i. The proposed kinetic scheme of polyamide 12 aging in SLS considering the coupled oxygen and laser effects includes the basic autoxidation model, σ_{i-SLS}^{ol} and fitting equations between $\tilde{\mu}_i$ and t_i. From there, we can predict the sample degradation in SLS through powder combination and oxidation time.

Table 4-6 The coefficients of the actual coupled laser and oxygen effects in SLS, σ_{i-SLS}^{ol}, and the fitting equations between the updated modelling degradation rates $\tilde{\mu}_i$ and oxidation time t_i

Sample	σ_{i-SLS}^{ol} /mol·L^{-1}	The fitting equations between the updated modelling degradation rates $\tilde{\mu}_i$ and oxidation time t_i
Part using 100% new powders	4.772	$\tilde{\mu} = 1.268\times10^{-4}-3.015\times10^{-7}\cdot t + 3.250\times10^{-10}\cdot t^2-1.244\times10^{-13}\cdot t^3$
Part using 70% new powders	4.868	$\tilde{\mu} = 1.265\times10^{-4}-3.008\times10^{-7}\cdot t + 3.246\times10^{-10}\cdot t^2-1.244\times10^{-13}\cdot t^3$
Part using 60% new powders	5.170	$\tilde{\mu} = 1.259\times10^{-4}-2.884\times10^{-7}\cdot t + 3.050\times10^{-10}\cdot t^2-1.155\times10^{-13}\cdot t^3$
Part using 50% new powders	4.037	$\tilde{\mu} = 1.149\times10^{-4}-2.841\times10^{-7}\cdot t + 3.123\times10^{-10}\cdot t^2-1.209\times10^{-13}\cdot t^3$
Part using 40% new powders	5.332	$\tilde{\mu} = 1.228\times10^{-4}-2.908\times10^{-7}\cdot t + 3.450\times10^{-10}\cdot t^2-1.547\times10^{-13}\cdot t^3$
Part using 30% new powders	5.216	$\tilde{\mu} = 1.195\times10^{-4}-2.784\times10^{-7}\cdot t + 3.263\times10^{-10}\cdot t^2-1.449\times10^{-13}\cdot t^3$
Part using 20% new powders	4.504	$\tilde{\mu} = 1.127\times10^{-4}-2.759\times10^{-7}\cdot t + 3.335\times10^{-10}\cdot t^2-1.513\times10^{-13}\cdot t^3$
Part using 10% new powders	4.505	$\tilde{\mu} = 1.096\times10^{-4}-2.639\times10^{-7}\cdot t + 3.150\times10^{-10}\cdot t^2-1.416\times10^{-13}\cdot t^3$
Part using 100% aged powders	2.772	$\tilde{\mu} = 1.096\times10^{-4}-2.639\times10^{-7}\cdot t + 3.150\times10^{-10}\cdot t^2-1.416\times10^{-13}\cdot t^3$

Inserting the modelling related parameters of SLS sample group 2 (Table 4-7) into the proposed kinetic model, we predicted the degradation rates of these samples. Figure 4-11 compares the predicted degradation $\tilde{\mu}_i$ using the proposed kinetic model and the measured actual SLS degradation η_i of sample group 2. Small deviations between the predicted $\tilde{\mu}_i$ and the actual degradation results η_i exist. Figure 4-11 presents average deviations of 9.43% between $\tilde{\mu}_i$ and η_i, respectively, exhibiting a substantial improvement compared to the results in Figure 4-7. The proposed kinetic model is capable to predict the SLS degradation rates of polyamide 12 accurately.

Table 4-7 SLS sample group 2

Sample	Oxidation time/seconds
Parts using 100% new powders	540, 720
Parts using 70% new and 30% aged powders	720
Parts using 60% new and 40% aged powders	720

Parts using 50% new and 50% aged powders	720
Parts using 40% new and 60% aged powders	420
Parts using 30% new and 70% aged powders	720
Parts using 20% new and 80% aged powders	720
Parts using 10% new and 90% aged powders	420
Parts using 100% aged powders	540, 720

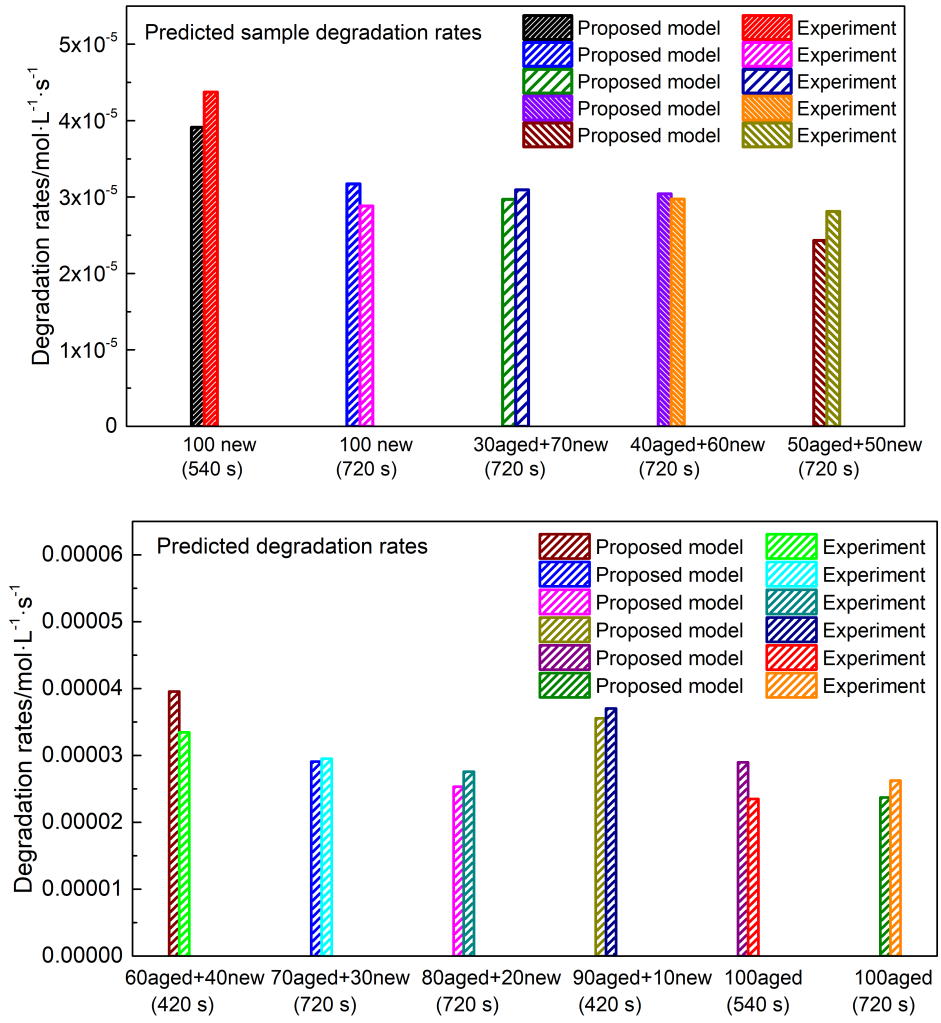

Figure 4-11 The comparisons between the predicted degradation rates $\tilde{\mu}_i$ and the actual SLS degradation rates η_i of the SLS sample group 2 (Parts using polyamide 12 powders of different combinations)

4.3.2.4 Discussions

Table 4-8 presents the actual SLS degradation rates η_i from experimentation, the modelling degradation rates μ_i from the basic autoxidation model, and the updated modelling degradation rates $\tilde{\mu}_i$ from the proposed kinetic model. The modelling degradation rates μ_i have large deviations compared to the actual SLS degradation rates η_i, while the updated modelling degradation rates $\tilde{\mu}_i$

are close to η_i. The predicted degradations $\tilde{\mu}_i$ from the proposed kinetic model match on average 89.53% with the actual SLS degradation rates η_i, in contrast to a 34.48% accuracy from a basic autoxidation model.

Table 4-8 Comparisons between the actual SLS degradation rates η_i, the modelling degradation rates μ_i from the basic autoxidation model, and the updated modelling degradation $\tilde{\mu}_i$ from the proposed kinetic model

Sample	The actual SLS degradation rates η_i/mol·L^{-1}·s^{-1}	The basic autoxidation model		The proposed kinetic model	
		Degradation rates μ_i /mol·L^{-1}·s^{-1}	Deviation/ %	Degradation rates $\tilde{\mu}_i$ /mol·L^{-1}·s^{-1}	Deviation/ %
Part/100% new powder/540 s	4.726×10^{-5}	1.347×10^{-5}	71.505	3.913×10^{-5}	17.177
Part/100% new powder/720 s	3.021×10^{-5}	1.023×10^{-5}	66.129	3.174×10^{-5}	5.054
Part/70% new powder/720 s	3.065×10^{-5}	9.819×10^{-6}	67.964	2.971×10^{-5}	3.065
Part/60% new powder/720 s	3.386×10^{-5}	9.538×10^{-6}	71.832	2.971×10^{-5}	10.156
Part/50% new powder/720 s	3.128×10^{-5}	9.648×10^{-6}	69.162	2.432×10^{-5}	22.260
Part/40% new powder/420 s	3.4974×10^{-5}	1.577×10^{-5}	54.894	3.954×10^{-5}	13.058
Part/30% new powder/720 s	3.354×10^{-5}	9.545×10^{-6}	71.542	2.907×10^{-5}	13.319
Part/20% new powder/720 s	2.634×10^{-5}	6.678×10^{-6}	74.647	2.533×10^{-5}	3.823
Part/10% new powder/420 s	4.100×10^{-5}	1.560×10^{-5}	61.943	3.554×10^{-5}	13.311
Part/100% aged powder/540 s	2.560×10^{-5}	1.253×10^{-5}	51.069	2.894×10^{-5}	13.044
Part/100% aged powder/720 s	2.395×10^{-5}	9.568×10^{-6}	60.045	2.372×10^{-5}	0.936

4.4 Characteristics of the updated modelling degradation rates $\tilde{\mu}_i$

4.4.1 Influences of the coupled laser and oxygen effects on $\tilde{\mu}_i$

4.4.1.1 Degradation characteristics in presence of decreasing oxidations

To identify the degradation trend here, we reduce $\sigma_{i-SLS}^{ol}[O_2]$ for different part samples in Table 4-9. Inserting the $\sigma_{i-SLS}^{ol}[O_2]$ into the proposed kinetic model, we obtained $\tilde{\mu}_i - t_i$ curves

between the updated modelling degradation rates $\tilde{\mu}_i$ and oxidation time t_i (Figure 4-12). Figure 4-12 a, b, and c are the results for, respectively, SLS 3D-printed part using 100% new powders, part using 50%-50% new-aged powders, and part using 100% aged powders. The $\tilde{\mu}_i - t_i$ curves in different colors point out the nonlinear relationship between $\sigma_{i-SLS}^{ol}[O_2]$ and the degradation rate. The black curves in Figure 4-12 a-c are the benchmark $\tilde{\mu}_i - t_i$ curves with the original $\sigma_{i-SLS}^{ol}[O_2]$.

For different samples in Figure 4-12, when $\sigma_{i-SLS}^{ol}[O_2]$ reduces, the updated modelling degradation rates increase from zero to the maximum quickly, then decrease with time. For a specific sample (e.g., Figure 4-12a, the new-SLS part), the maximum of $\tilde{\mu}_i$ drops as $\sigma_{i-SLS}^{ol}[O_2]$ decreases. The new-SLS part (Figure 4-12a) always has the largest degradation rate, while the aged-SLS part (Figure 4-12c) has the smallest $\tilde{\mu}_i$. For the mixed (Figure 4-12b) and aged-SLS parts (Figure 4-12c), curves with $\sigma_{i-SLS}^{ol}[O_2]/2$ (7.267×10^{-4} mol/L for mixed and 4.989×10^{-4} mol/L for aged) and $\sigma_{i-SLS}^{ol}[O_2]/5$ (2.907×10^{-4} mol/L for mixed and 1.996×10^{-4} mol/L for aged) result in a large drop of $\tilde{\mu}_i$ compared to the benchmark $\tilde{\mu}_i - t_i$ curves, especially at the peak degradation points. However, further curves (curves with $\sigma_{i-SLS}^{ol}[O_2]/10$, $\sigma_{i-SLS}^{ol}[O_2]/20$, and $\sigma_{i-SLS}^{ol}[O_2]/100$) show small changes in comparison to the curve with $\sigma_{i-SLS}^{ol}[O_2]/5$. After about 1200 s of oxidation (t_i=1200 s), the rates of degradation all approach the steady state. This convergence is much faster when the oxidation effect is reduced. In addition, when reusing powders, degradation significantly slows down when oxidation is reduced by a factor of 5, and remains afterwards (Figure 4-12bc).

Table 4-9 The decreasing $\sigma_{i-SLS}^{ol}[O_2]$

Sample	The actual coupled laser and oxygen effects in SLS, $\sigma_{i-SLS}^{ol}[O_2]$ /mol·L^{-1}	$\sigma_{i-SLS}^{ol}[O_2]$ /2	$\sigma_{i-SLS}^{ol}[O_2]$ /5	$\sigma_{i-SLS}^{ol}[O_2]$ /10	$\sigma_{i-SLS}^{ol}[O_2]$ /20	$\sigma_{i-SLS}^{ol}[O_2]$ /50	$\sigma_{i-SLS}^{ol}[O_2]$ /100
		Unit: mol·L^{-1}					
Part using 100% new powders	1.718×10^{-3}	8.589×10^{-4}	3.435×10^{-4}	1.718×10^{-4}	8.589×10^{-5}	3.435×10^{-5}	1.718×10^{-5}
Part using 50% new powders	1.453×10^{-3}	7.267×10^{-4}	2.907×10^{-4}	1.453×10^{-4}	7.267×10^{-5}	2.907×10^{-5}	1.453×10^{-5}
Part using 100% aged powders	9.978×10^{-4}	4.989×10^{-4}	1.996×10^{-4}	9.978×10^{-5}	4.989×10^{-5}	1.996×10^{-5}	9.978×10^{-6}

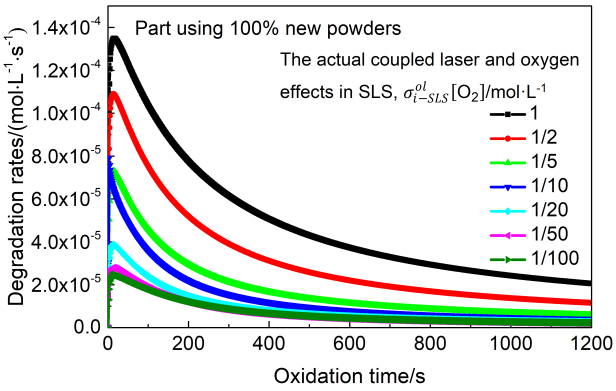

(a) Part using 100% new powders

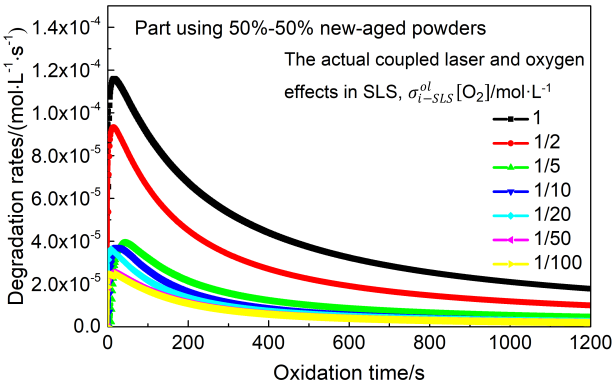

(b) Part using 50%-50% new-aged powders

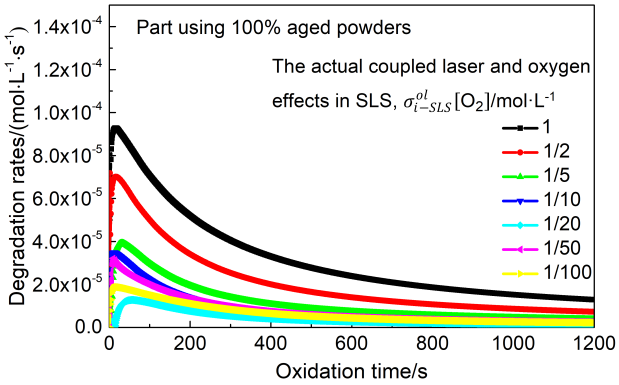

(c) Part using 100% aged powders

Figure 4-12 Curves between the updated modelling degradation rates $\tilde{\mu}_i$ and oxidation time t_i with decreasing $\sigma_{i-SLS}^{ol}[O_2]$ for different part samples

4.4.1.2 Degradation characteristics in presence of increasing oxidations

Table 4-10 presents the designed experiments with increasing $\sigma_{i-SLS}^{ol}[O_2]$ for different part samples. Applying the increasing $\sigma_{i-SLS}^{ol}[O_2]$ to the proposed kinetic model, we obtain the $\tilde{\mu}_i - t_i$ curves between the updated modelling degradation rates and oxidation time (Figure 4-13). Figure 4-13 a, b, and c are respectively for SLS 3D-printed part using 100% new powders, part using 50%-50% new-aged powders, and part using 100% aged powders. The curves in different colors represent differently increased $\sigma_{i-SLS}^{ol}[O_2]$. The black curves in Figure 4-13 a-c are the benchmark $\tilde{\mu}_i - t_i$ curves with the original $\sigma_{i-SLS}^{ol}[O_2]$.

In Figure 4-13, $\tilde{\mu}_i$ increases from zero to the maximum quickly, then decreases with time. For any specific sample (e.g., Figure 4-13a, the new-SLS part), the maximum of $\tilde{\mu}_i$ rises as $\sigma_{i-SLS}^{ol}[O_2]$ increases. Having the same increasing degree for $\sigma_{i-SLS}^{ol}[O_2]$ (e.g., $\sigma_{i-SLS}^{ol}[O_2]$×10), the new-SLS

part always has the largest $\tilde{\mu}_i$, while the aged-SLS part has the smallest $\tilde{\mu}_i$. For new, mixed, and aged-SLS parts, curves with $\sigma_{i-SLS}^{ol}[O_2]\times2$ and $\sigma_{i-SLS}^{ol}[O_2]\times5$ lead to obvious increases of $\tilde{\mu}_i$. However, the other curves (curves with $\sigma_{i-SLS}^{ol}[O_2]\times10$, $\sigma_{i-SLS}^{ol}[O_2]\times20$, $\sigma_{i-SLS}^{ol}[O_2]\times50$, $\sigma_{i-SLS}^{ol}[O_2]\times100$) differ little compared to the curve with $\sigma_{i-SLS}^{ol}[O_2]\times5$. The result indicates that further increasing $\sigma_{i-SLS}^{ol}[O_2]$ does not influence $\tilde{\mu}_i$ significantly. Till 1200 s, all the curves are at or close to reaching the steady state.

Table 4-10 The increasing $\sigma_{i-SLS}^{ol}[O_2]$

Sample	The actual coupled laser and oxygen effects in SLS, $\sigma_{i-SLS}^{ol}[O_2]$ /mol·L^{-1}	$\sigma_{i-SLS}^{ol}[O_2]$ ×2	$\sigma_{i-SLS}^{ol}[O_2]$ ×5	$\sigma_{i-SLS}^{ol}[O_2]$ ×10	$\sigma_{i-SLS}^{ol}[O_2]$ ×20	$\sigma_{i-SLS}^{ol}[O_2]$ ×50	$\sigma_{i-SLS}^{ol}[O_2]$ ×100
		Unit: mol·L^{-1}					
Part using 100% new powders	1.718×10^{-3}	3.435×10^{-3}	8.589×10^{-3}	1.718×10^{-2}	3.435×10^{-2}	8.589×10^{-2}	1.718×10^{-1}
Part using 50% new powders	1.453×10^{-3}	2.907×10^{-3}	7.267×10^{-3}	1.453×10^{-2}	2.907×10^{-2}	7.267×10^{-2}	1.453×10^{-1}
Part using 100% aged powders	9.978×10^{-4}	1.996×10^{-3}	4.989×10^{-3}	9.978×10^{-3}	1.996×10^{-2}	4.989×10^{-2}	9.978×10^{-2}

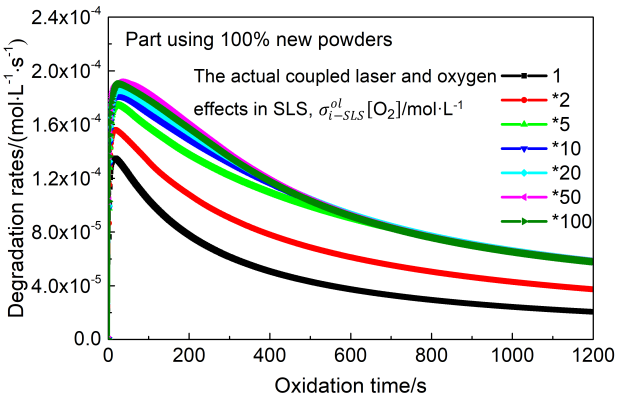

(a) Part using 100% new powders

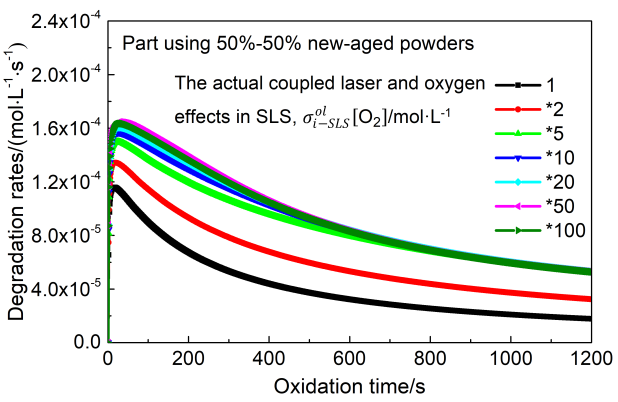

(b) Part using 50%-50% new-aged powders

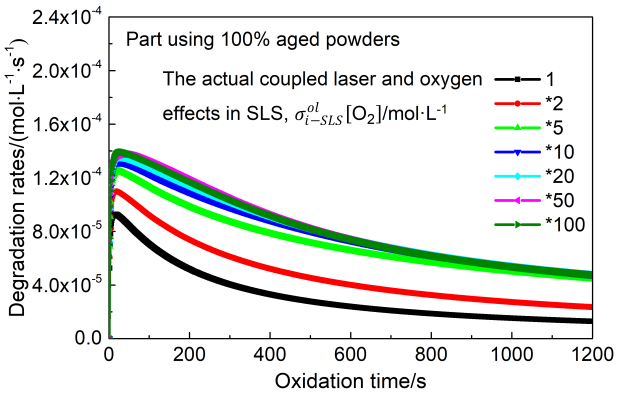

(c) Part using 100% aged powders

Figure 4-13 Curves between the updated modelling degradation rates $\tilde{\mu}_i$ and oxidation time t_i with increasing $\sigma_{i-SLS}^{ol}[O_2]$ for different part samples

4.4.1.3 Comparisons

Figure 4-14 compares $\tilde{\mu}_i$ at 1200 s for different samples to reveal material degradation rates at the steady state. In Figure 4-14, the purple bars are the benchmark $\tilde{\mu}_i$@1200 s data with the original $\sigma_{i-SLS}^{ol}[O_2]$. When $\sigma_{i-SLS}^{ol}[O_2]$ decreases (increases), the $\tilde{\mu}_i$@1200 s decreases (increases) quickly first. Further decreasing (increasing) $\sigma_{i-SLS}^{ol}[O_2]$ has little effects on $\tilde{\mu}_i$@1200 s.

Table 4-11 compares $\tilde{\mu}_i$@1200 s between the original $\sigma_{i-SLS}^{ol}[O_2]$ and the decreased/increased $\sigma_{i-SLS}^{ol}[O_2]$ for different samples. In contrast to the case with the original $\sigma_{i\text{-}SLS}^{ol}[O_2]$, $\tilde{\mu}_i$@1200 s with $\sigma_{i\text{-}SLS}^{ol}[O_2]/100$ decreased by, respectively, 89.02%, 88.77%, and 81.90% for the new, mixed and aged-SLS parts. On the other hand, $\tilde{\mu}_i$@1200 s with $\sigma_{i\text{-}SLS}^{ol}[O_2]\times100$ increased by, respectively, 181.78%, 197.35%, and 183.42% for the new, mixed and aged-SLS parts.

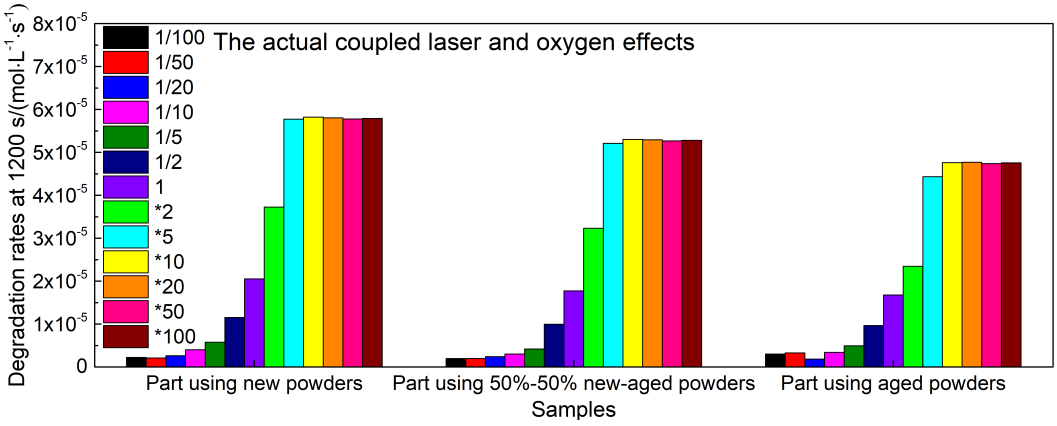

Figure 4-14 Comparisons of $\tilde{\mu}_i$ at 1200 s for different samples to compare material degradation rates at a more stable state

Table 4-11 Comparisons of $\tilde{\mu}_i$@1200 s between the original $\sigma_{i-SLS}^{ol}[O_2]$ and the decreased/increased $\sigma_{i-SLS}^{ol}[O_2]$ for different samples

Samples	Part using new powders	Part using 50%-50% new-aged powders	Part using aged powders
The decreasing $\sigma_{i-SLS}^{ol}[O_2]$	Percentages of $\tilde{\mu}_i$@1200 s decreasing when $\sigma_{i-SLS}^{ol}[O_2]$ decreasing		
$\sigma_{i-SLS}^{ol}[O_2]/100$	89.02	88.77	81.9
$\sigma_{i-SLS}^{ol}[O_2]/50$	89.73	88.77	80.53
$\sigma_{i-SLS}^{ol}[O_2]/20$	87.13	86.45	88.89
$\sigma_{i-SLS}^{ol}[O_2]/10$	80.38	82.86	79.73
$\sigma_{i-SLS}^{ol}[O_2]/5$	71.96	76.27	70.54
$\sigma_{i-SLS}^{ol}[O_2]/2$	43.83	43.82	42.4
The increasing $\sigma_{i-SLS}^{ol}[O_2]$	Percentages of $\tilde{\mu}_i$@1200 s increasing when $\sigma_{i-SLS}^{ol}[O_2]$ increasing		
$\sigma_{i-SLS}^{ol}[O_2]\times2$	81.41	82.13	39.87
$\sigma_{i-SLS}^{ol}[O_2]\times5$	180.91	193.45	164.06
$\sigma_{i-SLS}^{ol}[O_2]\times10$	183.34	198.76	183.6
$\sigma_{i-SLS}^{ol}[O_2]\times20$	182.53	198.23	184.14
$\sigma_{i-SLS}^{ol}[O_2]\times50$	181.13	196.76	182.41
$\sigma_{i-SLS}^{ol}[O_2]\times100$	181.78	197.35	183.42

4.4.2 Influences of the preheating temperature on $\tilde{\mu}_i$

Figure 4-15 presents the curves ($\tilde{\mu}_i - t_i$ curves) between the updated modelling degradation rates $\tilde{\mu}_i$ and oxidation time t_i with different preheating temperatures for (a) Part using 100% new powders, (b) Part using 50%-50% new-aged powders, and (c) Part using 100% aged powders. In Figure 4-15 a-c, the decreased preheating temperatures lower the $\tilde{\mu}_i - t_i$ curves. When at the same temperature (e.g., 150 °C, 140 °C), the new-SLS part has the largest $\tilde{\mu}_i$ (Figure 4-15 a), while the aged-SLS part has the smallest $\tilde{\mu}_i$ (Figure 4-15 c). As the preheating temperature decreases, the peaks in the $\tilde{\mu}_i - t_i$ curves diminish (from 160 °C to 140 °C) and disappear gradually (from 120 °C to 90 °C). Therefore, the peaks in the $\tilde{\mu}_i - t_i$ curves are likely caused by the high temperature. Besides, when the preheating temperatures are below 120 °C, $\tilde{\mu}_i$ are nearly zero, indicating that a low storage temperature below 120 °C can effectively reduce material degradation.

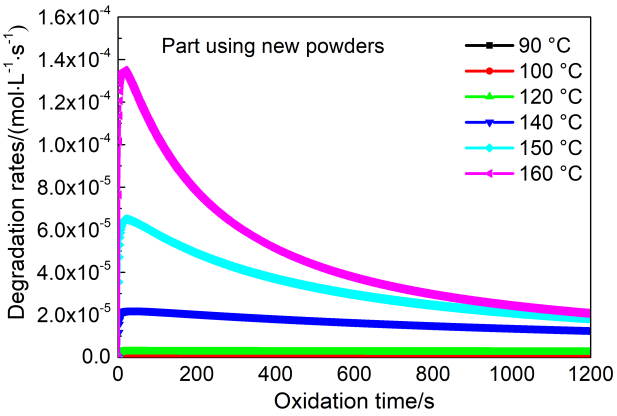

(a) Part using 100% new powders

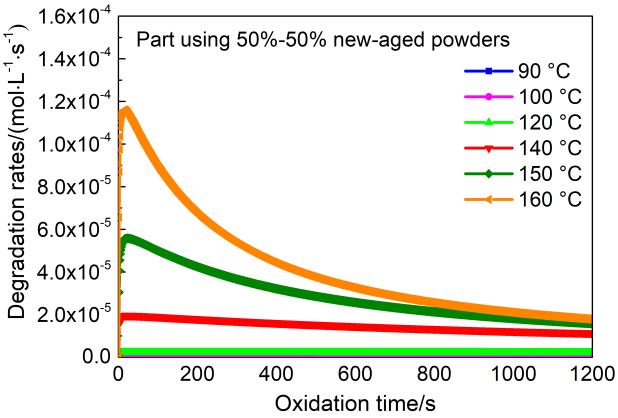

(b) Part using 50%-50% new-aged powders

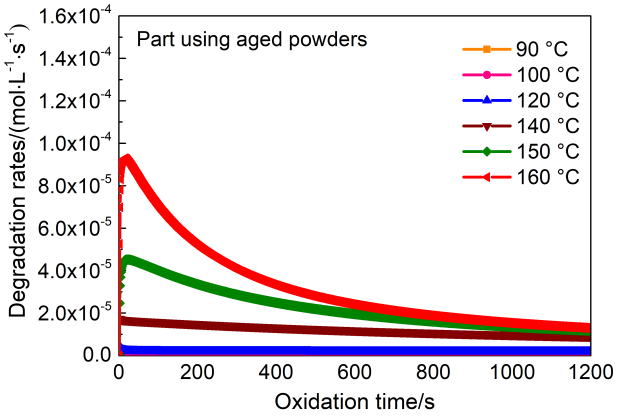

(c) Part using 100% aged powders

Figure 4-15 Curves between the updated modelling degradation rates $\tilde{\mu}_i$ and oxidation time t_i with different preheating temperatures for different part samples

Figure 4-16 shows comparisons of $\tilde{\mu}_i$ at 1200 s between (a) Samples with different preheating temperatures, and (b) Preheating temperatures for different samples. At 90 °C, $\tilde{\mu}_i$@1200 s approaches to zero, leading to almost no degradation for the material at this temperature (Figure 4-16b). $\tilde{\mu}_i$@1200 s decreased evenly with decreasing preheating temperatures (Figure 4-16a). At high temperatures (150 °C – 160 °C), the differences of $\tilde{\mu}_i$@1200 s between different samples are large; those differences reduce quickly at lower temperatures below 120 °C (Figure 4-16b).

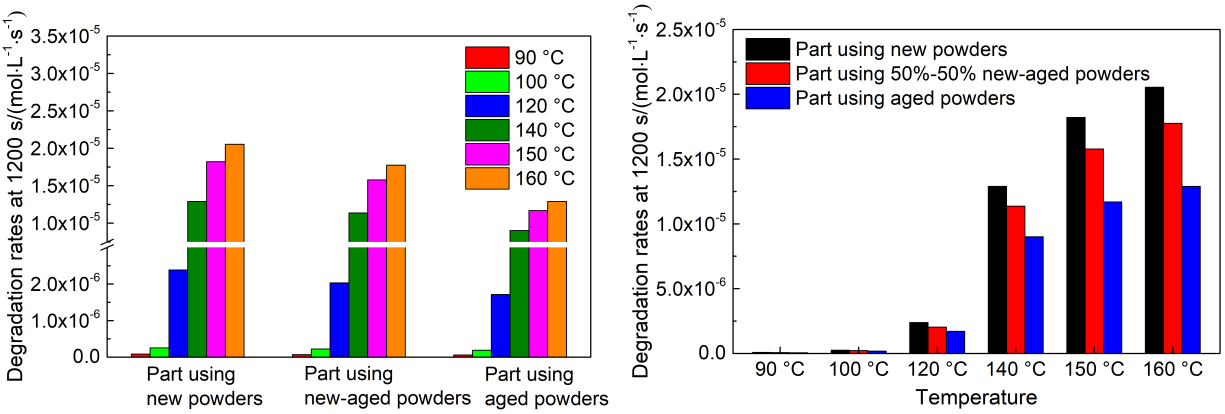

(a) Samples with different preheating temperatures (b) Preheating temperatures for different samples

Figure 4-16 Comparisons of $\tilde{\mu}_i$ at 1200 s ($\tilde{\mu}_i$@1200 s) between (a) Samples with different preheating temperatures, and (b) Preheating temperatures for different samples

4.5 Conclusions

In SLS, a considerable amount of expensive polyamide 12 powders remains un-sintered but reusable after going through severely irreversible chemical degradations. The degradation originates from the thermal energy controlled by the coupled oxygen and laser effects. Through experimentation, and by fitting the actual SLS degradation rates to the basic autoxidation model, we obtained the coefficients of coupled oxygen and laser effects. A further sensitivity analysis suggests the existence of a polynomial fitting between the sample degradation rates and oxidation time. From there, we propose a new kinetic scheme for SLS degradation of polyamide 12 composed of the basic autoxidation model, the coefficients of coupled oxygen and laser effects, and the relationships between the sample degradation rates and oxidation time. The new model can predict the oxidation rates of pure or mixed (different degradation levels) polyamide 12 using two easily available parameters: materials density and oxidation time. The predicted degradations from the proposed kinetic model match on average 89.53% with the actual SLS degradation rates, in contrast to a 34.48% accuracy from a conventional aging model. We found that the laser effects are 4-time stronger than oxygen effects on polyamide 12 degradation. Furthermore, we identified the influences of the coupled oxygen and laser effects in SLS and preheating temperatures on the degradation rates. The findings provide a first-instance knowledge of quantitative material degradation related to the estimated parameters, and insights to reduce degradation in SLS. This work established a novel effective model to obtain the kinetic scheme of polyamide 12 degradation to aid future studies of materials degradation and reuse in the SLS process.

Chapter 5. QUANTITATIVE INFLUENCES OF SUCCESSIVE REUSE ON POLYAMIDE 12 RESIDUES

5.1 Introduction

Involving various materials, methods, and equipment, additive manufacturing translates directly three-dimensional virtual models into physical objects layer by layer [46, 104, 117]. SLS additive manufacturing is capable of producing functional applications with complex geometries through fusing materials and adjacent layers together by controlled laser-material interactions [85, 118]. Capable of processing a wide range of materials (including polymers, metals, ceramics, and composites), SLS has attracted increased industrial and academic interests in recent years [14, 119]. The semi-crystalline thermoplastic polymer, polyamide 12, appears to be the most suitable material to date, and dominates the SLS market thanks to its good flowability, low processing temperature, stable thermal property, and high mechanical strength [120, 121].

Though extensive applications of polyamide 12 materials exist in SLS, the average total volume of the sintered powders during each batch of printing is small (5% ~ 15%) [18]. Most of the loaded materials (between 85% and 95%) remain un-sintered and can be reused for other practices [20, 25]. However, the elevated temperature, laser radiation, and repeated heating/cooling cycles in SLS lead to complex physical and chemical changes in the un-sintered materials [19]. Post-condensation and degradation-induced macro-structural chain changes also reduce the powder and product quality [26, 122].

The degradation of polyamide 12 in SLS attributes to thermo-oxidative reactions [21]. The oxidations result in increased average molecular weight, decreased melt flow index (MFI) [59], and increased melt viscosity [25, 27, 67]. Besides, numerous high-melting-point pieces in the reclaimed powders delay the particle coalescence and affect part mechanical strength [59, 60]. When the environmental temperature is below the melting temperature, the high-melting-point particles serve as sites for spherulites growth. Many spherulite structures cannot spread smoothly in the limited amorphous regions, forming coarse spherulites and coarse surface finish of 3D-printed parts [52].

Reusing the costly polyamide 12 residues will not only introduce economic benefits but also reduce environmental pollutions [123]. Y. Way et al. [123] and P. Magi et al. [124] reclaimed polyamide 12 SLS powders into (i) filaments for fused deposition modelling (FDM) at different printing speeds and building orientations, and (ii) composite filaments for FDM blended with thermoplastic polyurethane (TPU), aramid, and graphite. L. Wang et al. [92] processed the SLS polyamide 12 powder residues with milled carbon fibers into composite filaments for extrusion-based additive manufacturing (EAM). S. Dadbakhsh et al. [24] examined the microstructure and mechanical properties of single-layer SLS parts from (i) new, (ii) aged, and (iii) new and aged powder mixtures, providing new protocols for powder reuse. K. DePalma et al. [122] developed process flow and economic models to compare the economic and environmental feasibility of reusing polyamide 12 residues from SLS.

Despite the previous research, quantitative degradation and thermal decompositions of polyamide 12 residues with successive reuse in SLS remain not well understood. The absence of such knowledge hinders sustainable SLS manufacturing in both academia and industry. This work experiments successive reuse of polyamide 12 residues and quantitatively monitors the material thermal decomposition, molecular evolution, and composition changes in SLS. Importantly, we tested basic flowability energy, Thermogravimetric Analysis (TGA), X-ray Photoelectron Spectroscopy (XPS), and ^{1}H Nuclear Magnetic Resonance (NMR) for powders/parts, and found significant changes between differently reused samples. These findings provide first-instance knowledge for polyamide 12 under successive reuse to the best of our knowledge. We reused the same bucket of polyamide 12 powders up to 8 times. Powder samples, part samples with 3- and 32-layers were collected during each printing batch for various characterizations. In particular, we uncover the priorly uncharted evolution of material properties in successfully printing 32-layer samples with 8-time reused polyamide 12 powders.

5.2 Materials and method

5.2.1 SLS printing, powder reuse, and sample collection

Figure 5-1a presents the proposed flowchart on successive reuse of polyamide 12 in SLS. The material used in our research was a 2 kg bucket of Sinterit polyamide 12 grey powders. The machine used was the Sharebot SnowWhite SLS 3D printer. We set the following parameter settings on this machine (Table 5-1) to sinter polyamide 12 powders: 25% of the 14 W maximum laser power; 100 μm layer thickness; in powder temperature control mode; 160 °C plate

temperature; 600-second pre-heating time; and 20 powder layers warmed before printing. Identifying these parameters are essential because no existing parameter settings are available for printing Sinterit polyamide 12 using the Sharebot SnowWhite SLS 3D printer. The dimensions of the printed parts were set as the ASTM standard Type 5 specimen (Figure 5-1b) and kept consistent for all samples in this work. At each printing, we collected samples and characterized both the powder materials and the printed parts [47].

Table 5-1 Processing parameters in successive reuse of polyamide 12

Parameter	Value	Parameter	Value
Material	Sinterit polyamide 12 powders	Machine	Sharebot SnowWhite SLS 3D printer
Laser power	25% of the 14 W maximum	Layer thickness	100 μm
Control mode	Powder temperature control	Plate temperature	160 °C
Pre-heating time	600 seconds	Layers warmed	20 powder layers
Sample dimension	ASTM standard Type 5	Time for one printing	Around 200 minutes

Starting with the new powders, we collected powder samples before loading the powder bed. We sintered the new powder and collected part samples at the thickness of 3- and 32-layer, respectively. The whole printing process took around 200 minutes. After printing, we held the remaining powders in the SLS machine for at least 24 hours to cool down completely the powders and the machine.

From there, we started the powder reclaim and reuse. We evaluated whether enough powders exist or not in the chamber for the next printing. When enough (the powders can cover the whole chamber with thickness larger than 5 mm), we collected and sieved the powders in a fume hood, and named the sieved fine powders as one-time reused powders. After collecting powder samples, we loaded and sintered the one-time reused powder to get the next set of 3- and 32-layer part samples. We repeated the above procedures to proceed with the powder recycle. When tensile strength or Young's Modulus of the 32-layer tensile bars using the newly reclaimed powders decrease to 65% of the case using the original powders, we terminated the experiment.

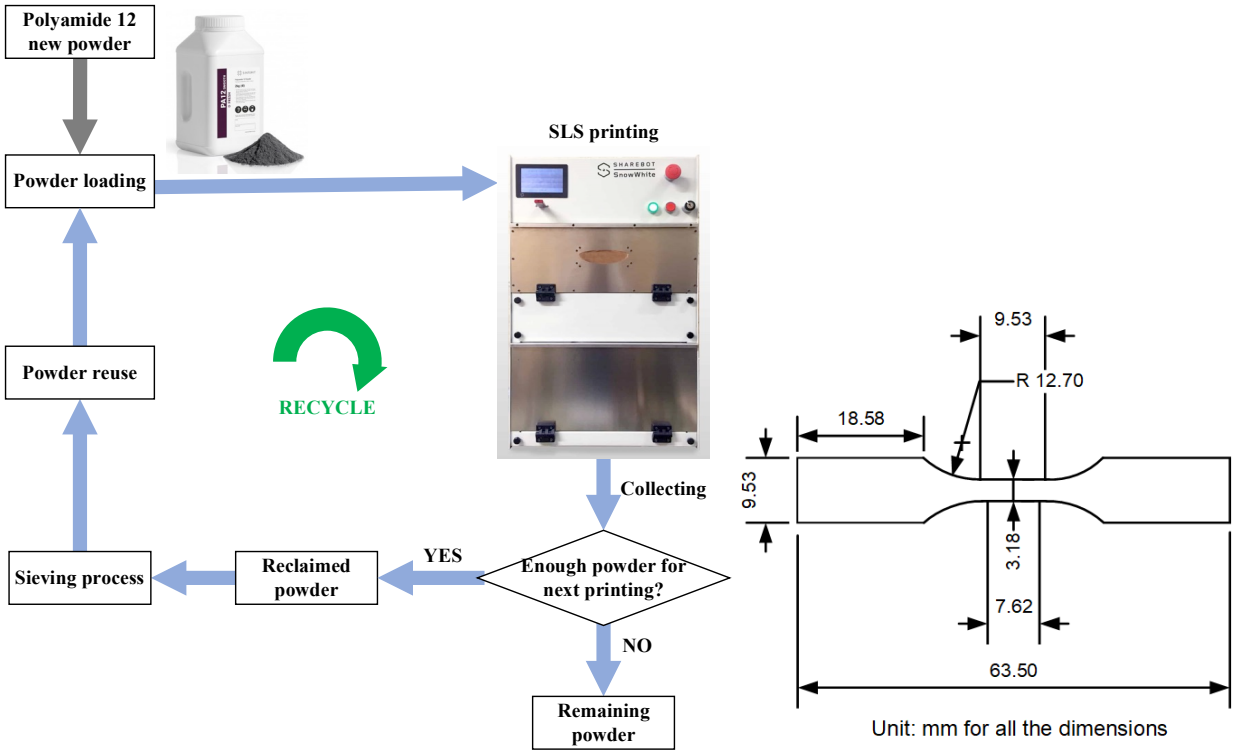

(a) (b)

Figure 5-1 (a) The flowchart to successively reuse polyamide 12 in the studied SLS process, and (b) Dimensions of ASTM standard Type 5 specimen used in this study

5.2.2 Characterizations

5.2.2.1 Powder flowability and particle size distribution

An FT4 powder rheometer measures the flowability of powders with successive reuse. In the test vessel, a blade rotates and moves downwards and upwards through the powder to simulate a forced flow pattern, causing many thousands of particles to flow relative to one another. The difficulty experienced by the blade to move represents the resistance of powder to flow. In our research, the measured variable in forced flow represents the powder basic flowability energy measured in mJ. In addition to flowability, we used a laser-diffraction based Malvern mastersizer 2000 analyzer (measurement ranges: 0.02 μm to 2000 μm) to quantitatively examine the particle size distributions of powder samples with successive reuse (average diameter: 50 ~ 60 μm [76, 125]).

5.2.2.2 Material thermal decomposition, melting, and crystallization behaviors

We performed Thermogravimetric Analysis (TGA) using a TA Instrument TGA Q5000 to monitor the thermal decomposition of polyamide 12 samples after successive reuse. We tested new

powders, differently reused powders, parts using new powders, and parts printed using differently reused powders. Through TGA, we measured the sample mass over time as the temperature changes from 20 °C to 800 °C at a heating rate of 10 °C/min, under both air atmosphere and nitrogen blanketing.

We used Differential Scanning Calorimetry (DSC) test on a TA Instrument DSC Q100 to examine the melting and crystallization behaviors of both powder and part samples (heating and cooling cycles between room temperatures and 225 °C, at a rate of 10 °C/min and under a nitrogen atmosphere).

5.2.2.3 Material molecular evolution

We carried out Nuclear Magnetic Resonance (NMR) tests to obtain the molecular evolution of both powder and part samples with successive reuse, by measuring the interactions between nuclear spins and materials placed in a strong magnetic field. The samples were prepared by dissolving 20 mg of each material into a 50 uL of HFIP / 550 uL of CDCl3 mixture. We acquired ^{1}H NMR spectra of each sample using a Bruker AV400 NMR spectrometer at 40 °C.

5.2.2.4 Material surface elemental composition and surface morphology

Apart from the previous tests, we performed X-ray Photoelectron Spectroscopy (XPS) for both powder and part samples to evaluate the elemental composition and the chemical states of surface atoms. To evaluate the variations in micro surface morphologies, we carried out Scanning Electron Microscope (SEM) tests for both reused powder and part samples. The material samples were drop-dispersed onto adhesive pads on aluminum mounts and coated with 3 nm gold to eliminate electrostatic charging. A JEOL JSM-7200FLV FESEM performed the analysis using LED detectors at a 5 kV accelerating voltage.

5.2.2.5 Density and mechanical property of SLS 3D-printed parts

We conducted density measurement and tensile tests on the 3D-printed tensile bars to identify the quantitative changes with successive reuse. We calculated sample density through the corresponding weight (measured using analytical balance) and volume (measured using vernier caliper). We tested all specimens at ambient conditions using the MTS Alliance RT/10 test frame, 1,000 N load cell, and wedge action metal grips. During the test, the initial grip separation was 25.4 mm, and testing speed was 10.0 mm/min until specimen failure. We tested replicates for each kind of sample.

5.3 Results and discussions

5.3.1 SLS printing results

We successfully reused the same bucket of polyamide 12 powders for an impressive record of eight times. The tensile strength using 8-time reused powders decreased by 35% compared to that of the new tensile bars (we will introduce the details in section 5.3.2.5). After the printing experiments, we collected powder samples (from new powders to eight-time reused powders), 3-layer part samples (from parts 3D-printed with new powders to parts 3D-printed with eight-time reused powders), and 32-layer part samples (from parts 3D-printed using new powders to parts 3D-printed using eight-time reused powders) for different characterizations. Figure 5-2 presents pictures of 3D-printed specimens with no apparent visual differences.

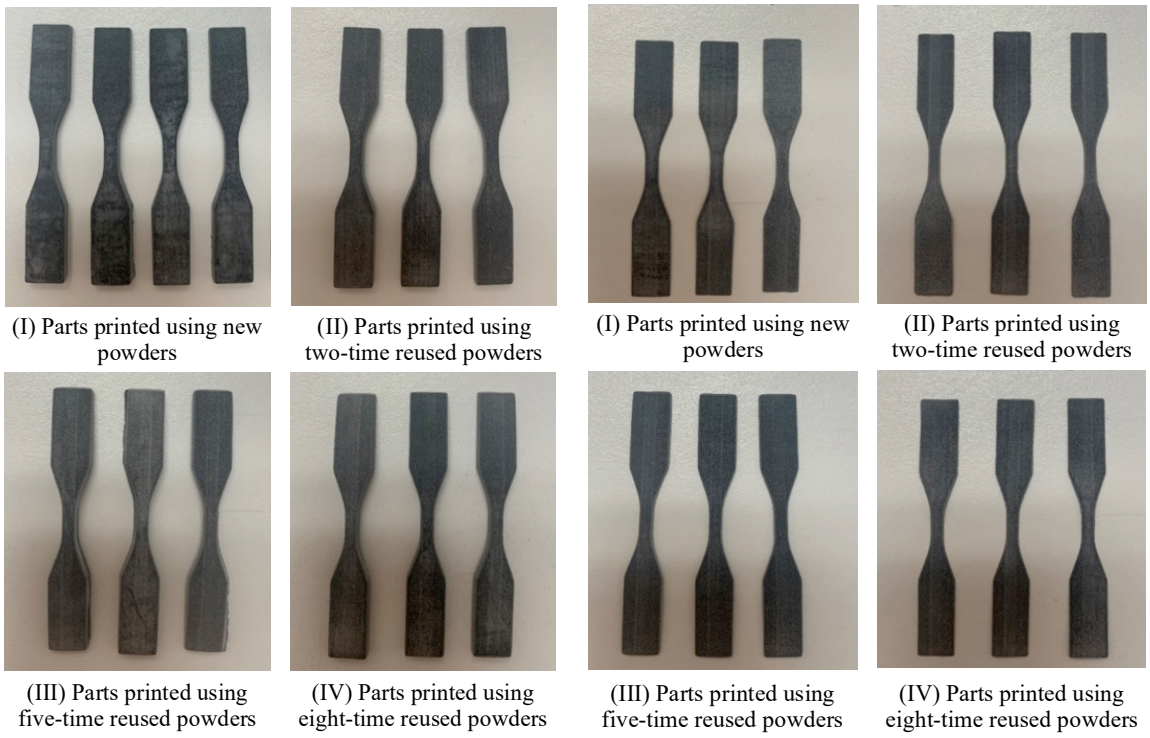

(a) 32-layer part samples (b) 3-layer part samples

Figure 5-2 Samples of parts 3D-printed from the surveyed list of polyamide 12 materials in this research

5.3.2 Characterizations

5.3.2.1 Effects of successive reuse on powder flowability and particle size distribution

Figure 5-3 compares the basic flowability energy between powder samples (we tested each sample 7 times). The average basic flowability energies of new powders, 2-time, 5-time, and 8-time reused powders are 924, 905, 846, and 822 mJ, respectively, decreasing after each reuse (Figure 5-3b). The results indicate the decreased energy needed to flow. Compared to new powders, the basic flowability energy of 2-time, 5-time, and 8-time reused powders decreased by

2.14%, 8.43%, and 11.03%, respectively. The decreased basic flowability energies per reuse calculated from 2-time, 5-time, and 8-time reused powders are 9.90, 15.59, and 12.74 mJ, respectively. These values are essential to control or optimize the flowability of polyamide 12 in SLS. The improved flowability can be attributed to the successive pre-heating and sintering cycles during reuse. These cycles can accelerate the evaporation of the remaining alcohol and moisture in powders or partially melt the particles to form a more spherical shape, resulting in decreased flow resistance. The other possible reason for the improved flowability is the reduced particle-particle cohesion and interlockings.

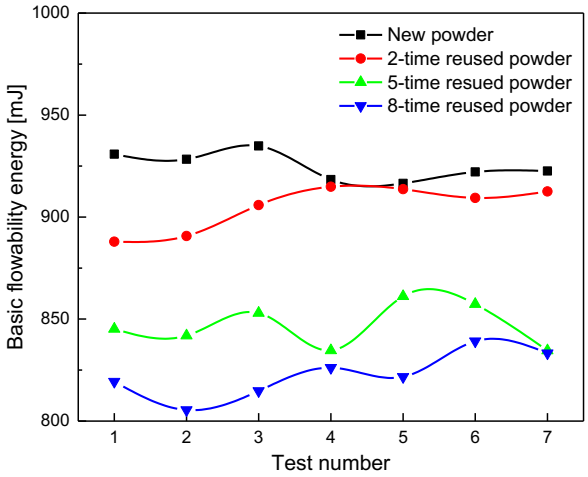

(a) Basic flowability energies of powder samples

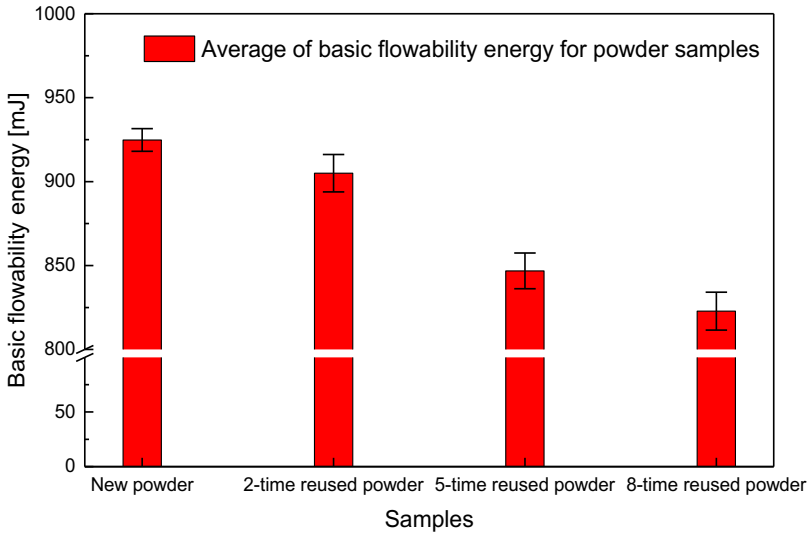

(b) Average of sample basic flowability energies

Figure 5-3 Identified differences of the basic flowability energies between powder samples

Next, we compare particle size distributions of polyamide 12 powder samples in Figure 5-4a (new powder), Figure 5-4b (two-time reused powder), Figure 5-4c (five-time reused powder), and Figure 5-4d (eight-time reused powder). In all figures, particles with a diameter of 45.00 μm were dominant in percentage. The percentages of particles with diameters larger than 45.00 μm were (i) 32.78% in Figure 5-4a, (ii) 33.49% in Figure 5-4b, (iii) 33.90% in Figure 5-4c and (iv) 34.74% in Figure 5-4d. The volume-weighted mean diameters of samples in Figure 5-4 (a)-(d) are respectively 41.476, 41.672, 41.787, and 42.022 μm. Thus, successive reuse of the polyamide 12 materials led to a minor increase in particle sizes due to the powder bed temperature being held near but below the material melting temperature for processability.

(a) Polyamide 12 new powder

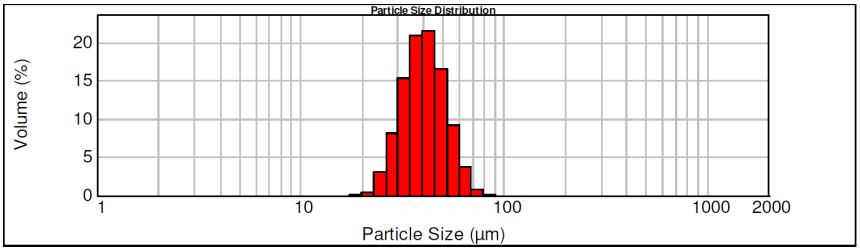

(b) Polyamide 12 two-time reused powder

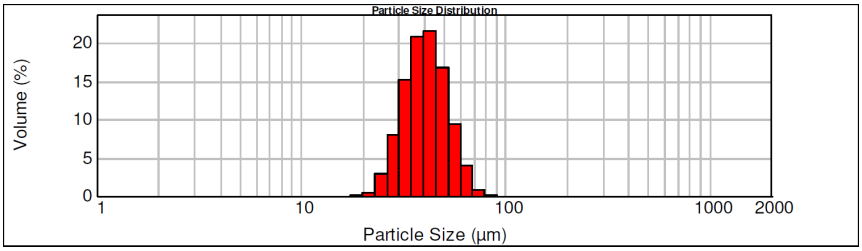

(c) Polyamide 12 five-time reused powder

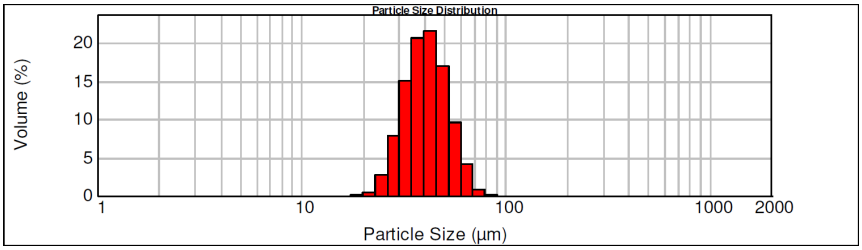

(d) Polyamide 12 eight-time reused powder

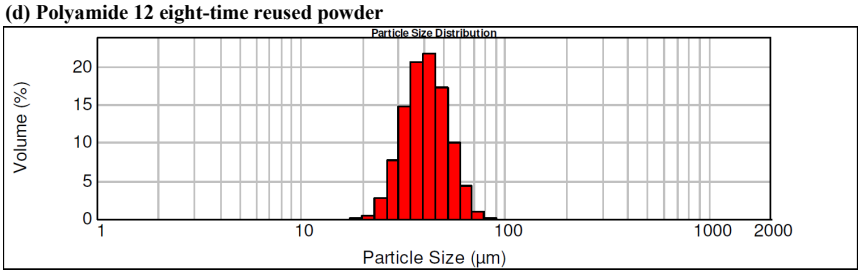

Figure 5-4 Observed differences of particle size distributions between different reclaimed powder samples in this research

5.3.2.2 Effects of successive reuse on material thermal decomposition, melting and crystallization behaviors

Figure 5-5 shows the TGA results of polyamide 12 samples in the air (Figure 5-5a), and in nitrogen (Figure 5-5b). We derive the onset decomposition temperatures, the signal change percentages, the peak change temperatures, and residue percentages from Figure 5-5, and list the data in Table 5-2. For the results obtained in the air atmosphere (Table 5-2a), the onset decomposition temperatures of powder samples exhibit minor changes with reusing, while those of part samples decrease mildly from the new SLS part (417.05 °C) to part 3D-printed using 8-time reused powders (412.88 °C). The average onset decomposition temperatures of part samples (around 415 °C) decreased more substantially in contrast to the powder samples (around 427 °C), while the average residue percentages increased. During TGA in the air, oxygen accelerates the degradation rates, lowering the onset decomposition temperature [126]. In addition, the onset decomposition temperature decreases more in laser-sintered samples. This is because laser sintering accelerates the decomposition of the long-chain backbone of polyamide 12, accelerating macrostructure chain changes (e.g., cross-linking or scission) during TGA and further lowering the onset decomposition temperatures.

When conducting TGA in the nitrogen atmosphere (Table 5-2b), the average residue percentages slightly increased from powder samples to part samples. The average onset decomposition temperatures of part samples (around 425 °C) were close to the powder samples (around 429 °C). The onset decomposition temperatures of part samples in nitrogen (around 425 °C) were larger than that in the air (around 415 °C). The onset decomposition temperatures of powder samples with different reuse times exhibited similar trends compared to powder samples tested in air, while those of part samples decreased mildly from the new SLS part (430.33 °C) to part 3D printed using 8-time reused powders (420.81 °C). During TGA in nitrogen, the degradation rates and long-chain backbone of polyamide 12 are more stable than in air and less affected by heat and laser. The larger percentages of powder and part residues than in air further verify the fact. Consequently, the nitrogen atmosphere is necessary for SLS and is significant for keeping materials stable for long-term applications. These identified data will be essential for controlling the stable states of polyamide 12 during processing in SLS.

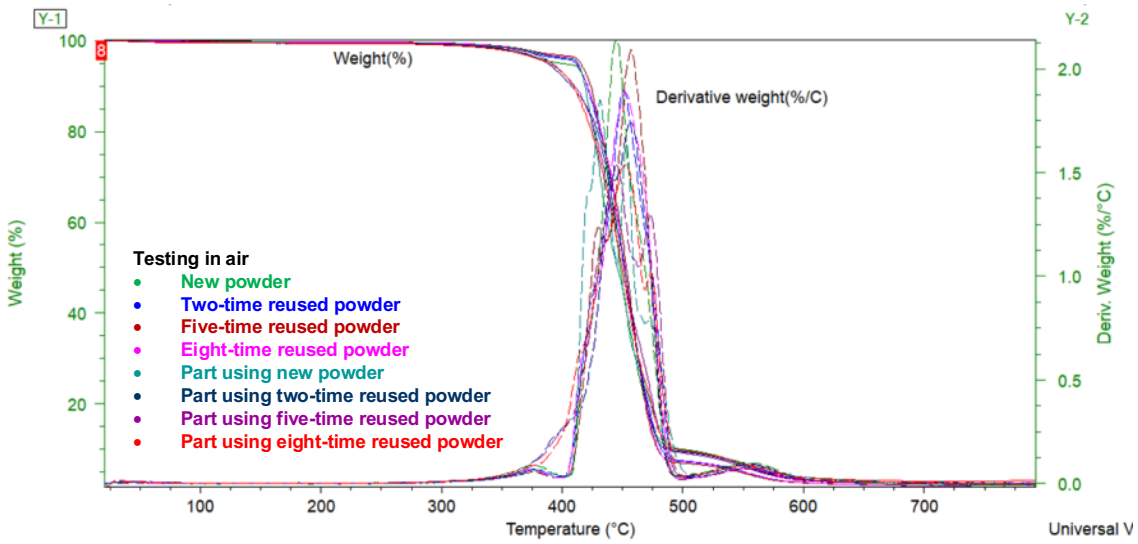

(a) TGA in air

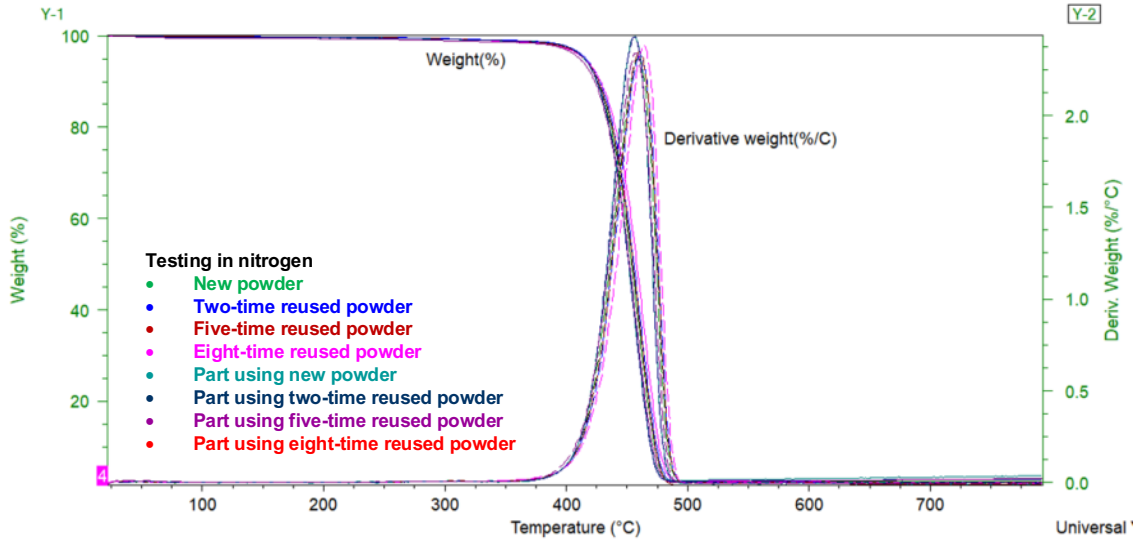

(b) TGA in nitrogen

Figure 5-5 Observed differences of TGA curves between polyamide 12 samples in the air (a) and nitrogen (b)

Table 5-2 Identified differences of thermal decompositions between polyamide 12 samples in this study

(a) TGA in air

	Powder samples				
20-800 °C		Onset T/°C	Signal change/%	Peak change at T/°C	Residue/%
	New in air	427.30	97.66	444.79	2.05
	Two-time reused in air	428.09	97.84	451.25	1.749

	Five-time reused in air	427.91	97.92	456.9	1.724
	Eight-time reused in air	427.43	97.92	452.06	1.739
	Part samples				
		Onset T/°C	Signal change/%	Peak change at T/°C	Residue/%
	New in air	417.05	97.18	431.05	2.568
	Two-time reused in air	417.77	97.38	456.81	2.554
	Five-time reused in air	414.14	97.1	444.8	2.552
	Eight-time reused in air	412.88	97.01	452.83	2.976

(b) TGA in nitrogen

20-800 °C	Powder samples				
		Onset T/°C	Signal change/%	Peak change at T/°C	Residue/ %
	New in nitrogen	429.89	97.38	459.32	2.467
	Two-time reused in nitrogen	430.73	97.53	460.93	2.292
	Five-time reused in nitrogen	429.01	98.07	456.9	1.717
	Eight-time reused in nitrogen	431	97.68	463.36	2.133
	Part samples				
		Onset T/°C	Signal change/%	Peak change at T/°C	Residue/ %
	New in nitrogen	430.33	96.58	456.9	3.494
	Two-time reused in nitrogen	427.23	97.08	456.09	2.834
	Five-time reused in nitrogen	424.45	96.76	456.68	2.989
	Eight-time reused in nitrogen	420.81	96.88	454.76	3.016

Figure 5-6 exhibits the melting behaviors of the grey polyamide 12 samples in the first heating cycle. The DSC curves exhibit apparent differences between the powder and the part samples. Only one melting peak is observed in curves of the powder samples, suggesting there is only one spherulite structure in the powder samples. However, two melting peaks present in curves of the part samples, an indicator that the part samples contain two spherulite structures, including spherulite chains and high-melting-point spherulite cores. In reference [24], the authors reported two melting peaks in SLS parts, and verified the different melting points of spherulite chains and spherulite cores using hot stage microscopy.

We derive the onset melting temperature, peak melting temperature, melting enthalpy, and glass transition temperature of the polyamide 12 samples from Figure 5-6, and summarize the data in Table 5-3. Due to the laser radiations and the repeated heating/cooling cycles in the reuse process, the melting behaviors of reused powders and the corresponding SLS parts change significantly compared to the new samples. In Table 5-3a, the onset melting temperatures of powder samples increase by 1.89 °C from new to eight-time reused powders. The peak melting temperatures of powder samples show minor changes. The melting enthalpies and glass transition temperatures of powder samples both decrease noticeably. In Table 5-3b, however, the onset melting temperatures of part samples decrease by 2.84 °C with reusing. The peak melting temperatures and melting enthalpies of part samples increased respectively by 2.86 °C and 19.86% after 8 times of reuse. Moreover, the glass transition temperatures of part samples decrease by 1.06 °C after reuse. Compared to Table 5-3a, the melting enthalpies and glass transition temperatures of part samples in Table 5-3b decrease largely.

The decreased melting enthalpy for part samples indicate decreased energy needed to form the molten phase and decreased internal cohesion. Under the same temperature and pressure conditions, in addition to molecular weights, the internal cohesion of material influence intermolecular forces [127]. After laser irradiation and repeated heating-cooling cycles, materials are more prone to decreased internal cohesion, reduced intermolecular forces and molecular weight, leading to decreased melting enthalpy. The material glass transition temperature mainly depends on molecular weight [128], intermolecular force [129], and chemical-chain flexibility [130].

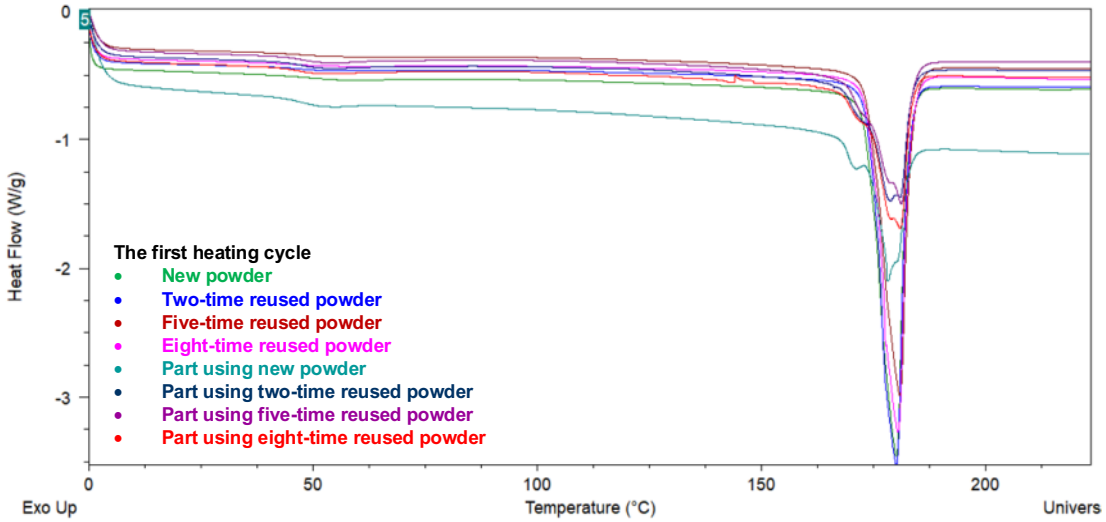

Figure 5-6 Obtained differences of melting curves between polyamide 12 samples - The first heating cycle

Table 5-3 Identified differences in melting behaviors of polyamide 12 samples in the first heating cycle in this study

(a) Powder samples

Sample	The first heating cycle			
	Onset melting temperature/°C	Peak melting temperature/°C	Melting enthalpy/J·g^{-1}	Glass transition temperature/°C
New powder	173.72	180.15	108.80	55.06
Two times reused powder	174.72	180.13	107.10	53.86
Five times reused powder	174.13	180.87	98.17	48.85
Eight times reused powder	175.61	180.49	99.94	47.36

(b) Part samples

Sample	First heating cycle			
	Onset melting temperature/°C	Peak melting temperature/°C	Melting enthalpy/J·g^{-1}	Glass transition temperature/°C
Part using new powder	176.37	178.11	44.30	47.55
Part using two-time reused powder	172.95	178.86	48.86	47.58
Part using five-time reused powder	172.54	181.19	50.57	47.28
Part using eight-time reused powder	173.53	180.97	53.10	46.49

Figure 5-7 shows the crystallization behaviors of polyamide 12 samples in the cooling cycle, exhibiting similar shapes for all samples. Table 5-4 summarizes the derived sample onset crystallization temperature, peak crystallization temperature, and crystallization enthalpy. As the data shows, the onset and peak crystallization temperatures of the powders and the parts remain nearly unchanged after reuse. However, the crystallization enthalpies respectively decrease by 7.19% and 6.85% after 8 times of reuse in powder and part samples. Furthermore, the onset crystallization temperatures, peak crystallization temperatures, and crystallization enthalpies of the printed parts are slightly smaller than those of the powder samples. The decreases in crystallinity degree and crystal size may reduce the crystallization enthalpies [131]. Compared to powders, the weaker nucleating effects in laser-sintered part samples result in the lower onset and peak crystallization temperatures [132].

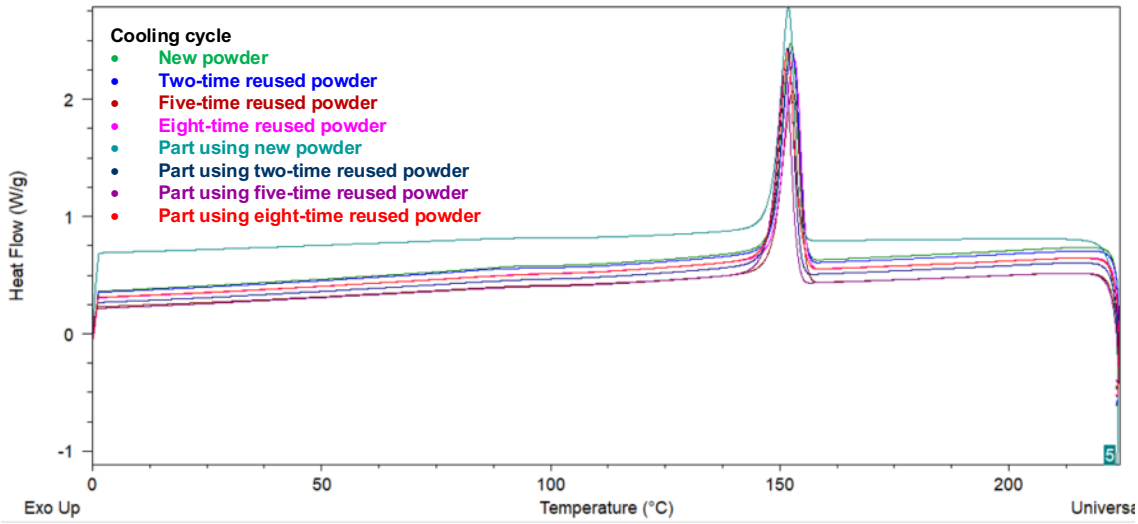

Figure 5-7 Observed differences of crystallization curves between polyamide 12 samples - The cooling cycle

Table 5-4 Analyzed differences of crystallization behaviors between polyamide 12 samples in the cooling cycle in this study

(a) Powder samples

Sample	Cooling cycle		
	Onset crystallization temperature/°C	Peak crystallization temperature/°C	Crystallization enthalpy/J·g^{-1}
New powder	155.46	152.40	54.39
Two times reused powder	155.63	152.56	54.36
Five times reused powder	155.67	152.83	51.40
Eight times reused powder	155.78	153.07	50.48

(b) Part samples

Sample	Cooling cycle		
	Onset crystallization temperature/°C	Peak crystallization temperature/°C	Crystallization enthalpy/J·g^{-1}
Part using new powder	154.26	151.90	51.37
Part using two-time reused powder	154.26	151.73	49.42
Part using five-time reused powder	153.80	151.15	47.52
Part using eight-time reused powder	154.58	151.67	47.85

Figure 5-8 lists the melting behaviors of the studied polyamide 12 samples in the second heating cycle. All curves exhibit similar shapes with two melting peaks observed. Table 5-5 summarizes the sample onset and peak melting temperatures in the first and second melting peaks, and the total melting enthalpies. Although the total melting enthalpies decreased for both powder and part samples, we find no apparent changes for the onset and peak melting temperatures of samples in the two melting peaks. Molecular symmetry primarily controls the melting temperatures of material over the intermolecular forces [133]. Though reuse lowers the intermolecular forces, the molecular symmetry tends to remain unchanged for both powder and part samples during the second heating cycle.

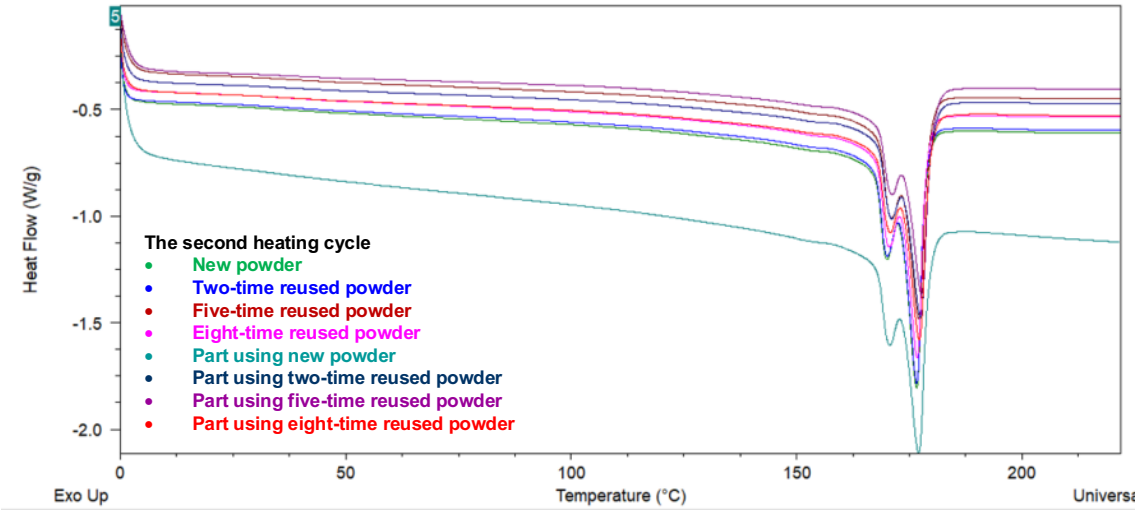

Figure 5-8 Observed differences in melting curves between polyamide 12 samples - The second heating cycle

Table 5-5 Identified differences of melting behaviors between polyamide 12 samples in the second heating cycle in this study

(a) Powder samples

Sample	The second heating cycle				
	The first melting peak		The second melting peak		Total melting enthalpy /J·g^{-1}
	Onset melting temperature 1/°C	Peak melting temperature 1/°C	Onset melting temperature 2/°C	Peak melting temperature 2/°C	
New powder	168.22	169.89	172.06	176.65	44.12
Two times reused powder	168.33	169.94	172.08	176.64	42.29
Five times reused powder	169.01	170.73	172.34	177.16	38.06

Eight times reused powder	168.75	170.34	172.20	176.71	39.74

(b) Part samples

Sample	The second heating cycle				
	The first melting peak		The second melting peak		Total melting enthalpy /J·g^{-1}
	Onset melting temperature /°C	Peak melting temperature /°C	Onset melting temperature /°C	Peak melting temperature /°C	
Part using new powder	168.71	170.40	172.46	177.09	38.13
Part using two-time reused powder	169.00	170.87	172.62	177.45	39.12
Part using five-time reused powder	168.91	170.96	172.73	177.71	33.86
Part using eight-time reused powder	168.47	170.46	172.52	177.22	34.99

5.3.2.3 Effects of successive reuse on material molecular evolution

Figure 5-9 shows the ^{1}H NMR spectra of polyamide 12: the normal curve in subfigure (a), and then the identified results for materials in this study in subfigure (b). In Figure 5-9a, the following peaks relate to different microstructures [33, 134]:

- peak #1 (5.80 ppm), N-H bond;
- peak #3 (2.20 ppm), C-H bond adjacent to carbon and oxygen double bond;
- peak #4-12 (1.55 ppm), hydrocarbon chain;
- peak #13 (3.23 ppm), C-H bond adjacent to nitrogen.

It has been verified that oxidation reactions mainly occur on the weakest C-H bonds located on the carbon atoms close to the nitrogen atoms [33, 134]. Below, we analyze in detail the changes of the peak #13 to explore the molecular evolution of polyamide 12 with reuse in SLS.

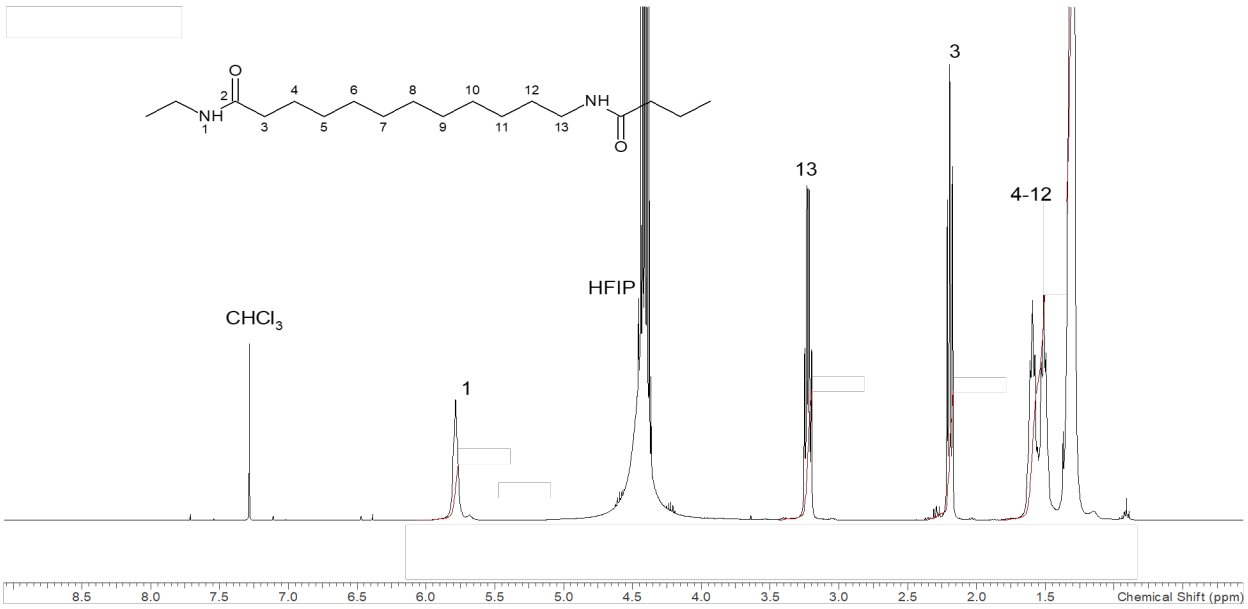

(a) The general ^{1}H NMR peaks of polyamide 12

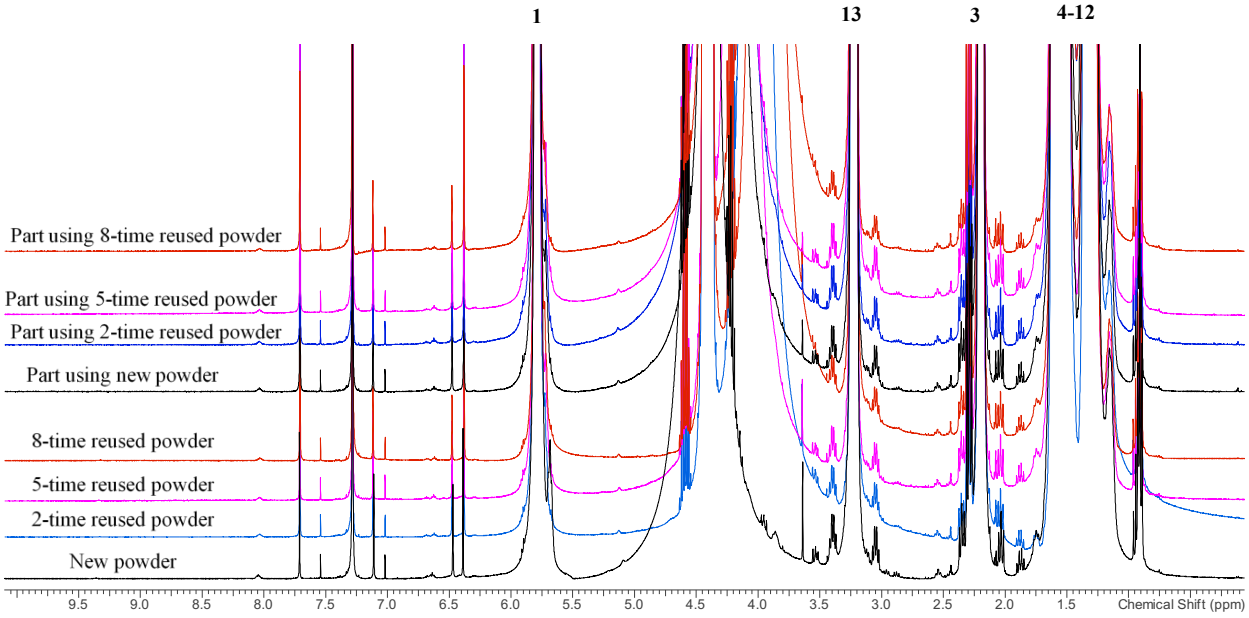

(b) ^{1}H NMR spectra of polyamide 12 powders and printed parts

Figure 5-9 Identified differences of ^{1}H NMR (a) general peaks of polyamide 12, and (b) spectra of polyamide 12 powders and printed parts in this research

After each material reuse in Figure 5-9b, the bandwidth of Peak #13 decreased. We took out the NMR spectra of new powders and part 3D printed using eight-time reused powders, and calculated the areas of the structure-based peaks, as shown in Figure 5-10. The relative area of peak #13 in Figure 5-10b has a 50 % reduction compared to that of new powders in Figure 5-10a, indicating the disappearances of C-H bonds adjacent to nitrogen with material reuse. The carbon

adjacent to nitrogen in peak #13 is easy to be oxidized during heat and laser atmosphere. Initiated by dehydrogenation, the oxidation reactions propagate to form peroxides [33, 134]. In the termination stage, another carbon and oxygen double bond [24] forms, accompanied by the cross-linking and scission of molecular chains [19], and removing the C-H bonds adjacent to nitrogen.

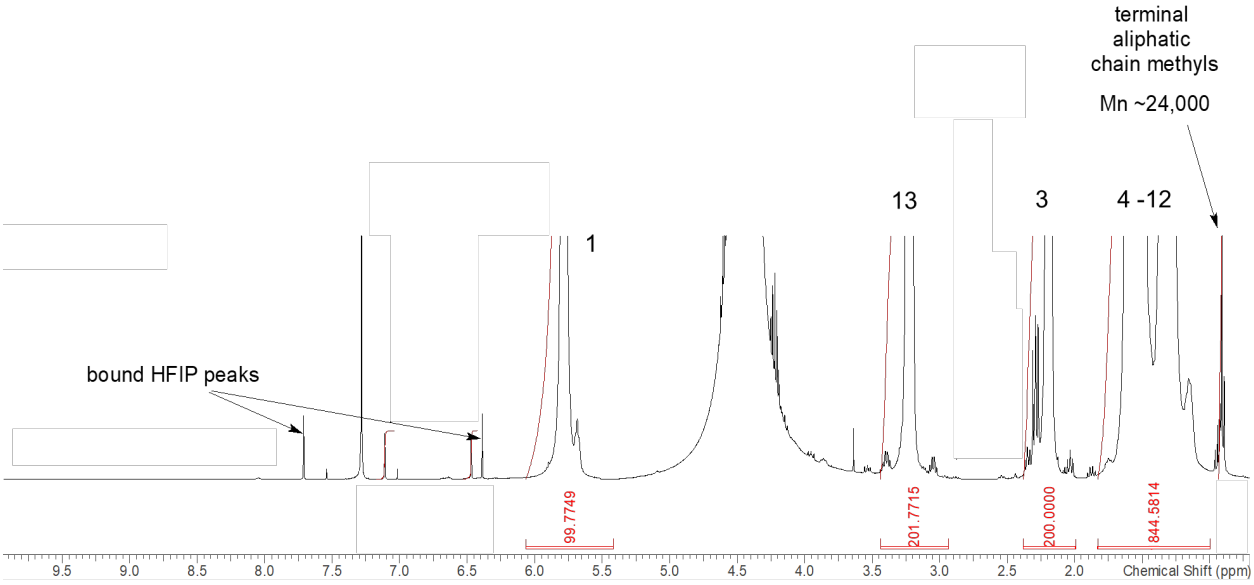

(a) ^{1}H NMR spectra of polyamide 12 new powders

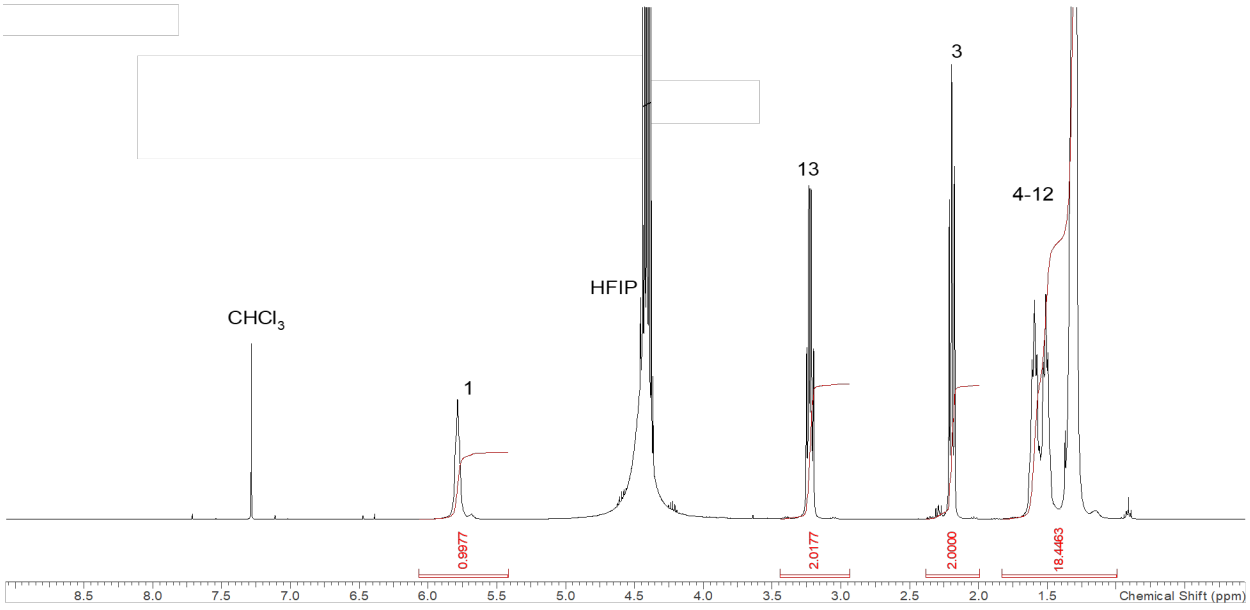

(b) ^{1}H NMR spectra of polyamide 12 part 3D printed using 8-time reused powders

Figure 5-10 Analyzed differences of ^{1}H NMR spectra comparisons of polyamide 12 (a) new powders, and (b) part 3D printed using 8-time reused powders in this study

5.3.2.4 Effects of successive reuse on the material surface chemical state, elemental composition, and surface morphology

Figure 5-11 exhibits the XPS results of polyamide 12 powder and part samples with successive reuse. The results present material surface chemical states and elemental compositions.

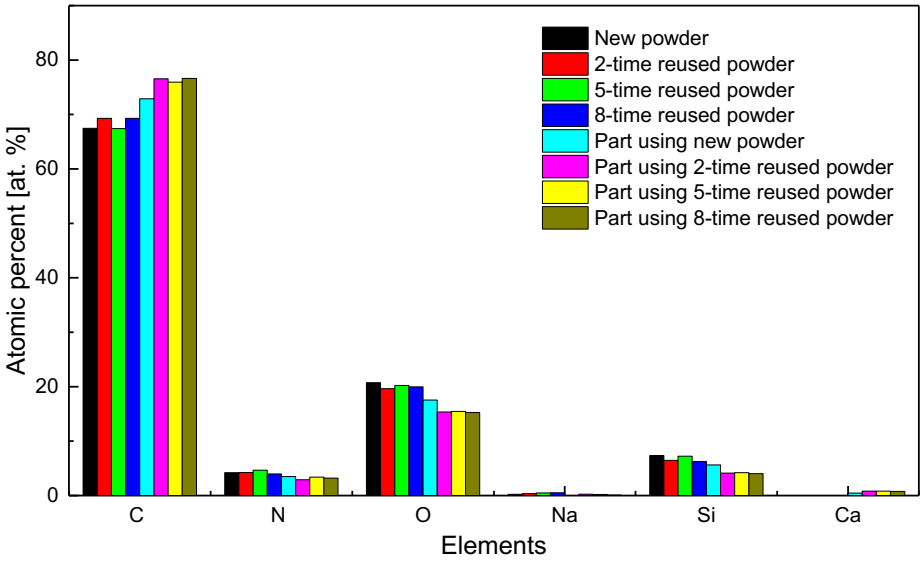

Figure 5-11 Obtained differences of elemental atomic percentage between polyamide 12 with different reuse times in this study

With a melting temperature of around 1700 °C, SiO_2 is very stable in the SLS process when preheated to 160 °C. Consequently, we took the amount of the SiO_2 as a reference to compare the content of the other elements in powder and part samples. In Figure 5-11, the content of Na and Ca is minimal, and not summarized in Table 5-6. As the tested polyamide 12 got reused and reprinted, the atomic percentages of C and O increase by 72.49% and 7.13%, respectively, while the amount of N showed a minor increase. The increase of C comes from the polyamide 12 decomposition and surface carbon deposition when subject to high temperatures and laser irradiation. Carbon deposition, also known as pyrolytic carbon, is a phenomenon where hydrocarbons (polyamide 12 in this work) crack or degrade when subject to high thermo energy, resulting in deposited C-precursors [126]. The surface carbon deposition of polyamide 12 is newly found during SLS successive processing, indicating that apart from high temperature, laser irradiation is the other factor to induce polymer decomposition. The increase of O results from the thermal-oxidative reactions.

Table 5-6 Identified differences of elemental compositions between polyamide 12 samples

(a) Powder samples

Sample	Total	C (at%)	N (at%)	O (at%)	Si (at%)
New powder	100	67.46	4.21	20.74	7.36
Two-time reused powder	113.5802	78.71	4.80	22.29	7.36
Five-time reused powder	101.6575	68.52	4.73	20.54	7.36
Eight-time reused powder	117.3844	81.34	4.66	23.43	7.36

(b) Part samples

Sample	Total	C (at%)	N (at%)	O (at%)	Si (at%)
Part using new powders	130.9609	95.44	4.58	22.97	7.36
Part using two-time reused powder	178.6408	136.76	5.18	27.42	7.36
Part using five-time reused powder	175.6563	133.39	5.95	27.15	7.36
Part using eight-time reused powder	182.6303	139.94	5.88	27.86	7.36

At a magnification ratio of 500, Figure 5-12 and Figure 5-13 show the SEM images of polyamide 12 powder and part samples, respectively. The different materials turn out to have similar surface morphology. The reason is that compared to higher-throughput machines, the SLS machine used is equipped with a lower laser power rating, and thus did not change significantly the surface morphologies of the materials.

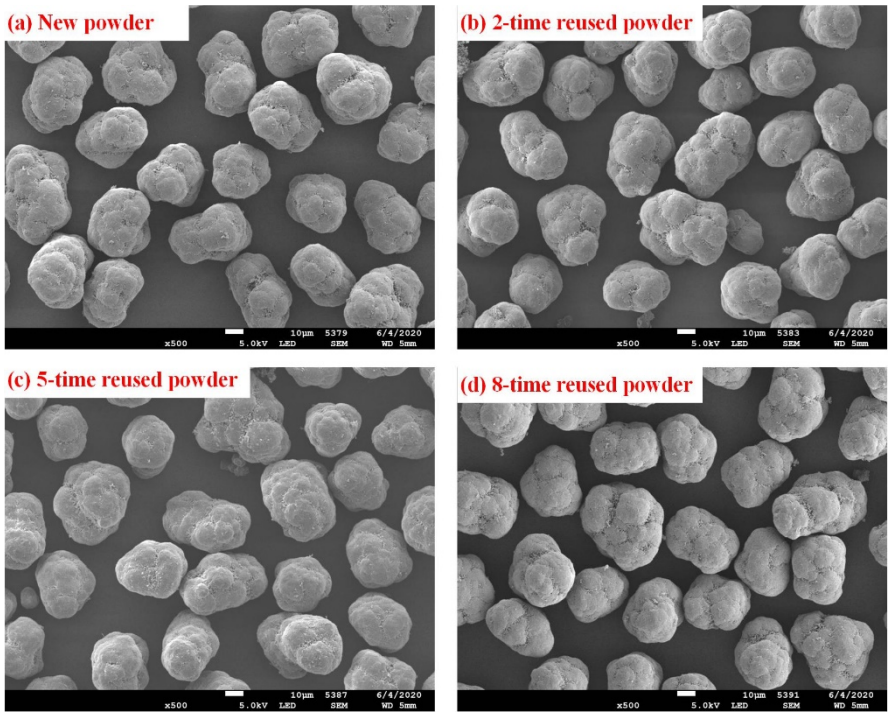

Figure 5-12 SEM images of polyamide 12 powder samples at a magnification ratio of 500 for new and three classes of reused powders

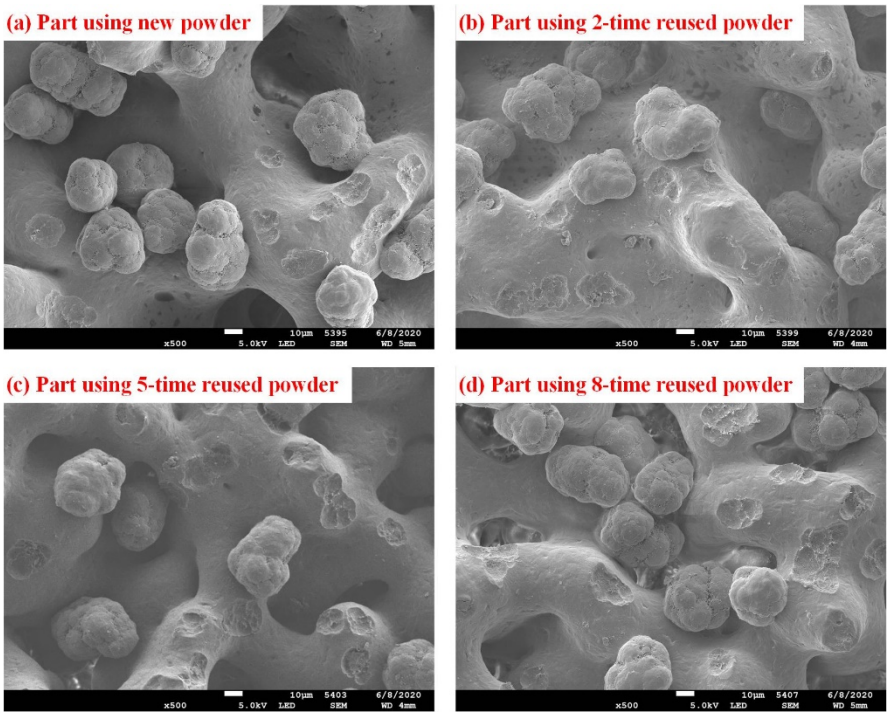

Figure 5-13 Obtained SEM images of polyamide 12 part samples at a magnification ratio of 500 for parts using new and three classes of reused powders

5.3.2.5 Effects of successive reuse on the density and mechanical properties of SLS parts

Microstructure evolution (at different temperatures and pressures) and the type of material in sintering affect material density [135]. At a specific temperature and pressure, uniformly sized particles tend to form parts with high density. Through analyzing the particle size distributions, successive reuse of polyamide 12 leads to slightly increased particle sizes and decreased part density. Figure 5-14 compares the density of tensile bars printed using differently reused polyamide 12 powders. The columns with different colors in the graph represent tensile bars printed using differently reused powders, and as the data shows, densities of tensile bars decrease with reusing: the average densities of parts printed using new powders, using two-time, five-time, and eight-time reused powders are, respectively, 0.97, 0.91, 0.83, and 0.81 $g \cdot cm^{-3}$.

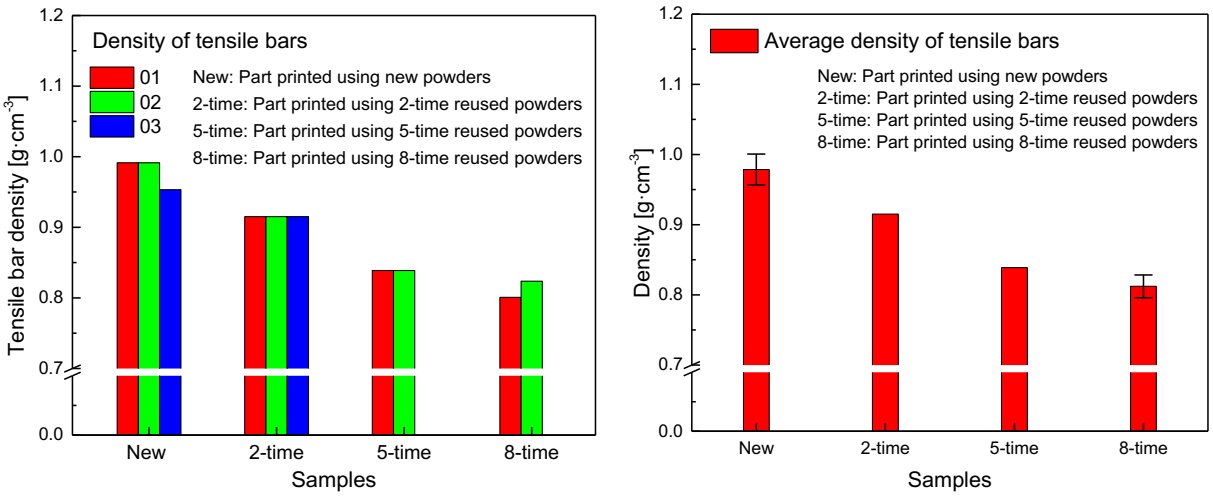

(a) Density of different tensile bars (b) Average density of tensile bars

Figure 5-14 Densities of tensile bars 3D printed using differently reused polyamide 12 powders

Figure 5-15 plots the stress-strain curves of polyamide 12 tensile bars, presenting noticeable differences among these samples. Table 5-7 compares the mechanical properties between these tensile bars. The average tensile strengths, average Young's Modulus, and average percent elongations all decrease after each reuse of materials. Such decreased mechanical properties are understandable from the degraded coalescence of the reused polyamide 12 particles and the weak solidification between layers [46, 117]. However, the results do support the possibility of multiple-layer SLS printing of up to 8 times reused powders at a reasonable material strength.

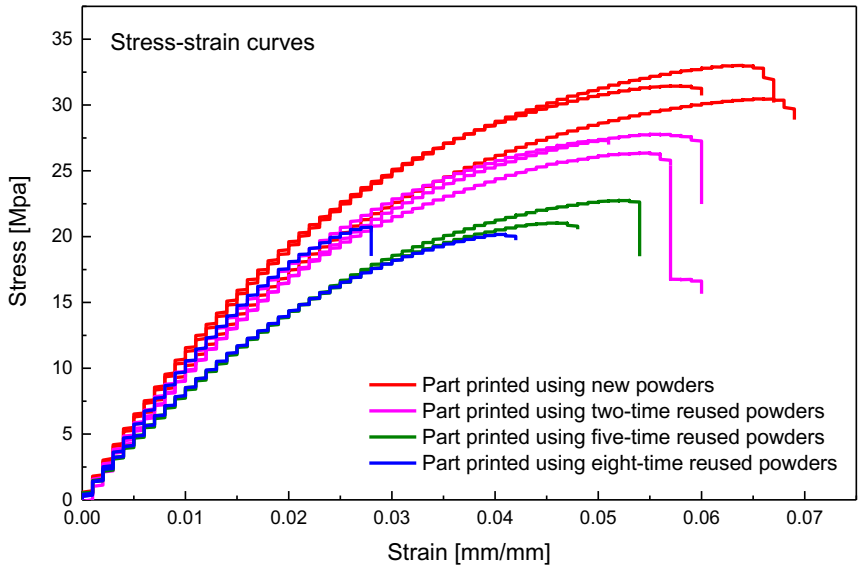

Figure 5-15 Stress-strain curves of polyamide 12 parts

Table 5-7 The comparisons on the mechanical properties of polyamide 12 tensile bars

Sample	Width/mm	Thickness/mm	Tensile strength/Mpa	Young's Modulus/Mpa	Percent elongation/%
Part printed using new powders					
Sample 01	2.78	2.50	31.47	1312	5.77
Sample 02	2.78	2.51	30.47	1197	6.60
Sample 03	2.78	2.50	33.01	1318	6.35
Average	2.78	2.50	31.65	1275.67	6.24
Result ranges	2.78 ± 0	2.50 ± 0.01	31.65 ± 1.36	1275.67 ± 78	6.24 ± 0.47
Standard deviations	0	0.01	1.28	68.19	0.42
Part printed using two-time reused powders					
Sample 01	2.67	2.49	27.35	1231	5.54
Sample 02	2.78	2.48	26.38	1196	5.46
Sample 03	2.75	2.51	27.78	1143	5.54
Average	2.73	2.49	27.17	1190	5.52
Result ranges	2.73 ± 0.06	2.49 ± 0.02	27.17 ± 0.79	1190 ± 47	5.52 ± 0.06
Standard deviations	0.05	0.01	0.72	44.31	0.04
Part printed using five-time reused powders					
Sample 01	2.51	2.54	21.06	990	5.22
Sample 02	2.5	2.54	22.76	979	4.57
Average	2.50	2.54	21.91	984.5	4.89
Result ranges	2.50 ± 0.01	2.54 ± 0	21.91 ± 0.85	984.5 ± 5.5	4.89 ± 0.33
Standard deviations	0	0	1.20	7.78	0.46
Part printed using eight-time reused powders					
Sample 01	2.57	2.52	20.17	995	4.11
Sample 02	2.57	2.5	20.72	1074	4.99
Average	2.57	2.51	20.45	1034.5	4.55
Result ranges	2.57 ± 0	2.51 ± 0.01	20.45 ± 0.28	1034.5 ± 39.5	4.55 ± 0.44
Standard deviations	0	0.01	0.39	55.86	0.62

5.4 Conclusions

This work experimented with successive reuse of polyamide 12 materials in SLS. We reused the same bucket of polyamide 12 powders up to eight times, and quantitatively tested the changes of material flowability, thermal decomposition, molecular evolution, and elemental composition in the material reclaim and reuse. With proper material processing and management, the tested 3D printing successfully produced 3- and 32-layer samples with 8-time reused polyamide 12 powders while retaining more than 65% of the baseline Young's Modulus from fresh powders. The basic

flowability energy of 2-time, 5-time, and 8-time reused powders decreased by 2.14%, 8.43%, and 11.03%, respectively, compared to new powders. These values are essential to control or optimize the flowability of polyamide 12. In the air, heat and laser in SLS were impetus to destabilizing the long-chain backbone of polyamide 12. On the other hand, in the nitrogen atmosphere, the long-chain backbone of polyamide 12 was more stable and less affected by heat and laser. The ^{1}H NMR spectra revealed the disappearances of C-H bonds adjacent to nitrogen caused by degradation. In polyamide 12 parts 3D-printed using 8-time reused powders, the relative area of the peak on C-H bonds adjacent to nitrogen reduced by 50% compared to parts using new powders. From new powders to part printed using 8-time reused powders, the atomic percentages of C and O increased by 72.49% and 7.13%, respectively. Besides, after 8-time of reuse, part density decreased by 16.49%; the averages of part tensile strength, Young's Modulus, and percent elongation respectively decreased by 35.39%, 18.91% and 27.08%.

Chapter 6. PROCESS-ORIENTED AND MASS-TRANSFER BASED METHODOLOGY TO MODEL VOLATILE ORGANIC COMPOUND EMISSION

6.1 Introduction

Additive manufacturing introduces tremendous advantages over the traditional manufacturing approaches and has gained unprecedented industrial and academic attentions [136-138]. Alongside to industrial improvements and academic achievements, the environmental sustainability in additive manufacturing is also crucial and involves various environmental impacts [138-141]. Additive manufacturing sustainability assessment covers energy and material consumption, end-of-life and waste management, gas, liquid, solid, and sound pollution [142]. Air quality is the criterion most relevant to human health. However, 3D printers are generally located in indoor environments, and bring gaseous and ultrafine particle emissions [143]. These emissions adversely impact the indoor air quality, especially for offices with limited ventilation accessories [138, 143, 144].

Since emissions in additive manufacturing are harmful for human health, the evaluation and characterization appear to be critical. Researchers have reported the emissions of volatile organic compounds (VOCs) [137, 138, 145], particulate matter [137, 146], ultrafine particles [147, 148], carbon dioxide [149, 150], and aerosol [151-153] from 3D printers. Particularly, VOCs are a mixture of hydrocarbons, oxygenates, halogenates, released from material phase transition [154]. VOCs dominate in causing sick building syndrome symptoms related with indoor air quality, and the high concentrations may cause cancer, fetal malformations, and mutations/alterations [144, 155]. VOC oxidants cause secondary organic aerosols and are also poisonous [156-158].

Researchers have examined experimentally the effects of 3D printers and materials on VOC emissions. Azimi et al. [159] and Gu et al. [154] respectively quantified emissions and characterized the chemical compositions of VOC using different types of extrusion printers and filaments. Davis et al. [160] investigated a larger range of VOC through 25 combinations of printers and filaments, and evaluated the influences of printer settings on emission characteristics. Ding et al. [161] proposed the formation mechanisms of VOC from an extrusion printer through

the thermogravimetric analysis (TGA) and evolved gas analysis. Damanhuri et al. [149, 150, 162] reported the measurement of VOC emissions in selective laser sintering (SLS) with polyamide 12.

In addition, previous work reported the modelling of VOC emissions with different 3D printing processes. Afshar-Mohajer et al. [137] conducted a real-time measurement of VOC using a binder jetting 3D printer, coupling with a mass balance model. With experimental validation, Yang et al. [138] established an analytic model to evaluate VOC emissions in stereolithography 3D printing. Azimi et al. [163] predicted the magnitudes of environmental exposures and modeled to explore the impacts of control strategies on reducing VOC emission from a desktop 3D printer.

Aa a popular additive manufacturing technique, SLS is capable of translating any laser-absorbent powders into functional components [164, 165]. Building parts through a controlled deposition of layer-by-layer, SLS excels at fabricating objects with complex geometry and good mechanical property [166, 167]. However, the elevated temperature and high-energy laser beam in SLS may cause more detrimental VOC emissions than the other 3D printing. Yet, the modelling and prediction of VOC emission in SLS remain unexploited.

This work proposes a first-instance methodology with process-oriented and mass-transfer based approaches to model and predict VOC emission in SLS with variable printing parameters. We monitor the VOC emissions from polyamide 12 in 6 cases with five printing stages in each case. With emission curve segmentation, we use the mass-transfer based single- and multiple-layer models to simulate the VOC emission, and get the suitable model type and node number in each printing stage. Experimentally measured data verify the accuracy of the obtained model. Furthermore, we analyze the effects of critical parameters (mass-transfer coefficient, diffusion coefficient, and partition coefficient) on VOC emissions.

6.2 Process-oriented and mass-transfer based methodology to model volatile organic compound emission

6.2.1 Experimentation

We use an in-house-built SLS testbed (Figure 6-1a) to conduct the SLS printing experiments and monitor the VOC emissions from polyamide 12 (EOS PA2200). The E Instruments VOC monitor measures the concentration of VOC in space. We position the monitor 0.76 m (30 inches) away from the printer (the laser affected-zone) and at 1.20 m (47 inches) high (Figure 6-1b). Figure 6-1c shows the dimensions of the designed specimen to print. We design the monitoring experiments with 6 cases. Table 6-1 shows the used processing parameter sets in each case. Case

1 is the benchmark case, with preheating temperature: 160 °C, the layer number of sample: 3 layers, layer thickness: 0.15 mm, laser power: 20 W. Comparisons will be done between case 1 and the other cases (case 2 - case 6) to get the influents of printing parameter changing on VOC emissions. In case 2, we change the preheating temperature to 165 °C to check the effects of temperature on VOC emissions compared to case 1. In case 3, we use the sample layer number of 9 layers to check the effects of specimen layer on VOC emissions compared with case 1. Similarly, in cases 4 and 5, we adjust the layer thickness to 0.09 mm and 0.18 mm to check the effects of layer thickness. In case 6, we increase the laser power to 30 W to check the effects of laser power. Scan speed and scan spacing remain unchanged for all 6 cases. Besides, we perform 5 repetitive experiments for each case in Table 6-1.

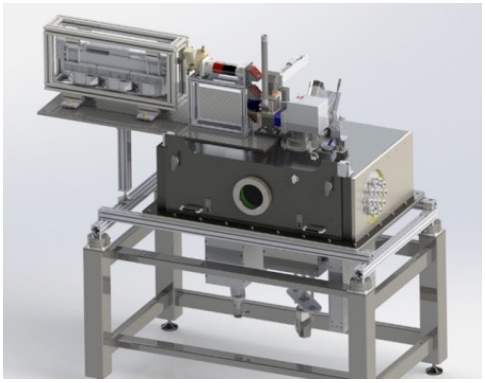

(a) SLS machine

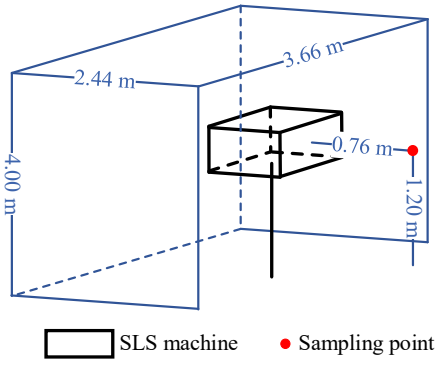

(b) Sampling point setup

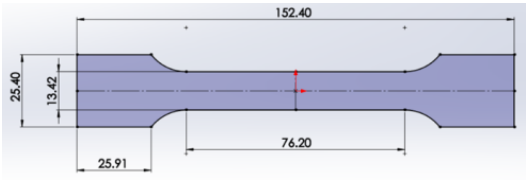

(c) Designed specimen (unit: mm)

Figure 6-1 Experiment setup

Table 6-1 Processing parameter sets in our study

Cases	Preheating temperature - The layer number of sample- Layer thickness - Laser power	Scan speed - Scan spacing
Case 1	160 °C – 3 layer – 0.15 mm – 20 W	3000 mm/s - 0.3 mm
Case 2	165 °C – 3 layer – 0.15 mm – 20 W	
Case 3	160 °C – 9 layer – 0.15 mm – 20 W	
Case 4	160 °C – 3 layer – 0.09 mm – 20 W	
Case 5	160 °C – 3 layer – 0.18 mm – 20 W	
Case 6	160 °C – 3 layer – 0.15 mm – 30 W	

In each printing, we label the start and end time points for background, recoating, preheating, printing, and post-printing stages. The background and post-printing stages both last 30 minutes. The preheating is 11 minutes. The time period of recoating and printing depend on the specific operations.

6.2.2 The proposed approach to model VOC emissions in SLS

6.2.2.1 Emission curve segmentation

Taking 4 of the 5 repetitive experiments in each case, we calculate the average emission and get the accumulated emission-time curve regarding the average emission. Labeling the background, recoating, preheating, printing, and post-printing stages in the accumulated emission-time curves, we obtain the multi-stage accumulated emission-time curve. In each subsection of the curve (5 subsections), we develop a mass-transfer based emission model to simulate the emission and find the suitable model types. Figure 6-2 presents the average emission-time curve and the multi-stage accumulated emission-time curve.

The nature of emission is the mass-transfer based diffusion to distribute uniformly the concentration of chemical species, which are released from material vaporization, sublimation, and degradation. The driving force of diffusion is the kinetic energy caused thermal motion of molecules in random directions. In the multi-stage accumulated emission-time curve in Figure 6-2, the emissions in the background and recoating stages depend mainly on the surrounding environment. In the preheating stage, the chamber temperature increases from room temperature to around 160 °C. The elevated temperature severely increases the energy, thermal motion, and diffusion rate of chemical species from the material surface. The temperature maintains at 160 °C during the printing stage, where the thermal movement of molecules continues, and the diffusion rate shows minor changes compared to that at the end of preheating stage. In the post-printing stage, the previously released chemical species on the material surface continue to diffuse since the chamber temperature is still higher than the room temperature.

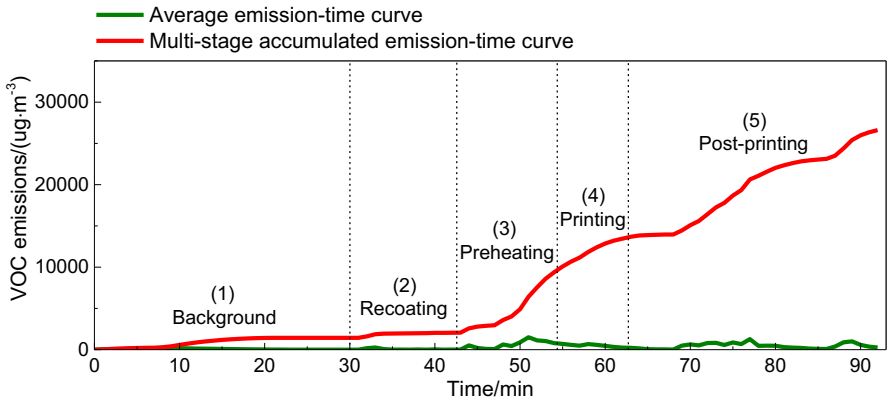

Figure 6-2 Average emission-time curve and multi-stage accumulated emission-time curve

6.2.2.2 Multi-stage modelling

6.2.2.2.1 Mass-transfer based emission model

Eq. (6-1) provides the governing equation of the mass-transfer based emission model. After finite element discretization, the diffusion physics can lead to single- [168] and multiple-layer models [169, 170]. In both models, the bottom surface of the material is impermeable for mass transfer, and we take the VOC concentrations on top layer as the VOC emitted.

$$\frac{\partial C}{\partial t} = D_{\mathrm{m}} \frac{\partial^2 C}{\partial x^2} \tag{6-1}$$

Single-layer model

In the single-layer model, we model the material in the build chamber as a single layer with finite nodes, as shown in Figure 6-3. For the single layer with i nodes (i = 1, 2, 3, …n), we chose node 1 at the bottom surface of the material. The discretized mass transfer function is defined in Eq. (6-2).

$$\frac{1}{2}\Delta x \frac{\mathrm{d}C_1}{\mathrm{d}t} = \frac{D_{\mathrm{m}}}{\Delta x}(C_2\text{-}C_1) \tag{6-2}$$

Here, C_1 and C_2 (unit in ug/m^3) are the emission concentrations at node 1 and 2; Δx (in meters) is the distance between node 1 and 2; D_{m} (in m^2/s) is the diffusion coefficient; t is time in seconds. Δx=L/(n-1), L (in meters) is the thickness of powder in the chamber to be heated.

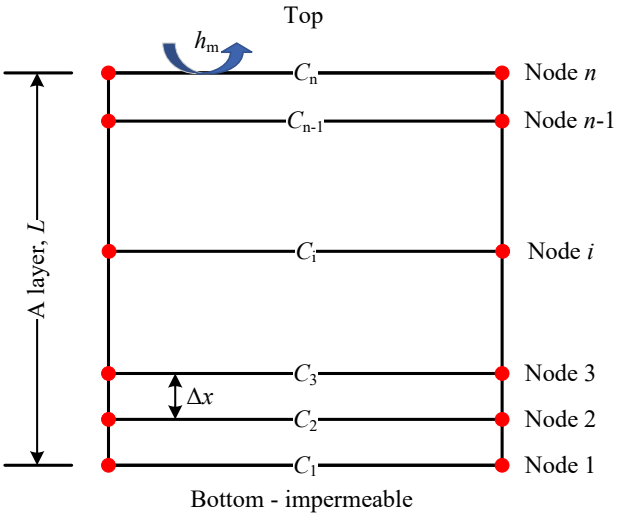

Figure 6-3 Schematic shown of single-layer model

At node i ($2 \le i \le n$-1), the mass transfer occurs in both sides:

$$\Delta x \frac{dC_i}{dt} = \frac{D_m}{\Delta x}(C_{i-1}-C_i) + \frac{D_m}{\Delta x}(C_{i+1}-C_i) \tag{6-3}$$

At node n, the upper side is air. The mass transfer involves both the mass-transfer and the material-air partition coefficients:

$$\frac{1}{2}\Delta x \frac{dC_n}{dt} = \frac{D_m}{\Delta x}(C_{n-1}-C_n) + h_m(C_\infty - \frac{C_n}{K}) \tag{6-4}$$

Finally, the mass balance in the air is described as:

$$\frac{dC_\infty}{dt} = (C_{in}-C_\infty) + \frac{A}{V}h_m(\frac{C_n}{K}-C_\infty) \tag{6-5}$$

Here, h_m is the mass-transfer coefficient, m/s; K is the partition coefficient; C_∞ is the VOC concentration in the air; C_{in} is the VOC concentration from the outside. A is the surface area of the material to be heated, m^2; V is the room volume, m^3.

Multiple-layer model

In the multiple-layer model [168], we regard the material in the build chamber as finite layers (j = 1, 2, 3, …p) with finite nodes (i = 1, 2, 3, …n) inside each layer, as shown in Figure 6-4.

At layer 1 node 1, the discretized mass transfer is

$$\frac{1}{2}\Delta x_1 \frac{dC_{1,1_1}}{dt} = D_{m,1}(\frac{C_{1,2_1}-C_{1,1_1}}{\Delta x_1}) \tag{6-6}$$

Here, $C_{1,1_1}$ and $C_{1,2_1}$ indicate VOC concentrations at layer 1 node 1 and node 2. Δx_1 is the distance between two nodes at layer 1. $D_{m,1}$ means the diffusion coefficient at layer 1, in m^2/s. We assume

the same node number in each layer. $\Delta x_j=L_j/(n\text{-}1)$, where L_j is powder thickness in layer j. Assuming the same thickness for all layers, we have $L_j=L/p$.

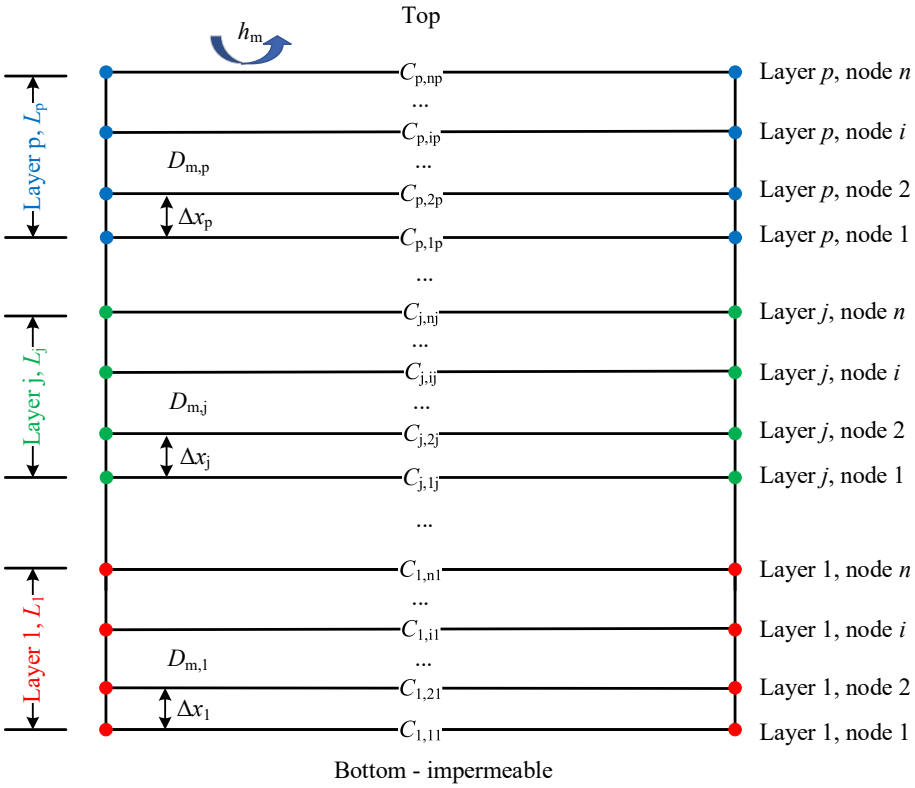

Figure 6-4 Schematic shown of multiple-layer model

At layer j+1, the first node 1 satisfies

$$\frac{1}{2}\Delta x_{j+1}\frac{dC_{j+1,1_{j+1}}}{dt}=D_{m,j}\left[\frac{C_{j,n_j}-(K_j/K_{j+1})C_{j+1,1_{j+1}}}{\Delta x_j/2+\Delta x_{j+1}/2}\right]+D_{m,j+1}\left[\frac{C_{j+1,2_{j+1}}-C_{j+1,1_{j+1}}}{\Delta x_{j+1}}\right] \quad (6\text{-}7)$$

Here, $C_{j+1,1_{j+1}}$ and $C_{j+1,2_{j+1}}$ mean VOC concentration at layer j+1 node 1 and node 2. C_{j,n_j} is the VOC concentration at layer j the last node n. $D_{m,j}$ and $D_{m,j+1}$ are the diffusion coefficient at layer j and j+1, in m^2/s. K_j and K_{j+1} are the partition coefficient at layer j and j+1. Δx_j and Δx_{j+1} are the distances between two nodes at layer j and j+1. We assume $D_{m,j}=D_{m,j+1}=D_m$, and $K_j=K_{j+1}=K$.

At layer j, the last node n satisfies

$$\frac{1}{2}\Delta x_j\frac{dC_{j,n_j}}{dt}=D_{m,j}\frac{C_{j,n\text{-}1_j}-C_{j,n_j}}{\Delta x_j}+D_{m,j+1}\left[\frac{C_{j+1,1_{j+1}}-(K_{j+1}/K_j)C_{j,n_j}}{\Delta x_j/2+\Delta x_{j+1}/2}\right] \quad (6\text{-}8)$$

and

$$\frac{C_{j,n_j}}{K_j} = \frac{C_{j+1,1_{j+1}}}{K_{j+1}} \tag{6-9}$$

$$\frac{1}{2}\Delta x_j \frac{\mathrm{d}C_{j,n_j}}{\mathrm{d}t} = \frac{1}{2}\Delta x_{j+1} \frac{\mathrm{d}C_{j+1,1_{j+1}}}{\mathrm{d}t} \tag{6-10}$$

At the last layer p, in node n we have

$$\frac{1}{2}\Delta x_p \frac{\mathrm{d}C_{p,n_p}}{\mathrm{d}t} = h_{\mathrm{m}}(C_{\infty}\text{-}\frac{C_{p,n_p}}{K_p}) + D_{\mathrm{m},p}(\frac{C_{p,n\text{-}1_p}\text{-}C_{p,n_p}}{\Delta x_p}) \tag{6-11}$$

Besides these boundary layer conditions, at any layer j, node i, we have

$$\Delta x_j \frac{\mathrm{d}C_{j,i_j}}{\mathrm{d}t} = \frac{D_{\mathrm{m},j}}{\Delta x_j}[(C_{j,i\text{-}1_j}\text{-}C_{j,i_j}) + (C_{j,i+1_j}\text{-}C_{j,i_j})] \tag{6-12}$$

Finally, the mass balance in the room satisfies

$$\frac{\mathrm{d}C_{\infty}}{\mathrm{d}t} = (C_{in}\text{-}C_{\infty}) + \frac{A}{V}h_{\mathrm{m}}(\frac{C_{p,n_p}}{K_p}\text{-}C_{\infty}) \tag{6-13}$$

6.2.2.2.2 Multi-stage emission modelling

As introduced in section 6.2.1, we design 6 cases for VOC measurement and comparison. In each case, with the multi-stage accumulated emission-time curve obtained in section 6.2.2.1, we respectively use the single-layer and multi-layer models to find the model type and node number that most fit the VOC emissions experimentally measured in each printing stage. Here we take the VOC concentrations on top layer C_n (single-layer model) or C_{p,n_p} (multiple-layer model) as emitted VOC. Table 6-2 shows the parameters used in multi-stage emission modeling.

Table 6-2 Parameters used in multi-stage emission modeling [168]

Parameter	Value	Unit	Parameter	Value	Unit
D_{m}	7.65×10^{-11}	m^2/s	h_{m}	0.0025	m/s
L	0.06	m	K	3289	-
C_{in}	8	ug/m^3	p	3	-
A	0.072	m^2	V	35.72	m^3

6.2.2.2.3 Prediction with parametric variations

In comparison to case 1, each of the other cases (case 2 – case 6) has one parameter changed. With the multi-stage emission modelling in all cases, we can predict the VOC emissions when time and parameter changes. In each stage of the SLS 3D printing process (e.g., background stage), comparisons between cases 1 and 2 will present VOC emission predictions when the preheating temperature increases from 160 °C to 165 °C. Cases 1 and 3 will compare VOC emission when

the number of 3D printed layers increases from 3 to 9. Cases 1, 4, and 5 will compare VOC emission when the sample layer thickness is between 0.09 mm and 0.18 mm. Cases 1 and 6 will cover VOC emission predictions when the printing laser power is between 20 W and 30 W. We exhibit the VOC emission predictions in all printing stages and cases with parameter changing (preheating temperature: 160 – 165 °C, number of layers: 3 – 9, layer thickness: 0.09 – 0.18 mm, laser power: 20 – 30 W).

6.2.3 The effects of hm, Dm, and K on VOC emissions

Table 6-3 shows the mass-transfer coefficient h_m, diffusion coefficient D_m, and partition coefficient K and the tested variations. According to the chosen model type and node number in subsections of each case, we analyze the effects of h_m, D_m, and K decreasing and increasing on VOC emissions.

Table 6-3 Parameters h_m, D_m, and K decreasing and increasing

Parameter	/100	/10	Original	*10	*100
$h_m/(m \cdot s^{-1})$	0.000025	0.00025	0.0025	0.025	0.25
$D_m/(m^2 \cdot s^{-1})$	7.65E-13	7.65E-12	7.65E-11	7.65E-10	7.65E-09
K	32.89	328.9	3289	32890	328900

6.3 Results and discussions

6.3.1 Using the proposed approach to model VOC emissions in SLS

6.3.1.1 Emission curve segmentation

Figure 6-5 shows the measured VOC emissions in cases 1-6. In each case (e.g., Figure 6-5a), subfigure (i) shows the VOC emissions tested from the experiment. We calculated the average emission of the four experiments and the accumulated emission from the average. Subfigure (ii) shows the average emission-time curve, and the accumulated emission-time curve. a, b, c, d, and e are the divided printing stages: background, recoating, preheating, printing, and post-printing stages. The accumulated section inside each printing stage is the corresponding segmented emission curve to be studied. From Figure 6-5 (a) – (e), it is obvious that most VOC emissions were in preheating, printing, and post-printing stages.

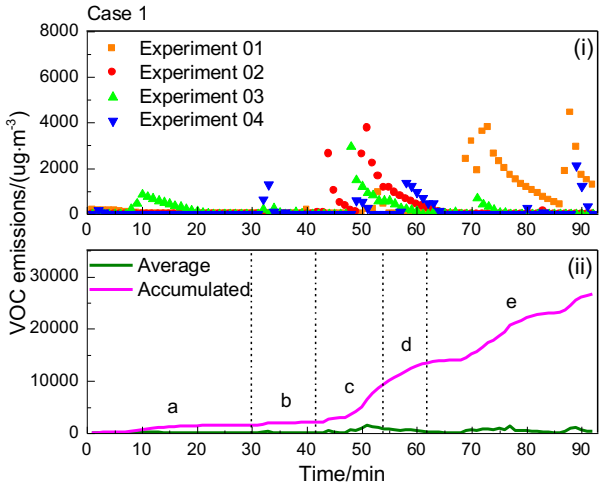

(a) Case 1

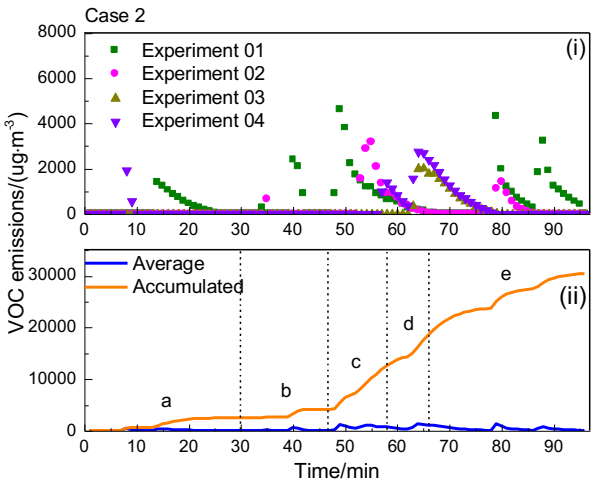

(b) Case 2

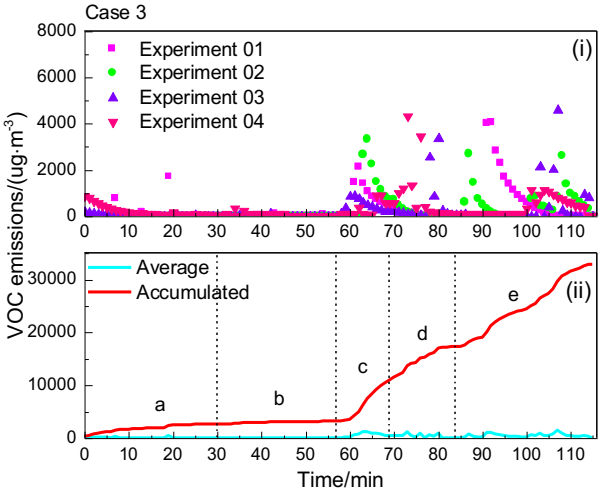

(c) Case 3

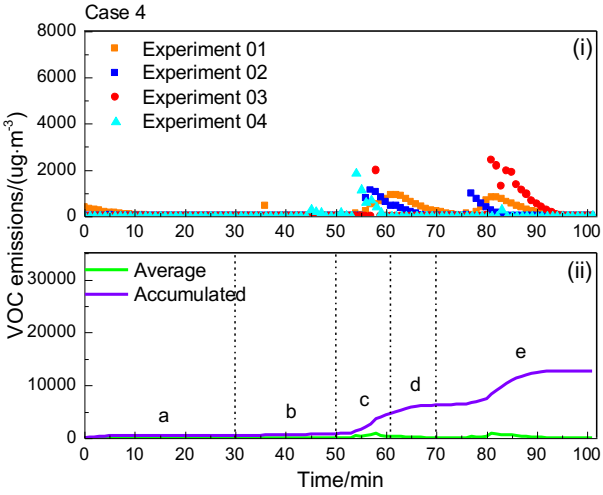

(d) Case 4

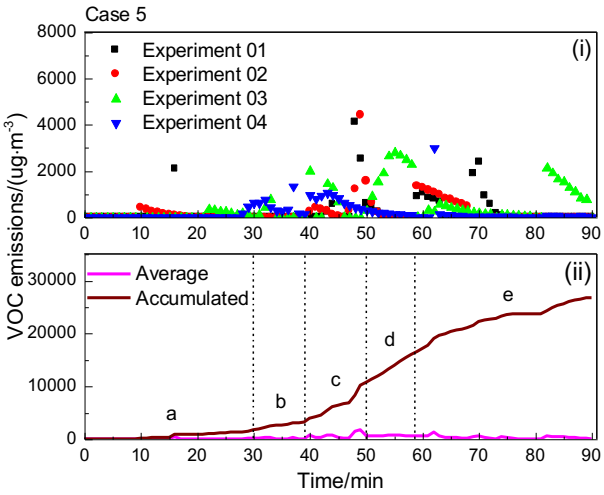

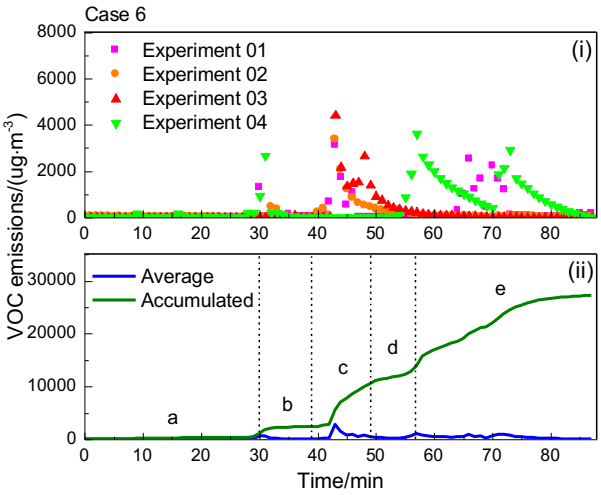

(e) Case 5 (f) Case 6

Figure 6-5 Experimentally tested VOC emissions in cases 1-6 (Stages a, b, c, d, and e are respectively background, recoating, preheating, printing, and post-printing stages.)

6.3.1.2 Multi-stage modelling

Figure 6-6 presents the modelling of VOC emissions in case 1 during different stages. The curve named Experiment is the segmented multi-stage accumulated emission-time curve. S refers to the single-layer model, and M indicates the multiple-layer model. The number following S and M means the node number in the model. In Figure 6-6, the models that most fit case 1 the background, recoating, preheating, printing, and post-printing stages are respectively S-2-node, S-2-node, M-7-node, S-15-node, and S-16-node. As the results show, emissions in background and recoating stages are weak, and single-layer mode with a few nodes are good enough to model the emissions in these stages. Single-layer model with more nodes indicates faster emission rates with time. With the same node number, the multiple-layer model presents the significant emissions over that of the multiple-layer model (e.g.: Figure 6-6 (a), S-5-node and M-5-node).

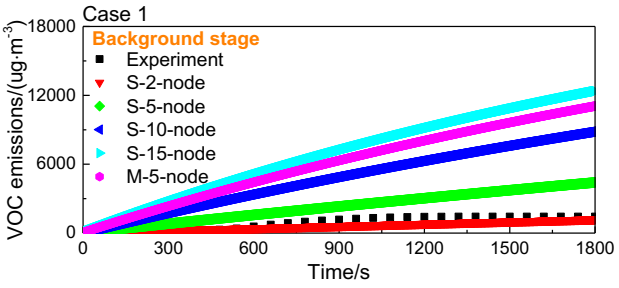

(a) Background stage

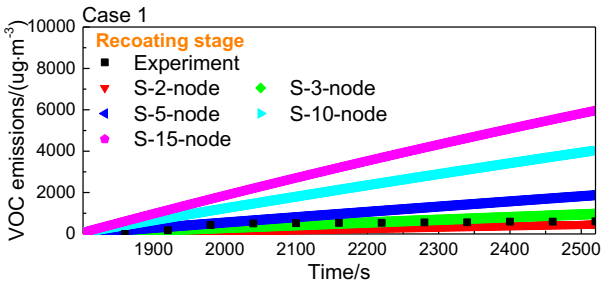

(b) Recoating stage

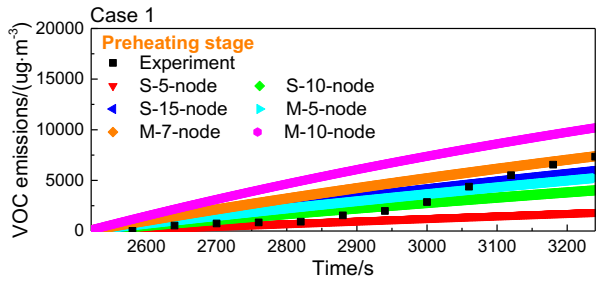

(c) Preheating stage

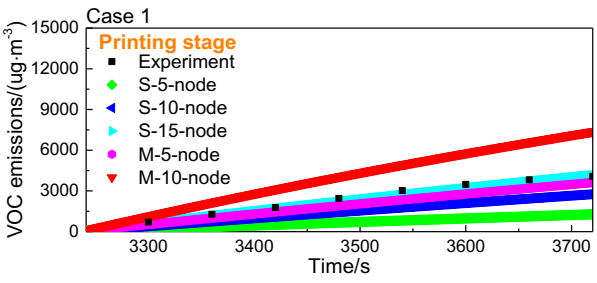

(d) Printing stage

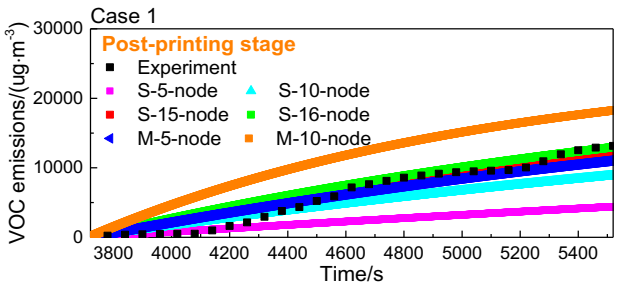

(e) Post-printing stage

Figure 6-6 Modelling of VOC emissions in Case 1 during different stages using different models

Using the same method, we got the models for cases 2-6. Table 6-4 exhibits the chosen models for cases 1-6. As shown in Table 6-4, emissions in background and recoating stages of all cases match a single-layer model with a small node number. Emissions in preheating, printing and post-printing stages match generally a multiple-layer model or a single-layer model with a large node number. Using the results, we are able to predict VOC emissions and compare emission rates with different printing parameters and different printing stages in SLS.

Table 6-4 The chosen models for cases 1-6

Cases	Parameter	Background	Recoating	Preheating	Printing	Post-printing
Case 1	160 C–3 layer–0.15 mm–20 W	S-2-node	S-2-node	M-7-node	S-15-node	S-16-node
Case 2	165 C–3 layer–0.15 mm–20 W	S-3-node	S-3-node	M-9-node	M-8-node	S-15-node
Case 3	160 C–9 layer–0.15 mm–20 W	S-3-node	S-2-node	M-7-node	M-5-node	M-8-node
Case 4	160 C–3 layer–0.09 mm–20 W	S-2-node	S-2-node	S-10-node	S-5-node	S-7-node
Case 5	160 C–3 layer–0.18 mm–20 W	S-2-node	S-5-node	M-7-node	M-7-node	M-5-node
Case 6	160 C–3 layer–0.15 mm–30 W	S-2-node	S-4-node	M-8-node	M-5-node	M-6-node

6.3.1.3 Prediction with parametric variations

With the results in Table 6-4, we predicted the VOC emission ranges when time and parameter changes in each printing stage. Figure 6-7 shows the prediction of VOC emissions in background stage in parameter ranges of (a) preheating temperature: 160–165 °C (30 min), (b) sample layer number: 3–9 layers (30 min), (c) layer thickness: 0.09–0.18 mm (30 min), and (d) laser power: 20–30 W (30 min). In (a) and (b), the accumulated VOC emissions range from 1200 to 2300 ug/m^3

(40-77 ug/m^3 per min). In (c) and (d), the accumulated VOC emissions remain unchanged at around 1200 ug/m^3 (40 ug/m^3 per min). The leading cause for emission in the background stage is the surrounding environment.

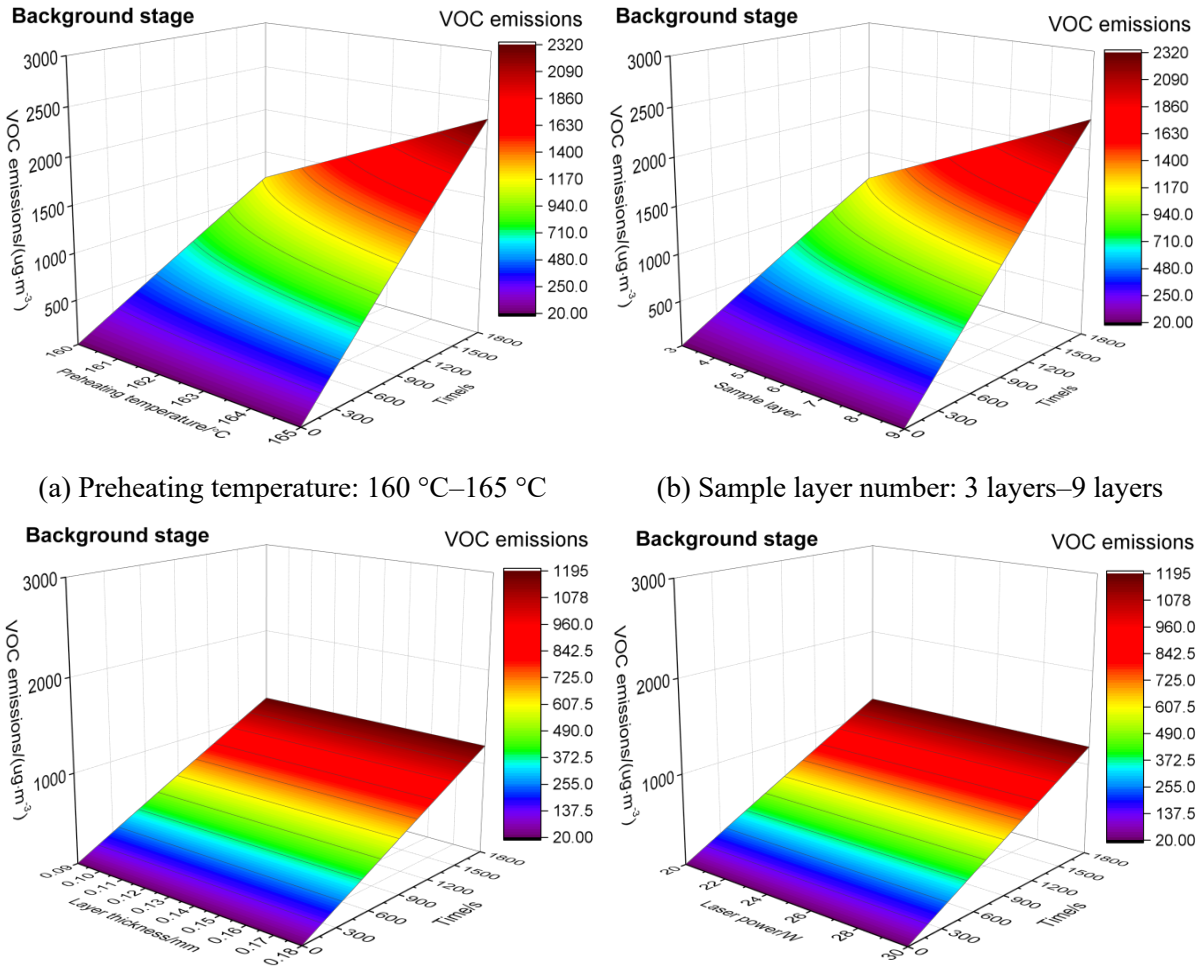

(a) Preheating temperature: 160 °C–165 °C

(b) Sample layer number: 3 layers–9 layers

(c) Layer thickness: 0.09 mm–0.18 mm

(d) Laser power: 20 W–30 W

Figure 6-7 The predictions of VOC emissions in the background stage

Figure 6-8 exhibits the predictions of VOC emissions in the recoating stage with the parameter ranges of (a) preheating temperature: 160–165 °C (17 min), (b) sample layer number: 3–9 layers (17 min), (c) layer thickness: 0.09–0.18 mm (9 min), and (d) laser power: 20–30 W (10 min). In (a)-(d), the accumulated VOC emission ranges are respectively 692-1347 ug/m^3, 692 ug/m^3(keep unchanged), 378-1425 ug/m^3, 418-1196 ug/m^3. The rates of VOC emissions are respectively (a) 41-79 ug/m^3 per min, (b) 41 ug/m^3 per min, (c) 42-158 ug/m^3 per min, and (d) 42-120 ug/m^3 per min. In the recoating stages, the atmosphere/environment is still the main cause for emission, and the emission rates are comparable to that in the background stage. The average VOC

concentrations in background and recoating stages are much lower than the exposure limits of VOC in the building design and construction guide, which is 500 ug/m^3 [149, 171].

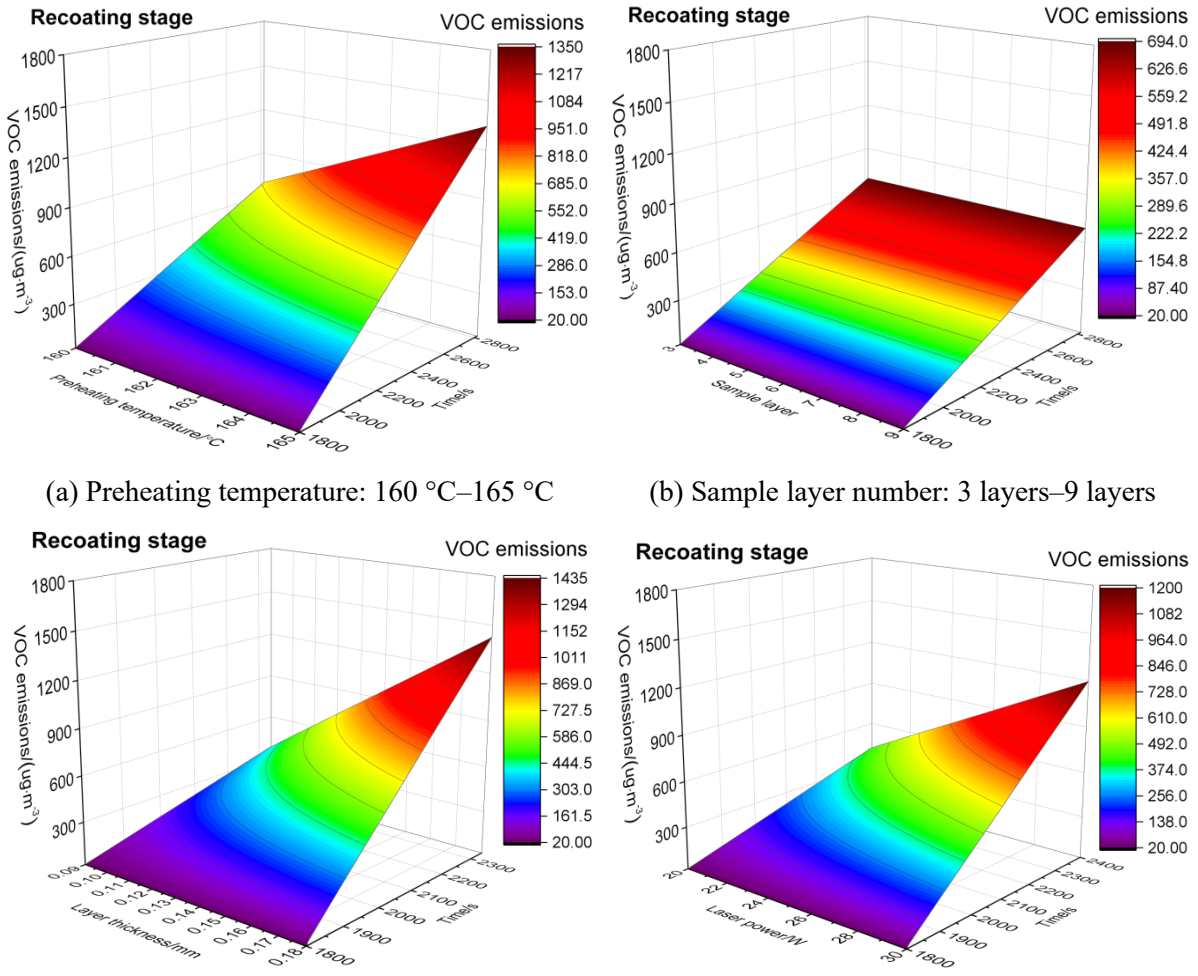

(a) Preheating temperature: 160 °C–165 °C

(b) Sample layer number: 3 layers–9 layers

(c) Layer thickness: 0.09 mm–0.18 mm

(d) Laser power: 20 W–30 W

Figure 6-8 The predictions of VOC emissions in the recoating stage

Figure 6-9 presents the predictions of VOC emissions in the preheating stage. The accumulated VOC emission ranges are respectively (a) 6870-8701 ug/m^3 (preheating temperature: 160–165 °C, 11 min), (b) 7364 ug/m^3 (sample layer number: 3–9 layers, 11 min), (c) 3701-6844 ug/m^3 (layer thickness: 0.09–0.18 mm, 11 min), and (d) 6844-7782 ug/m^3 (laser power: 20–30 W, 11 min). The rates of VOC emissions are respectively (a) 625-791 ug/m^3 per min, (b) 669 ug/m^3 per min, (c) 336-622 ug/m^3 per min, and (d) 622-707 ug/m^3 per min. It is obvious that the emission in the preheating stage is much more severe than the background and the recoating stages. In the preheating stage of Figure 6-9 (a) – (d), most of the average VOC concentrations are above the

exposure limits of VOC [149, 171]. Proper ventilation is thus needed to ensure the good working atmosphere.

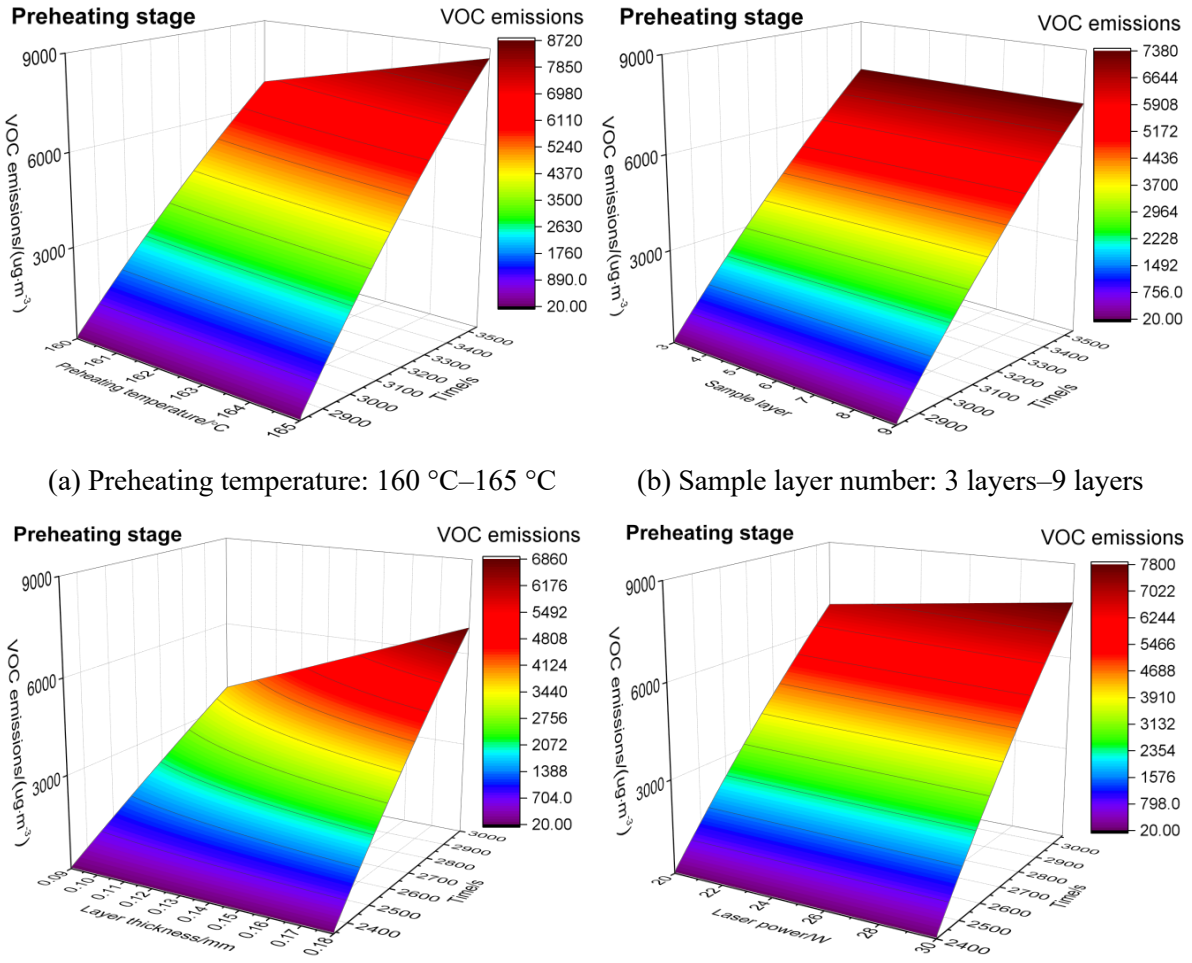

(a) Preheating temperature: 160 °C–165 °C

(b) Sample layer number: 3 layers–9 layers

(c) Layer thickness: 0.09 mm–0.18 mm

(d) Laser power: 20 W–30 W

Figure 6-9 The predictions of VOCs emission in the preheating stage

Figure 6-10 (a)-(d) shows the predictions of VOC emissions in the printing stage. The accumulated VOC emission ranges are respectively (a) 4145-5944 ug/m^3 (preheating temperature: 160-165 °C, 8 min), (b) 4161-6311 ug/m^3 (sample layer number: 3 layers, 8 min-9 layers, 15 min), (c) 1273-5194 ug/m^3 (layer thickness: 0.09-0.18 mm, 8 min), and (d) around 4145 ug/m^3 (laser power: 20-30 W, 8 min). The rates of the VOC emissions are respectively (a) 518-743 ug/m^3 per min, (b) around 421 ug/m^3 per min, (c) 159-649 ug/m^3 per min, and (d) around 518 ug/m^3 per min. Therefore, in the printing stage, most of the average VOC concentrations are still around or above the exposure limits of VOC [149, 171], affirming the needs for proper ventilation. We also

conclude that the average emission rates in the printing stage reduce a little compared to preheating stage in (a) – (d). The most possible reason is that emission with high temperature is the strongest at the beginning and then decreases with time, since emission is the mass-transfer based diffusion of chemical species driven by kinetic energy. We heat up the SLS chamber from room temperature to the preheating temperature in the preheating stage. The significant energy differences between the start and end of the preheating stage trigger a large part of chemical species to emit. The printing stage keeps the preheating temperature, while the chemical species decreases.

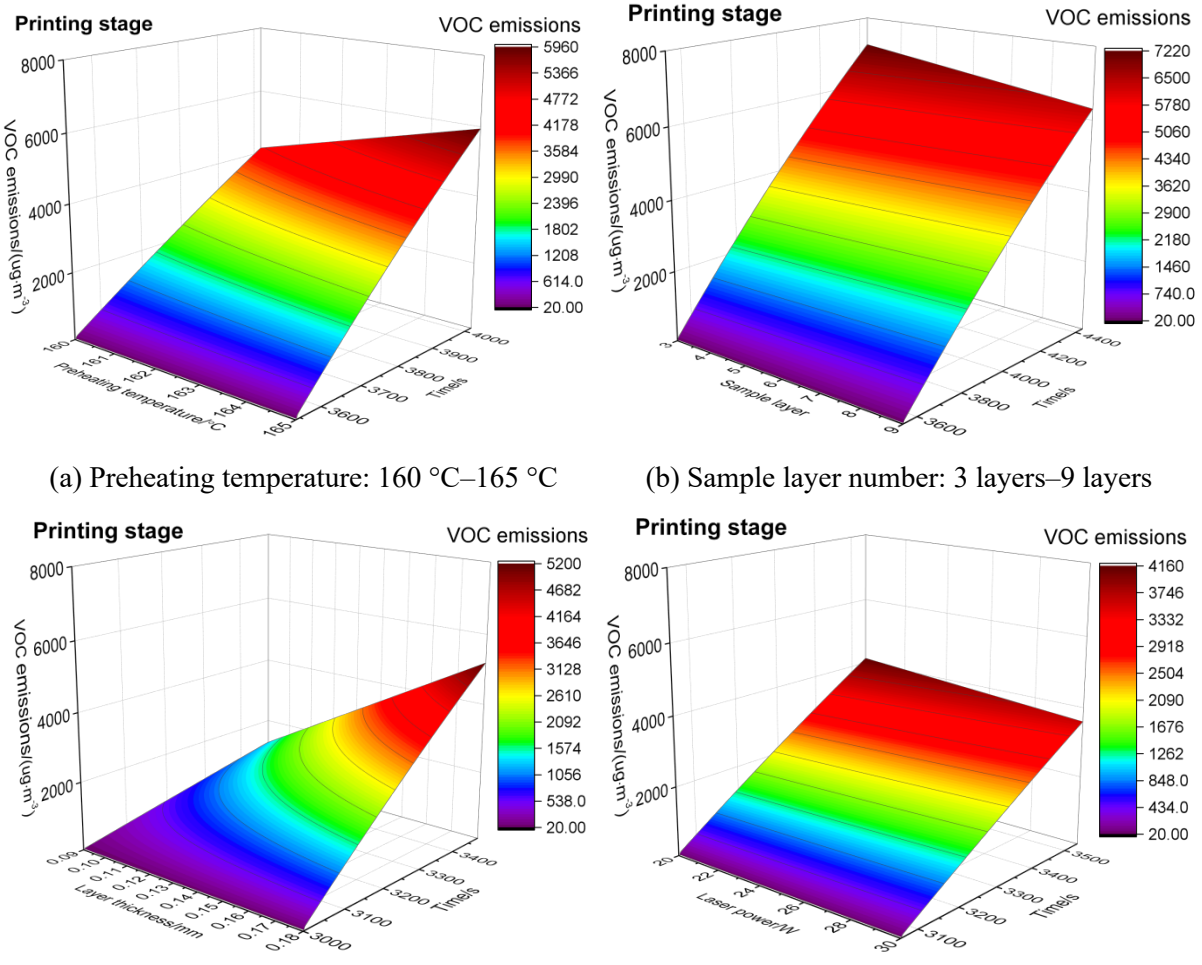

(a) Preheating temperature: 160 °C–165 °C

(b) Sample layer number: 3 layers–9 layers

(c) Layer thickness: 0.09 mm–0.18 mm

(d) Laser power: 20 W–30 W

Figure 6-10 The predictions of VOC emissions in the printing stage

Figure 6-11 presents the predictions of VOC emissions in the post-printing stage. The accumulated VOC emission ranges are respectively (a) 12959-12356 ug/m^3 (preheating temperature: 160 °C-165 °C, 30 min), (b) 12959-16008 ug/m^3 (sample layer number: 3 layers-9

layers, 30 min), (c) 6312-11056 ug/m^3 (layer thickness: 0.09 mm-0.18 mm, 30 min), and (d) 12959 ug/m^3 (laser power: 20 W-30 W, 30 min). The rates of the VOC emissions are respectively (a) 432-412 ug/m^3 per min, (b) 432-534 ug/m^3 per min, (c) 210-369 ug/m^3 per min, and (d) 432 ug/m^3 per min. In this stage, most of the average VOC concentrations are below the exposure limits of VOC [149, 171]. The emission rates in the post-printing stage decrease more than the printing stage. This phenomenon verifies that the emission decreases as temperature decreases, and time passes.

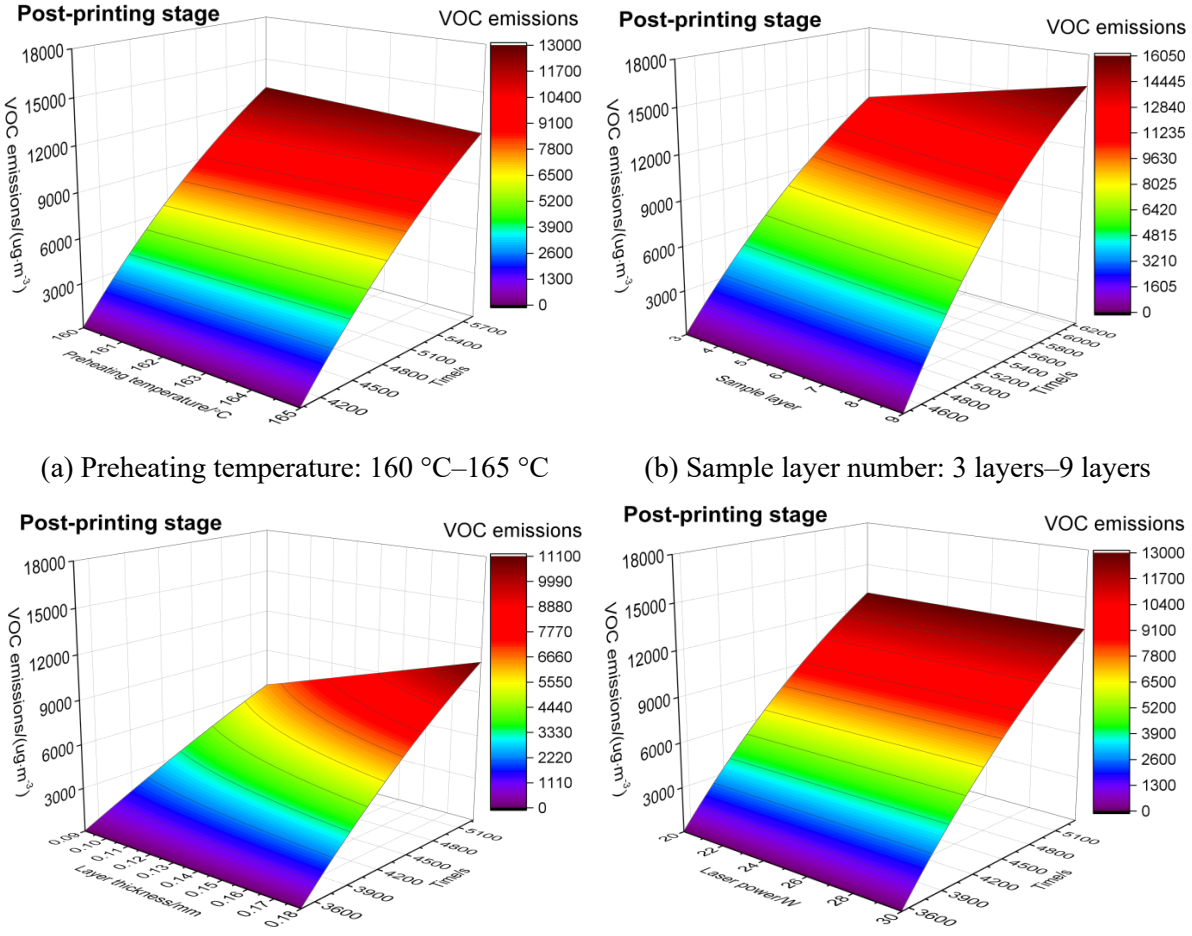

(a) Preheating temperature: 160 °C–165 °C

(b) Sample layer number: 3 layers–9 layers

(c) Layer thickness: 0.09 mm–0.18 mm

(d) Laser power: 20 W–30 W

Figure 6-11 The predictions of VOC emissions in the post-printing stage

6.3.2 Method verification

We use results from experiment 05 in each case to verify the proposed method. Figure 6-12 presents (a) comparison between the actual experimental data and the model prediction, and (b) accuracy of the modelling results. The method shows an average accuracy of 85.32% to the experiment results. Furthermore, the average relative standard deviation between the experimental

data and the predicted data is 15.14%, a number that is much lower than the acceptable relative standard deviation of 22% for engineering emission prediction in references [172, 173].

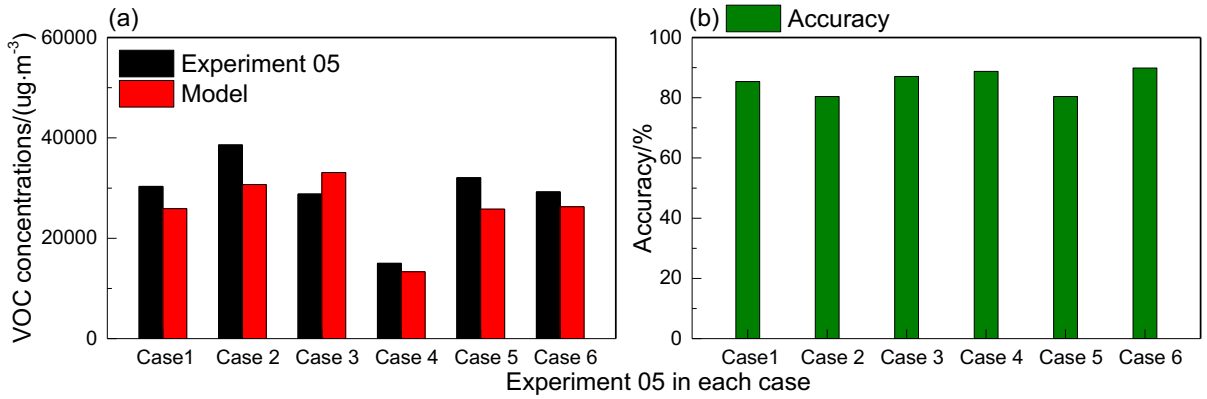

Figure 6-12 Method verification (a) comparison between experiment 05 and modelling, (b) accuracy of the modelling results

6.4 The effects of h_m, D_m, and K on VOC emissions

6.4.1 Mass-transfer coefficient hm

Figure 6-13 and Figure 6-14 respectively show the accumulated VOC emissions with h_m decreasing and increasing in cases 1-6. Emission increases (decreases) as h_m increases (decreases), since the emission rate of VOC is proportional to h_m. With h_m increasing 100 times, in each case, all stages (including weak emission in the background and recoating stages) have peak emissions (Figure 6-14 (a)&(b), when h_m is 0.0025×100) and are in the steady state. Further increase of h_m has little effect to the emission rate. With h_m decreasing 10 times (Figure 6-13 (a)&(b), when h_m is 0.0025/10), the average reduced emission in all cases is 87%. With h_m decreasing 100 times (Figure 6-13 (a)&(b), when h_m is 0.0025/100), in each case, emissions in all stages decrease to around 0, including the preheating, printing and post-printing stages with strong emissions. Decreasing h_m is thus useful to decrease emission as commonly expected. Moreover, in different printing stages, the emissions show different rates of changes with an increased or decreased h_m. With increased h_m, preheating and printing stages have more significantly increased emissions than background and recoating stages, while the post-printing stage has the most significant emissions. With decreased h_m, emissions in preheating and printing stages reduce more than background and recoating stages, and the post-printing stage has the highest speed to decrease emission.

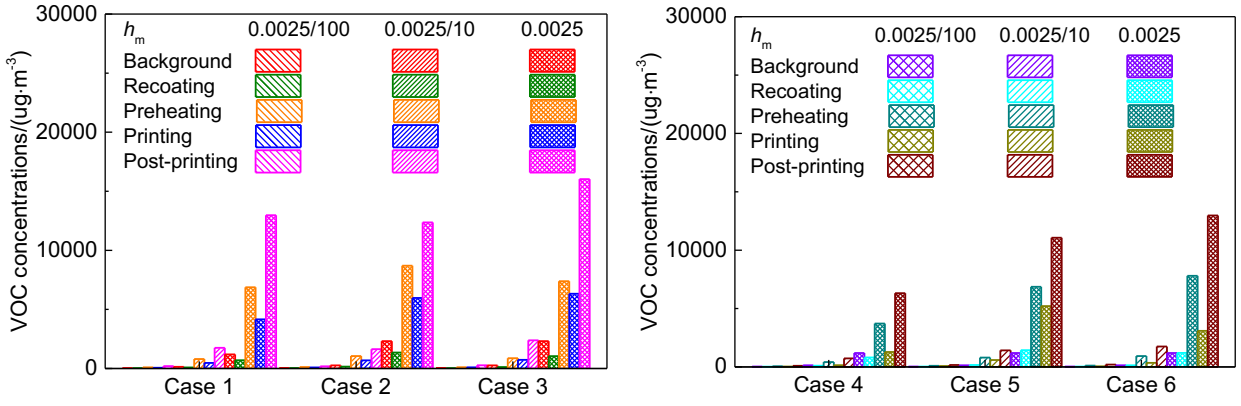

(a) Cases 1 – 3 (b) Cases 4 – 6

Figure 6-13 The accumulated VOC emissions with h_m decreasing in cases 1-6

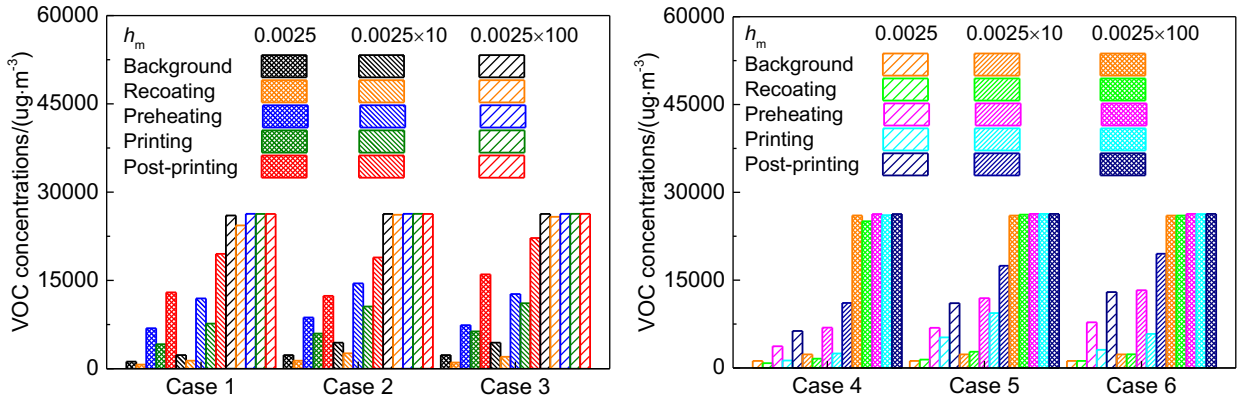

(a) Cases 1 – 3 (b) Cases 4 – 6

Figure 6-14 The accumulated VOC emissions with h_m increasing in cases 1-6

6.4.2 Diffusion coefficient Dm

Figure 6-15 and Figure 6-16 respectively present the accumulated VOC emissions with D_m decreasing and increasing in cases 1-6. In different stages, the effects of D_m on VOC emissions are quite different. In stages with weak emissions (e.g., background and recoating), decreased and increased D_m both have little effect on emissions. In stages with strong emissions (e.g., preheating, printing and post-printing), decreased D_m rarely affects emissions, while increased D_m decreases the VOC emissions. Diffusion always involves concentration gradients. In the background and recoating stages, the weak emissions result from the surrounding environment with little VOC concentration gradient. Decreased and increased D_m seldom have an influence on the concentration gradient and the emission. In the preheating, printing and post-printing stages with large concentration gradients, decreased D_m has no effects on the concentration gradients. However, increased D_m lowers the original concentration gradients and the corresponding emissions.

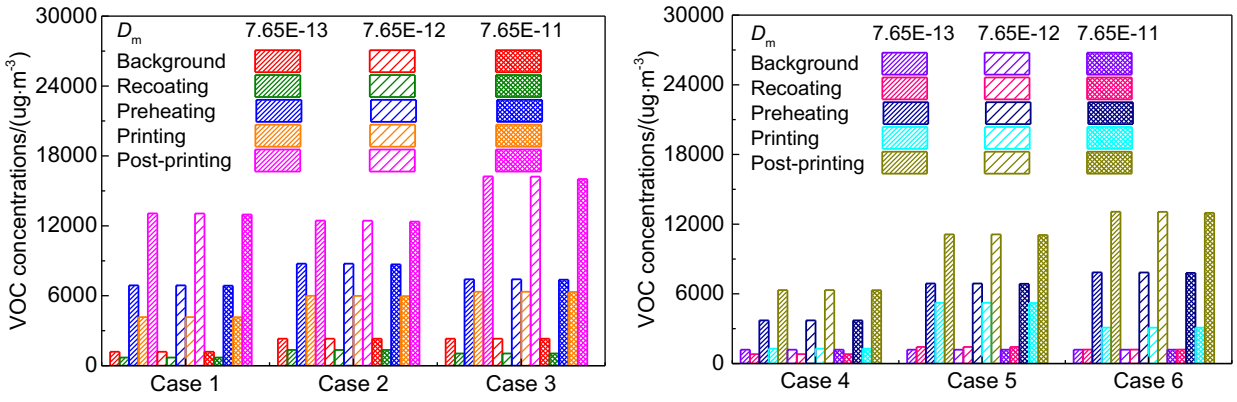

(a) Cases 1 – 3 (b) Cases 4 – 6

Figure 6-15 The accumulated VOC emissions with D_m decreasing in cases 1-6

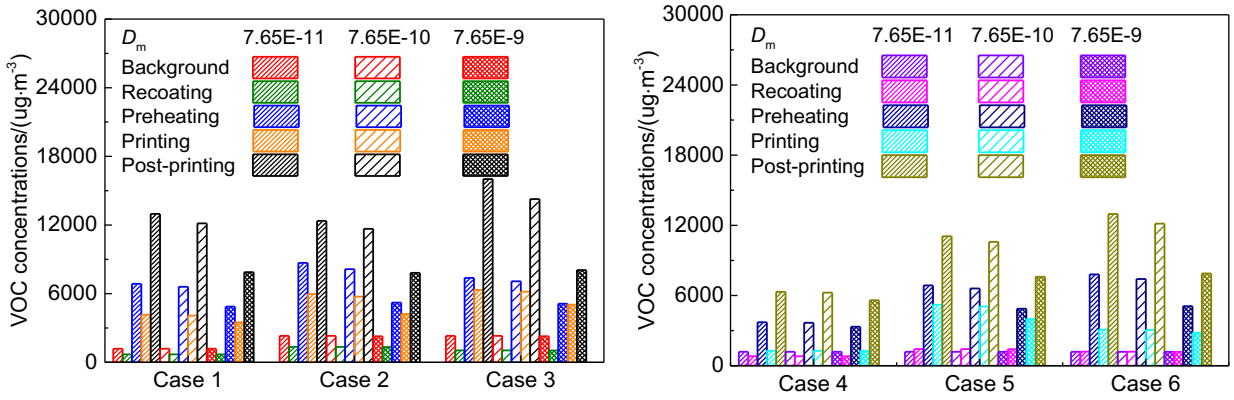

(a) Cases 1 – 3 (b) Cases 4 – 6

Figure 6-16 The accumulated VOC emissions with D_m increasing in cases 1-6

6.4.3 Partition coefficient K

Figure 6-17 and Figure 6-18 respectively present the accumulated VOC emissions with *K* decreasing and increasing in cases 1-6. In all cases, increased *K* slightly increases emissions, while decreased *K* largely reduces emissions. In each case, with *K* between 328.9 and 328900, the emissions at different stages have significant differences. In detail, the background and recoating stages have weak emissions, and preheating, printing, and post-printing stages have strong emissions. However, with *K* of 32.89, the emissions at all stages and cases decrease to a low level of around 250 ug/m^{-3}. Defined as the concentration ratio of VOC between material and air, large *K* leads to more emissions to air due to the significant concentration differences. Material with a small *K* helps to reduce emissions.

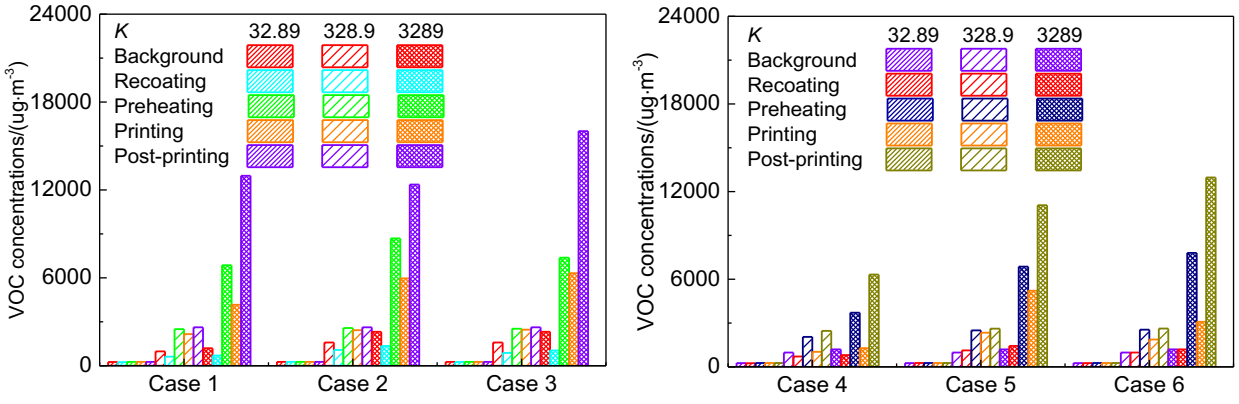

(a) Cases 1 – 3 (b) Cases 4 – 6

Figure 6-17 The accumulated VOC emissions with K decreasing in cases 1-6

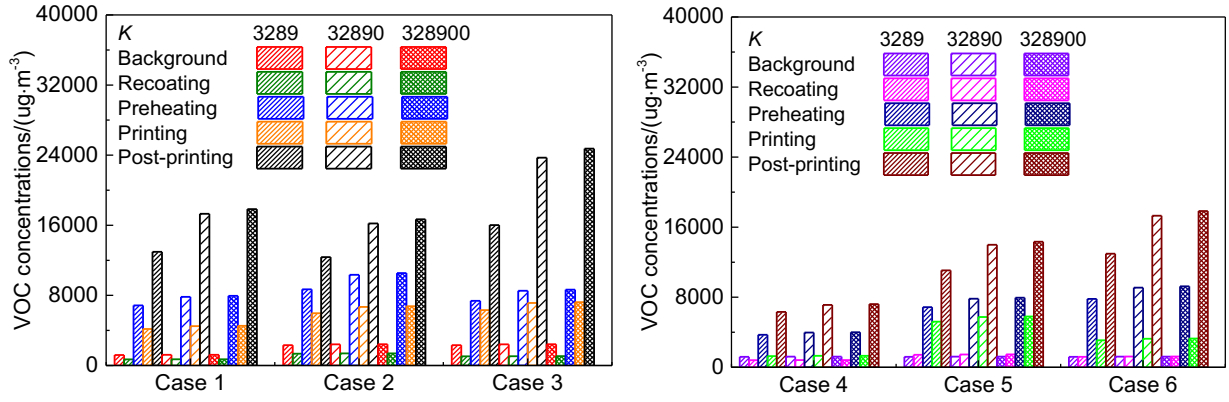

(a) Cases 1 – 3 (b) Cases 4 – 6

Figure 6-18 The accumulated VOC emissions with K increasing in cases 1-6

6.5 Conclusions

The elevated temperature and high-energy laser beam in SLS cause detrimental VOC emissions in SLS. This work proposes a mass-transfer based approach to model and predict VOC emissions in SLS with the combination of experimental measurements. We monitored the VOC emissions from polyamide 12 in 6 cases with varied printing parameters. With emission curve segmentation, we applied the mass-transfer based single-layer and multiple-layer models to simulate the VOC emissions, and obtained the suitable model type and node number in each case. The proposed method has an average accuracy of 85.32% to the experiment results in predicting VOC emissions. We also analyzed the effects of parameters h_m, D_m, and K on emissions. VOC emissions increase (decrease) as h_m increases (deceases). With h_m increasing 100 times, in each case, all stages have peak emissions. With h_m decreasing 100 times, emissions in all cases decrease to around 0. In stages with weak emissions (background and recoating), decreased and increased

D_m both have little effects on emissions. In stages with strong emissions (preheating, printing and post-printing), decreased D_m rarely has effects on emissions; while increased D_m speeds up the diffusion, and decreases the VOC emissions. Increased K slightly increases emissions, while decreased K largely reduces emissions.

Chapter 7. IN-PROCESS MONITORING WHEN SINTERING DIFFERENT POLYAMIDES

7.1 Introduction

Further industrialization of the SLS process is necessary to get better product quality. To achieve the objective, SLS process qualifications, production line control, and integrated process monitoring are useful approaches [26, 174]. In-process monitoring of the SLS powder bed can provide metrics and understanding of the health of the 3D printing process and part quality [175]. Previous study reported that various techniques and indexes (e.g.: optical coherence tomography, in-situ microscope) have been proposed and adopted for the SLS powder bed in-process monitoring [176, 177]. Especially, thermography process monitoring or infrared imaging of the powder bed is important and helpful, used to monitor surface temperature variations that contribute to part inadequacies [178].

Though the previous research, the powder bed temperature profiles of aged polyamide 12 remain largely unexploited, which are largely related to SLS sustainability, material reusability and specimen quality. We propose an in-process monitoring of temperature profiles from infrared images in various locations during SLS when printing with new, aged and extremely aged polyamide 12. The heating temperature will be 160 °C with repetitive tests. In one monitoring, the temperature profiles in each printing layer and the identified location will be recorded. We will also apply interlayer heating and post heating with different heating time to printing and investigate influences of extra heat treatment on the powder and part surface temperature profiles.

7.2 In-process monitoring when sintering different polyamides

First, we conduct heating experiments at different positions in the SLS chamber to check the influences of positions on the surface temperatures. The camera used for in-process monitoring is the FLIR A325sc. We label 8 different positions with designed part samples in the SLS chamber as seen in Figure 7-1a (from l1 to l8), and further choose 3 positions on each samples with the coordinates on the camera shown in Table 7-1. We also select 7 positions directly on the powder surface (from p1 to p7) without laser sintering, of which the coordinates are also in Table 7-1.

During the heating experiments, we heat the powder bed from room temperature to 80 °C, 100 °C, 120 °C, 140 °C, and 160 °C to check the temperature profiles.

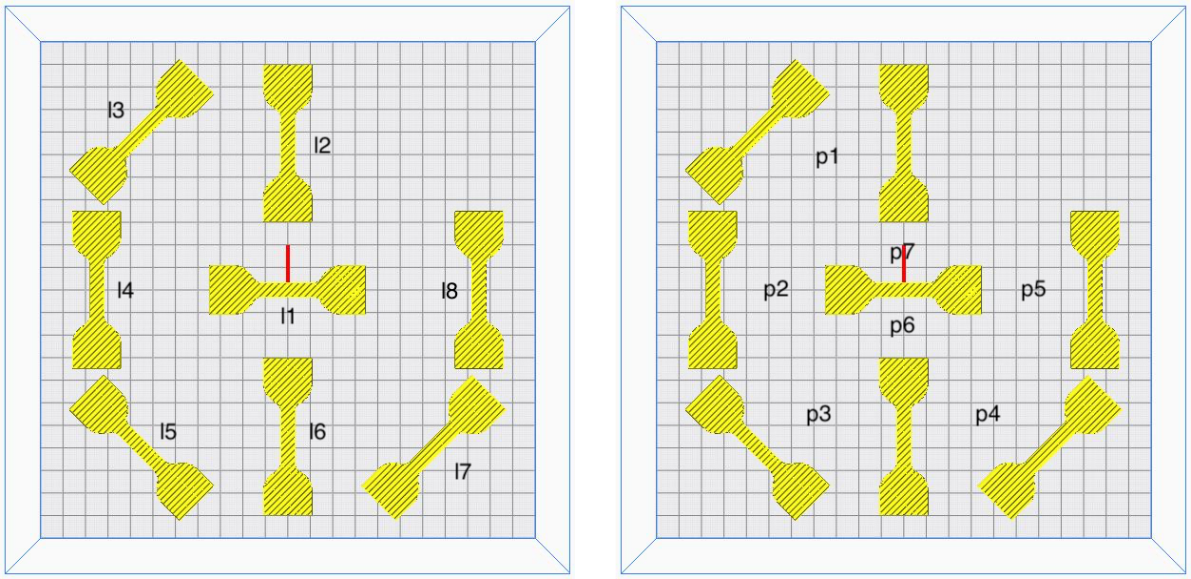

(a) Part sample positions (b) Positions on the powder surface

Figure 7-1 Sample position and number

Table 7-1 Coordinates of part sample positions and positions on the powder surface

Position	Position number		Position coordinate
Part sample positions	l1	1	(200, 125)
		2	(162, 118)
		3	(123, 110)
	l2	1	(103, 184)
		2	(121, 162)
		3	(137, 143)
	l3	1	(185, 199)
		2	(232, 192)
		3	(270, 184)
	l4	1	(285, 162)
		2	(294, 145)
		3	(301, 128)
	l5	1	(305, 109)
		2	(283, 97)
		3	(268, 85)
	l6	1	(181, 93)
		2	(200, 80)
		3	(202, 72)
	l7	1	(70, 72)
		2	(125, 65)
		3	(140, 65)

	l8	1	(23, 111)
		2	(39, 97)
		3	(55, 84)
Positions on the powder surface	p1		(189, 163)
	p2		(247, 136)
	p3		(234, 95)
	p4		(150, 83)
	p5		(83, 106)
	p6		(166, 108)
	p7		(155, 126)

Second, we perform in-process monitoring when sintering different polyamides at eight part sample positions in the SLS chamber. The polyamides used are respectively new polyamide 12, aged polyamide 12 and extremely aged polyamide 12. Using each kind of polyamide, we will print 3 times, without any additional heating treatment, with 60 seconds interlayer heating, and with 300 seconds post-heating. The sample to be printed is with the dimensions: 70 mm in length and 3 mm in width. The parameter settings are: 160 °C preheating temperature; 3000 mm/s scan speed; 18 W laser power; 0.3 mm scan spacing; and 150 µm layer thickness with 3 layers of printing.

7.3 Results and discussions

7.3.1 Heating experiments

Figure 7-2 shows different positions on the SLS powder bed heated to different target temperatures, (a) 80 °C, (b) 100 °C, (c) 120 °C, (d) 140 °C and (e) 160 °C. In all the figures, most positions arrive the target temperatures, while part sample positions l5, l6, l7 and powders surface positions p3, p4 tend to have temperatures below the target ones. At lower target temperatures (80 °C, 100 °C, 120 °C), more positions have temperatures below the target ones. At more higher target temperatures (140 °C and 160 °C), more positions arrive the target temperatures.

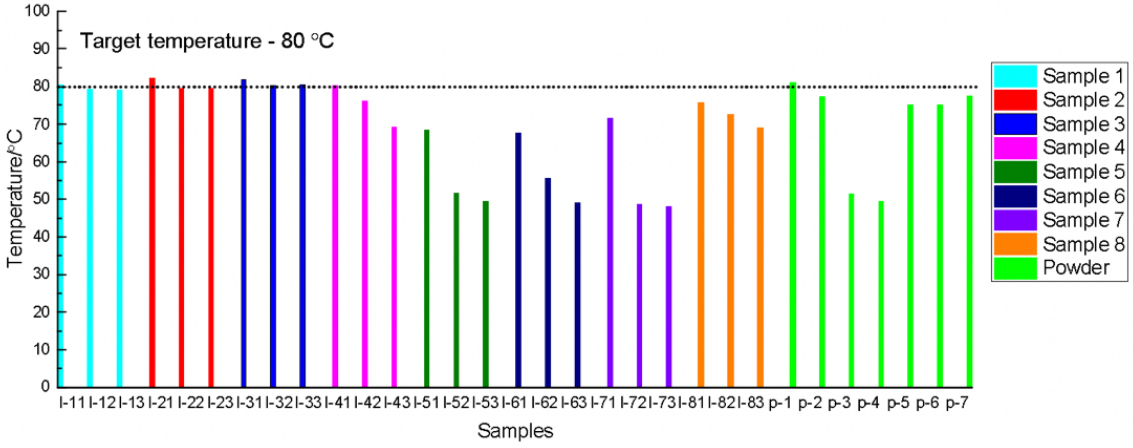

(a) Target temperature: 80 °C

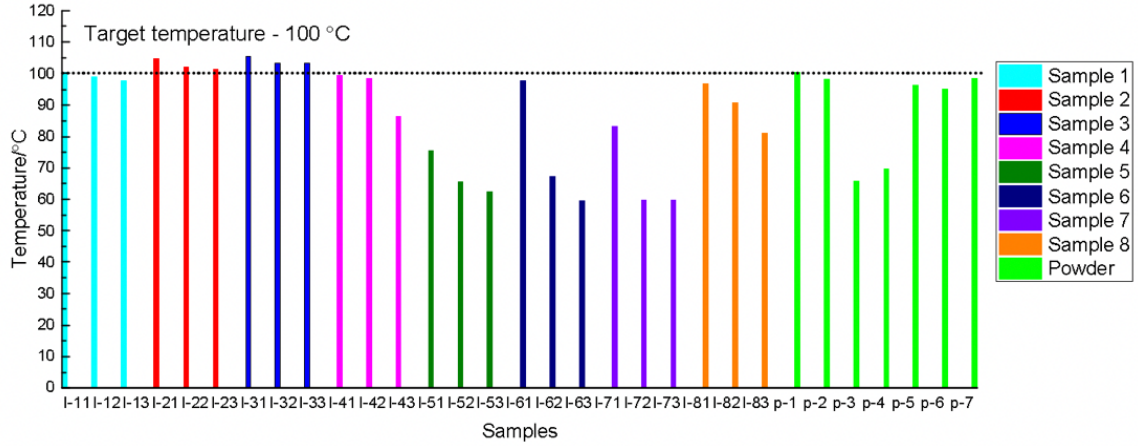

(b) Target temperature: 100 °C

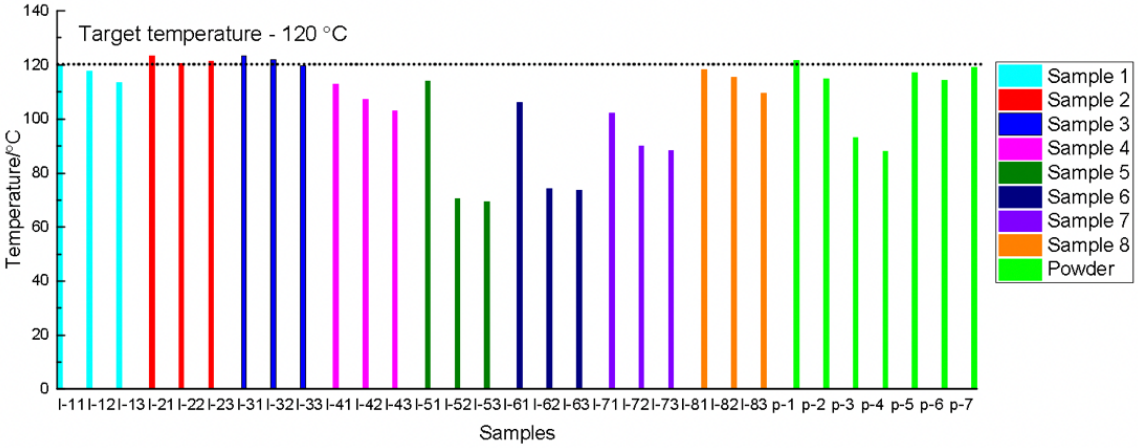

(c) Target temperature: 120 °C

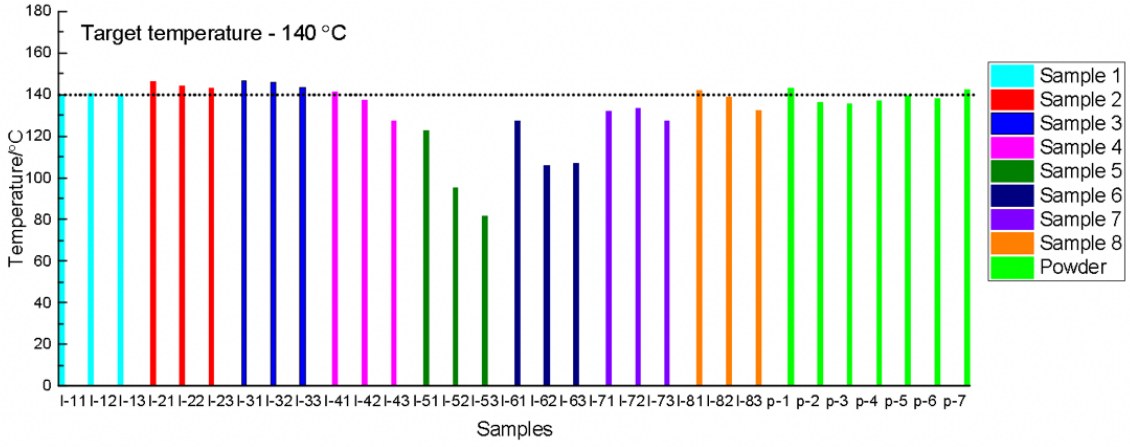

(d) Target temperature: 140 °C

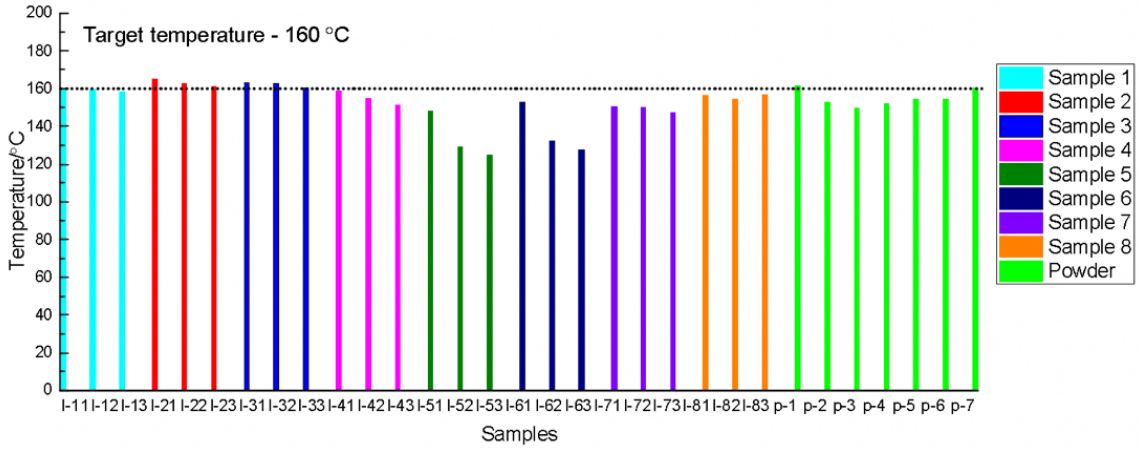

(e) Target temperature: 160 °C

Figure 7-2 Different positions on the SLS powder bed heated to different target temperatures

7.3.2 Energy absorption during laser sintering

From the part sample positions listed in Table 7-1, we chose the first laser on positions from the given 3 positions on each sample, shown in Table 7-2. For each sample, we recorded the laser sintering process to form a printed part, and documented the temperature profiles for the first laser on positions till laser move to the next sample. The temperatures profile with laser on forms an energy absorption curve, shown in Figure 7-3.

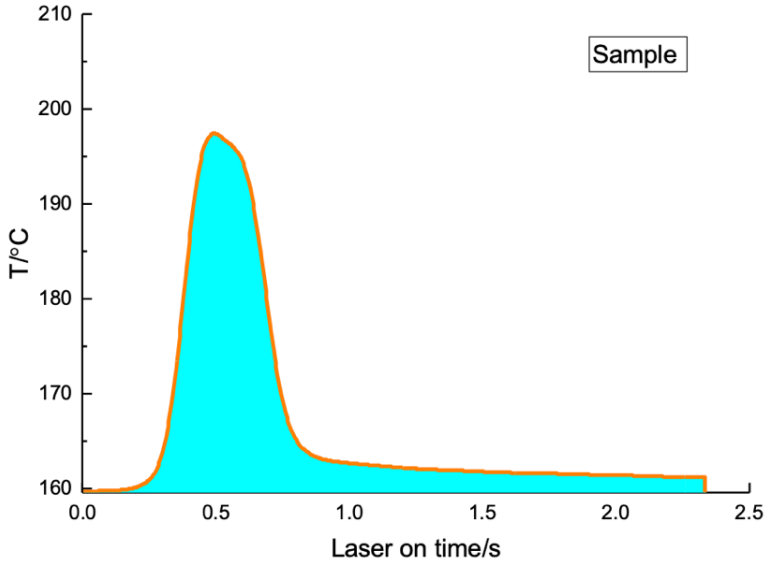

Figure 7-3 Energy absorption during laser sintering

Table 7-2 The first laser on positions on each part sample

Position	Position number		Position coordinate
Part sample positions	11	1	(200, 125)

	l2	3	(137, 143)
	l3	1	(185, 199)
	l4	1	(285, 162)
	l5	3	(268, 85)
	l6	1	(181, 93)
	l7	3	(140, 65)
	l8	3	(55, 84)

Energy absorbed during laser on is in direct proportion to temperature change ΔT. We calculated the ∑ΔT during laser on when sintering new, aged and extremely aged powders to part samples at the position coordinates in Table 7-2. The ∑ΔT results are in Figure 7-4, (a) new powder sample, (b) aged powder samples, (c) extremely aged powder samples, and (d) comparisons. Figure 7-4 (d) shows that the average ∑ΔT for reclaimed powders is larger at all positions from l1 to l8. This is an indicator that reclaimed powders absorbed more energy during laser on periods at all positions.

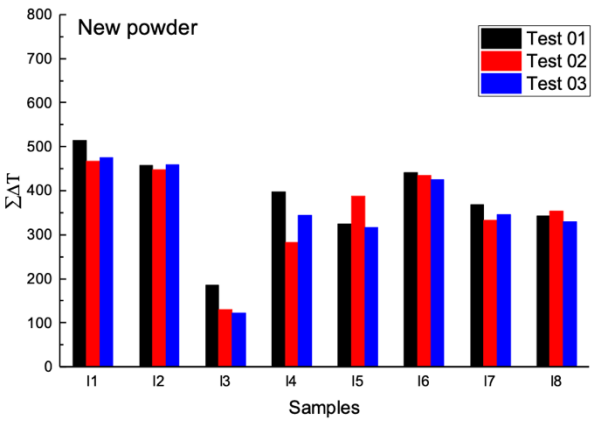

(a) New powder samples

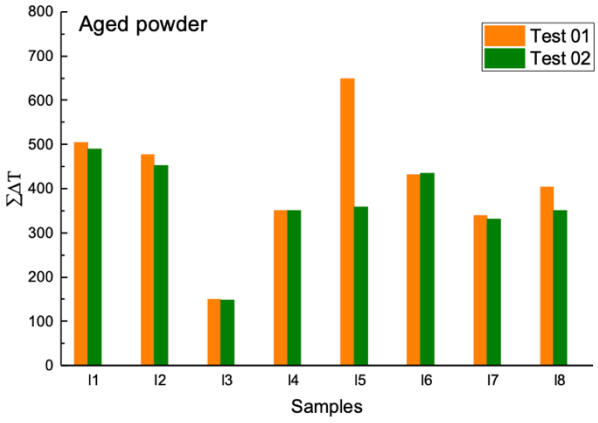

(b) Aged powder samples

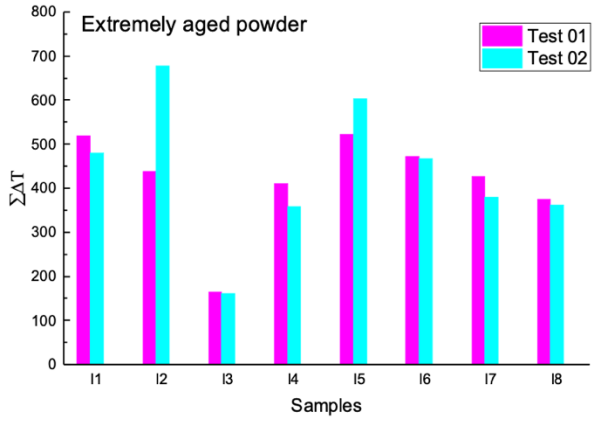

(c) Extremely aged powder samples

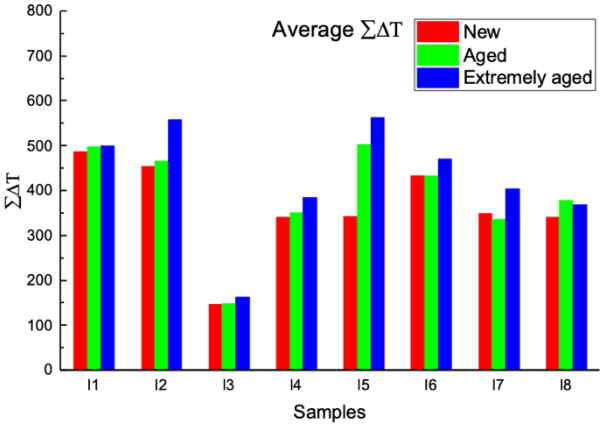

(d) Comparisons

Figure 7-4 ∑ΔT during laser on when sintering new, aged and extremely aged powders

To further investigate the problem, we plotted and compared the energy absorption curves during laser on for new and extremely aged powders at the position coordinates in Table 7-2. The comparison results are in Figure 7-5. At the same processing parameters (the same preheating temperature, laser power and energy density), most of the samples using extremely aged powders tend to have a delay before arriving the peak temperatures. Table 7-3 lists the detailed time to arrive the peak temperatures for each sample. This finding indicates that the thermal conductivity for extremely aged powders decreases compared to new powders. Therefore, the reclaimed powders need to absorb more energy during laser on period to form the molten phase. This conclusion can verify our previous results.

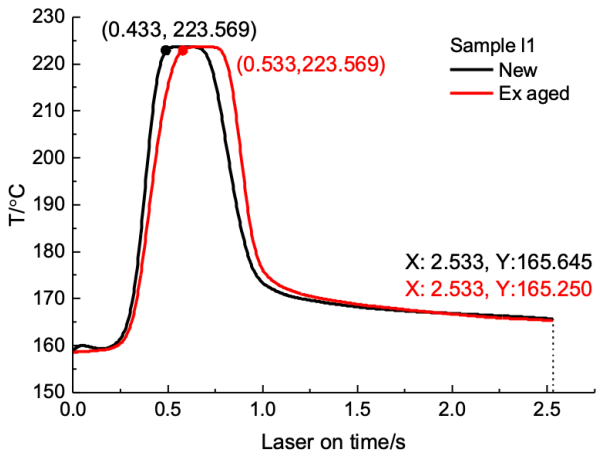

(a) Sample l1

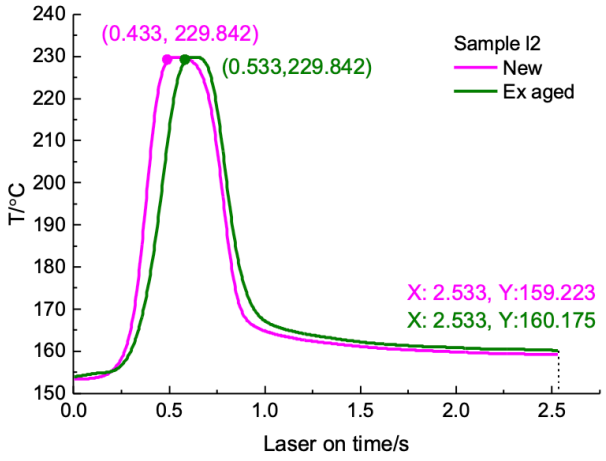

(b) Sample l2

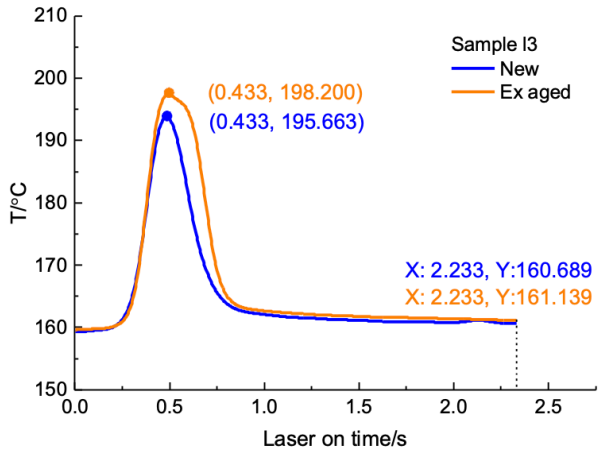

(c) Sample l3

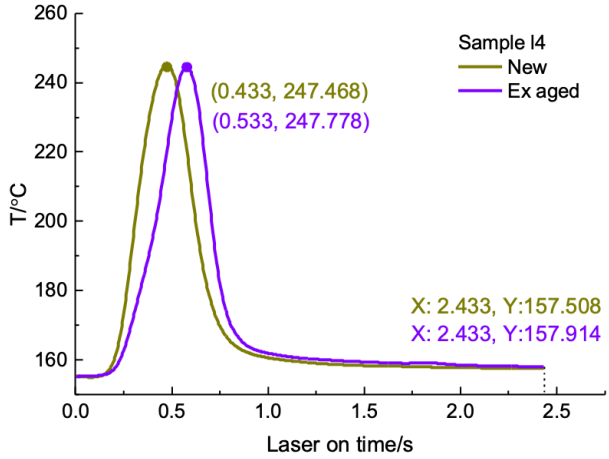

(d) Sample l4

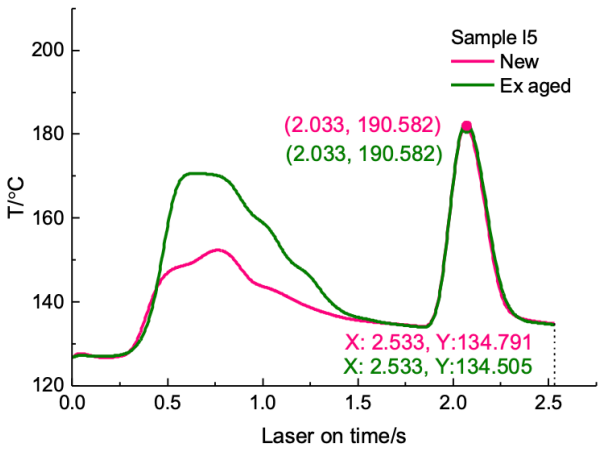

(e) Sample l5

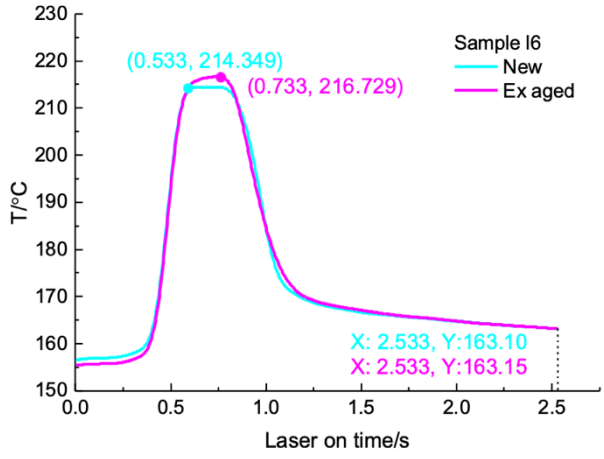

(f) Sample l6

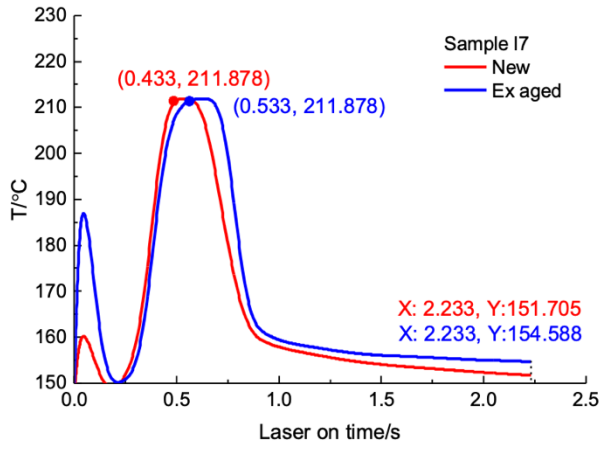

(g) Sample l7

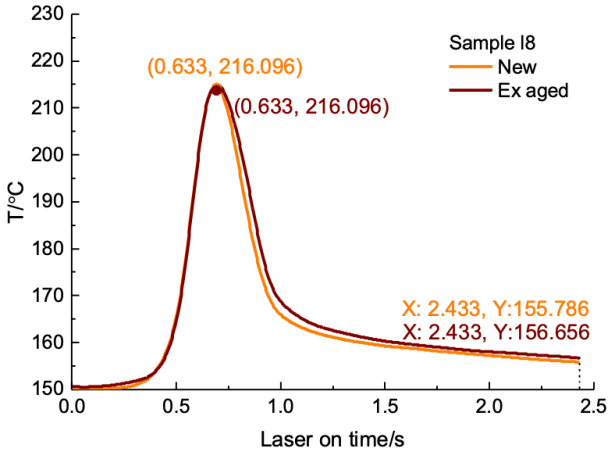

(h) Sample l8

Figure 7-5 Comparing the energy absorption curves during laser on for new and extremely aged powders

Table 7-3 Comparisons when sintering new powder and extremely aged powder

Sample position	Time to the peak temperature/s	
	New powder	Extremely aged powder
l1	0.433	0.533
l2	0.433	0.533
l3	0.433	0.433
l4	0.433	0.533
l5	2.033	2.033
l6	0.533	0.733
l7	0.433	0.533
l8	0.633	0.633

7.3.3 Thermal conductivity

The loose polyamide 12 powder was reported to have a thermal conductivity of 0.10 W/mK, and satisfies Eq. (7-1) [179]. F is the heat flux, λ is the thermal conductivity, and a is the particle contact radius. Known ∑ΔT for new, aged and extremely aged powders, we predicted the thermal conductivity for aged and extremely aged powders using Eq. (7-1), results presented in Table 7-4 and Figure 7-6.

$$\text{Constant} = \frac{F}{2a} = \Delta T \cdot \lambda \tag{7-1}$$

Table 7-4 Prediction of thermal conductivity for aged and extremely aged powders

Sample position	∑ΔT - New	$F/2a=\Delta T\cdot\lambda$	∑ΔT - Aged	λ- Aged	∑ΔT - Extremely aged	λ - Extremely aged
l1	486.6253	48662.53	498.3525	0.097647	500.7415	0.097181
l2	455.8807	45588.07	465.5335	0.097927	558.919	0.081565
l3	147.046	14704.6	149.102	0.098621	163.6225	0.089869
l4	342.5157	34251.57	351.397	0.097473	385.99	0.088737
l5	344.0303	34403.03	504.322	0.068216	563.729	0.061028
l6	434.4183	43441.83	434.214	0.100047	470.7935	0.092274
l7	350.269	35026.9	336.2225	0.104178	404.5105	0.086591
l8	342.483	34248.3	378.385	0.090512	370.0055	0.092562

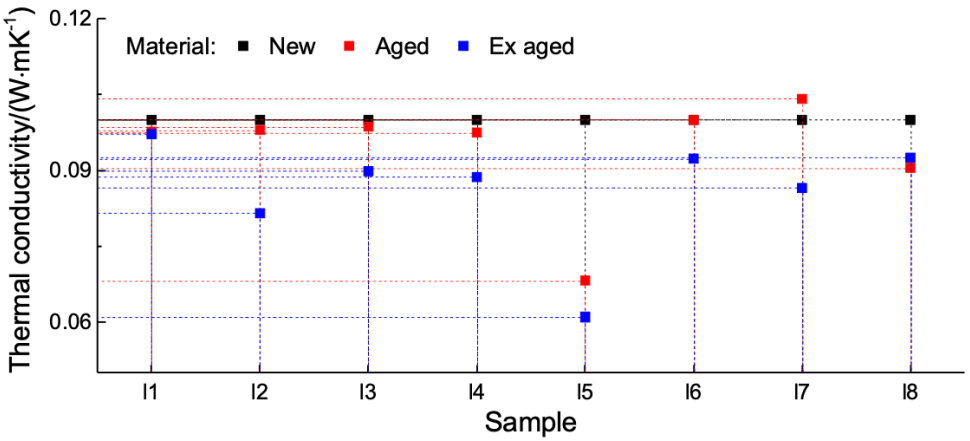

Figure 7-6 Thermal conductivity for aged and extremely aged powders

7.4 Conclusions

We conducted heating experiments at different positions (8 different positions with designed part samples and 7 positions directly on the powder surface) and performed in-process monitoring at 8 sample positions in the SLS chamber. Results from the heating experiments show that, at

lower target temperatures (80 °C, 100 °C, 120 °C), more positions have temperatures below the target ones. At more higher target temperatures (140 °C and 160 °C), more positions arrive the target temperatures. Results from the laser sinter monitoring experiments show that reclaimed powders absorbed more energy during laser on periods at all positions. At the same processing parameters, most of the samples using extremely aged powders tend to have a delay before arriving the peak temperatures, indicating the thermal conductivity for extremely aged powders decreases compared to new powders. We also predicted the thermal conductivity for aged and extremely aged powders.

Chapter 8. CONCLUSIONS AND FUTURE WORK

8.1 Conclusions

This dissertation contributes to the understanding and controlling on the reusability, aging kinetics, and sustainability of polyamide 12 in SLS. We conclude the main results of each topic as below:

1. In Chapter 2, a new process control method was proposed to explore the possibility and feasibility of reusing the differently degraded polyamide 12 powders. The proposed method of SLS created parts with improved mechanical properties: the largest tensile strength we obtained is 37.97 Mpa from tensile bars 3D printed using 60%-40% new-extremely aged powders with 60-second interlayer heating, a result 47.17% better than the baseline (25.80 Mpa). The tensile bars which have stably large elongations at break are from the 10%-90% new-extremely aged blends without or with interlayer heating (15.37% and 16.59% respectively). Compared to the baseline sample, the tensile bars 3D printed using 30%-40%-30% new-aged-extremely aged mixed powders with 60-second interlayer heating yield 18.04% higher tensile strength and 55.29% larger elongation at break.

2. In Chapter 3, we propose an SLS with post-heating to improve surface quality of 3D printed parts using reclaimed polyamide 12 powders. For parts using 100% extremely aged powders, a 300-second post-heating yields a well-consolidated surface with little porosity and a drastically reduced un-molten particles. The unmolten particles disappear on the parts using 50% or more new powders with 300-second post-heating, showing smooth and flat surfaces with high porosity. These surfaces are comparable to those of parts using 100% new powders. When using 80% or 90% reclaimed powders, numerous visible unmolten particles and multi-layer porous structures occur in the case with no post-heating. The surfaces are similar to those of the parts using 100% extremely aged powders. With the proposed 300-second post-heating, we obtain smooth and flat surfaces with almost zero porosity and only few unmolten particles. In particular, parts 3D-printed using the 30%-30%-40% new-aged-extremely-aged powder mixtures exhibit the smoothest and flattest surface with no unmolten particles and nearly zero porosity.

3. In Chapter 4, we propose a new kinetic scheme for SLS degradation of polyamide 12 composed of the basic autoxidation model, the coefficients of coupled oxygen and laser effects,

and the relationships between the sample degradation rates and oxidation time. The predicted degradations from the proposed kinetic model match on average 89.53% with the actual SLS degradation rates, in contrast to a 34.48% accuracy from a conventional aging model. We found that the laser effects are 4-time stronger than oxygen effects on polyamide 12 degradation. Furthermore, we identified the influences of the coupled oxygen and laser effects in SLS and preheating temperatures on the degradation rates. The findings provide a first-instance knowledge of quantitative material degradation related to the estimated parameters, and insights to reduce degradation in SLS. This work established a novel effective model to obtain the kinetic scheme of polyamide 12 degradation to aid future studies of materials degradation and reuse in the SLS process.

4. In Chapter 5, we experimented with successive reuse of polyamide 12 materials in SLS. The tested 3D printing successfully produced 3- and 32-layer samples with 8-time reused polyamide 12 powders while retaining more than 65% of the baseline Young's Modulus from fresh powders. The basic flowability energy of 2-, 5-, and 8-time reused powders decreased by 2.14%, 8.43%, and 11.03%, respectively, compared to new powders. With nitrogen, the long-chain backbone of polyamide 12 was more stable and less affected by heat and laser. In polyamide 12 parts 3D-printed using 8-time reused powders, the relative area of the peak on C-H bonds adjacent to nitrogen reduced by 50% compared to new parts. From new powders to part printed using 8-time reused powders, the atomic percentages of C and O increased by 72.49% and 7.13%, respectively. Besides, after 8-time of reuse, part density decreased by 16.49%; the averages of part tensile strength, Young's Modulus, and percent elongation respectively decreased by 35.39%, 18.91% and 27.08%.

5. In Chapter 6, we propose a mass-transfer based approach to model and predict VOC emissions in SLS with the combination of experimental measurements. The proposed method has an average accuracy of 85.32% to the experiment results in predicting VOC emissions. We also analyzed the effects of parameters h_m, D_m, and K on emissions. VOC emissions increase (decrease) as hm increases (deceases). With hm increasing 100 times, in each case, all stages have peak emissions. With h_m decreasing 100 times, emissions in all cases decrease to around 0. In stages with weak emissions (background and recoating), decreased and increased D_m both have little effects on emissions. In stages with strong emissions (preheating, printing and post-printing), decreased D_m rarely has effects on emissions; while increased D_m speeds up the diffusion, and

decreases the VOC emissions. Increased *K* slightly increases emissions, while decreased *K* largely reduces emissions.

6. In Chapter 7, we performed in-process monitoring in the SLS chamber. Results from the heating experiments show that, at lower target temperatures (80 °C, 100 °C, 120 °C), more positions have temperatures below the target ones. At more higher target temperatures (140 °C, 160 °C), more and more positions arrive the target temperatures. Results from the laser sinter monitoring experiments show that reclaimed powders absorbed more energy during laser on periods at all positions. At the same processing parameters, most of the samples using extremely aged powders tend to have a delay before arriving the peak temperatures, indicating the thermal conductivity for extremely aged powders decreases compared to new powders. We also predicted the thermal conductivity for aged and extremely aged powders.

8.2 Future work

Our work proposed new methods with process control to improve part properties when applying reclaimed polyamides, while the structural modification maybe the more effective ways to improve property of reclaimed materials. Therefore, one extension of the presented work can focus on the material structural and chemical modification using additive manufacturing or hybrid additive manufacturing. With the modified materials, both the particle scale and part scale properties can be checked with that of new materials. Structural and chemical modification for reclaimed materials maybe the most effective ways for material recycling.

Since we studied the degradation schemes of the polyamides in SLS, further extension of the work can try to find ways to reduce the materials degradation rates in SLS based on the degradation schemes from a micro perspective. Control theory maybe helpful tools here. Experimentations to find the most suitable environment for reducing the materials degradation rates are also promising. The importance here is to find the correlations between the degradation key factors and the environment from the material degradation schemes.

Sustainability is another significant direction to explore and extend the work. Useful ways and methodologies to reduce or eliminate emissions and other pollutions, to maximize the materials and energy usage, and to optimize the supply chains in SLS are urgently needed to ensure a sustainable and promising additive manufacturing process.

BIBLIOGRAPHY

[1] W. Gao, Y. Zhang, D. Ramanujan, K. Ramani, Y. Chen, C.B. Williams, C.C. Wang, Y.C. Shin, S. Zhang, P.D. Zavattieri, The status, challenges, and future of additive manufacturing in engineering, Computer-Aided Design, 69 (2015) 65-89.

[2] H. Tiismus, A. Kallaste, T. Vaimann, A. Rassõlkin, A. Belahcen, Additive Manufacturing of Prototype Axial Flux Switched Reluctance Electrical Machine, in: 2021 28th International Workshop on Electric Drives: Improving Reliability of Electric Drives (IWED), IEEE, 2021, pp. 1-4.

[3] R. JEMGHILI, A.A. TALEB, K. MANSOURI, Additive Manufacturing Progress as a New Industrial Revolution, in: 2020 IEEE 2nd International Conference on Electronics, Control, Optimization and Computer Science (ICECOCS), IEEE, 2020, pp. 1-8.

[4] M. Schmid, A. Amado, K. Wegener, Materials perspective of polymers for additive manufacturing with selective laser sintering, Journal of Materials Research, 29 (2014) 1824-1832.

[5] C. Zhou, Y. Chen, Additive manufacturing based on optimized mask video projection for improved accuracy and resolution, Journal of manufacturing processes, 14 (2012) 107-118.

[6] A.-N. Chen, J.-M. Wu, K. Liu, J.-Y. Chen, H. Xiao, P. Chen, C.-H. Li, Y.-S. Shi, High-performance ceramic parts with complex shape prepared by selective laser sintering: a review, Advances in Applied Ceramics, 117 (2018) 100-117.

[7] S. Müller, P. Woizeschke, Feasibility of a laser powder bed fusion process for additive manufacturing of hybrid structures using aluminum-titanium powder-substrate pairings, Additive Manufacturing, 48 (2021) 102377.

[8] S. Impey, P. Saxena, K. Salonitis, Selective Laser Sintering Induced Residual Stresses: Precision Measurement and Prediction, Journal of Manufacturing and Materials Processing, 5 (2021) 101.

[9] K. Hariharan, G. Arumaikkannu, T. Ramkumar, M. Selvakumar, Material stability investigation of polyamide material before and after laser sintering, International Journal of Polymer Analysis and Characterization, 25 (2020) 158-165.

[10] A. Awad, F. Fina, A. Goyanes, S. Gaisford, A.W. Basit, 3D printing: Principles and pharmaceutical applications of selective laser sintering, International Journal of Pharmaceutics, 586 (2020) 119594.
[11] C. Yan, Y. Shi, L. Hao, Investigation into the differences in the selective laser sintering between amorphous and semi-crystalline polymers, International polymer processing, 26 (2011) 416-423.
[12] Y. Zhuang, Y. Guo, J. Li, K. Jiang, H. Zhang, D. Meng, Study on process and parameter optimisation of selective laser sintering of thermoplastic polyurethane/carbon nanotube powder, The International Journal of Advanced Manufacturing Technology, 116 (2021) 993-1001.
[13] C.G. Campbell, D.J. Astorga, E. Martinez, M. Celina, Selective laser sintering (SLS)-printable thermosetting resins via controlled conversion, MRS Communications, (2021) 1-6.
[14] J.-P. Kruth, X. Wang, T. Laoui, L. Froyen, Lasers and materials in selective laser sintering, Assembly Automation, (2003).
[15] S. Kumar, A. Czekanski, Roadmap to sustainable plastic additive manufacturing, Materials Today Communications, 15 (2018) 109-113.
[16] M. Schmid, A. Amado, K. Wegener, Polymer powders for selective laser sintering (SLS), in: AIP Conference proceedings, AIP Publishing LLC, 2015, pp. 160009.
[17] Y. Zhou, S. Xi, Y. Huang, M. Kong, Q. Yang, G. Li, Preparation of near-spherical PA12 particles for selective laser sintering via Plateau-Rayleigh instability of molten fibers, Materials & Design, 190 (2020) 108578.
[18] L. Feng, Y. Wang, Q. Wei, PA12 Powder Recycled from SLS for FDM, Polymers, 11 (2019) 727.
[19] F. Paolucci, M. van Mook, L. Govaert, G. Peters, Influence of post-condensation on the crystallization kinetics of PA12: From virgin to reused powder, Polymer, 175 (2019) 161-170.
[20] D.T. Pham, K. Dotchev, W. Yusoff, Deterioration of polyamide powder properties in the laser sintering process, Proceedings of the Institution of Mechanical Engineers, Part C: Journal of Mechanical Engineering Science, 222 (2008) 2163-2176.
[21] P. Chen, M. Tang, W. Zhu, L. Yang, S. Wen, C. Yan, Z. Ji, H. Nan, Y. Shi, Systematical mechanism of Polyamide-12 aging and its micro-structural evolution during laser sintering, Polymer Testing, 67 (2018) 370-379.

[22] N. Ma, W. Liu, L. Ma, S. He, H. Liu, Z. Zhang, A. Sun, M. Huang, C. Zhu, Crystal transition and thermal behavior of Nylon 12, e-Polymers, 20 (2020) 346-352.
[23] K. Wudy, D. Drummer, Aging behavior of polyamide 12: interrelation between bulk characteristics and part properties, in: Solid Freeform Fabrication Symposium—an Additive Manufacturing Conference, 2016, pp. 770-781.
[24] S. Dadbakhsh, L. Verbelen, O. Verkinderen, D. Strobbe, P. Van Puyvelde, J.-P. Kruth, Effect of PA12 powder reuse on coalescence behaviour and microstructure of SLS parts, European Polymer Journal, 92 (2017) 250-262.
[25] K. Dotchev, W. Yusoff, Recycling of polyamide 12 based powders in the laser sintering process, Rapid Prototyping Journal, (2009).
[26] A. Wegner, C. Mielicki, T. Grimm, B. Gronhoff, G. Witt, J. Wortberg, Determination of robust material qualities and processing conditions for laser sintering of polyamide 12, Polymer Engineering & Science, 54 (2014) 1540-1554.
[27] K. Wudy, D. Drummer, F. Kühnlein, M. Drexler, Influence of degradation behavior of polyamide 12 powders in laser sintering process on produced parts, in: AIP Conference Proceedings, American Institute of Physics, 2014, pp. 691-695.
[28] A. Wörz, K. Wudy, D. Drummer, A. Wegner, G. Witt, Comparison of long-term properties of laser sintered and injection molded polyamide 12 parts, Journal of Polymer Engineering, 38 (2018) 573-582.
[29] N. Vidakis, M. Petousis, L. Tzounis, A. Maniadi, E. Velidakis, N. Mountakis, J.D. Kechagias, Sustainable additive manufacturing: Mechanical response of polyamide 12 over multiple recycling processes, Materials, 14 (2021) 466.
[30] A.K. Battu, T.R. Pope, T. Varga, J.F. Christ, M.D. Fenn, W.S. Rosenthal, W. Kuang, M. Thomas, A.M. Arnold, M. Schram, Build orientation dependent microstructure in polymer laser sintering: Relationship to part performance and evolution with aging, Additive Manufacturing, 36 (2020) 101464.
[31] D. Drummer, K. Wudy, M. Drexler, Modelling of the aging behavior of polyamide 12 powder during laser melting process, in: AIP Conference Proceedings, AIP Publishing LLC, 2015, pp. 160007.

[32] J. Bai, R.D. Goodridge, R.J. Hague, M. Song, M. Okamoto, Influence of carbon nanotubes on the rheology and dynamic mechanical properties of polyamide-12 for laser sintering, Polymer Testing, 36 (2014) 95-100.
[33] R. Li, X. Hu, Study on discoloration mechanism of polyamide 6 during thermo-oxidative degradation, Polymer degradation and Stability, 62 (1998) 523-528.
[34] F. Yang, X. Chen, A combined theoretical and experimental approach to model polyamide 12 degradation in selective laser sintering additive manufacturing, Journal of Manufacturing Processes, 70 (2021) 271-289.
[35] P. Chen, H. Wu, W. Zhu, L. Yang, Z. Li, C. Yan, S. Wen, Y. Shi, Investigation into the processability, recyclability and crystalline structure of selective laser sintered Polyamide 6 in comparison with Polyamide 12, Polymer Testing, 69 (2018) 366-374.
[36] F. Yang, T. Jiang, G. Lalier, J. Bartolone, X. Chen, A process control and interlayer heating approach to reuse polyamide 12 powders and create parts with improved mechanical properties in selective laser sintering, Journal of Manufacturing Processes, 57 (2020) 828-846.
[37] R.J. Young, P.A. Lovell, Introduction to polymers, CRC press, 2011.
[38] K. Wudy, D. Drummer, Aging effects of polyamide 12 in selective laser sintering: Molecular weight distribution and thermal properties, Additive Manufacturing, 25 (2019) 1-9.
[39] F. Yang, T. Jiang, G. Lalier, J. Bartolone, X. Chen, Process control of surface quality and part microstructure in selective laser sintering involving highly degraded polyamide 12 materials, Polymer Testing, 93 (2021) 106920.
[40] W. Yusoff, H. Ani, D. Pham, K. Dotchev, Influence of molecular weight average, degree of crystallinity, and viscosity of different polyamide PA12 powder grades on the microstructures of laser sintered part, in: MATEC Web of Conferences, EDP Sciences, 2015, pp. 03005.
[41] G. Craft, J. Nussbaum, N. Crane, J. Harmon, Impact of extended sintering times on mechanical properties in PA-12 parts produced by powderbed fusion processes, Additive Manufacturing, 22 (2018) 800-806.
[42] M. Pavan, M. Faes, D. Strobbe, B. Van Hooreweder, T. Craeghs, D. Moens, W. Dewulf, On the influence of inter-layer time and energy density on selected critical-to-quality properties of PA12 parts produced via laser sintering, Polymer testing, 61 (2017) 386-395.
[43] S. Yang, J. Evans, Metering and dispensing of powder; the quest for new solid freeforming techniques, Powder Technology, 178 (2007) 56-72.

[44] S. Ziegelmeier, F. Wöllecke, C. Tuck, R. Goodridge, R. Hague, Characterizing the bulk & flow behaviour of LS polymer powders, in: Proceedings SFF Symposium, Austin (TX), USA, 2013.
[45] M. Krantz, H. Zhang, J. Zhu, Characterization of powder flow: Static and dynamic testing, Powder Technology, 194 (2009) 239-245.
[46] S.C. Ligon, R. Liska, J.r. Stampfl, M. Gurr, R. Mülhaupt, Polymers for 3D printing and customized additive manufacturing, Chemical reviews, 117 (2017) 10212-10290.
[47] F. Yang, A. Schnuerch, X. Chen, Quantitative influences of successive reuse on thermal decomposition, molecular evolution, and elemental composition of polyamide 12 residues in selective laser sintering, The International Journal of Advanced Manufacturing Technology, (2021) 1-18.
[48] L. Verbelen, S. Dadbakhsh, M. Van den Eynde, J.-P. Kruth, B. Goderis, P. Van Puyvelde, Characterization of polyamide powders for determination of laser sintering processability, European Polymer Journal, 75 (2016) 163-174.
[49] S. Weinmann, C. Bonten, Recycling of PA12 powder for selective laser sintering, in: AIP Conference Proceedings, AIP Publishing LLC, 2020, pp. 020056.
[50] M.A. Schaffer, K.B. McAuley, M.F. Cunningham, E.K. Marchildon, Experimental study and modeling of nylon polycondensation in the melt phase, Industrial & engineering chemistry research, 42 (2003) 2946-2959.
[51] M. Uddin, D. Williams, A. Blencowe, Recycling of Selective Laser Sintering Waste Nylon Powders into Fused Filament Fabrication Parts Reinforced with Mg Particles, Polymers, 13 (2021) 2046.
[52] W. Yusoff, A. Thomas, The effect of employing an effective laser sintering scanning strategy and energy density value on eliminating “orange peel” on a selective laser sintered part, International Association for Management of Technology, (2008).
[53] R.S. Evans, D.L. Bourell, J.J. Beaman, M.I. Campbell, Rapid manufacturing of silicon carbide composites, Rapid Prototyping Journal, (2005).
[54] Y. Guo, K. Jiang, D.L. Bourell, Accuracy and mechanical property analysis of LPA12 parts fabricated by laser sintering, Polymer Testing, 42 (2015) 175-180.
[55] N. Zobeiry, A. Forghani, C. Li, K. Gordnian, R. Thorpe, R. Vaziri, G. Fernlund, A. Poursartip, Multiscale characterization and representation of composite materials during

processing, Philosophical Transactions of the Royal Society A: Mathematical, Physical and Engineering Sciences, 374 (2016) 20150278.
[56] R.-J. Wang, L. Wang, L. Zhao, Z. Liu, Influence of process parameters on part shrinkage in SLS, The International Journal of Advanced Manufacturing Technology, 33 (2007) 498-504.
[57] G. Strano, L. Hao, R. Everson, K. Evans, Multi-objective optimization of selective laser sintering processes for surface quality and energy saving, Proceedings of the Institution of Mechanical Engineers, Part B: Journal of Engineering Manufacture, 225 (2011) 1673-1682.
[58] C.C. Seepersad, T. Govett, K. Kim, M. Lundin, D. Pinero, A designer's guide for dimensioning and tolerancing SLS parts, in: 2012 International Solid Freeform Fabrication Symposium, University of Texas at Austin, 2012.
[59] T. Gornet, K. Davis, T. Starr, K. Mulloy, Characterization of Selective Laser Sintering™ Materials to Determine Process Stability 546, in: 2002 International Solid Freeform Fabrication Symposium, 2002.
[60] H. Zarringhalam, N. Hopkinson, N. Kamperman, J. De Vlieger, Effects of processing on microstructure and properties of SLS Nylon 12, Materials Science and Engineering: A, 435 (2006) 172-180.
[61] E. Moeskops, N. Kamperman, B. van de Vorst, R. Knoppers, Creep behaviour of polyamide in selective laser sintering, in: 2004 International Solid Freeform Fabrication Symposium, 2004.
[62] L. Telen, P. Van Puyvelde, B. Goderis, Random copolymers from polyamide 11 and polyamide 12 by reactive extrusion: Synthesis, eutectic phase behavior, and polymorphism, Macromolecules, 49 (2016) 876-890.
[63] C. Cai, W.S. Tey, J. Chen, W. Zhu, X. Liu, T. Liu, L. Zhao, K. Zhou, Comparative study on 3D printing of polyamide 12 by selective laser sintering and multi jet fusion, Journal of Materials Processing Technology, 288 (2021) 116882.
[64] L. Li, M.H. Koch, W.H. de Jeu, Crystalline structure and morphology in nylon-12: A small- and wide-angle X-ray scattering study, Macromolecules, 36 (2003) 1626-1632.
[65] C.C. Kai, Y.W. Yee, T.M. Jen, L.E. Jia, Understanding the link between process parameters, microstructure and mechanical properties of laser sintered PA12 parts through X-ray computed tomography, (2016).

[66] B. Van Hooreweder, F. De Coninck, D. Moens, R. Boonen, P. Sas, Microstructural characterization of SLS-PA12 specimens under dynamic tension/compression excitation, Polymer testing, 29 (2010) 319-326.
[67] F. Kuehnlein, D. Drummer, D. Rietzel, A. Seefried, Degradation Behavior and Material Properties of PA 12 Plastic Powders Processed by Powder Based Additive Manufacturing Technologies, na, 2010.
[68] R. Goodridge, R. Hague, C. Tuck, Effect of long-term ageing on the tensile properties of a polyamide 12 laser sintering material, Polymer Testing, 29 (2010) 483-493.
[69] K. Kozlovsky, J. Schiltz, T. Kreider, M. Kumar, S. Schmid, Mechanical properties of reused nylon feedstock for powder-bed additive manufacturing in orthopedics, Procedia Manufacturing, 26 (2018) 826-833.
[70] A. Touris, A. Turcios, E. Mintz, S.R. Pulugurtha, P. Thor, M. Jolly, U. Jalgaonkar, Effect of molecular weight and hydration on the tensile properties of polyamide 12, Results in Materials, 8 (2020) 100149.
[71] S. Chatterjee, F. Nüesch, B. Chu, Crystalline and tensile properties of carbon nanotube and graphene reinforced polyamide 12 fibers, Chemical Physics Letters, 557 (2013) 92-96.
[72] S.-L. Sindinger, C. Kralovec, D. Tasch, M. Schagerl, Thickness dependent anisotropy of mechanical properties and inhomogeneous porosity characteristics in laser-sintered polyamide 12 specimens, Additive Manufacturing, 33 (2020) 101141.
[73] F. Bobaru, Influence of van der Waals forces on increasing the strength and toughness in dynamic fracture of nanofibre networks: a peridynamic approach, Modelling and Simulation in Materials Science and Engineering, 15 (2007) 397.
[74] A. Gleadall, Mechanical properties of biodegradable polymers for medical applications, in: Modelling degradation of bioresorbable polymeric medical devices, Elsevier, 2015, pp. 163-199.
[75] J. Beauson, G. Schillani, L. Van der Schueren, S. Goutianos, The effect of processing conditions and polymer crystallinity on the mechanical properties of unidirectional self-reinforced PLA composites, Composites Part A: Applied Science and Manufacturing, 152 (2022) 106668.
[76] E.C. Hofland, I. Baran, D.A. Wismeijer, Correlation of process parameters with mechanical properties of laser sintered PA12 parts, Advances in materials science and engineering, 2017 (2017).

[77] X.-f. Li, J.-h. Dong, Study on curve of Pe-heating temperature control in selective laser sintering, in: Proceedings. The 2009 International Symposium on Web Information Systems and Applications (WISA 2009), Citeseer, 2009, pp. 156.
[78] M. Schmid, R. Kleijnen, M. Vetterli, K. Wegener, Influence of the origin of polyamide 12 powder on the laser sintering process and laser sintered parts, Applied Sciences, 7 (2017) 462.
[79] V. Beal, R. Paggi, G. Salmoria, A. Lago, Statistical evaluation of laser energy density effect on mechanical properties of polyamide parts manufactured by selective laser sintering, Journal of Applied Polymer Science, 113 (2009) 2910-2919.
[80] A. Wegner, G. Witt, Correlation of process parameters and part properties in laser sintering using response surface modeling, Physics Procedia, 39 (2012) 480-490.
[81] S. Akande, K. Dalgarno, J. Munguia, J. Pallari, Assessment of tests for use in process and quality control systems for selective laser sintering of polyamide powders, Journal of Materials Processing Technology, 229 (2016) 549-561.
[82] T.L. Starr, T.J. Gornet, J.S. Usher, The effect of process conditions on mechanical properties of laser ‐ sintered nylon, Rapid Prototyping Journal, (2011).
[83] P.K. Jain, P.M. Pandey, P. Rao, Effect of delay time on part strength in selective laser sintering, The International Journal of Advanced Manufacturing Technology, 43 (2009) 117-126.
[84] M. Monzón, P.M. Hernández, A.N. Benftez, M.D. Marrero, Á. Fernández, Predictability of plastic parts behaviour made from rapid manufacturing, Tsinghua Science and Technology, 14 (2009) 100-107.
[85] R. Goodridge, C. Tuck, R. Hague, Laser sintering of polyamides and other polymers, Progress in Materials science, 57 (2012) 229-267.
[86] B. Chen, Y. Wang, S. Berretta, O. Ghita, Poly Aryl Ether Ketones (PAEKs) and carbon-reinforced PAEK powders for laser sintering, Journal of Materials Science, 52 (2017) 6004-6019.
[87] S. Berretta, K.E. Evans, O. Ghita, Processability of PEEK, a new polymer for high temperature laser sintering (HT-LS), European Polymer Journal, 68 (2015) 243-266.
[88] K. McAlea, Materials and applications for the Selective Laser Sintering, in: Process, Proc. 7^< th> Int. Conf. on Rapid Prototyping, 1997, pp. 23-33.
[89] S. Ziegelmeier, P. Christou, F. Wöllecke, C. Tuck, R. Goodridge, R. Hague, E. Krampe, E. Wintermantel, An experimental study into the effects of bulk and flow behaviour of laser

sintering polymer powders on resulting part properties, Journal of Materials Processing Technology, 215 (2015) 239-250.
[90] G. Wang, P. Wang, Z. Zhen, W. Zhang, J. Ji, Preparation of PA12 microspheres with tunable morphology and size for use in SLS processing, Materials & Design, 87 (2015) 656-662.
[91] S. Arai, S. Tsunoda, R. Kawamura, K. Kuboyama, T. Ougizawa, Comparison of crystallization characteristics and mechanical properties of poly (butylene terephthalate) processed by laser sintering and injection molding, Materials & Design, 113 (2017) 214-222.
[92] L. Wang, A. Kiziltas, D.F. Mielewski, E.C. Lee, D.J. Gardner, Closed-loop recycling of polyamide12 powder from selective laser sintering into sustainable composites, Journal of Cleaner Production, 195 (2018) 765-772.
[93] F. Yang, T. Jiang, X. Chen, G. Lalier, J. Bartolone, Active Interlayer Heating for Sustainable Selective Laser Sintering With Reclaimed Polyamide 12 Powders, in: International Symposium on Flexible Automation, American Society of Mechanical Engineers, 2020, pp. V001T009A007.
[94] P. Obst, M. Launhardt, D. Drummer, P. Osswald, T. Osswald, Failure criterion for PA12 SLS additive manufactured parts, Additive Manufacturing, 21 (2018) 619-627.
[95] P. Peyre, Y. Rouchausse, D. Defauchy, G. Régnier, Experimental and numerical analysis of the selective laser sintering (SLS) of PA12 and PEKK semi-crystalline polymers, Journal of Materials Processing Technology, 225 (2015) 326-336.
[96] G. Salmoria, J. Leite, R. Paggi, A. Lago, A. Pires, Selective laser sintering of PA12/HDPE blends: Effect of components on elastic/plastic behavior, Polymer Testing, 27 (2008) 654-659.
[97] T. Childs, M. Berzins, G. Ryder, A. Tontowi, Selective laser sintering of an amorphous polymer—simulations and experiments, Proceedings of the Institution of Mechanical Engineers, Part B: Journal of Engineering Manufacture, 213 (1999) 333-349.
[98] J. Kim, T. Creasy, Selective laser sintering characteristics of nylon 6/clay-reinforced nanocomposite, Polymer Testing, 23 (2004) 629-636.
[99] C. Yan, L. Hao, L. Xu, Y. Shi, Preparation, characterisation and processing of carbon fibre/polyamide-12 composites for selective laser sintering, Composites Science and Technology, 71 (2011) 1834-1841.

[100] D. Pham, K. Dotchev, W. Yusoff, Improvement of part surface finishing in laser sintering by experimental design optimisation (DOE), in: 3rd Intelligent Production Machines and Systems Virtual International Conference, Elsevier, 2007.
[101] J. Guo, J. Bai, K. Liu, J. Wei, Surface quality improvement of selective laser sintered polyamide 12 by precision grinding and magnetic field-assisted finishing, Materials & Design, 138 (2018) 39-45.
[102] F. Yang, T. Jiang, X. Chen, G. Lalier, J. Bartolone, A Control of Surface Quality in Selective Laser Sintering Additive Manufacturing with Reclaimed Polyamide Materials, in: 2021 International Solid Freeform Fabrication Symposium, University of Texas at Austin, 2021.
[103] C. Balemans, S.F. Looijmans, G. Grosso, M.A. Hulsen, P.D. Anderson, Numerical analysis of the crystallization kinetics in SLS, Additive Manufacturing, 33 (2020) 101126.
[104] T.D. Ngo, A. Kashani, G. Imbalzano, K.T. Nguyen, D. Hui, Additive manufacturing (3D printing): A review of materials, methods, applications and challenges, Composites Part B: Engineering, 143 (2018) 172-196.
[105] C. Majewski, H. Zarringhalam, N. Hopkinson, Effect of the degree of particle melt on mechanical properties in selective laser-sintered Nylon-12 parts, Proceedings of the Institution of Mechanical Engineers, Part B: Journal of Engineering Manufacture, 222 (2008) 1055-1064.
[106] D. Drummer, K. Wudy, F. Kühnlein, M. Drexler, Polymer blends for selective laser sintering: material and process requirements, Physics Procedia, 39 (2012) 509-517.
[107] C. El-Mazry, M.B. Hassine, O. Correc, X. Colin, Thermal oxidation kinetics of additive free polyamide 6-6, Polymer degradation and stability, 98 (2013) 22-36.
[108] T.T. Diller, M. Yuan, D.L. Bourell, J.J. Beaman, Thermal model and measurements of polymer laser sintering, Rapid Prototyping Journal, (2015).
[109] M. Yuan, T.T. Diller, D. Bourell, J. Beaman, Thermal conductivity of polyamide 12 powder for use in laser sintering, Rapid Prototyping Journal, (2013).
[110] S. Bernard, L. Youinou, P. Gillard, MIE determination and thermal degradation study of PA12 polymer powder used for laser sintering, Journal of Loss Prevention in the Process Industries, 26 (2013) 1493-1500.
[111] K.T. Gillen, J. Wise, R.L. Clough, General solution for the basic autoxidation scheme, Polymer Degradation and Stability, 47 (1995) 149-161.

[112] L. Rincon-Rubio, B. Fayolle, L. Audouin, J. Verdu, A general solution of the closed-loop kinetic scheme for the thermal oxidation of polypropylene, Polymer Degradation and Stability, 74 (2001) 177-188.
[113] X. Colin, B. Fayolle, L. Audouin, J. Verdu, About a quasi-universal character of unstabilised polyethylene thermal oxidation kinetics, Polymer Degradation and Stability, 80 (2003) 67-74.
[114] X. Colin, L. Audouin, J. Verdu, Determination of thermal oxidation rate constants by an inverse method. Application to polyethylene, Polymer Degradation and Stability, 86 (2004) 309-321.
[115] S. Laun, H. Pasch, N. Longiéras, C. Degoulet, Molar mass analysis of polyamides-11 and-12 by size exclusion chromatography in HFiP, Polymer, 49 (2008) 4502-4509.
[116] N. Khelidj, X. Colin, L. Audouin, J. Verdu, C. Monchy-Leroy, V. Prunier, Oxidation of polyethylene under irradiation at low temperature and low dose rate. Part II. Low temperature thermal oxidation, Polymer degradation and stability, 91 (2006) 1598-1605.
[117] P. Parandoush, D. Lin, A review on additive manufacturing of polymer-fiber composites, Composite Structures, 182 (2017) 36-53.
[118] S. Singh, V. Sharma, A. Sachdeva, Progress in selective laser sintering using metallic powders: a review, Materials Science and Technology, 32 (2016) 760-772.
[119] K. McAlea, Materials and applications for the Selective Laser Sintering, in: Process 7th International Conference on Rapid Prototyping, 1997, pp. 23-33.
[120] Z. Xu, Y. Wang, D. Wu, K.P. Ananth, J. Bai, The process and performance comparison of polyamide 12 manufactured by multi jet fusion and selective laser sintering, Journal of Manufacturing Processes, 47 (2019) 419-426.
[121] W.L. Hawkins, Polymer degradation, in: Polymer Degradation and Stabilization, Springer, 1984, pp. 3-34.
[122] K. DePalma, M. Walluk, A. Murtaugh, J. Hilton, S. McConky, B. Hilton, Assessment of 3D printing using fused deposition modeling and selective laser sintering for a circular economy, Journal of Cleaner Production, (2020) 121567.
[123] Y. Way, D. Pham, K. Dotchev, Investigation of the thermal properties of different grades Polyamide 12 (PA12) in improving laser sintering process (SLS), in: Applied Mechanics and Materials, Trans Tech Publ, 2014, pp. 294-296.

[124] P. Mägi, A. Krumme, M. Pohlak, Recycling of PA-12 in Additive Manufacturing and the Improvement of its Mechanical Properties, in: Key Engineering Materials, Trans Tech Publ, 2016, pp. 9-14.
[125] G. Salmoria, V. Lauth, M. Cardenuto, R. Magnago, Characterization of PA12/PBT specimens prepared by selective laser sintering, Optics & Laser Technology, 98 (2018) 92-96.
[126] K. Król-Morkisz, K. Pielichowska, Thermal decomposition of polymer nanocomposites with functionalized nanoparticles, in: Polymer Composites with Functionalized Nanoparticles, Elsevier, 2019, pp. 405-435.
[127] A. Gavezzotti, Molecular symmetry, melting temperatures and melting enthalpies of substituted benzenes and naphthalenes, Journal of the Chemical Society, Perkin Transactions 2, (1995) 1399-1404.
[128] G. Pezzin, F. Zilio-Grandi, P. Sanmartin, The dependence of the glass transition temperature on molecular weight for polyvinylchloride, European Polymer Journal, 6 (1970) 1053-1061.
[129] T. Kwei, E.M. Pearce, J.R. Pennacchia, M. Charton, Correlation between the glass transition temperatures of polymer mixtures and intermolecular force parameters, Macromolecules, 20 (1987) 1174-1176.
[130] G.G. Naumis, Glass transition phenomenology and flexibility: An approach using the energy landscape formalism, Journal of non-crystalline solids, 352 (2006) 4865-4870.
[131] A. Silberman, E. Raninson, I. Dolgopolsky, S. Kenig, The effect of pigments on the crystallization and properties of polypropylene, Polymers for Advanced Technologies, 6 (1995) 643-652.
[132] M. Huda, L. Drzal, D. Ray, A. Mohanty, M. Mishra, Natural-fiber composites in the automotive sector, in: Properties and performance of natural-fibre composites, Elsevier, 2008, pp. 221-268.
[133] R. Pinal, Effect of molecular symmetry on melting temperature and solubility, Organic & biomolecular chemistry, 2 (2004) 2692-2699.
[134] P. Gijsman, D. Tummers, K. Janssen, Differences and similarities in the thermooxidative degradation of polyamide 46 and 66, Polymer degradation and stability, 49 (1995) 121-125.
[135] R. Ningthoujam, Synthesis and Characterization of Borides, Carbides, and Nitrides and Their Applications, in: Materials under extreme conditions, Elsevier, 2017, pp. 337-375.

[136] B. Berman, 3-D printing: The new industrial revolution, Business horizons, 55 (2012) 155-162.
[137] N. Afshar-Mohajer, C.-Y. Wu, T. Ladun, D.A. Rajon, Y. Huang, Characterization of particulate matters and total VOC emissions from a binder jetting 3D printer, Building and Environment, 93 (2015) 293-301.
[138] Y. Yang, L. Li, Total volatile organic compound emission evaluation and control for stereolithography additive manufacturing process, Journal of Cleaner Production, 170 (2018) 1268-1278.
[139] R. Huang, M. Riddle, D. Graziano, J. Warren, S. Das, S. Nimbalkar, J. Cresko, E. Masanet, Energy and emissions saving potential of additive manufacturing: the case of lightweight aircraft components, Journal of Cleaner Production, 135 (2016) 1559-1570.
[140] S. Ford, M. Despeisse, Additive manufacturing and sustainability: an exploratory study of the advantages and challenges, Journal of cleaner Production, 137 (2016) 1573-1587.
[141] T. Peng, K. Kellens, R. Tang, C. Chen, G. Chen, Sustainability of additive manufacturing: An overview on its energy demand and environmental impact, Additive Manufacturing, 21 (2018) 694-704.
[142] S.H. Huang, P. Liu, A. Mokasdar, L. Hou, Additive manufacturing and its societal impact: a literature review, The International Journal of Advanced Manufacturing Technology, 67 (2013) 1191-1203.
[143] R. Betha, V. Selvam, D.R. Blake, R. Balasubramanian, Emission characteristics of ultrafine particles and volatile organic compounds in a commercial printing center, Journal of the Air & Waste Management Association, 61 (2011) 1093-1101.
[144] L. Bravi, F. Murmura, G. Santos, Additive manufacturing: possible problems with indoor air quality, Procedia Manufacturing, 41 (2019) 952-959.
[145] C.-C. Kuo, L.-C. Liu, W.-F. Teng, H.-Y. Chang, F.-M. Chien, S.-J. Liao, W.-F. Kuo, C.-M. Chen, Preparation of starch/acrylonitrile-butadiene-styrene copolymers (ABS) biomass alloys and their feasible evaluation for 3D printing applications, Composites Part B: Engineering, 86 (2016) 36-39.
[146] S. Khaki, E. Duffy, A.F. Smeaton, A. Morrin, Monitoring of Particulate Matter Emissions from 3D Printing Activity in the Home Setting, Sensors, 21 (2021) 3247.

[147] H. Jeon, J. Park, S. Kim, K. Park, C. Yoon, Effect of nozzle temperature on the emission rate of ultrafine particles during 3D printing, Indoor Air, 30 (2020) 306-314.
[148] J. Gu, E. Uhde, M. Wensing, F. Xia, T. Salthammer, Emission control of desktop 3D printing: the effects of a filter cover and an air purifier, Environmental Science & Technology Letters, 6 (2019) 499-503.
[149] A. Damanhuri, A. Subki, A. Hariri, B. Tee, M. Fauadi, M. Hussin, M. Mustafa, Comparative study of selected indoor concentration from selective laser sintering process using virgin and recycled polyamide nylon (PA12), in: IOP Conference Series: Earth and Environmental Science, IOP Publishing, 2019, pp. 012014.
[150] A.A.M. Damanhuri, M.H.F.M. Fauadi, A. Hariri, M.R. Alkahari, M.R. Omar, Emission of selected environmental exposure from selective laser sintering (SLS) polyamide nylon (PA12) 3D printing process, Journal of Safety, Health & Ergonomics, 1 (2019).
[151] Q. Zhang, G. Sharma, J.P. Wong, A.Y. Davis, M.S. Black, P. Biswas, R.J. Weber, Investigating particle emissions and aerosol dynamics from a consumer fused deposition modeling 3D printer with a lognormal moment aerosol model, Aerosol Science and Technology, 52 (2018) 1099-1111.
[152] M.E. Vance, V. Pegues, S. Van Montfrans, W. Leng, L.C. Marr, Aerosol emissions from fuse-deposition modeling 3D printers in a chamber and in real indoor environments, Environmental Science & Technology, 51 (2017) 9516-9523.
[153] E.F. Katz, J.D. Goetz, C. Wang, J.L. Hart, B. Terranova, M.L. Taheri, M.S. Waring, P.F. DeCarlo, Chemical and physical characterization of 3D printer aerosol emissions with and without a filter attachment, Environmental Science & Technology, 54 (2019) 947-954.
[154] J. Gu, M. Wensing, E. Uhde, T. Salthammer, Characterization of particulate and gaseous pollutants emitted during operation of a desktop 3D printer, Environment international, 123 (2019) 476-485.
[155] B.E. Cummings, M.S. Waring, Potted plants do not improve indoor air quality: a review and analysis of reported VOC removal efficiencies, Journal of exposure science & environmental epidemiology, 30 (2020) 253-261.
[156] Y.-H. Lin, M. Arashiro, P.W. Clapp, T. Cui, K.G. Sexton, W. Vizuete, A. Gold, I. Jaspers, R.C. Fry, J.D. Surratt, Gene expression profiling in human lung cells exposed to isoprene-derived secondary organic aerosol, Environmental science & technology, 51 (2017) 8166-8175.

[157] Y. Yang, M. Waring, Secondary organic aerosol formation initiated by α‐terpineol ozonolysis in indoor air, Indoor Air, 26 (2016) 939-952.
[158] B.E. Cummings, M.S. Waring, Predicting the importance of oxidative aging on indoor organic aerosol concentrations using the two‐dimensional volatility basis set (2D‐VBS), Indoor air, 29 (2019) 616-629.
[159] P. Azimi, D. Zhao, C. Pouzet, N.E. Crain, B. Stephens, Emissions of ultrafine particles and volatile organic compounds from commercially available desktop three-dimensional printers with multiple filaments, Environmental science & technology, 50 (2016) 1260-1268.
[160] A.Y. Davis, Q. Zhang, J.P. Wong, R.J. Weber, M.S. Black, Characterization of volatile organic compound emissions from consumer level material extrusion 3D printers, Building and Environment, 160 (2019) 106209.
[161] S. Ding, B.F. Ng, X. Shang, H. Liu, X. Lu, M.P. Wan, The characteristics and formation mechanisms of emissions from thermal decomposition of 3D printer polymer filaments, Science of the Total Environment, 692 (2019) 984-994.
[162] A.A.M. Damanhuri, A. Hariri, M.R. Alkahari, M.H.F.M. Fauadi, S.F.Z. Bakri, Indoor air concentration from selective laser sintering 3D printer using virgin polyamide nylon (PA12) powder: a pilot study, International Journal of Integrated Engineering, 11 (2019) 140-149.
[163] P. Azimi, T. Fazli, B. Stephens, Predicting concentrations of ultrafine particles and volatile organic compounds resulting from desktop 3D printer operation and the impact of potential control strategies, Journal of Industrial Ecology, 21 (2017) S107-S119.
[164] T. Phillips, S. Fish, J. Beaman, Development of an automated laser control system for improving temperature uniformity and controlling component strength in selective laser sintering, Additive Manufacturing, 24 (2018) 316-322.
[165] F. Sillani, R.G. Kleijnen, M. Vetterli, M. Schmid, K. Wegener, Selective laser sintering and multi jet fusion: Process-induced modification of the raw materials and analyses of parts performance, Additive Manufacturing, 27 (2019) 32-41.
[166] B. Van Hooreweder, D. Moens, R. Boonen, J.-P. Kruth, P. Sas, On the difference in material structure and fatigue properties of nylon specimens produced by injection molding and selective laser sintering, Polymer Testing, 32 (2013) 972-981.
[167] M. Schmidt, D. Pohle, T. Rechtenwald, Selective laser sintering of PEEK, CIRP annals, 56 (2007) 205-208.

[168] W. Yan, Y. Zhang, X. Wang, Simulation of VOC emissions from building materials by using the state-space method, Building and Environment, 44 (2009) 471-478.
[169] H. Hu, Y. Zhang, X. Wang, J. Little, An analytical mass transfer model for predicting VOC emissions from multi-layered building materials with convective surfaces on both sides, International Journal of Heat and Mass Transfer, 50 (2007) 2069-2077.
[170] Y. Zhang, J. Jiang, Y. Bai, J. Liu, H. Shao, C. Wu, Z. Guo, A fractional mass transfer model for simulating VOC emissions from porous, dry building material, Building and Environment, 152 (2019) 182-191.
[171] A. Stamatelopoulou, D. Asimakopoulos, T. Maggos, Effects of PM, TVOCs and comfort parameters on indoor air quality of residences with young children, Building and Environment, 150 (2019) 233-244.
[172] Y. Wang, T. Yang, Z. He, L. Sun, X. Yu, J. Zhao, Y. Hu, S. Zhang, J. Xiong, A general regression method for accurately determining the key parameters of VOC emissions from building materials/furniture in a ventilated chamber, Atmospheric Environment, 231 (2020) 117527.
[173] J. Xiong, F. Chen, L. Sun, X. Yu, J. Zhao, Y. Hu, Y. Wang, Characterization of VOC emissions from composite wood furniture: Parameter determination and simplified model, Building and Environment, 161 (2019) 106237.
[174] S.H. Klippstein, F. Heiny, N. Pashikanti, M. Gessler, H.-J. Schmid, Powder Spread Process Monitoring in Polymer Laser Sintering and its Influences on Part Properties, Jom, 74 (2022) 1149-1157.
[175] N. Southon, P. Stavroulakis, R. Goodridge, R. Leach, In-process measurement and monitoring of a polymer laser sintering powder bed with fringe projection, Materials & Design, 157 (2018) 227-234.
[176] A. Lewis, M. Gardner, A. McElroy, T. Milner, S. Fish, J. Beaman, In-situ process monitoring and ex-situ part quality assessment of selective laser sintering using optical coherence tomography, in: 2016 International Solid Freeform Fabrication Symposium, University of Texas at Austin, 2016.
[177] D.M. Sassaman, M.S. Ide, D. Kovar, J.J. Beaman, Design of an In-situ microscope for selective laser sintering, Additive Manufacturing Letters, 2 (2022) 100033.

[178] M. Abdelrahman, T.L. Starr, Quality certification and control of polymer laser sintering: layerwise temperature monitoring using thermal imaging, The International Journal of Advanced Manufacturing Technology, 84 (2016) 831-842.
[179] A. Gusarov, T. Laoui, L. Froyen, V. Titov, Contact thermal conductivity of a powder bed in selective laser sintering, International Journal of Heat and Mass Transfer, 46 (2003) 1103-1109.